

University of Windsor

Scholarship at UWindor

Electronic Theses and Dissertations

Theses, Dissertations, and Major Papers

3-12-2020

Development of a Vibroacoustic Noise Prediction Model for Multi-Layered Concentric Cylinders Under Electromagnetic Forced Vibration

Frank Angione
University of Windsor

Follow this and additional works at: <https://scholar.uwindsor.ca/etd>

Recommended Citation

Angione, Frank, "Development of a Vibroacoustic Noise Prediction Model for Multi-Layered Concentric Cylinders Under Electromagnetic Forced Vibration" (2020). *Electronic Theses and Dissertations*. 8315. <https://scholar.uwindsor.ca/etd/8315>

This online database contains the full-text of PhD dissertations and Masters' theses of University of Windsor students from 1954 forward. These documents are made available for personal study and research purposes only, in accordance with the Canadian Copyright Act and the Creative Commons license—CC BY-NC-ND (Attribution, Non-Commercial, No Derivative Works). Under this license, works must always be attributed to the copyright holder (original author), cannot be used for any commercial purposes, and may not be altered. Any other use would require the permission of the copyright holder. Students may inquire about withdrawing their dissertation and/or thesis from this database. For additional inquiries, please contact the repository administrator via email (scholarship@uwindsor.ca) or by telephone at 519-253-3000ext. 3208.

**Development of a Vibroacoustic Noise Prediction Model for Multi-Layered
Concentric Cylinders Under Electromagnetic Forced Vibration**

By

Frank Angione

A Dissertation
Submitted to the Faculty of Graduate Studies
through the Department of Mechanical, Automotive and Materials Engineering
in Partial Fulfillment of the Requirements for
the Degree of Doctor of Philosophy
at the University of Windsor

Windsor, Ontario, Canada

2020

© 2020 Frank Angione

**Development of a Vibroacoustic Noise Prediction Model for Multi-Layered
Concentric Cylinders Under Electromagnetic Force Vibration**

by

Frank Angione

APPROVED BY:

A. Lenzi, External Examiner
Federal University of Santa Catarina

E. Tam
Department of Civil and Environmental Engineering

V. Stoilov
Department of Mechanical, Automotive and Materials Engineering

R. Gaspar
Department of Mechanical, Automotive and Materials Engineering

C. Novak, Advisor
Department of Mechanical, Automotive and Materials Engineering

February 4th, 2020

DECLARATION OF ORIGINALITY

I hereby certify that I am the sole author of this thesis and that no part of this thesis has been published or submitted for publication.

I certify that, to the best of my knowledge, my thesis does not infringe upon anyone's copyright nor violate any proprietary rights and that any ideas, techniques, quotations, or any other material from the work of other people included in my thesis, published or otherwise, are fully acknowledged in accordance with the standard referencing practices. Furthermore, to the extent that I have included copyrighted material that surpasses the bounds of fair dealing within the meaning of the Canada Copyright Act, I certify that I have obtained a written permission from the copyright owner(s) to include such material(s) in my thesis and have included copies of such copyright clearances to my appendix.

I declare that this is a true copy of my thesis, including any final revisions, as approved by my thesis committee and the Graduate Studies office, and that this thesis has not been submitted for a higher degree to any other University or Institution.

ABSTRACT

Vibroacoustic noise prediction models for electrically excited cylinders are used to predict the noise emissions for operating dry-type air-core reactors. These reactors are used to limit current and regulate voltage in electrical transmission and distribution grids. During operation, these reactors produce unwanted, electrically induced noise which is created by forced vibration due to the generated magnetic field from the electrical load being applied to the coil. The reactors designed with complex constructions having multiple winding coils will produce greater amounts of structure-borne sound. Given that these dynamically behave as multiple layers of concentric cylinders, cylindrical vibration theory can be used to predict their behaviour. The goal of this research was to construct and validate an innovative vibroacoustic prediction model that accurately represents the mechanisms of the structure-borne noise generation of the reactor to accurately predict the noise emission levels during the design phase.

For the Trench Limited Coil Operations, having the ability to accurately predict the noise produced by a reactor in the early design stage is critical to maintain a competitive edge in the competitive reactor market by ensuring that acoustic specifications are met. A review of the literature has shown very little work has been done to develop the science to accurately predict the noise generation for complex reactor construction with multiple winding coil packages. Also, the validation process for the current models do not consider a large frequency range and various electrical excitation frequencies. The novelty of this research is the construction of a cylindrical vibroacoustic noise prediction model for complex reactors of multiple

winding packages in conjunction with the validation across a wide range of electrical excitation frequencies.

In this dissertation, a detailed test and literature review is simultaneously presented in order to guide the development of an improved vibroacoustic model and to validate the noise prediction outcomes. A comprehensive literature review found various vibroacoustic models have been developed to represent the vibrational excitation of the reactor cylinder, and in turn compute the output noise emissions. Comprehensive noise and vibration testing of two prototype reactors with induced electrical excitation was conducted using CPB, FFT, directivity, noise source identification (NSI) and Modal analysis. From these analyses, the construction of the model was guided by considering the natural structural modes. In addition, a bank of noise emission data for validation of the proposed models was compiled.

Through the validation process of comparing the proposed vibroacoustic models with the collected reactor noise data, a recommended method for noise prediction was developed. The models coined the Cylindrical Vibroacoustic Model (both single and multiple layered models) were deemed to be the most effective and accurate method for reactor noise prediction. The methodology considers the cylindrical construction of the reactor with multiple layers of concentric cylinders and has been validated over a large electrical excitation frequency range. The outcome of this more versatile vibroacoustic model is the ability to better predict the noise emissions for complex reactor constructions having multiple winding coil packages.

ACKNOWLEDGEMENTS

I would like to acknowledge Trench Canada Limited for their cooperation in this project. Trench provided expertise, equipment and prototypes for the completion of this project.

TABLE OF CONTENTS

DECLARATION OF ORIGINALITYiii

ABSTRACT.....iv

ACKNOWLEDGEMENTSvi

LIST OF FIGURES x

LIST OF TABLESxiv

LIST OF APPENDICES..... xv

NOMENCLATURExvi

CHAPTER 1 INTRODUCTION 1

CHAPTER 2 LITERATURE SURVEY..... 5

 2.1 Reactor Noise Emissions..... 5

 2.2 MRI Noise Emissions..... 11

 2.3 Multi-Degree of Freedom Systems 13

 2.4 Hollow Cylinder Vibration..... 17

 2.5 Review..... 27

CHAPTER 3 EXPERIMENT DETAILS 28

 3.1 Radial Sound Measurements 29

 3.1.1 Equipment and Instrumentation 29

 3.1.2 Experimental Design Setup and Procedure..... 30

 3.1.3 Environmental Considerations..... 33

 3.1.4 Measurement Procedure..... 33

 3.2 Noise Source Identification Measurements..... 34

 3.2.1 Equipment and Instrumentation 34

 3.2.2 Experimental Design Setup and Procedure..... 35

 3.2.3 Environmental Considerations..... 37

3.2.4	Measurement Procedure.....	38
3.3	Modal Analysis Measurements	38
3.3.1	Equipment and Instrumentation.....	39
3.3.2	Experimental Design Setup and Procedure.....	40
3.3.3	Environmental Considerations.....	43
3.3.4	Measurement Procedure.....	43
CHAPTER 4 DATA ANALYSIS AND DISCUSSION		45
4.1	Radial Sound Measurements.....	45
4.1.1	FFT Analysis.....	45
4.1.2	CPB Analysis.....	47
4.1.3	Overall Level Analysis	51
4.1.4	Directivity Analysis	60
4.2	Noise Source Identification (NSI).....	64
4.3	Modal Analysis	80
CHAPTER 5 PROPOSED MODEL.....		92
5.1	Distributed Velocity Model.....	92
5.2	Eigenfrequency MDOF Model.....	95
5.3	Cylindrical Vibroacoustic Model (Single Layered).....	97
5.4	Cylindrical Vibroacoustic Model (Multi-Layered).....	102
CHAPTER 6 MODEL VERIFICATION AND VALIDATION.....		107
6.1	Model Correlation to Test Data.....	107
6.1.1	Reactor 1 Test Data Correlation	108
6.1.2	Reactor 2 Test Data Correlation	114
6.2	Discussion of Model Validity	120
6.2.1	Distributed Velocity Model	120

6.2.2	Eigenfrequency MDOF Model	121
6.2.3	Cylindrical Vibroacoustic Model (Single Layered).....	123
6.2.4	Cylindrical Vibroacoustic Model (Multi-Layered).....	124
6.2.5	Model Comparison.....	125
CHAPTER 7 RECOMMENDATION AND CONCLUSIONS		127
7.1	Conclusions	127
7.2	Recommendations	128
7.3	Future Work	129
REFERENCES/BIBLIOGRAPHY.....		132
Appendix A FFT Analysis Results.....		136
Appendix B CPB Analysis Results		153
Appendix C Noise Source Identification Results.....		170
Appendix D Modal Analysis Results		176
VITA AUCTORIS		205

LIST OF FIGURES

Figure 1-1 – Air-core dry-type reactor construction. [1]	1
Figure 2-1 – Sketch of resulting forces on reactor winding. [2]	6
Figure 2-2 – Stresses in the plane perpendicular to r and z direction. [30]	21
Figure 3-1 – Microphone locations for signal recordings.....	31
Figure 3-2 – Radial sound measurement experimental test setup for the first prototype reactor.	32
Figure 3-3 – Radial sound measurement experimental test setup for the second prototype reactor.	32
Figure 3-4 – Array measurement locations relative to the reactor.....	36
Figure 3-5 – NSI data acquisition setup using a Brüel & Kjær 60-channel sector array.	36
Figure 3-6 – NSI data acquisition top view setup using a Brüel & Kjær 60-channel sector array.....	37
Figure 3-7 – First prototype reactor modal analysis experimental setup.....	41
Figure 3-8 – First prototype reactor modal analysis experimental setup (interior of reactor).	42
Figure 3-9 – Second prototype reactor modal analysis experimental setup.	42
Figure 4-1 – CPB output for 510 Hz electrical excitation frequency at 210 A - prototype reactor 2.	48
Figure 4-2 – Directivity radar plots of overall sound pressure levels at 2 m for each supplied electrical excitation frequency for reactor 1.....	60
Figure 4-3 – Directivity radar plots of overall sound pressure levels at 3 m for each supplied electrical excitation frequency for reactor 2.....	61
Figure 4-4 – Overall NSI contour plot of reactor sound intensity level energized at 300 Hz - Location 1.	66
Figure 4-5 – NSI 1/3-octave sound power level plot of reactor energized at 300 Hz - Location 1.	66
Figure 4-6 – Overall NSI contour plot of reactor sound intensity level energized at 300 Hz - Location 2.	67

Figure 4-7 – NSI 1/3-octave sound power level plot of reactor energized at 300 Hz - Location 2.	67
Figure 4-8 – Overall NSI contour plot of reactor sound intensity level energized at 300 Hz - Location 3.	68
Figure 4-9 – NSI 1/3-octave sound power level plot of reactor energized at 300 Hz - Location 3.	68
Figure 4-10 – Overall NSI contour plot of reactor sound intensity level energized at 300 Hz aerial view.	69
Figure 4-11 – NSI 1/3-octave sound power level plot of reactor energized at 300 Hz aerial view.	69
Figure 4-12 – Overall NSI contour plot of reactor sound intensity level energized at 360 Hz - Location 1.	70
Figure 4-13 – NSI 1/3-octave sound power level plot of reactor energized at 360 Hz - Location 1.	70
Figure 4-14 – Overall NSI contour plot of reactor sound intensity level energized at 360 Hz - Location 2.	71
Figure 4-15 – NSI 1/3-octave sound power level plot of reactor energized at 360 Hz - Location 2.	71
Figure 4-16 – Overall NSI contour plot of reactor sound intensity level energized at 360 Hz - Location 3.	72
Figure 4-17 – NSI 1/3-octave sound power level plot of reactor energized at 360 Hz - Location 3.	72
Figure 4-18 – Overall NSI contour plot of reactor sound intensity level energized at 360 Hz - aerial view.	73
Figure 4-19 – NSI 1/3-octave sound power level plot of reactor energized at 360 Hz - aerial view.	73
Figure 4-20 – Overall NSI contour plot of reactor sound intensity level energized at 420 Hz - Location 1.	74
Figure 4-21 – NSI 1/3-octave sound power level plot of reactor energized at 420 Hz - Location 1.	74

Figure 4-22 – Overall NSI contour plot of reactor sound intensity level energized at 420 Hz - Location 2.	75
Figure 4-23 – NSI 1/3-octave sound power level plot of reactor energized at 420 Hz - Location 2.	75
Figure 4-24 – Overall NSI contour plot of reactor sound intensity level energized at 420 Hz - Location 3.	76
Figure 4-25 – NSI 1/3-octave sound power level plot of reactor emerged 420 Hz - Location 3.	76
Figure 4-26 – Overall NSI contour plot of reactor sound intensity level energized at 420 Hz - aerial view.	77
Figure 4-27 – NSI 1/3-octave sound power level plot of reactor energized at 420 Hz - aerial view.	77
Figure 4-28 – Reactor 1 40.7 Hz Structural Mode.....	87
Figure 4-29 – Reactor 2 42.8 Hz Structural Mode.....	88
Figure 4-30 – Reactor 1 723.2 Hz Structural Mode.....	89
Figure 4-31 – Reactor 2 743.3 Hz Structural Mode.....	90
Figure 5-1 – Illustration of Lorentz force acting on segments along a wire package length.....	93
Figure 5-2 – Mass spring representation of a three-wire package reactor.	96
Figure 6-1 – Benchmarked A-weighted sound pressure levels normalized to 100 A at 2 m for reactor 1.....	107
Figure 6-2 – Benchmarked A-weighted sound pressure levels normalized to 100 A at 2 m for reactor 2.....	108
Figure 6-3 – Current reactor noise emission prediction state of science from literature correlation to reactor 1 test data.	109
Figure 6-4 – Distributed velocity model correlation to reactor 1 test data.	110
Figure 6-5 – Eigenfrequency model correlation to reactor 1 test data.....	111
Figure 6-6 – Cylindrical vibroacoustic single package model correlation to reactor 1 test data.	112
Figure 6-7 – Cylindrical Vibroacoustic multi-package model correlation to reactor 1 test data.	113

Figure 6-8 – Current reactor noise emission prediction state of science from literature correlation to reactor 2 test data. 115

Figure 6-9 – Distributed velocity model correlation to reactor 2 test data. 116

Figure 6-10 – Eigenfrequency model correlation to reactor 2 test data..... 117

Figure 6-11 – Cylindrical vibroacoustic single package model correlation to reactor 2 test data. 118

Figure 6-12 – Cylindrical vibroacoustic multi-package model correlation to reactor 2 test data. 119

LIST OF TABLES

Table 4-1 – A-weighted 1/3-octave sound pressure levels for corresponding electrical excitation frequencies for reactor 1.....	49
Table 4-2 – A-weighted 1/3-octave sound pressure levels for corresponding electrical excitation frequencies for reactor 2.....	50
Table 4-3 – Overall sound pressure levels for each signal, measurement, and supplied electrical frequency for prototype reactor 1.....	51
Table 4-4 – Overall sound pressure levels for each signal, measurement, and supplied electrical frequency for prototype reactor 2.....	56
Table 4-5 – Directivity Index for each measured electrical excitation frequency at each radial measurement location for reactor 1.....	63
Table 4-6 – Directivity Index for each measured electrical excitation frequency at each radial measurement location for reactor 2.....	63
Table 4-7 – Natural Structural Mode Frequencies and Damping Ratios for Reactor 1.....	82
Table 4-8 – Natural Structural Mode Frequencies and Damping Ratios for Reactor 2.....	83
Table 6-1 – Comparison of model performance in predicting reactor operating noise emissions to measure test data.....	125
Table 6-2 – Comparison of model fundamental methodologies.....	126

LIST OF APPENDICES

Appendix A FFT Analysis Results.....	136
Appendix B CPB Analysis Results.....	153
Appendix C Noise Source Identification Results.....	170
Appendix D Modal Analysis Results.....	176

NOMENCLATURE

MOECC	Ministry of the Environment and Climate Change
Reactor(s)	Dry-type air-core reactor(s)
Trench	Trench Limited Coil Operations
NSI	Noise source identification
Pa	Pascal
SPL (L_p)	Sound pressure level
$L_{p,avg}$	Average sound pressure level
FFT	Fast Fourier Transform
SWL (L_w)	Sound power level
dB	Decibel
dBA	A-weighted Decibel
CPB	Constant Percentage Bandwidth
HVDC	High voltage direct current
MRI	Magnetic resonance imaging
MDOF	Multi-degree of freedom
$J_n(\lambda r)$	Bessel function of the first kind of the n order for λr
$Y_n(\lambda r)$	Bessel function of the second kind of the n order for λr
FRF(s)	Frequency response function(s)
NNLS	Non-negative least square
RFP	Rational fraction polynomial
MIF	Mode indicator functions
λ	Eigenvalues
ω	Natural frequency
u_r	Radial vibration displacement
n	Radial wave number
ζ	Axial wave number
r_a	Inner wire package radius
r_b	Outer wire package radius

CHAPTER 1

INTRODUCTION

The dry-type air-core reactor (henceforth, referred to as “reactor(s)”) is an electrical power inductor used for large power systems and industrial applications to limit current and regulate voltage in electrical transmission and distribution grids and for load balancing. The typical construction of the reactor is shown in Figure 1-1. Regardless of their use, these reactors produce unwanted noise during operation. It is important for the manufacturers of these reactors to be able to accurately predict the noise emissions in order to maintain a market competitiveness and to ensure that given acoustic specifications are met. Moreover, having the ability to accurately predict the noise emissions of a reactor at the tender stage of a project will better allow the likelihood of the manufacturer meeting the customer’s “guaranteed” sound levels during the commissioning phase of the installation. This will improve the quality assurance of manufacturing program and reduce costs and lead times for delivery for orders requiring a sound level verification test.

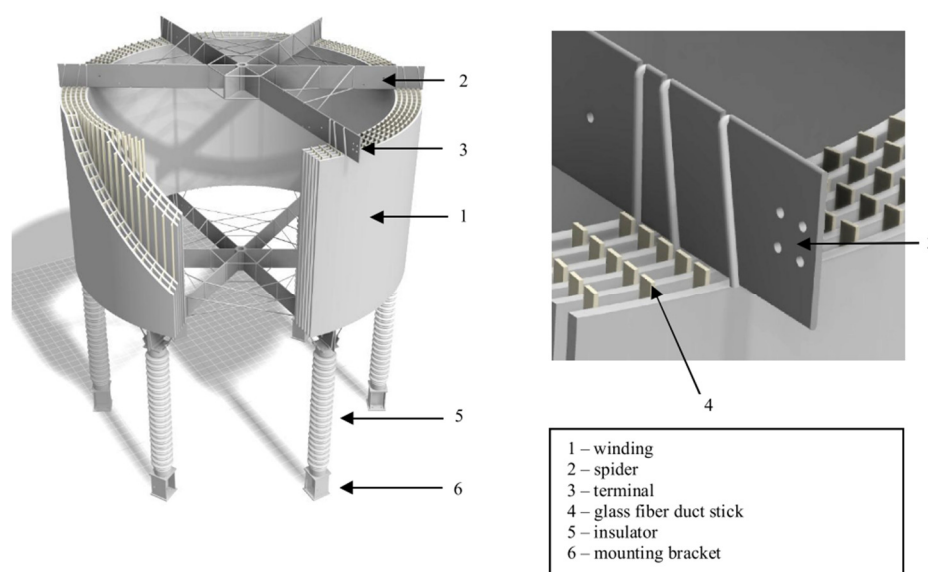


Figure 1-1 – Air-core dry-type reactor construction. [1]

As electrical demands vary depending on the industrial operation or electrical parameters for large power systems, air-core dry-type reactors are typically custom designed and manufactured on an order-by-order basis. Thus, having the ability to predict the expected noise emissions is even more crucial as the reactors are individually custom designed and the noise emissions cannot be quantified or rated by test until the reactor has been constructed. In addition, the reactors coils are hand wound to facilitate the custom construction requirements. As such, there exists some variability in each build. This variability adds to the need for individual prediction of noise given that tested noise emissions for one reactor design are not directly transferable to another.

Although most of the research in the area of reactor noise emission prediction has been published in recent years, there is very limited literature with respect to the topic. Intellectual property in this area is crucial to the success of reactor manufacturers; as such, this has resulted in a lack of much needed published research in the area. In addition, environmental noise guidelines have become stricter in recent years along with industrial operations being encroached upon by residential receptors. This problem is further compounded by the tonal nature of the electrical reactor noise as it is deemed especially annoying. This has had an impact on the reactor manufacturing business given that the need to understand and predict reactor noise emissions is even more critical to meet the stricter environmental noise guidelines and to remain a competitive position in the market.

The current state of the science for the prediction of reactor noise emission levels are based on simplified methodologies used to simulate the reactor's vibroacoustic behaviours based on assumptions that do not accurately represent the physical behaviour of the reactor. The basis of reactor noise emission prediction in recent literature has been

to determine the forced vibration impacts of the reactor due to the reactor's geometry and supplied input current. For this, determining the Lorentz force and estimating the vibration velocity is fundamental to predicting the vibroacoustic behaviour, and in turn, the emitted sound level of the reactor.

The goals for this investigation are to conduct a comparative analysis of the current state of the science for reactor vibroacoustic models and to propose a new methodology that will give a more accurate physical representation of the reactor's vibroacoustic behaviours. To facilitate this, the current vibroacoustic methodologies found in the literature are assessed using measured acoustic data for two prototype reactors provided by Trench Limited Coil Operations (henceforth, referred to as "Trench"). Fast Fourier Transform (FFT) analysis of time signals, Noise Source Identification (NSI) and structural modal analysis were used to assess the accuracy of both the currently used vibroacoustic methodologies and the proposed method to better predict the reactor operating noise emissions developed in this work.

The methods developed in this research to predict a coil's vibration velocity involve the calculation of parameters which more accurately represent the physical construction of the reactor. This includes consideration of the multilayered concentric cylinders which are exposed to forced vibration inputs due to the electromagnetic forces. It is the consideration of the reactions of the multiple cylinders that contributes to the originality of this work.

In summary, the plan and intended outcomes of this dissertation are as follow:

- To provide a comprehensive literature review of the history and current state of science for reactor noise emission prediction. This will include a discussion of the applicability and critical analysis of these methods,
- Develop experimental procedures and approaches for data analysis to validate the modelled outcomes for the prediction of reactor noise emissions under specific operating parameters,
- Investigate and develop alternative approaches to predict reactor noise emissions for specific electrical input conditions and geometrical constraints,
- Discuss the validity of the proposed methodologies for predicting noise,
- Recommend an improved reactor noise prediction model that is more accurate than current approaches and better represents the actual physical makeup of the reactor in the resulting vibroacoustic behaviour.

CHAPTER 2

LITERATURE SURVEY

2.1 Reactor Noise Emissions

The dry-type air-core reactor is used for high voltage, direct current and flexible alternating current transmission system applications. Due to the increased use of power electronics in the transmission and distribution grid, the importance of reactors is ever increasing. However, the reactor also produces noise emissions with strong tonal components; an additional source of undesirable noise to what are often already noisy environments. Further, as the size of the reactor increases, typically so does the amplitude of the produced noise. Also, of concern is the annoyance that is often attributed to the discrete, tonal noise frequencies. As such, solutions to the mitigation of sound levels and sound planning are required for the implantation of power equipment having reactors [2]. Given that substations are often located in densely populated areas, and with increasingly stricter noise emissions guidelines, sound planning has become a large consideration for reactor manufacturers, including Trench. As such, having a better understanding from the literature of the mechanisms associated with the generation of reactor noise will aid in the development of both prediction models and mitigation strategies of the noise during the design of the reactor.

The fundamental mechanism for the generation of reactor noise can be attributed to the Lorentz forces present in the winding body [2]. Lorentz forces are body forces which are caused by the electromagnetic field created by the induced current and voltage in the winding packages of the reactor. These forces, for which most are in the radial direction,

are the driving factor in the generation of vibrations as stated by *Dopplmair et al.* In his research, the Lorentz force is computed as the vector cross product of the reactor's magnetic field density and the current flowing through the coil windings. As shown in Equation 2-1, F is the Lorentz force, I is the current in the windings, and B is the magnetic field density.

$$\vec{F} = I \cdot \vec{l} \times \vec{B} \quad 2-1$$

The radial displacement due to an alternating current generates vibration, which appear as a 'breathing' of the reactor according to *Dopplmair et al.* This behaviour is depicted in the Figure 2-1:

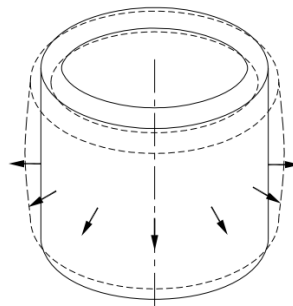


Figure 2-1 – Sketch of resulting forces on reactor winding. [2]

According to *Dopplmair et al.*, this simplistic description of the structural excitation has been the basis for much of the research and practice in this area. These cylindrical 'breathing' modes are similar to that describe by *Blevins* which he took for a cylinder of infinite length [3]. This has been shown to be the best practice in the 2016 publication,

Acoustic Aspects of Dry-Type Air-Core Reactors Specification, Design, Testing, Field Measurements. [2]

In his 2016 research, *Fiorentin et al* compared collected test data to an analytical and a numerical modelling approach to predict the noise emissions of a reactor [4]. The reactor in Fiorentin's research used a simple geometry having only two winding packages which were separated using duct sticks which are plastic or glass fibre spacers that are used to allow airflow between winding packages. This differs from the research considered in this dissertation, which considers significantly more complex reactor geometries with higher numbers of winding packages.

Fiorentin's work used the same electrical theories as Dopplmair to calculate and represent the Lorentz forces as the driving force for the cylinder mechanical excitation. The publications describe an acoustic model that computes the sound power from the RMS vibration velocity of the radiating surface. The sound power equation for the vibration of the sound radiating from the reactor surface is given as:

$$W = \rho_0 c_0 S_W \sigma < \bar{v} >^2 \quad 2-2$$

Where:

- W is the radiated sound power in Watts
- ρ_0 is the density of the air in kg/m^3
- c_0 is the speed of sound in air in m/s
- S_W is the are of the sound radiating surface in m^2

- σ is the radiation efficiency, and
- v is the RMS vibration velocity in m/s over the surface ($\langle \rangle$) and time ($\bar{}$).

The sound pressure can be calculated from the sound power by the following equation:

$$p = \sqrt{\frac{\rho_0 c_0 (W_{rad} + W_{axi})}{2\pi r_{sr}^2}} \quad 2-3$$

where, r_{sr} is the distance from the centre of the reactor winding to the receptor.

Fiorentin determined that the reactor can be considered comparable to a cylindrical source if $\frac{r_{sr}}{H} < 10$. At these dimensions, the sound radiation of the interior wall is negligible, and the axial mode may be neglected. As such, this assumption provides the following:

$$p = \sqrt{\frac{\rho_0 c_0 W_{rad}}{4\pi (r_{sr} + R_e) H}} \quad 2-4$$

where, R_e is the outer radius of the winding. From this pressure, the sound pressure level is calculated with respect to the standard reference pressure of 20×10^{-6} Pa.

The numerical and analytical results given in the research by *Fiorentin et al* were compared to measured sound pressure level data taken at one metre from the outer surface of the reactor. For the experimental measurements, the reactor was loaded with 300 amperes (A) at an electrical excitation frequency of 60 Hz. This resulted in a dominate

acoustic frequency peak at 120 Hz. For the reactor loaded with this configuration, the analytical prediction was 1.0 dB lower than the experimental results, while the numerical simulation gave results that were 4 dB lower. This demonstrated that for a simple geometry reactor, the analytical acoustic model provided close correlation to the experimental sound pressure level. [4]

Previous to the research conducted by *Dopplmair* and *Fiorentin*, a research paper titled *Acoustic noise generated by air power reactor in open-air substation* by *Lilien* was published [5]. The scope of *Lilien's* research was the evaluation of acoustic emissions of a single winding package reactor. In his research, *Lilien* explained the electromagnetic force as the product of the magnetic field and the current in the winding package. This is equivalent to the Lorentz force described by *Dopplmair*. In addition, the Lorentz force was expanded to compute the radial vibration velocity in order to compute the emitted sound pressure. *Lilien* compared his simple model results to multiple versions of measured data for a variety of electrical excitation frequencies. He concluded that his simple method is good enough and within an acceptable range to the measured data. [5]

As *Lilien's* scope of work was limited to a single core reactor, a simple model may be deemed acceptable. In comparison to the research in this dissertation, the present research considers the considerably more complex mechanisms associated with the vibroacoustic behaviour of the reactor.

In the research conducted by *Smede et al*, the design of high-voltage, direct current (HVDC) converter stations for audible noise requirements was considered. To estimate the noise generation from the HVDC converter stations, the sound generated from other

industrial electromagnetic equipment, including air-core reactors, was considered [6]. *Smede* identified transformers, air-core reactors and capacitors as the main electrical sources of the noise emissions for the HVDC stations. These components generate sound through the applied electrical load which creates forces that are distributed within the components. The electromagnetic force on the reactor was again described as the multiplication of the current and magnetic field, or the Lorentz force. This work reiterated that the sound generating forces were primarily in the radial direction, with the excited outer surface of the reactor generating the propagating acoustic waves.

Another significant outcome from *Smede's* research was his explanation for the dominant breathing mode of the charged reactor. It was described that a reactor has one mode shape that dominates the mechanical behaviour for each case of electrical input. This is defined as the breathing mode and is described as follows:

$$f_0 = \frac{1}{\pi D} \sqrt{\frac{E}{\rho}} \quad 2-5$$

Where:

- D is the diameter
- E is the Youngs modulus, and
- ρ is the density of the reactor

Smede claimed that it is possible to design a silent reactor by mismatching the force-harmonics and resonances and increasing the stiffness of the reactor. The research also claimed that they were able to predict the sound power of a reactor with an accuracy of ± 2

dB. The research gave verification of this through full scale measurements. However, in the description of the model, no details were given to the reactor geometry, the number of winding packages in the reactor or the frequency range for which the model was validated. [6]

While very little work has been published regarding reactor noise emissions, the significance of the research found and described in this review is significantly important. For example, the need for the consideration of environmental noise emission impacts on sensitive receptors was emphasised for the case of HVDC stations. The present state of science for the prediction of reactor noise has so far been applied only to reactor models having simple geometry and using overly simplified methodologies. The focus of this research is to expand on the simple approaches and consider the implications associated with the dynamic modelling of complex reactor geometries and construction.

2.2 *MRI Noise Emissions*

Magnetic Resonance Imaging (MRI) noise generation mechanisms have compelling similarities to the design of the reactor considered in this research. The presence of a coil undergoing electro-magnetic forces as the driving factor of excitation is the key mechanism in noise generation for both MRI and reactor noise emissions. MRI noise emissions have been well researched in the past 20 years; as such, exploration into this phenomenon provides significant insight to the generation of reactor noise emissions.

The main focus of MRI noise is for hearing safety for patients inside the gradient coil [7]. The high intensity noise inside the MRI coil is said to have the potential to cause discomfort as well as hearing loss in patients [8]. Higher magnetic field strength systems

produce higher acoustic sound pressure levels than conventional clinical systems. These experimental systems can provide rapid, detailed spectroscopic analysis and high temporal and spatial resolution imaging with good signal-to-noise ratios in animal models [8]. As shown, it is desired to have high resolution for clinical applications, but safety is a concern. In this, it is important to quantify the noise emissions from MRI systems and to understand the mechanisms of noise generation.

Several papers considered and quantified the noise emissions of different MRI systems and imaging signals [7][8][9][10]. Specific research was carried out to predict and simulate the sound pressure level output of the MRI system as received by the patient inside of the coil. This research will be the focus of this literature review as it has relevance to the application for reactor noise considered in this dissertation.

Different methods for acoustic noise prediction of MRI systems were found in literature. One of the earlier methods was described in the research by *Hedeen and Edelstein*, which described a method of prediction through the use of calculated frequency response functions [11]. Noise levels in high field scanners have been observed to exceed 115 dBA [11]. In addition, the levels can vary by 10 dB dependant on the patients position in the scanner. *Hedeen and Edelstein* investigated a GE SIGNA 1.5 T scanner excited with a white noise signal. Using the physical input signal and the system output as a weighted linear summation over the time history, a complex frequency response function (FRF) and noise transfer function of the scanner was determined. Using the developed functions for this scanner, a typical pulse protocol was used to excite the scanner. It was found that the measurement of overall spectral energy agreed with the predicted results within 3 dB. As such, it was determined that the empirically derived frequency response function provided

an accurate and simple tool to predict the acoustic noise by a given scan protocol. [11] Similar research titled *Acoustic noise analysis and prediction in a 4-T MRI scanner* by *Mechefske et al* concluded that FRFs were able to show acoustic characteristics of an MRI system as well as able to accurately predict the SPL for scanning sequences. [12]

In other work, more theoretical approaches were used to predict the sound generation of the MRI coil structure. Specifically, in research conducted by *Mansfield et al*, a methodology for determining the generated noise as a function of the electromagnetic forces was studied [13]. In this research, the Lorentz force was the principle driving force for vibration. This finding agrees with reactor noise emissions theory as described in the previous section of this chapter. In research on similar topics for MRI scanners as that of *Mansfield et al*, the Lorentz force is known as the external driving force for MRI gradient coils [14][10][15][16][17][18].

Using the Lorentz force to predict the noise emissions of an MRI scanner differ in theory from reactor noise emissions. In the case of the MRI scanner, a gradient coil is applied; this does not match the physical representation of a simple winded coil package found in the reactor. Physically representing the structural response due to the Lorentz forces generated for the MRI scanner and an electrical reactor differ due to vast difference in the coil windings. In order to represent the reactors physical response, research on vibration response of multi-degree of freedom systems and hollow cylinders is necessary.

2.3 *Multi-Degree of Freedom Systems*

Reactors are geometrically concentric hollow cylinders that are rigidly connected using duct sticks and top and bottom supports, known as spiders. To represent these in a

model, a multi-degree of freedom (MDOF) system is assumed. Many publications exist that detail this type of vibration and the mathematics necessary to calculate the natural frequencies and vibration amplitude of the system. Cylindrical vibration is handled differently than a simple lumped mass spring-damper system. There are more components due to the stress within the cylinder itself. As such exploration into cylindrical vibration of multiple concentric systems can provide worthwhile methods to the application of this research.

Vibration and radial wave propagation velocity in functionally graded thick hollow cylinder by *Shakeri et al*, describes the analysis of functionally graded hollow cylinders under dynamic load. This explains the induced vibration in an assumed sub-cylinder of the functionally graded cylinder. The shell in this research is assumed to be in plane strain condition and is subjected to dynamic loading. The Navier equation is solved by Galerkin finite element and Newmark methods, which are assessed. [19]

The governing equation for a cylindrical shell layer under axisymmetric load is as follows:

$$\frac{\partial^2 u}{\partial r^2} + \frac{1}{r} \left(\frac{\partial u}{\partial r} \right) - \frac{u}{r^2} = \frac{\rho}{c_1} \left(\frac{\partial^2 u}{\partial t^2} \right) \quad 2-6$$

where $c_1 = \frac{E(1-\nu)}{(1+\nu)(1-2\nu)}$ and u is the displacement component in the radial direction.

To solve the governing equation of the shell, finite element analysis was used. By applying the Galerkin method to the governing equation 2-6, the following equilibrium equation is obtained:

$$[M]\{\ddot{X}\} + [K]\{X\} = \{f\} \quad 2-7$$

where $[M]$ is the mass matrix and $[K]$ is the stiffness matrix.

In this research, *Shakeri et al* used the Newmark direct integration method to solve the equilibrium equation. Thick hollow cylinder natural frequencies were determined through transferring the time response to the frequency domain by using FFT.

Equation 2-7 is the basis of MDOF vibration problems. Using this it is possible to form the eigenvalue problem and determine natural frequencies of a MDOF system. [19]

Moving forward in vibration and acoustic noise modelling, research conducted by *Li et al* depicted a model to determine noise emissions of reactors using the eigenvalue problem [20]. In this research, the motion equation is defined as:

$$[M]\{d''\} + [D]\{d'\} + [S]\{d\} = \{F\} \quad 2-8$$

where in this case $\{d\}$ is the displacement vector, $\{d'\}$ is the velocity vector, $\{d''\}$ is the acceleration vector, $[D]$ is the damping matrix, $[S]$ is the stiffness matrix, and $[F]$ is the force vector.

Further, as free vibration of a reactor is simple harmonic vibration, the displacement and acceleration were determined to be:

$$\begin{aligned} \{d\} &= \{\phi\} \sin(\omega t) \\ \{d''\} &= -\omega^2 \{\phi\} \sin(\omega t) \end{aligned} \quad 2-9$$

where ω represents the angular frequency.

Substituting 2-9 into 2-8, and setting conditions of undamped free vibration for determination of natural frequencies ($\{F\} = 0$ and $[D] = 0$), the following equation was obtained:

$$([S] - \omega^2[M])\{\phi\} = \{0\} \quad 2-10$$

Equation 2-10 defined the eigenvalue problem. The determination of the eigenvalues, ω , and the corresponding eigenvectors, $\{\phi\}$, is the fundamental of modal analysis. The eigenvalues correspond to the natural frequencies of the MDOF system.

In this research by *Li et al*, the driving force of noise emissions was again the Lorentz force inside the coil winding packages. *Li et al*, described the Lorentz force as the vector cross product of the magnetic field density and the current flowing through the windings. As we know from previous literature reviewed, the Lorentz force is the driving force in reactor sound generation. The following is the Lorentz force equation as depicted by *Li et al*:

$$dF = idl \times B \quad 2-11$$

where i is the current in the winding packages and B is the magnetic field density, and dF is the electromagnetic force on the winding of unit length dl .

Another key aspect of the research conducted by *Li et al* was the calculation of the amplification factor. The amplification factor compares the operating mechanical

frequency to the determined natural frequency and computes a factor which the amplitude of vibration at such an operating frequency would be amplified by. The amplification factor is given by:

$$\lambda = \frac{1}{\sqrt{\left[1 - \left(\frac{\omega}{\omega_j}\right)^2\right]^2 + \left[2\eta \left(\frac{\omega}{\omega_j}\right)\right]^2}} \quad 2-12$$

where, η is the damping ratio of the structural resonance. [20]

2.4 Hollow Cylinder Vibration

Vibration of hollow cylindrical structures, also known as cylindrical shells, has been a focal research area for decades [21][22][23][24][25][26][27]. Typical application of this area of study is applied to cylindrical structures for fatigue and design worthiness under vibrational loads. The vibration studied in this research differs from typical cylindrical vibration as it investigates an electromagnetic body force applied to the hollow cylinder of multiple cylindrical layers. In this research, the multiple winding packages are separated by duct sticks which adds another dynamic to the composite hollow cylinder.

Research publish by *Abd-Alla et al* in 2008, provided information on the modelling of vibrational effects of a composite cylinder. In showing the effects of a composite cylinder, the method used to calculate the displacement of vibration for a single layer of the composite cylinder was also obtained. [28] In his research, it was explained that the determination of the amplitude of vibration of a cylinder is dependent on the stress within the cylinder. The stresses within the cylinder resist, amplify and control the shape of

vibration that the cylinder undergoes. This makes the stresses within a vibrating cylinder important in estimating the natural frequencies, modes and determining the amplitude of vibration for different excitation frequencies.

Abd-Alla et al began to define the problem by outlining the stresses-displacement relations for a composite cylinder in cylindrical coordinates (r, θ, z) . The following equations are the stresses-displacement relations as defined by *Abd-Alla et al*:

$$\begin{aligned}\tau_{rr} &= \frac{2\mu}{1-2\nu} \left[(1-\nu) \left(\frac{\partial u}{\partial r} \right) + \nu \left(\frac{u}{r} \right) \right] \\ \tau_{\theta\theta} &= \frac{2\mu}{1-2\nu} \left[(1-\nu) \left(\frac{u}{r} \right) + \nu \left(\frac{\partial u}{\partial r} \right) \right] \\ \tau_{zz} &= \frac{2\mu\nu}{1-2\nu} \left[\frac{\partial u}{\partial r} + \frac{u}{r} \right] \\ \tau_{r\theta} &= \tau_{rz} = \tau_{\theta z} = 0\end{aligned}\tag{2-13}$$

where ν is the Poisson's ratio and μ is the rigidity modulus (Shear Modulus or Lamé's Constant).

In the research by *Abd-Alla et al*, the dynamic equation of motion was considered with the absence of a body force in the r direction. This equation of motion is given by:

$$\frac{\partial \tau_{rr}}{\partial r} + \frac{1}{r} (\tau_{rr} - \tau_{\theta\theta}) = \rho \left(\frac{\partial^2 u}{\partial t^2} \right)\tag{2-14}$$

where ρ is the density of the cylinder material.

With the problem defined by the stress-displacement relations and the equation of motion, *Abd-Alla et al* used Bessel functions to define the general solution to the problem. To summarize what was done, the equation of motion was rearranged to be variable based on displacement in the radial direction and time. By further rearranging the equation of motion, the equation was found to be in the form of Bessel's Equation, as shown below in equation 2-15.

$$r^2 \left(\frac{d^2 \Phi}{dr^2} \right) + r \left(\frac{d\Phi}{dr} \right) + [\lambda^2 r^2 - n^2] \Phi = 0 \quad 2-15$$

The general solution to Bessel's equation is in the form of:

$$\Phi(r) = AJ_n(\lambda r) + BY_n(\lambda r) \quad 2-16$$

where A and B are arbitrary constants and $J_n(\lambda r)$ and $Y_n(\lambda r)$, denote Bessel functions of the first and second kind of the order n , respectively.[28]

In future research by *Abd-Alla et al*, titled *Effect of magnetic field and non-homogeneity on the radial vibrations in hollow rotating elastic cylinder*, the determination of natural frequencies of radial vibration of a hollow cylinder exposed to magnetic force was studied. The determination of displacement and stress components were obtained by the use of Bessel function solutions of the first and second kind of the order of n , as shown in his previous research. [29]

The equation of motion was reshaped for the effects of cylinder rotation as well as the exposure to a magnetic field. The magneto-electrodynamic equation of a hollow cylinder was expressed as:

$$\frac{\partial \sigma_r}{\partial r} + \frac{1}{r}(\sigma_r - \sigma_\theta) + \rho \Omega^2 u + F_r = \rho \frac{\partial^2 u}{\partial t^2}, a \leq r \leq b, t \geq 0 \quad 2-17$$

where ρ is the mass density, Ω is the rotation and F_r is the Lorentz force. [29]

Given this, with a similar procedure to the previous research, rearranging to Bessel's equation and using the same general solution as equation 2-16, a solution for the radial displacement was obtained. *Abd-Alla et al* then adapted this solution for a hollow cylinder. This is obtained given that the free inner and outer surfaces of the hollow cylinder are free traction from stresses, and this was defined as:

$$\begin{aligned} \sigma_{rr}(R, T) + \tau_{rr}(R, T) &= 0 \text{ at } R = a \\ \sigma_{rr}(R, T) + \tau_{rr}(R, T) &= 0 \text{ at } R = b \end{aligned} \quad 2-18$$

given that a and b are inner and outer radii of the hollow cylinder, respectively. [29]

From this, the matrix D_{ij} was described in the publication by *Abd-Alla et al* [29].

Given this, *Abd-Alla et al* described the following:

$$|D_{ij}| = 0, (i, j = 1, 2) \quad 2-19$$

By solving equation 2-19, the eigenvalues of the natural frequency, ω , are obtained. Some call these the eigenfrequencies. These represent the natural frequencies of vibration

for the hollow cylinder. This method provides a solution to radial vibration displacement due to magnetic fields of different driving frequencies.

Vibration of Thick Cylindrical Structures is a textbook that covers the modelling and determination of natural frequencies and mode shapes of cylindrical shells [30]. In this work, the modelling and theory behind the governing equations of cylindrical shells are derived. The theory of vibration for a cylinder begins by determining the state of stresses at a point within the cylinder body. Below is the diagram of the direct and shear stresses in the radial and transverse directions and the variation of stresses due to vibration in cylindrical coordinates.

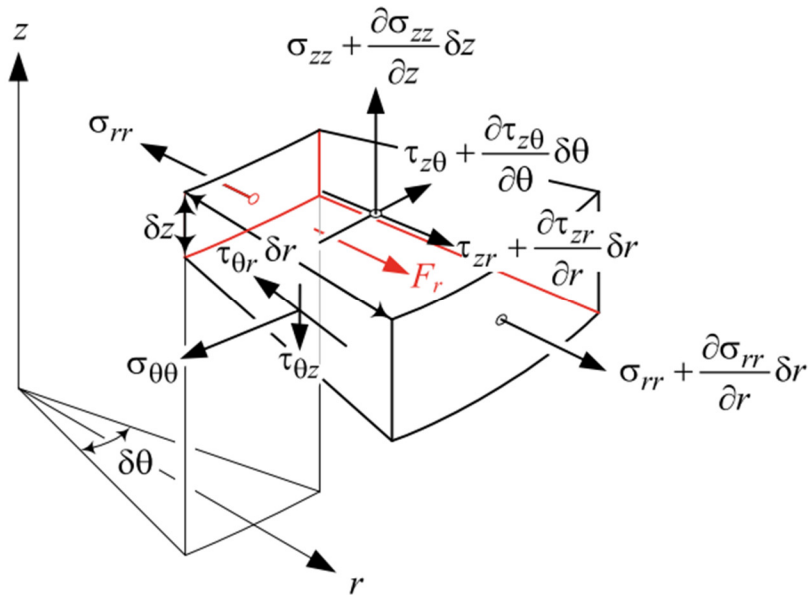


Figure 2-2 – Stresses in the plane perpendicular to r and z direction. [30]

Given this, the equation of motion is derived in vector form as follows:

$$\mu \nabla^2 \mathbf{u} + (\lambda + \mu) \nabla (\nabla \cdot \mathbf{u}) = \rho \left(\frac{\partial^2 \mathbf{u}}{\partial t^2} \right) \quad 2-20$$

where ∇ is the cylindrical gradient, which is defined as follows:

$$\nabla = \left(\frac{\partial}{\partial r} + \frac{1}{r} \right) \hat{i}_r + \frac{\partial}{r \partial \theta} \hat{i}_\theta + \frac{\partial}{\partial z} \hat{i}_z \quad 2-21$$

From this, and by using the Lamé potential function, the governing equation of motion is reduced to two wave equations. These equations were derived as follows:

$$v_1^2 \nabla^2 \phi = \frac{\partial^2 \phi}{\partial t^2} \quad 2-22$$

$$v_2^2 \nabla^2 \mathbf{H} = \frac{\partial^2 \mathbf{H}}{\partial t^2} \quad 2-23$$

In order to solve the wave equations, it was shown that the assumed solutions to be in the form of:

$$\phi = f(r) \cos(n\theta) \cos(\omega t + \zeta z) \quad 2-24$$

$$H_r = g_r(r) \sin(n\theta) \sin(\omega t + \zeta z) \quad 2-25$$

$$H_\theta = g_\theta(r) \cos(n\theta) \sin(\omega t + \zeta z) \quad 2-26$$

$$H_z = g_3(r) \sin(n\theta) \cos(\omega t + \zeta z) \quad 2-27$$

In subsequent chapters of the textbook, it was proven that the function $f(r)$, $g_r(r)$, $g_\theta(r)$, and $g_3(r)$ are in fact solutions to Bessel differential equations. Given this, the following solutions to the functions were derived as the following Bessel functions:

$$f(r) = A_1 J_n(\alpha r) + B_1 Y_n(\alpha r) \quad 2-28$$

$$g_3(r) = A_2 J_n(\beta r) + B_2 Y_n(\beta r) \quad 2-29$$

$$2g_1(r) = g_r(r) - g_\theta(r) = A_3 J_{n+1}(\beta r) + B_3 Y_{n+1}(\beta r) \quad 2-30$$

$$2g_2(r) = g_r(r) + g_\theta(r) = A_4 J_{n-1}(\beta r) + B_4 Y_{n-1}(\beta r) \quad 2-31$$

Further solving the four wave equations, the solution to the Lamé's potential functions ϕ , H_r , H_θ , and H_z are determined. The components of displacement in cylindrical coordinates at any point within the medium of the cylindrical structure are determined by substituting the Lamé's potential functions into the proposed solution for displacement. The resultant is the following equations for vibrational displacement:

$$u_r = \left(f' + \frac{n}{r} g_3 + \zeta g_1 \right) \cos(n\theta) \cos(\omega t + \zeta z) \quad 2-32$$

$$u_\theta = \left(-\frac{n}{r} f + \zeta g_1 - g_3' \right) \sin(n\theta) \cos(\omega t + \zeta z) \quad 2-33$$

$$u_z = \left(-\zeta f - g_1' - \frac{n+1}{r} g_1 \right) \cos(n\theta) \sin(\omega t + \zeta z) \quad 2-34$$

in these cases, prime indicates differentiation with respect to r .

Using the displacement equations and the stress-displacement relations, the equations for direct and shear stresses of interest are derived as follows:

$$\sigma_{rr} = \left(-\lambda(\alpha^2 + \zeta^2)f + 2\mu \left(f'' + \frac{n}{r} \left(g'_3 - \frac{g_3}{r} \right) + \zeta g'_1 \right) \right) h_1 \quad 2-35$$

$$\tau_{r\theta} = \left(-\frac{2n}{r} \left(f' - \frac{f}{r} \right) - \frac{n^2}{r^2} g_3 - g'_3 + \frac{g'_3}{r} - \frac{n\zeta}{r} g_1 + \zeta g'_1 - \frac{\zeta}{r} g_1 \right) \mu h_2 \quad 2-36$$

$$\tau_{rz} = \left(-2\zeta f' + \left(\frac{n+1}{r^2} - \zeta^2 \right) g_1 - \frac{n+1}{r} g'_1 - g''_1 - \frac{n\zeta}{r} g_3 \right) \mu h_3 \quad 2-37$$

where, primes indicate the derivation with respect to r , and h_1, h_2, h_3 are defined as follows:

$$h_1 = \cos(n\theta) \cos(\omega t + \zeta z) \quad 2-38$$

$$h_2 = \sin(n\theta) \cos(\omega t + \zeta z) \quad 2-39$$

$$h_3 = \cos(n\theta) \sin(\omega t + \zeta z) \quad 2-40$$

By substituting the Bessel differential equations into the three stress components and assuming arbitrary boundary condition values for the inner and outer surfaces of the cylinder structure, a linear non-homogeneous system of equations is developed. This system of equations is expressed in matrix form as follows:

$$T\mathbf{X} = \mathbf{S} \quad 2-41$$

such that:

$$\mathbf{X} = \begin{Bmatrix} A_1 \\ B_1 \\ A_2 \\ B_2 \\ A_3 \\ B_3 \end{Bmatrix} \quad 2-42$$

$$\mathbf{S} = \begin{Bmatrix} \frac{\sigma_{rr}(r=a)}{h_1} \\ \frac{\tau_{r\theta}(r=a)}{h_2} \\ \frac{\tau_{rz}(r=a)}{h_3} \\ \frac{\sigma_{rr}(r=b)}{h_1} \\ \frac{\tau_{r\theta}(r=b)}{h_2} \\ \frac{\tau_{rz}(r=b)}{h_3} \end{Bmatrix} \quad 2-43$$

The elements of the T matrix are developed by substituting the boundary conditions into equations 2-35, 2-36, and 2-37 along with the Bessel solutions.

From the stress matrix and known boundary conditions, the coefficient vector \mathbf{X} is determined by the following reorientation of equation 2-41.

$$\mathbf{X} = T^{-1}\mathbf{S} \quad 2-44$$

From the known displacement and stress functions and Bessel equation solutions, a system of linear equations with displacement can be constructed as follows:

$$D\mathbf{X} = \mathbf{C} \quad 2-45$$

where, the vector \mathbf{C} is defined as:

$$\mathbf{C} = \begin{Bmatrix} u_r(r=a)/h_1 \\ u_\theta(r=a)/h_2 \\ u_z(r=a)/h_3 \\ u_r(r=b)/h_1 \\ u_\theta(r=b)/h_2 \\ u_z(r=b)/h_3 \end{Bmatrix} \quad 2-46$$

Using these systems of linear equations, stress, natural frequencies and displacement of the cylinder under vibration can be determined for a single material cylinder. The methodology was further expanded to compensate for multi-layer cylindrical structures.

$$\begin{Bmatrix} u_r/h_1 \\ u_\theta/h_2 \\ u_z/h_3 \\ \sigma_{rr}/h_1 \\ \tau_{r\theta}/h_2 \\ \tau_{rz}/h_3 \end{Bmatrix} = \begin{bmatrix} D_{1,1} & D_{1,2} & D_{1,3} & D_{1,4} & D_{1,5} & D_{1,6} \\ D_{2,1} & D_{2,2} & D_{2,3} & D_{2,4} & D_{2,5} & D_{2,6} \\ D_{3,1} & D_{3,2} & D_{3,3} & D_{3,4} & D_{3,5} & D_{3,6} \\ T_{1,1} & T_{1,2} & T_{1,3} & T_{1,4} & T_{1,5} & T_{1,6} \\ T_{2,1} & T_{2,2} & T_{2,3} & T_{2,4} & T_{2,5} & T_{2,6} \\ T_{3,1} & T_{3,2} & T_{3,3} & T_{3,4} & T_{3,5} & T_{3,6} \end{bmatrix} \begin{Bmatrix} A_1 \\ B_1 \\ A_2 \\ B_2 \\ A_3 \\ B_3 \end{Bmatrix} \quad 2-47$$

which can be presented as:

$$\{d\}_n = [D]_n \{X\}_n \quad 2-48$$

where $\{d\}_n$ is defined as:

$$\{d\}_n = \left\{ \frac{u_r}{h_1} \quad \frac{u_\theta}{h_1} \quad \frac{u_z}{h_1} \quad \frac{\sigma_{rr}}{h_1} \quad \frac{\sigma_{r\theta}}{h_2} \quad \frac{\sigma_{rz}}{h_1} \right\}_n^T \quad 2-49$$

and $[D]_n$ was defined in equation 2-45 and n represents the circumferential wave number.

Using this relation for each of the layers, the propagation matrix equation for a three-layer cylinder was derived in *Vibrations of Thick Cylindrical Structures*. The following is the displacement relations of a n -layer cylinder under free vibration:

$$\begin{Bmatrix} u_r/h_1 \\ u_\theta/h_2 \\ u_z/h_3 \\ 0 \\ 0 \\ 0 \end{Bmatrix}_n = \begin{bmatrix} P_{1,1} & P_{1,2} & P_{1,3} & P_{1,4} & P_{1,5} & P_{1,6} \\ P_{2,1} & P_{2,2} & P_{2,3} & P_{2,4} & P_{2,5} & P_{2,6} \\ P_{3,1} & P_{3,2} & P_{3,3} & P_{3,4} & P_{3,5} & P_{3,6} \\ P_{4,1} & P_{4,2} & P_{4,3} & P_{4,4} & P_{4,5} & P_{4,6} \\ P_{5,1} & P_{5,2} & P_{5,3} & P_{5,4} & P_{5,5} & P_{5,6} \\ P_{6,1} & P_{6,2} & P_{6,3} & P_{6,4} & P_{6,5} & P_{6,6} \end{bmatrix} \begin{Bmatrix} u_r/h_1 \\ u_\theta/h_2 \\ u_z/h_3 \\ 0 \\ 0 \\ 0 \end{Bmatrix}_1 \quad 2-50$$

Using these equations, it is possible to determine the displacement due to vibration at any point within the multi-layer cylindrical structure for free or forced vibration. Adapting matrix $[D]$ for each of the layers in the cylindrical structure will allow for the determination of the propagation displacement relations in the form of equation 2-50. [30].

2.5 Review

The state of science for the investigation and theory for cylindrical vibration has been laid out in this chapter of the review of the literature. Components and specific applications from the research detailed in this review have been adapted in this research in the development of different models for applications of cylindrical vibration. Subsequent chapters in this dissertation derive the various vibration equations for the prediction of the vibration dynamics and noise for the specific application of cylindrical structure vibration.

CHAPTER 3

EXPERIMENT DETAILS

In order to access the vibroacoustic behaviour of a reactor, a set of comprehensive experiments were established. Due to the complex nature of forced vibration resulting from electromagnetic excitation; structural vibration and noise emission experiments were required to characterize the entirety of the vibroacoustic behaviour of the reactor. The combined use of post-processed acoustic measurements, structural modal analysis, and noise source identification (NSI) techniques provided a comprehensive understanding to the relationship of induced vibration and resulting noise emissions.

Extensive testing of the noise emissions provided a comprehensive source of data used to correlate and verify the predicted noise emissions values. Data was collected from two prototype reactors that were manufactured and provided by Trench for this project. The two reactors were of different geometry and magnetic field characteristics. The scope of this project is to design a proposed model based on the collected data and insight from the structural testing. The combination of the structural natural frequency information and measured damping of the reactor, along with the noise emission data, a more realistic methodology for computing the vibroacoustic noise emissions of a reactor is developed.

The three test methods used to characterise the reactor were extensive in nature to ensure quality and completeness of capturing the entire noise generation mechanism of the reactor from the structural excitation to the noise propagation. The three test types included radial sound measurements, noise source identification, and modal test and analysis. The tests selected required independent experimental setups. The following sections of this

chapter outline the experimental setups, instrumentation, experiment design, and testing procedure used for each of the three tests.

3.1 Radial Sound Measurements

Generation of reactor noise is a complex system. The generated sound field surrounding the reactor is due to the physical deflections of the various parts of the reactor. The deflections are caused by induced electromagnetic forces between the electrical current in the winding packages and the magnetic field surrounding them. These forces are quantified as Lorentz forces and cause the wind packages to pulsate. This pulsation produces pressure waves that radiate from the surfaces of the reactor and generate the sound field surrounding the reactor. To capture and quantify the reactor's noise emissions, a radial sound measurement test was designed to acquire sound data from the reactor with varied supplied electrical currents.

3.1.1 Equipment and Instrumentation

Sound levels from the reactors were acquired using nine Type 4189-A-021 Brüel & Kjær microphones which were placed around the reactor at a radial distance of two metres from the surface of the first reactor and three metres for the second reactor. The microphone and preamplifier combination in conjunction with a Brüel & Kjær Front End D-frame, equipped two Brüel & Kjær LAN XI Type 3050-A-060/042 front end modules, and Brüel & Kjær Pulse Labshop data acquisition software was used to acquire noise data. Before and after the collection of the data, the measurement system was calibrated using a Brüel & Kjær Type 4231 calibrator. This equipment configuration permitted the simultaneous recording of nine signals.

3.1.2 Experimental Design Setup and Procedure

Sound level recordings were acquired by positioning nine microphones evenly spaced on an arc at a radial distance of two metres from the reactor. The microphones were not positioned near the power supply bus for reasons of safety. This resulted in an absence of data for a quarter of the circumference. The absence of the microphones in this area is not a concern as this side is adjacent to a wall of a building and would have provided elevated sound levels in this quadrant due to reflectivity of the building. In addition, the sound pressure level to quantify the reactor is a logarithmic average and with nine microphone signals it is unlikely that the average sound pressure level would result in a significant difference with the addition of a few more measurements along the circumference. The microphone locations, as shown in Figure 3-1, were positioned such that each of the nine microphones would be either in-line or off-line to a spider termination. This was done to ensure no bias was present in measuring the full directivity effect of the reactor. The microphone heights were set to the midplane of the reactor. As such, the height of the microphones depended on the height of the reactor tested. The test setup is shown in Figure 3-2 and Figure 3-3 for the first and second prototype reactors, respectively.

With this equipment setup, 10 second signal recordings with a high-resolution frequency span of 25.6 kHz were collected for each of the electrical excitation frequencies. The nine signal recording locations were collected simultaneously, and as such, were synchronized in time. The electrical test excitation frequencies included all excitation frequencies that the Trench facility is capable of supplying to the reactor. Thus, the electrical excitation frequencies varied depending on the reactor and the current required to excite the reactor for each excitation frequency. This resulted in 17 electrical excitation

frequencies for the first prototype reactor and 16 electrical excitation frequencies for the second prototype reactor. Each of the test excitation frequency were increments of 30 Hz from 180 Hz to 660 Hz (first prototype) or 630Hz (second prototype).

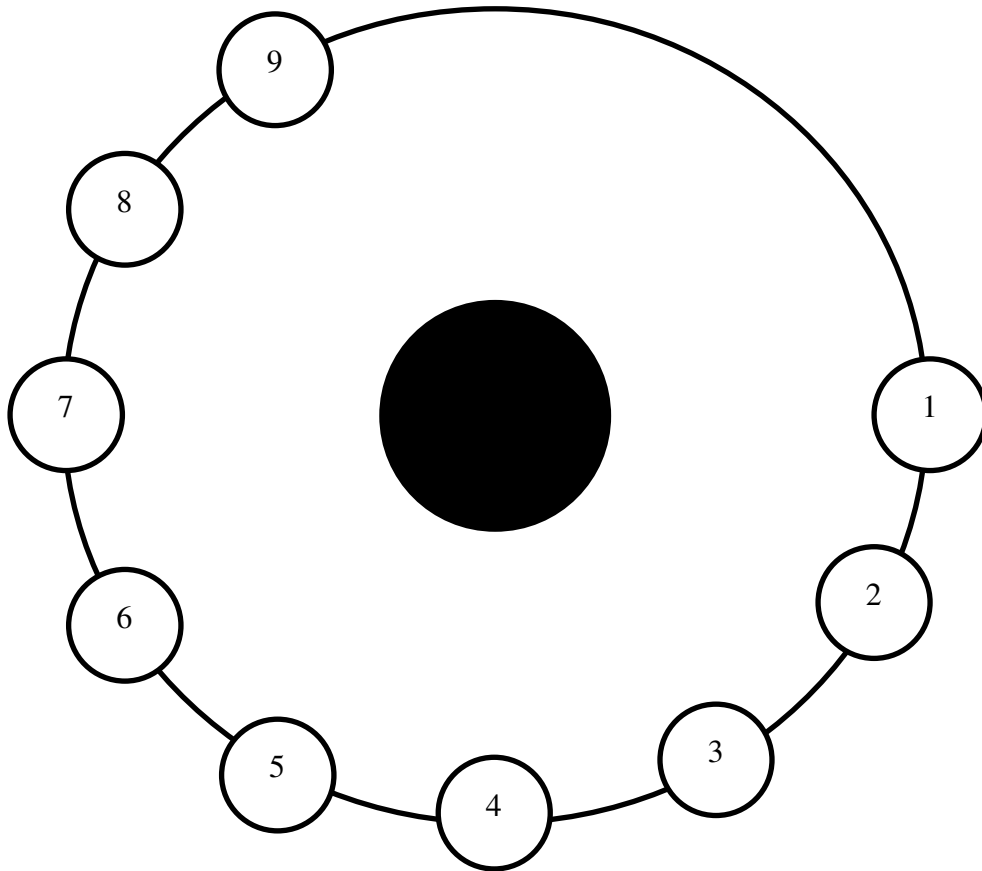


Figure 3-1 – Microphone locations for signal recordings.



Figure 3-2 – Radial sound measurement experimental test setup for the first prototype reactor.



Figure 3-3 – Radial sound measurement experimental test setup for the second prototype reactor.

3.1.3 *Environmental Considerations*

The radial sound measurement tests for both reactors were conducted at the Trench facility in Scarborough, Ontario on July 26, 2016, June 21, 2017, May 30, 2018, and July 12, 2018. The testing was conducted on their research and development outdoor sound test pad which is a gated area that is fitted to supply high voltage current to the reactor. The gated area is just large enough to facilitate the measurements with enough distance from the reactor to allow safe operation. Meteorological conditions were monitored to ensure that the conditions were within the acceptable guidelines for outdoor sound pressure level measurements. Wind speed and relative humidity were verified to be less than 15 km/hr and 90%, respectively. The meteorological condition limits used are in line with environmental standards for outdoor acoustic measurements which ensures microphone performance is not compromised and that the acquired data is representative of the noise source.

3.1.4 *Measurement Procedure*

The procedure used to acquire the sound measurements for the radial emissions for the electrically excited reactors was as follows:

1. Microphones were placed at nine locations equally spaced on an arc at a radial distance of two metres (three metres for the second reactor) from the reactor.
2. The reactor was excited with a high voltage current at a specific electrical excitation frequency.

3. The reactor would remain excited until the reactor was stable at the intended current and electrical frequency.
4. Brüel & Kjær Pulse Labshop data acquisition software was used to take ten second sound measurements of the excited reactor.
5. Steps 2-5 were repeated for all electrical excitation frequencies that Trench was able to supply to the reactor (17 frequencies for the first reactor and 16 frequencies for the second reactor).

3.2 Noise Source Identification Measurements

Noise Source Identification is a technique that can “see” the noise emissions of a sound source. Like a thermal image, the amplitude and frequencies of a noise can be determined and plotted to facilitate a better understanding of the noise propagation and properties of a noise source. Using beamforming and spatial filtering as well as algorithms which are applied to the signals from an array of microphones, a recreation of the sound field is created which can be used to investigate a source of noise and its propagation.

Through NSI, the noise generators propagating from complex systems can be more easily identified. Given that the reactor noise originates from a complex structural excitation, the use of NSI can provide insight to the mechanisms that generate the greatest amount of sound energy.

3.2.1 Equipment and Instrumentation

To perform the NSI technique, a Brüel & Kjær 60-channel sector array was used to collect the necessary data for the analysis. The Brüel & Kjær 60-channel sector array was

used in conjunction with, a Brüel & Kjær D-Frame front end equipped with five Brüel & Kjær LAN XI Type 3053 12-channel front end modules and Brüel & Kjær Pulse Labshop data acquisition software. Due to the high density of microphones operating simultaneously, a high channel count is necessary to perform NSI acquisition and subsequent analysis.

Before collecting the data, the spatial configuration of each microphone signal was synchronized with the data acquisition software. This was performed by identifying the location of the microphone in the software followed by inputting a noise signal to the corresponding microphone on the array. This is required for each of the 60 microphone channels on the array for the analysis to perform beamforming and spatial filtering.

3.2.2 Experimental Design Setup and Procedure

NSI measurements were performed by locating the array at four representative locations around the reactor: three radial locations on a two-metre arc and one location directly above the reactor. The measurement locations were selected to provide a satisfactory view of most of the reactor's outer surface. The array locations are shown in Figure 3-4. The NSI measurements were performed for three electrical excitation frequencies for the first prototype reactor. At each location, and for each electrical excitation frequency, a 10 second snapshot of the excited reactor noise was recorded. Using the Brüel & Kjær NSI Array Acoustic Post-Processing software, contour plots were overlaid on an image of the reactor. Also processed was the 1/3-octave sound power level data, which was computed on an imaginary plane for the surface of the reactor.

The radial NSI test setup and top view NSI test setup are shown in Figure 3-5 and Figure 3-6, respectively.

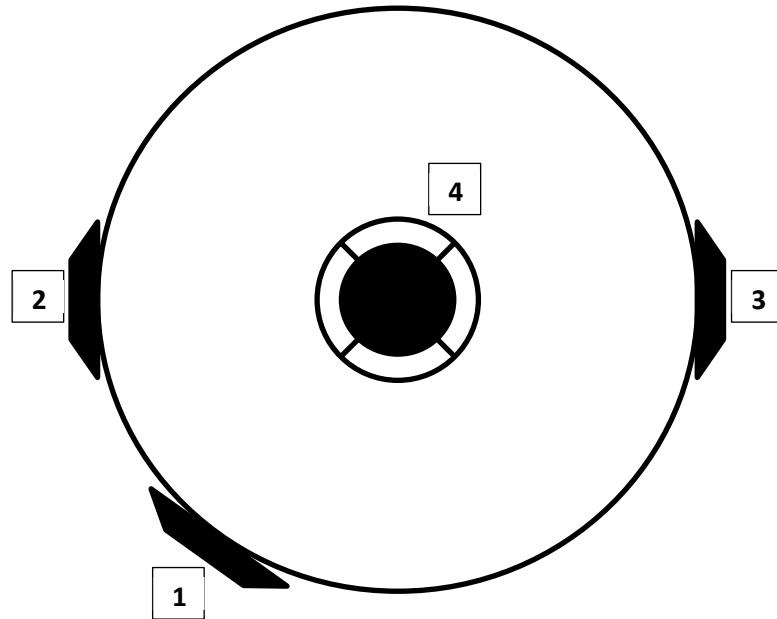


Figure 3-4 – Array measurement locations relative to the reactor.



Figure 3-5 – NSI data acquisition setup using a Brüel & Kjær 60-channel sector array.



Figure 3-6 – NSI data acquisition top view setup using a Brüel & Kjær 60-channel sector array.

3.2.3 *Environmental Considerations*

The NSI measurement tests for the first prototype reactor was conducted at the Trench facility on July 26, 2016. The tests were again conducted on their outdoor sound test pad.

Meteorological conditions were monitored to ensure that the conditions were within the acceptable guidelines for sound pressure level measurements. Wind speed and relative humidity were verified to be less than 15 km/hr and 90%, respectively.

3.2.4 Measurement Procedure

The procedure to acquire data for the NSI analysis was as follows:

1. The Brüel & Kjær 60-channel sector array was connected to the Brüel & Kjær Pulse D Frame LAN XI front end.
2. The microphones on the array were mapped in Brüel & Kjær Pulse Labshop to provide the spatial relations for NSI algorithms.
3. The sector array was positioned at a two-metre radial distance at position 1 shown in Figure 3-4.
4. The reactor was excited and allowed to stabilize.
5. A ten second snapshot recording was taken of the excited reactor.
6. Steps 3-4 were repeated for the other three measurement locations.
7. Steps 3-6 were repeated for a total of three electrical frequencies.

3.3 Modal Analysis Measurements

Structural modal test analysis is the study of the structural dynamic properties of a structure while it undergoes vibrational excitation. The test measures the dynamic response of the structure at various points and relates them back to the excitation input to determine

how the structure reacts to the excitation. Typically, this requires multiple accelerometers at different locations along with one or more modal shakers equipped with force transducers to induce and measure the excitation force into the structure. From the collected data, the frequency response functions (FRFs) are calculated and used to identify the structural modes. The structural modes correspond to natural frequencies where excitation at such a frequency would cause greater response and deflection from the structure.

The purpose of this analysis was to determine the FRFs for the test reactors and to determine the structural modes, mode shapes, natural frequencies, and damping ratios. The modal analysis provided insight in the structural resonance of the reactor and at which mechanical frequencies provide the greatest excitation. Measuring the damping ratio of the reactor is important because of its use in the proposed model.

3.3.1 Equipment and Instrumentation

The modal testing and analysis was performed by instrumenting the reactors with vibration accelerometers and exciting the structure using modal shakers. Three Brüel & Kjær modal shakers, types 4825, 4826, and 4827 fitted with Brüel & Kjær Type 8230-001 and Brüel & Kjær Type 8230-002 force transducers were used to excite the reactors completely. The use of three modal shakers allowed for excitation in all three axes. For the first reactor, 20 Brüel & Kjær Type 4524-B triaxial accelerometers were positioned at 156 locations (a total of 8 measurements per orientation of the modal shakers) to measure the resulting excitation at the outermost wire package, inner most wire package, and the top and bottom spiders. For the second reactor, twelve Brüel & Kjær Type 4524-B triaxial accelerometers were positioned at 96 locations (a total of 8 measurements per orientation

of the modal shaker). The inner wire package as well as the top spiders were not measured for the second prototype reactor due to the restricted access of the inside of the reactor and the large height of the reactor. The measurement locations were positioned at twelve locations evenly spaced around the circumference of the reactor at five different heights along the length of the first reactor and seven different heights along the length of the second reactor. The same locations were also mapped for the inner wire package of the first reactor. The accelerometers were calibrated using a Type 4294 vibration calibrator.

3.3.2 Experimental Design Setup and Procedure

The reactor was fitted with modal shakers and triaxial accelerometers to perform the modal analysis. Careful instrumentation choices were essential to correctly measure the excitation response and quantify the complete response of the reactor. As specified earlier, for complete response measurement of the two reactors 156 accelerometer locations were necessary for the first prototype reactor and 96 accelerometer locations for the second prototype reactor. The difference in the number of locations was due to the different geometry and limited access to the interior of the second prototype reactor. For both reactors a total of eight measurement setups with the accelerometers roved over all the measurement points on the reactor were required to collect a complete structural response for the entire reactor.

Along with the placement of the accelerometers, the reactor was fitted with three modal shakers to excite all three directions of the reactors. Two of the modal shakers were positioned 90-degrees apart and on opposite ends of the length of the reactor. The third modal shaker was positioned at the bottom of the reactor in the axial direction. This shaker

was able to produce a much larger force input than the other two modal shakers, as more force was required to excite the axial direction of the reactors.

The modal shakers were driven by 100 broadband burst random signals for each of the eight measurement setups for each reactor. The response of the induced excitation was measured along with the input force which were then used to determine the resultant FRFs averaged over the 100 burst random inputs. Using the FRF curves the structural modes were identified with curve fitters and several validation algorithms.



Figure 3-7 – First prototype reactor modal analysis experimental setup.

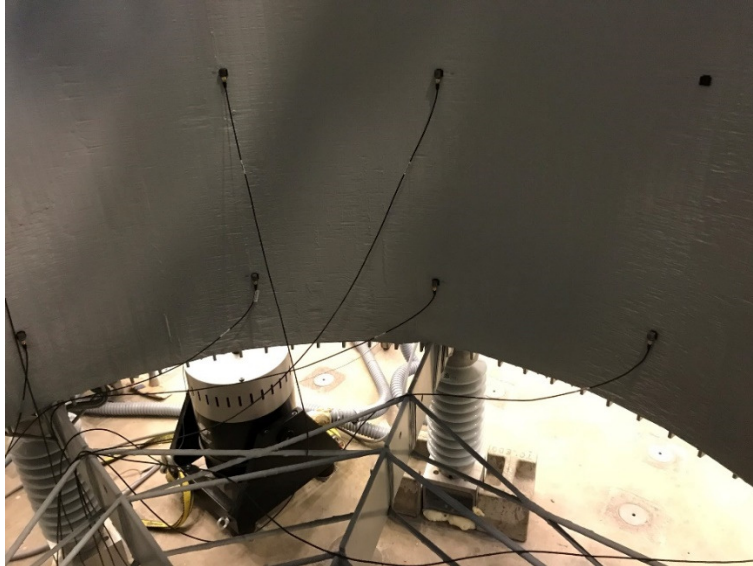


Figure 3-8 – First prototype reactor modal analysis experimental setup (reactor interior)



Figure 3-9 – Second prototype reactor modal analysis experimental setup.

3.3.3 *Environmental Considerations*

The modal measurements for both reactors were conducted at the University of Windsor during the months of November and December of 2017 and April of 2018. The testing was conducted in the University of Windsor's Structures Laboratory and Industrial Courtyard. These locations were used as they were equipped with overhead cranes which were used to suspend the reactor above the ground during data collection to represent a free-free condition of the reactor. Expanding foam was applied under the reactor isolators (feet) to restrict the swinging movement of the reactor during the data acquisition. Suspension of the reactor was necessary to isolate the reactor and ensure that the modal results are representative of the reactors' mechanical properties without any affects from the local environment.

3.3.4 *Measurement Procedure*

The procedure to acquire data for the structural modal analysis was as follows:

1. The reactor was fitted with three modal shakers with force transducers.
2. In Brüel & Kjær Reflex software the reactor was modelled geometrically, and accelerometers and modal shakers were placed on measurement nodes geometrically determined in the modal software package.
3. Using the spatial relations created in the previous step the accelerometers were placed at the appropriate measurement locations for the first measurement orientation.

4. Using Brüel & Kjær Reflex software, 100 broadband burst random signals were supplied to the modal shakers and the response was measured for each of the accelerometer locations.
5. Data acquired for the first measurement was stored for all the representative locations.
6. Steps 3 – 5 were repeated for the remaining seven measurement orientation necessary to cover all the accelerometer measurement locations.

CHAPTER 4

DATA ANALYSIS AND DISCUSSION

4.1 Radial Sound Measurements

The mechanisms for noise generation of electrical reactors are complex. Sound measurements taken radially at a uniform distance from the reactors were used to characterize the sound field. The collected sound data was post-processed using FFT analysis, constant percentage bandwidth (CPB) analysis, directivity analysis, and overall level analysis. This chapter details the process and outcomes from these analyses.

4.1.1 FFT Analysis

The FFT algorithm converts a measured sound signal from the time domain to the frequency domain. The FFT spectral results can typically give higher frequency resolution compared to other techniques, such as CPB, which allows for a greater detailed analysis of the frequency characteristics of a signal.

FFT analysis identified the frequency characteristics of the reactor noise emissions with a detailed frequency resolution. From the measured sound data, an FFT analysis was performed on both prototype reactors at each of the generated excitation frequencies. Given that the Trench facility is capable of only supplying a single excitation frequency to the reactors at a time, it was only possible to perform the FFT analysis to each discrete electrical input frequency. In the practical application, the reactors are subjected to multiple electrical excitation frequencies simultaneously.

The sound measurements were post-processed into the frequency domain using Brüel & Kjær BK Connect software. The setup of the FFT analyzer had a linear time averaging over the entirety of the recording and a frequency span of 25.6 kHz with 800 lines to give a high resolution of the data showing the minute details of the results. This resulted in a frequency resolution of 32 Hz. An A-weighting filter was applied to the output so the results could be later compared to environmental noise standards.

Analysis of the frequency domain data showed a significant noise contribution in the frequency range of 0 to 1600 Hz. Given this, the time signals were reprocessed for a new frequency span of 1.6 kHz with 1600 lines. This resulted in a frequency resolution of 1 Hz, allowing for higher accuracy in the identification of maximum noise peaks and their corresponding frequencies. The FFT analysis for each electrical excitation frequency was plotted against the ambient noise emissions. The corresponding FFT plots are provided in Appendix A FFT Analysis Results.

The FFT analysis confirmed that the primary acoustic frequency of the noise emission was found at exactly twice the electrical excitation frequency. This corresponds to the mechanical frequency, which is also twice the electrical frequency. This is the basis to the current state of science in reactor noise prediction, as detailed in chapter 2. The magnitude of the primary peak frequency was found to be within a few decibels of the calculated overall sound pressure levels; the significance of which is explained in the later sections of this dissertation. This confirms that the acoustic frequency peak at twice the electrical excitation frequency is in fact the primary noise generating mechanism of the reactor. The secondary peaks were identified to be from other ambient sources of noise as shown on the overlay of measured ambient noise on the FFT plots. (See Appendix A FFT

Analysis Results). While some of the secondary frequencies may be harmonics of the fundamental acoustic frequency, their magnitude was found to be insignificant compared to the primary peak frequencies.

It is worthy to note that, having multiple electrical excitation frequencies operating at once; some of the secondary harmonics may be the cause of increasingly large errors in the noise prediction model if amplified by structural resonance. The experimental setup was not capable of providing this type of testing and confirmation.

4.1.2 CPB Analysis

The process of CPB filtering isolates a range of frequencies, or bands, and reports the sound level contribution contained within the band. Each bandwidth is equal to a percentage of the centre frequency of that frequency band. The most common CPB filters are the 1/1 octave which is approximately 70% wide and the 1/3 octave band which has an approximate width of 23%.

1/3 octave CPB filtering, in addition to the A-weighting filter, was applied to the recorded sound measurements using Brüel & Kjær BK Connect post-processing software. The CPB results were compared to the predicted results from the proposed models. The procedure taken for the comparison was to logarithmically average each 1/3 octave band across each microphone signal and for the three consecutive sound recordings corresponding to the 1/3 octave band of the reactor's operating excitation frequency. This was compared to the predicted value generated using the proposed prediction methods. A sample of the CPB results is provided in the Figure 4-1. All CPB results are provided in the Appendix B CPB Analysis Results.

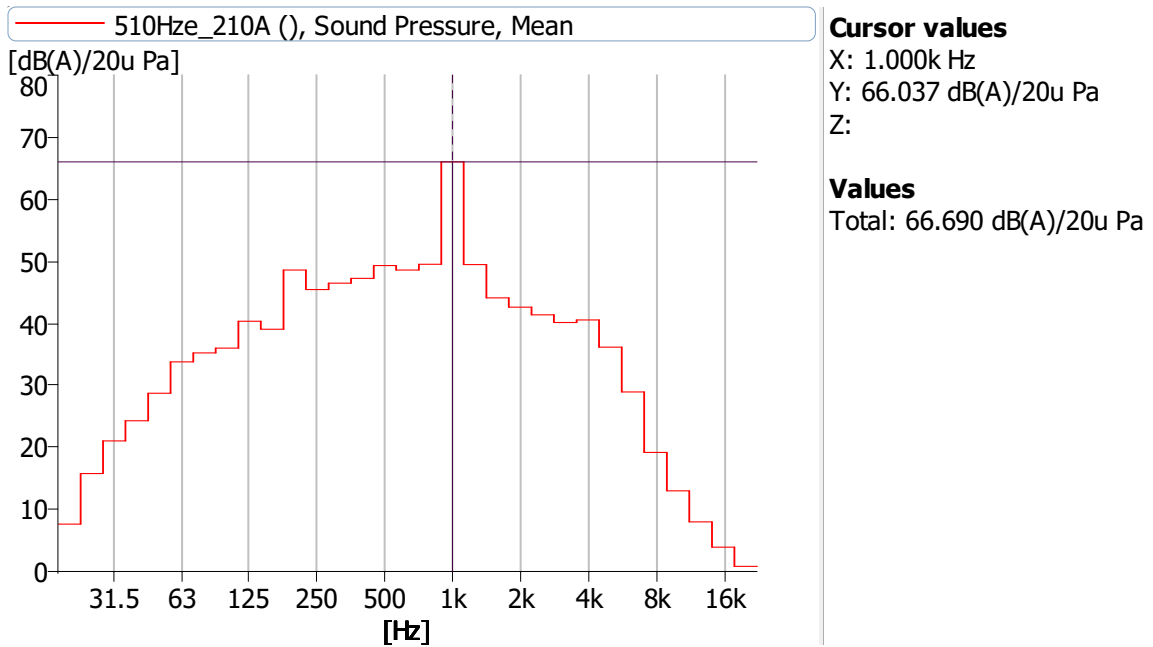


Figure 4-1 – CPB output for 510 Hz electrical excitation frequency at 210 A - prototype reactor 2.

The reactor noise emissions were quantified by taking the value of the 1/3 octave band for the frequency corresponding to the reactor’s operating frequency. This value was used to represent the noise generated by the reactor operating at a single electrical excitation frequency. The acoustic frequency is quantified as double the electrical excitation frequency. This is due to fact that the resultant mechanical vibrating frequency is double the excitation frequency. As shown by the FFT analysis, the peak frequency of the excited reactor was precisely double the electrical excitation frequency. As the sound pressure level peak is more than 10 dB greater than the adjacent frequency levels, the value of the 1/3 octave band is quantified as the overall sound pressure level. As such, the 1/3 octave value better describes the noise emissions solely of the excited reactor for the respective electrical excitation frequency. This result is crucial in verifying the validity of the models proposed in this research. The following table describes the logarithmically

averaged sound pressure levels at the corresponding 1/3-octave bands to represent the noise emissions of the excited electrical reactor.

Table 4-1 – A-weighted 1/3-octave sound pressure levels for corresponding electrical excitation frequencies for reactor 1.

Electrical Excitation Frequency [Hz]	Current [A]	Fundamental Acoustic Frequency [Hz]	Fundamental 1/3-Octave Centre Frequency [Hz]	1/3-Octave L_p [dBA]	Normalized 1/3-Octave L_p [dBA]
180	400	360	400	65.61	41.53
210	400	420	400	65.49	41.40
240	400	480	500	59.16	35.07
270	400	540	500	61.65	37.57
300	300	600	630	67.41	48.33
330	200	660	630	62.27	50.23
360	200	720	800	64.71	52.67
390	150	780	800	67.99	60.95
420	175	840	800	69.63	59.91
450	250	900	1000	71.88	55.96
480	250	960	1000	73.13	57.21
510	230	1020	1000	69.50	55.03
540	225	1080	1000	64.86	50.77
570	230	1140	1250	66.36	51.89
600	250	1200	1250	63.96	48.04
630	180	1260	1250	61.74	51.53
660	185	1320	1250	54.64	43.95

Table 4-2 – A-weighted 1/3-octave sound pressure levels for corresponding electrical excitation frequencies for reactor 2.

Electrical Excitation Frequency [Hz]	Current [A]	Fundamental Acoustic Frequency [Hz]	Fundamental 1/3-Octave Centre Frequency [Hz]	1/3-Octave Lp [dBA]	Normalized 1/3-Octave Lp [dBA]
180	400	360	400	51.656	27.57
210	400	420	400	56.593	32.51
240	400	480	500	58.462	34.38
270	400	540	500	63.793	39.71
300	300	600	630	60.073	40.99
330	200	660	630	55.322	43.28
360	200	720	800	55.041	43.00
390	200	780	800	52.956	40.91
420	175	840	800	57.852	48.13
450	250	900	1000	60.23	44.31
480	250	960	1000	64.19	48.27
510	210	1020	1000	66.04	53.15
540	225	1080	1000	72.79	58.70
570	210	1140	1250	67.16	54.28
600	225	1200	1250	65.44	51.35
630	170	1260	1250	58.11	48.89

These results represent the primary noise generated by the reactor at the specified electrical excitation frequencies. Data provided in the above tables includes sound pressure levels at two metres for reactor 1 and three metres for reactor 2, which are normalized to a 100 A current for comparability. These values are used for validation of proposed models in subsequent sections of this dissertation.

Unlike the FFT analysis, the CPB analysis does not provide results relating to specific frequencies; the 1/3-octave band charts (A-weighted) are used for the comparison of noise emission levels intended for evaluating environmental noise exposure.

4.1.3 Overall Level Analysis

An analysis of the measured overall sound level was used to quantify the sound pressure level at each microphone location around the circumference of the reactor. This data was averaged to determine the single overall sound pressure level of the reactor operating at each given electrical excitation frequency. This was performed for seventeen excitation frequencies for the first prototype reactor and sixteen excitation frequencies for the second reactor. As was the case for the previous analysis, the overall A-weighted sound levels were computed using Brüel & Kjær BK Connect post-processing software. The overall A-weighted sound levels for each electrical excitation frequency and individual microphone signal values are given in Table 4-3 and Table 4-4 for prototype reactors one and two, respectively. The overall L_p level represents the A-weighted overall sound pressure level for each microphone signal at 2 m and 3 m for reactors 1 and 2, respectively. The $L_{p,avg}$ value is the logarithmically averaged sound pressure level for each electrical excitation frequency across all the microphones, a value which can be used to nominally report the sound level of the reactor.

Table 4-3 – Overall sound pressure levels for each signal, measurement, and supplied electrical frequency for prototype reactor 1.

Measurement	Signal (Microphone)	Overall L_p [dBA]	$L_{p,avg}$ [dBA]
180Hz 400A	Signal 1	68.16	68.25
	Signal 2	65.15	
	Signal 3	70.57	
	Signal 4	68.93	
	Signal 5	67.07	
	Signal 6	70.13	
	Signal 7	65.62	
	Signal 8	65.96	
	Signal 9	69.12	

Measurement	Signal (Microphone)	Overall L _p [dBA]	L _{p,avg} [dBA]
210Hz 400A	Signal 1	65.67	66.21
	Signal 2	68.82	
	Signal 3	65.91	
	Signal 4	66.70	
	Signal 5	62.50	
	Signal 6	64.88	
	Signal 7	68.49	
	Signal 8	66.70	
	Signal 9	60.59	
240Hz 400A	Signal 1	59.92	61.96
	Signal 2	62.91	
	Signal 3	64.59	
	Signal 4	61.39	
	Signal 5	62.63	
	Signal 6	59.94	
	Signal 7	59.96	
	Signal 8	59.42	
	Signal 9	63.57	
270Hz 400A	Signal 1	62.04	63.90
	Signal 2	65.77	
	Signal 3	62.31	
	Signal 4	60.94	
	Signal 5	63.94	
	Signal 6	64.80	
	Signal 7	63.44	
	Signal 8	62.14	
	Signal 9	66.45	
300Hz 300A	Signal 1	73.41	67.80
	Signal 2	67.34	
	Signal 3	68.01	
	Signal 4	59.02	
	Signal 5	59.77	
	Signal 6	59.10	
	Signal 7	65.89	
	Signal 8	66.96	
	Signal 9	69.63	
330Hz 200A	Signal 1	63.55	64.02
	Signal 2	62.44	

Measurement	Signal (Microphone)	Overall L _p [dBA]	L _{p,avg} [dBA]
	Signal 3	62.49	
	Signal 4	64.42	
	Signal 5	63.39	
	Signal 6	64.66	
	Signal 7	65.62	
	Signal 8	66.32	
	Signal 9	60.46	
360Hz 200A	Signal 1	61.37	70.29
	Signal 2	73.91	
	Signal 3	70.29	
	Signal 4	62.80	
	Signal 5	71.60	
	Signal 6	65.11	
	Signal 7	72.31	
	Signal 8	72.13	
	Signal 9	68.25	
390Hz 150A	Signal 1	68.94	68.78
	Signal 2	69.08	
	Signal 3	73.69	
	Signal 4	62.65	
	Signal 5	66.57	
	Signal 6	67.44	
	Signal 7	63.93	
	Signal 8	66.94	
	Signal 9	69.67	
420Hz 175A	Signal 1	71.43	70.20
	Signal 2	74.85	
	Signal 3	67.80	
	Signal 4	64.05	
	Signal 5	70.82	
	Signal 6	70.24	
	Signal 7	67.65	
	Signal 8	70.34	
	Signal 9	62.92	
450Hz 250A	Signal 1	65.94	74.17
	Signal 2	75.60	
	Signal 3	72.75	
	Signal 4	68.59	

Measurement	Signal (Microphone)	Overall L _p [dBA]	L _{p,avg} [dBA]
	Signal 5	74.46	
	Signal 6	75.45	
	Signal 7	69.74	
	Signal 8	79.75	
	Signal 9	62.84	
480Hz 250A	Signal 1	73.91	73.30
	Signal 2	77.38	
	Signal 3	73.89	
	Signal 4	64.89	
	Signal 5	71.68	
	Signal 6	70.79	
	Signal 7	69.17	
	Signal 8	69.92	
	Signal 9	76.09	
510Hz 230A	Signal 1	70.34	69.87
	Signal 2	69.23	
	Signal 3	68.04	
	Signal 4	67.75	
	Signal 5	75.20	
	Signal 6	63.38	
	Signal 7	69.26	
	Signal 8	66.71	
	Signal 9	68.75	
540Hz 225A	Signal 1	66.91	65.93
	Signal 2	66.82	
	Signal 3	61.82	
	Signal 4	64.84	
	Signal 5	60.53	
	Signal 6	70.14	
	Signal 7	66.41	
	Signal 8	65.14	
	Signal 9	62.74	
570Hz 230A	Signal 1	71.77	68.34
	Signal 2	70.76	
	Signal 3	67.68	
	Signal 4	70.09	
	Signal 5	65.93	
	Signal 6	60.98	

Measurement	Signal (Microphone)	Overall L _p [dBA]	L _{p,avg} [dBA]
	Signal 7	65.33	
	Signal 8	64.83	
	Signal 9	68.33	
600Hz 250A	Signal 1	64.63	64.97
	Signal 2	63.93	
	Signal 3	62.16	
	Signal 4	64.84	
	Signal 5	68.74	
	Signal 6	66.72	
	Signal 7	61.89	
	Signal 8	62.58	
	Signal 9	64.21	
630Hz 180A	Signal 1	61.34	61.70
	Signal 2	65.89	
	Signal 3	60.47	
	Signal 4	60.46	
	Signal 5	61.52	
	Signal 6	61.40	
	Signal 7	59.53	
	Signal 8	60.43	
	Signal 9	60.18	
660Hz 185A	Signal 1	59.96	60.31
	Signal 2	59.75	
	Signal 3	60.43	
	Signal 4	61.01	
	Signal 5	60.46	
	Signal 6	60.05	
	Signal 7	61.01	
	Signal 8	60.43	
	Signal 9	59.39	

Table 4-4 – Overall sound pressure levels for each signal, measurement, and supplied electrical frequency for prototype reactor 2.

Measurement	Signal (Microphone)	Overall L _p [dBA]	L _{p,avg} [dBA]
180Hz 400A	Signal 1	60.69	59.04
	Signal 2	58.74	
	Signal 3	59.32	
	Signal 4	59.05	
	Signal 5	59.54	
	Signal 6	57.97	
	Signal 7	58.28	
	Signal 8	58.65	
	Signal 9	58.45	
210Hz 400A	Signal 1	61.36	61.95
	Signal 2	61.24	
	Signal 3	61.52	
	Signal 4	61.83	
	Signal 5	61.33	
	Signal 6	61.53	
	Signal 7	61.47	
	Signal 8	63.91	
	Signal 9	62.58	
240Hz 400A	Signal 1	61.28	62.01
	Signal 2	62.21	
	Signal 3	60.55	
	Signal 4	60.77	
	Signal 5	60.51	
	Signal 6	60.69	
	Signal 7	61.17	
	Signal 8	62.31	
	Signal 9	65.64	
270Hz 400A	Signal 1	63.04	65.43
	Signal 2	63.65	
	Signal 3	66.93	
	Signal 4	61.22	
	Signal 5	65.35	
	Signal 6	67.76	
	Signal 7	61.75	
	Signal 8	62.99	
	Signal 9	68.98	
300Hz 300A	Signal 1	61.18	62.14

Measurement	Signal (Microphone)	Overall L _p [dBA]	L _{p,avg} [dBA]
	Signal 2	60.27	
	Signal 3	62.64	
	Signal 4	62.89	
	Signal 5	60.46	
	Signal 6	62.10	
	Signal 7	63.29	
	Signal 8	62.84	
	Signal 9	62.55	
330Hz 200A	Signal 1	59.70	60.60
	Signal 2	59.59	
	Signal 3	60.79	
	Signal 4	61.23	
	Signal 5	60.31	
	Signal 6	60.20	
	Signal 7	60.46	
	Signal 8	60.98	
360Hz 200A	Signal 1	59.51	59.23
	Signal 2	59.24	
	Signal 3	60.74	
	Signal 4	59.89	
	Signal 5	59.58	
	Signal 6	56.85	
	Signal 7	59.88	
	Signal 8	56.84	
390Hz 200A	Signal 1	59.01	59.09
	Signal 2	58.49	
	Signal 3	58.82	
	Signal 4	59.15	
	Signal 5	60.02	
	Signal 6	59.71	
	Signal 7	59.20	
	Signal 8	58.21	
420Hz 175A	Signal 1	58.17	60.21
	Signal 2	60.62	
	Signal 3	60.81	

Measurement	Signal (Microphone)	Overall L _p [dBA]	L _{p,avg} [dBA]
	Signal 4	60.78	
	Signal 5	62.21	
	Signal 6	57.85	
	Signal 7	61.26	
	Signal 8	57.41	
	Signal 9	60.30	
450Hz 250A	Signal 1	62.68	63.47
	Signal 2	66.47	
	Signal 3	62.46	
	Signal 4	62.98	
	Signal 5	59.38	
	Signal 6	61.32	
	Signal 7	58.88	
	Signal 8	65.97	
480Hz 250A	Signal 9	64.83	65.17
	Signal 1	67.34	
	Signal 2	62.04	
	Signal 3	63.65	
	Signal 4	64.21	
	Signal 5	66.20	
	Signal 6	65.39	
	Signal 7	68.63	
	Signal 8	60.77	
510Hz 210A	Signal 9	61.83	66.63
	Signal 1	64.17	
	Signal 2	69.32	
	Signal 3	68.36	
	Signal 4	62.76	
	Signal 5	64.26	
	Signal 6	60.47	
	Signal 7	68.89	
	Signal 8	62.88	
540Hz 225A	Signal 9	69.08	73.10
	Signal 1	78.90	
	Signal 2	63.29	
	Signal 3	69.82	
	Signal 4	70.80	
	Signal 5	64.41	

Measurement	Signal (Microphone)	Overall L _p [dBA]	L _{p,avg} [dBA]
	Signal 6	72.62	
	Signal 7	77.33	
	Signal 8	66.42	
	Signal 9	64.79	
570Hz 210A	Signal 1	73.61	68.93
	Signal 2	63.94	
	Signal 3	65.83	
	Signal 4	70.31	
	Signal 5	69.90	
	Signal 6	64.62	
	Signal 7	65.34	
	Signal 8	69.33	
	Signal 9	67.57	
600Hz 225A	Signal 1	61.16	65.93
	Signal 2	66.44	
	Signal 3	71.44	
	Signal 4	65.00	
	Signal 5	62.53	
	Signal 6	59.70	
	Signal 7	66.48	
	Signal 8	66.06	
	Signal 9	60.92	
630Hz 170A	Signal 1	62.76	61.11
	Signal 2	60.01	
	Signal 3	60.69	
	Signal 4	61.04	
	Signal 5	60.54	
	Signal 6	62.41	
	Signal 7	59.82	
	Signal 8	58.62	
	Signal 9	62.40	

The analysis results were used to quantify the total noise emission of the reactor at each electrical excitation frequency. The individual signal values along with the average sound pressure level of each excitation frequency were used to conduct directivity analysis that is discussed in the following section of this chapter.

4.1.4 Directivity Analysis

Directivity is the measure of the directional characteristics of the noise emissions from a sound source. The overall sound pressure level for each microphone location was compared to quantify the directivity characteristics of the reactors' noise emissions. The A-weighted overall sound pressure levels were plotted for the nine microphone locations on a radial diagram to show the radial directivity of the energized reactor for each measured electrical excitation frequency. The radial directivity plots are provided in Figure 4-2 and Figure 4-3.

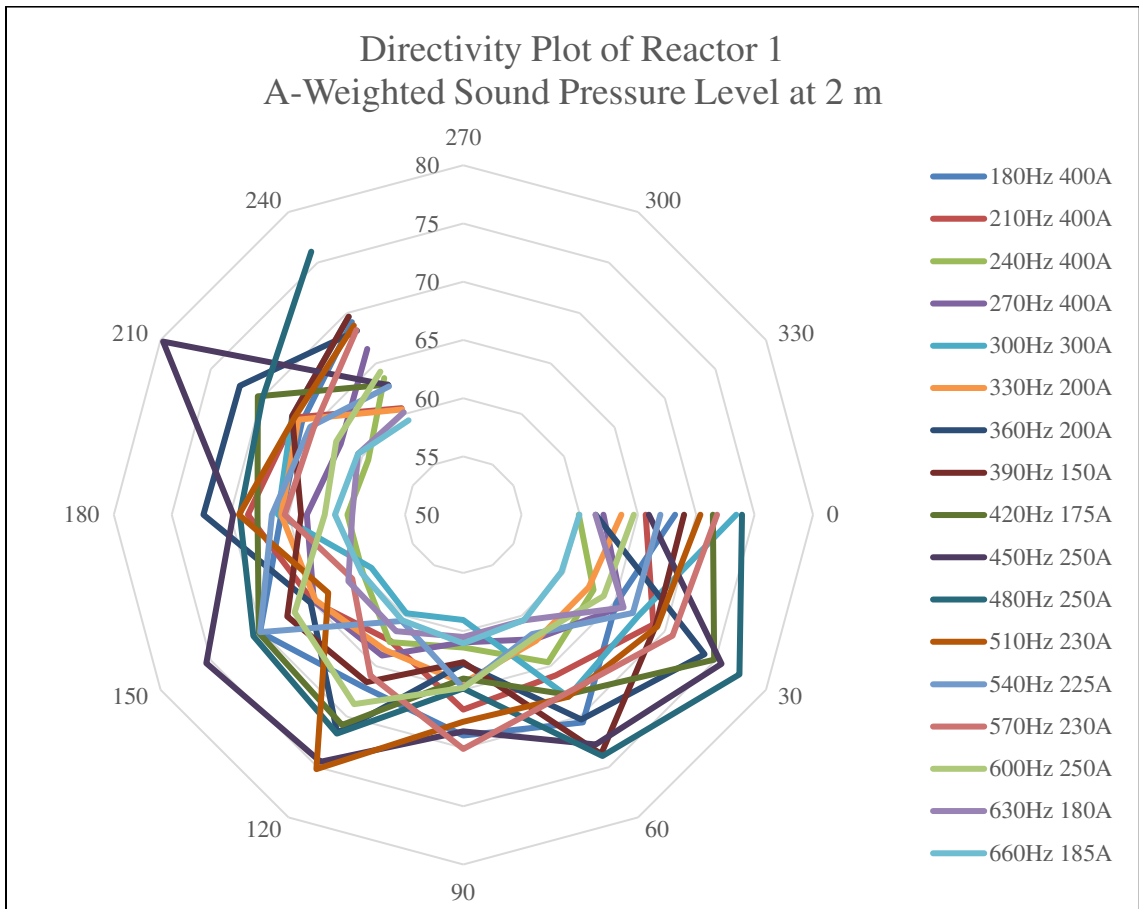


Figure 4-2 – Directivity radar plots of overall sound pressure levels at 2 m for each supplied electrical excitation frequency for reactor 1.

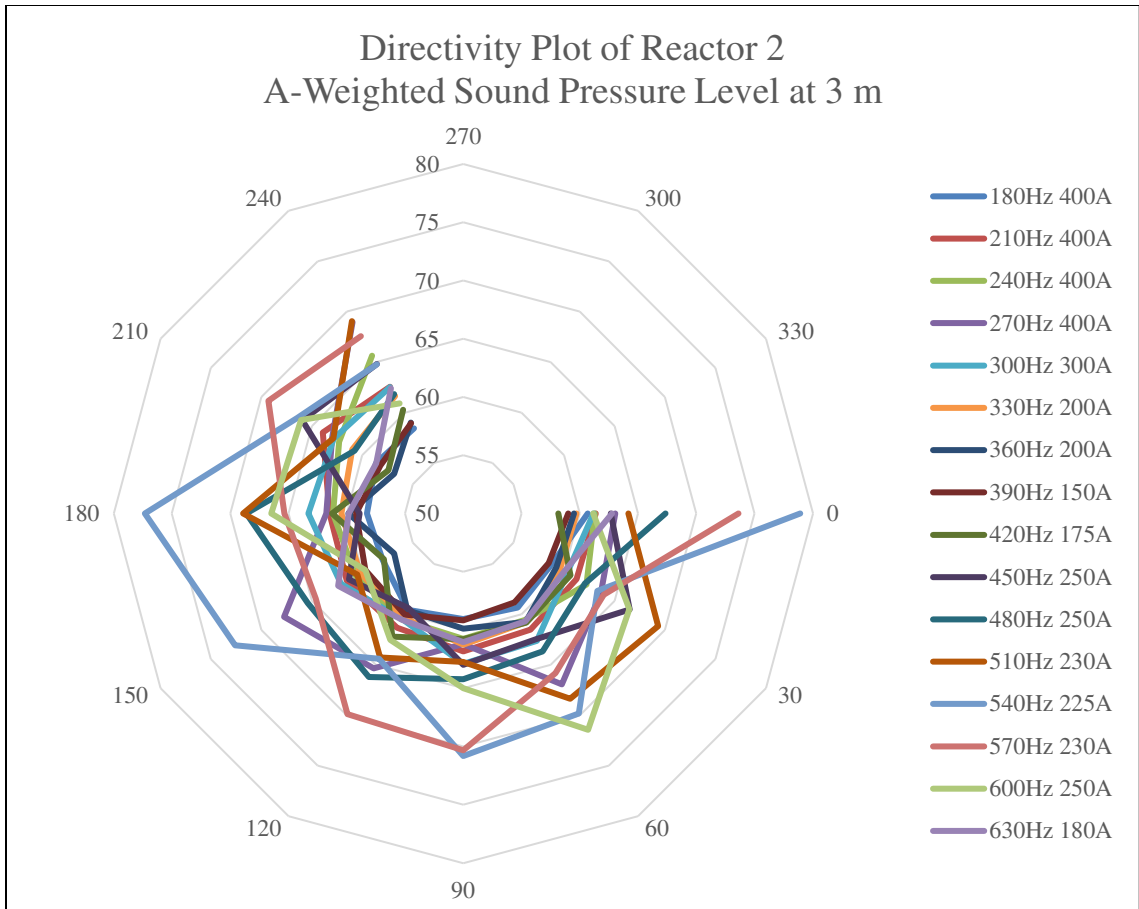


Figure 4-3 – Directivity radar plots of overall sound pressure levels at 3 m for each supplied electrical excitation frequency for reactor 2.

While initially assumed to radiate noise uniformly in all directions, it is apparent from the directivity radar plots that the reactor is a directive sound source. The radar plots also illustrate large differences in the directivity pattern at the various electrical frequencies. For example, when comparing the directivity curves for 540 Hz and 600 Hz of prototype reactor 2, the curves trending differs from one another with respect to sound level at each microphone location. The 540 Hz measurements showed elevated levels at 180° while the 600 Hz measurements displayed the greatest sound pressure level at 60°. When comparing the directivity curve for each electrical excitation frequency to one

another for each prototype reactor, it is apparent that there is no consistent pattern for directivity.

Depending on the excitation frequency some directivity patterns are similar, but this analysis alone cannot deduce the reasoning behind these results. Given that the reactor is a cylindrical source, an even radial sound distribution was expected. The test results proved this assumption to be incorrect. A potential source of this unexpected phenomenon could be resulting structural mode shapes of excited resonate frequencies, structure-borne noise of the wire package support spiders or influences from the termination points at the ends of the wire packages. In addition, if long enough, structural waves may cause deflections of different circumferential mode shapes (i.e., lobular circumferential deflection shapes).

The directivity indexes for each electrical excitation frequency were calculated for both reactors. The directivity index represents the difference in sound pressure level of a single microphone location from the average sound pressure level of all nine microphone signals. The calculated directivity index values are shown in Table 4-5 and Table 4-6.

Table 4-5 – Directivity Index for each measured electrical excitation frequency at each radial measurement location for reactor 1.

Signal	1	2	3	4	5	6	7	8	9
DI_{θ} 180Hz [dB]	-0.09	-3.10	2.31	0.67	-1.19	1.88	-2.64	-2.29	0.87
DI_{θ} 210Hz [dB]	-0.54	2.61	-0.30	0.49	-3.71	-1.33	2.27	0.48	-5.62
DI_{θ} 240Hz [dB]	-2.04	0.95	2.63	-0.57	0.66	-2.03	-2.01	-2.55	1.60
DI_{θ} 270Hz [dB]	-1.86	1.87	-1.59	-2.96	0.05	0.90	-0.46	-1.75	2.55
DI_{θ} 300Hz [dB]	5.61	-0.46	0.20	-8.78	-8.04	-8.70	-1.91	-0.85	1.83
DI_{θ} 330Hz [dB]	-0.46	-1.58	-1.53	0.40	-0.63	0.64	1.60	2.30	-3.56
DI_{θ} 360Hz [dB]	-8.92	3.62	-0.01	-7.50	1.31	-5.18	2.01	1.84	-2.05
DI_{θ} 390Hz [dB]	0.16	0.30	4.91	-6.13	-2.21	-1.33	-4.85	-1.83	0.89
DI_{θ} 420Hz [dB]	1.22	4.65	-2.40	-6.15	0.62	0.04	-2.55	0.14	-7.28
DI_{θ} 450Hz [dB]	-8.24	1.43	-1.43	-5.58	0.29	1.28	-4.43	5.58	-11.33
DI_{θ} 480Hz [dB]	0.61	4.08	0.59	-8.40	-1.62	-2.51	-4.13	-3.38	2.79
DI_{θ} 510Hz [dB]	0.47	-0.64	-1.83	-2.12	5.32	-6.50	-0.62	-3.17	-1.12
DI_{θ} 540Hz [dB]	0.98	0.89	-4.11	-1.10	-5.40	4.21	0.48	-0.79	-3.19
DI_{θ} 570Hz [dB]	3.43	2.42	-0.66	1.75	-2.41	-7.36	-3.02	-3.52	-0.02
DI_{θ} 600Hz [dB]	-0.34	-1.04	-2.80	-0.13	3.78	1.75	-3.08	-2.39	-0.76
DI_{θ} 630Hz [dB]	-0.36	4.19	-1.23	-1.24	-0.18	-0.30	-2.17	-1.27	-1.52
DI_{θ} 660Hz [dB]	-0.34	-0.56	0.12	0.71	0.15	-0.26	0.71	0.12	-0.92

Table 4-6 – Directivity Index for each measured electrical excitation frequency at each radial measurement location for reactor 2.

Signal	1	2	3	4	5	6	7	8	9
DI_{θ} 180Hz [dB]	1.65	-0.29	0.29	0.01	0.50	-1.06	-0.76	-0.39	-0.59
DI_{θ} 210Hz [dB]	-0.59	-0.72	-0.43	-0.12	-0.62	-0.42	-0.48	1.96	0.63
DI_{θ} 240Hz [dB]	-0.73	0.19	-1.47	-1.25	-1.51	-1.33	-0.84	0.30	3.63
DI_{θ} 270Hz [dB]	-2.39	-1.77	1.51	-4.21	-0.07	2.34	-3.67	-2.44	3.55
DI_{θ} 300Hz [dB]	-0.97	-1.87	0.49	0.74	-1.68	-0.04	1.15	0.70	0.40
DI_{θ} 330Hz [dB]	-0.89	-1.01	0.19	0.64	-0.28	-0.40	-0.13	0.39	1.07
DI_{θ} 360Hz [dB]	0.28	0.01	1.51	0.66	0.35	-2.38	0.65	-2.39	-0.22
DI_{θ} 390Hz [dB]	-0.08	-0.61	-0.27	0.05	0.93	0.62	0.10	-0.88	-0.15
DI_{θ} 420Hz [dB]	-2.03	0.41	0.60	0.57	2.00	-2.36	1.06	-2.80	0.09
DI_{θ} 450Hz [dB]	-0.80	2.99	-1.01	-0.49	-4.10	-2.15	-4.59	2.50	1.36
DI_{θ} 480Hz [dB]	2.16	-3.13	-1.52	-0.97	1.03	0.22	3.46	-4.40	-3.34
DI_{θ} 510Hz [dB]	-2.46	2.68	1.72	-3.88	-2.37	-6.16	2.26	-3.75	2.44
DI_{θ} 540Hz [dB]	5.80	-9.81	-3.28	-2.31	-8.70	-0.49	4.23	-6.68	-8.31
DI_{θ} 570Hz [dB]	4.68	-5.00	-3.10	1.38	0.96	-4.31	-3.59	0.40	-1.36
DI_{θ} 600Hz [dB]	-4.77	0.51	5.51	-0.93	-3.40	-6.23	0.55	0.13	-5.01
DI_{θ} 630Hz [dB]	1.65	-1.11	-0.42	-0.07	-0.57	1.29	-1.29	-2.50	1.29

The results from the analysis of the directivity of the reactor noise has shown an unexpected complexity to the produced noise emissions as is illustrated by the directivity index and radar plots. The directional sound levels vary as much as 17 dB for the first prototype reactor and 16 dB for the second prototype reactor over the nine measurement locations for a given electrical frequency. This is a large variation for locations that are only 30° apart at a radial distance of two or three metres from the reactor. To date, there is no discussion or scientific model in the literature to predict the reactor acoustic directivity; it can only be measured after construction. A more thorough discussion of the complex mechanisms that cause the noise emission of the reactor is discussed in later sections of this dissertation.

4.2 *Noise Source Identification (NSI)*

In the simplest of terms, NSI is the process of collecting noise data using an array of microphones and calculating an output that visually represents the noise characteristics in both amplitude and sometimes frequency. For this work, a one-meter diameter Brüel & Kjær array having 60 microphones was used to acquire the NSI data with the Brüel & Kjær Array Acoustic Post-Processing software package used to output the acoustic propagation plots for the reactors. While different beamforming calculation algorithms exist, for this work, a refined beamforming algorithm was used to process the recorded data. Refined beamforming applies the non-negative least square (NNLS) algorithm to localize and characterize the source of sound. The NNLS algorithm is an advanced approach which is a derivation of the deconvolution beamforming method and was selected as it provides the highest spatial resolution.

Using the refined beamforming approach, contour plots were produced and overlaid on images (imported photographs) of the reactors. The software also calculated the sound intensity level in 1/3 octaves, and within the 50 Hz to 5000 Hz frequency range, on the imaginary hologram plane over the reactor surface. The calculated contour plots, along with corresponding overall sound power level graphs, are given in Figure 4-4 to Figure 4-27 for the electrical frequencies of 300 Hz, 360 Hz and 420 Hz, respectively.



Figure 4-4 – Overall NSI contour plot of reactor sound intensity level energized at 300 Hz - Location 1.

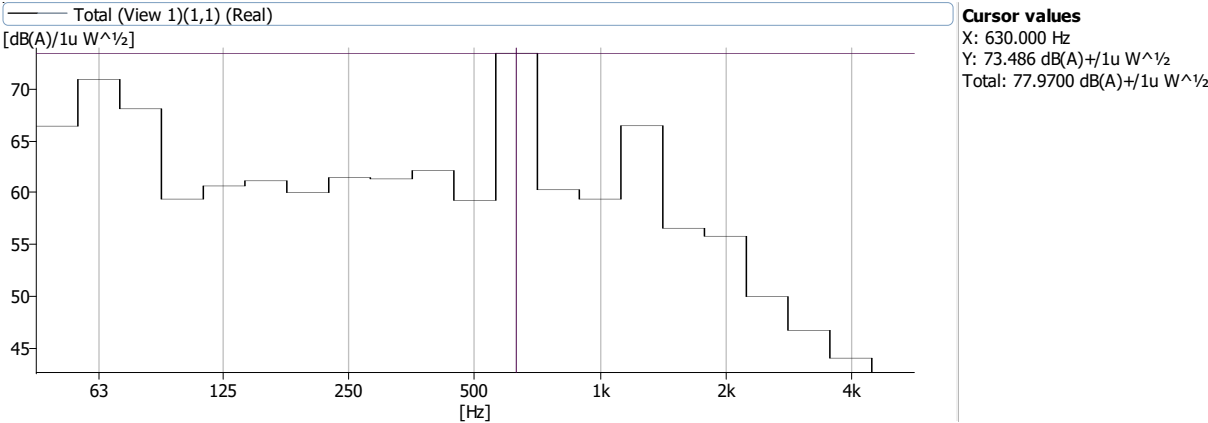


Figure 4-5 – NSI 1/3-octave sound power level plot of reactor energized at 300 Hz - Location 1.

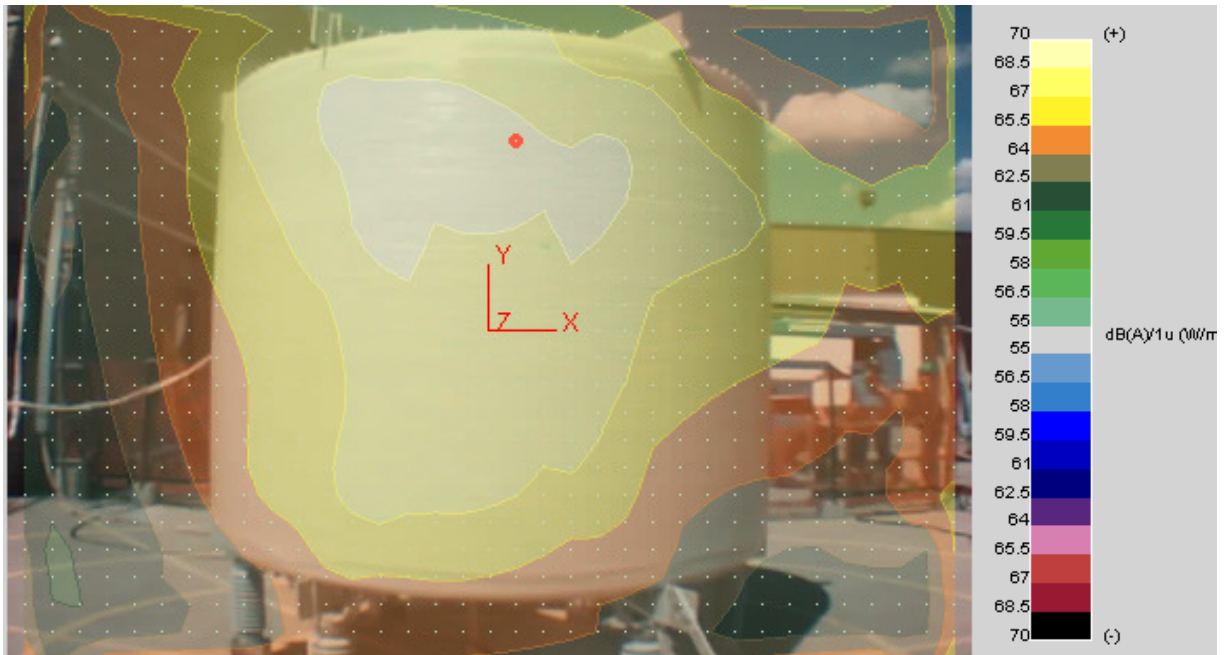


Figure 4-6 – Overall NSI contour plot of reactor sound intensity level energized at 300 Hz - Location 2.

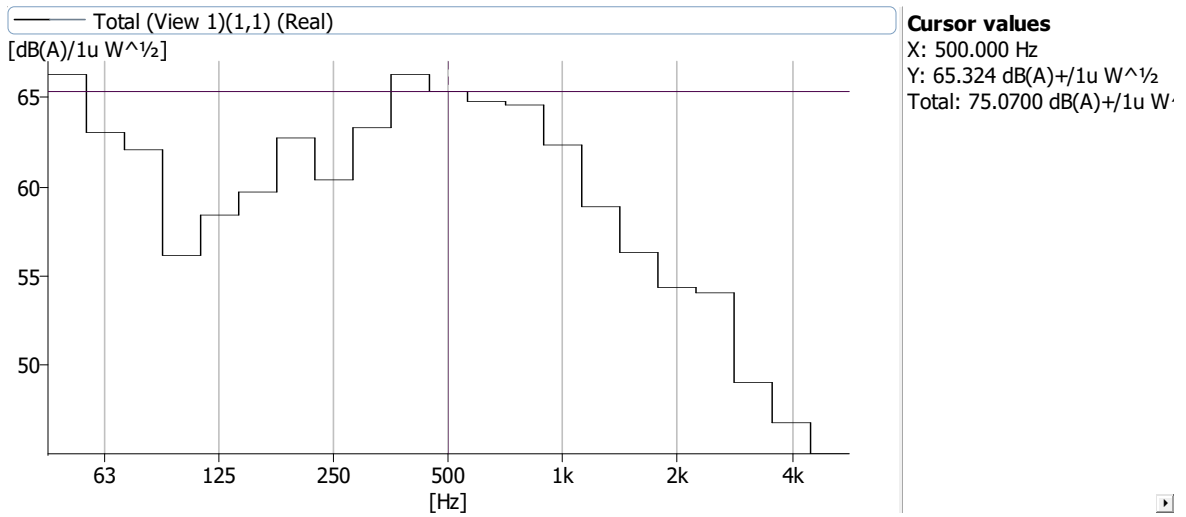


Figure 4-7 – NSI 1/3-octave sound power level plot of reactor energized at 300 Hz - Location 2.

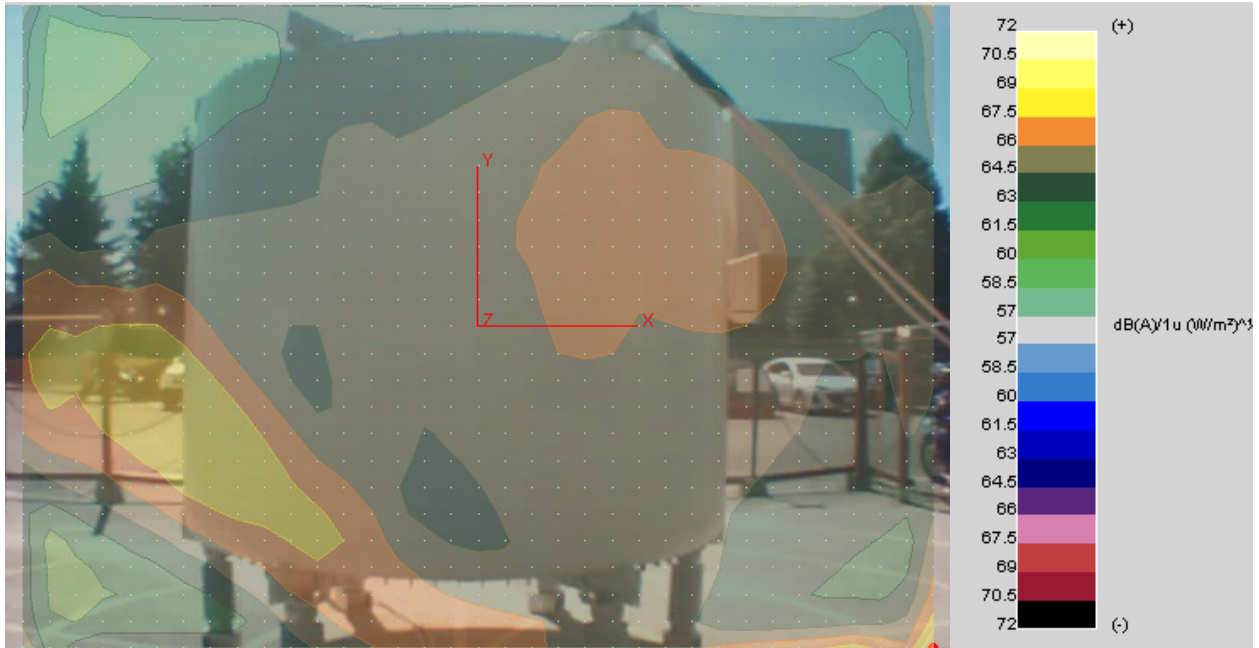


Figure 4-8 – Overall NSI contour plot of reactor sound intensity level energized at 300 Hz - Location 3.

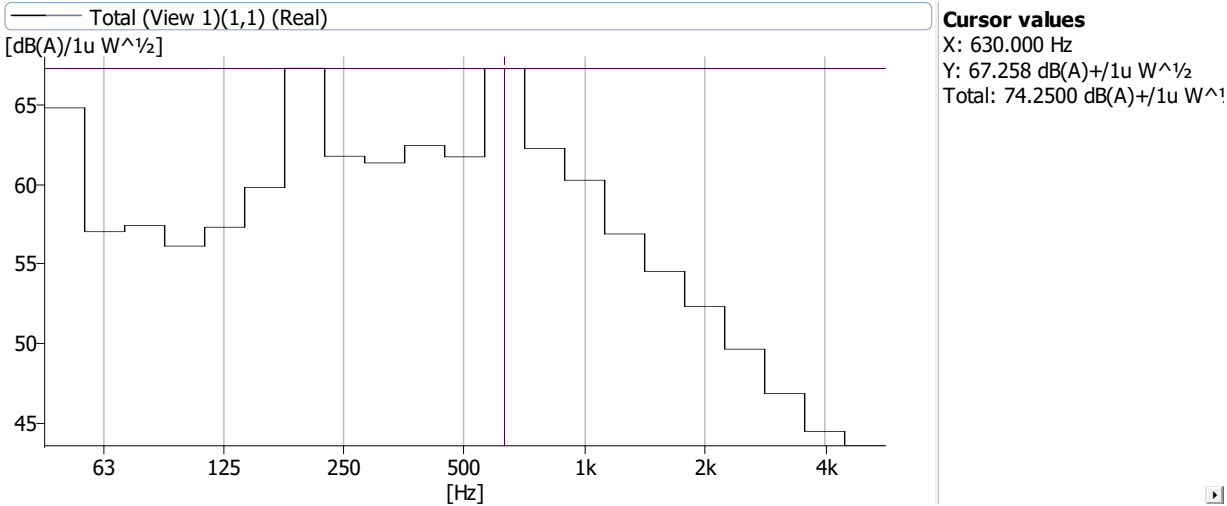


Figure 4-9 – NSI 1/3-octave sound power level plot of reactor energized at 300 Hz - Location 3.

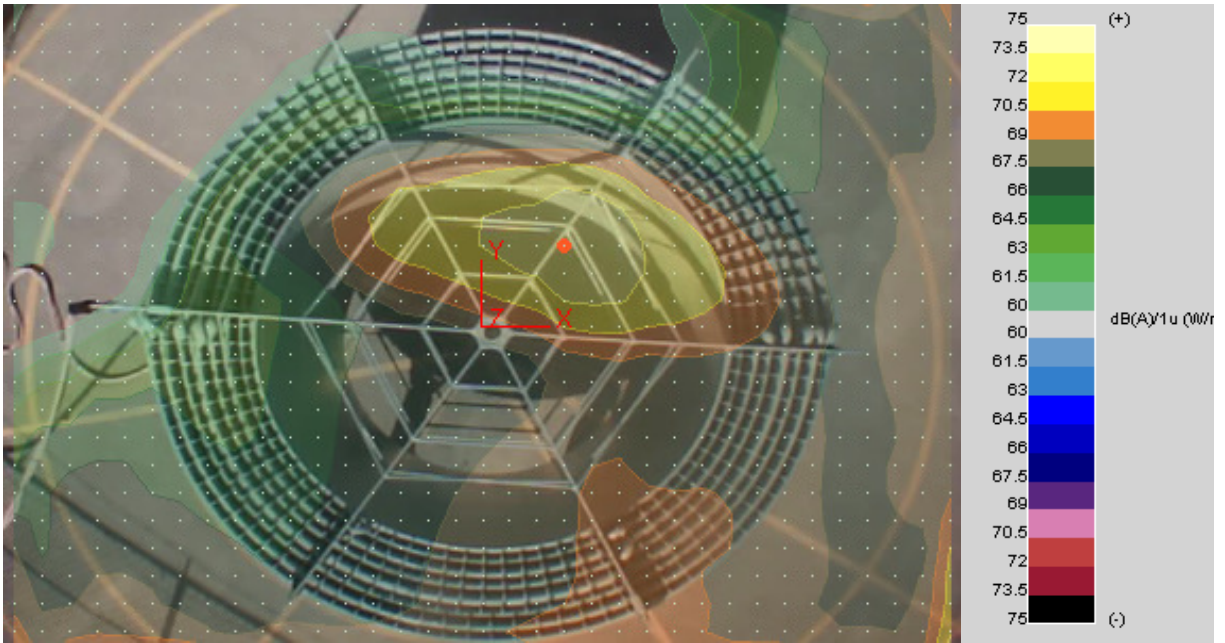


Figure 4-10 – Overall NSI contour plot of reactor sound intensity level energized at 300 Hz aerial view.

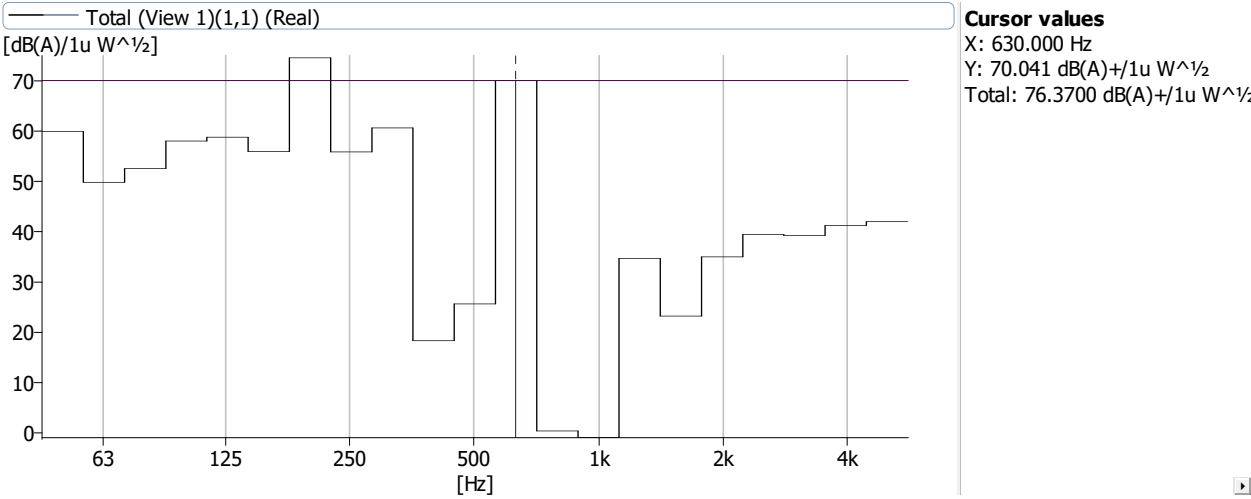


Figure 4-11 – NSI 1/3-octave sound power level plot of reactor energized at 300 Hz aerial view.

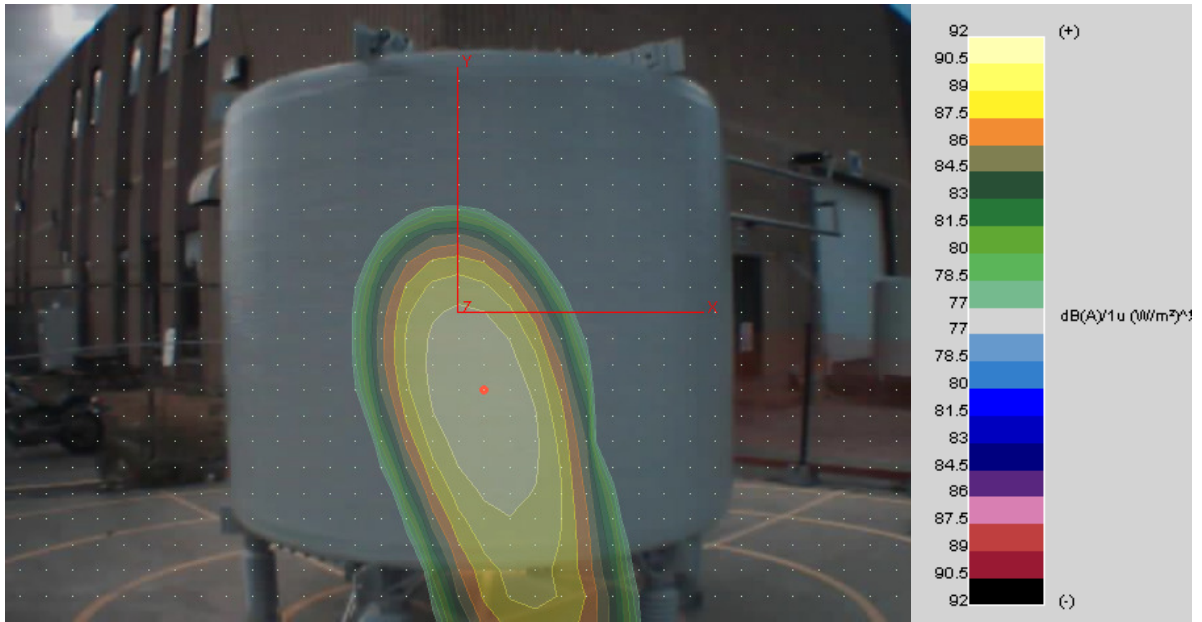


Figure 4-12 – Overall NSI contour plot of reactor sound intensity level energized at 360 Hz - Location 1.

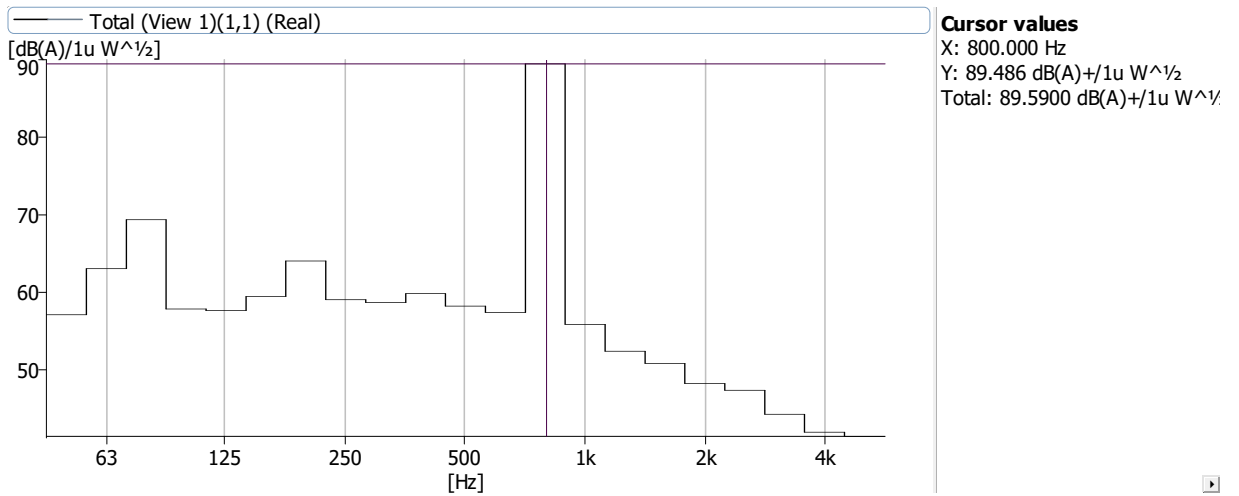


Figure 4-13 – NSI 1/3-octave sound power level plot of reactor energized at 360 Hz - Location 1.

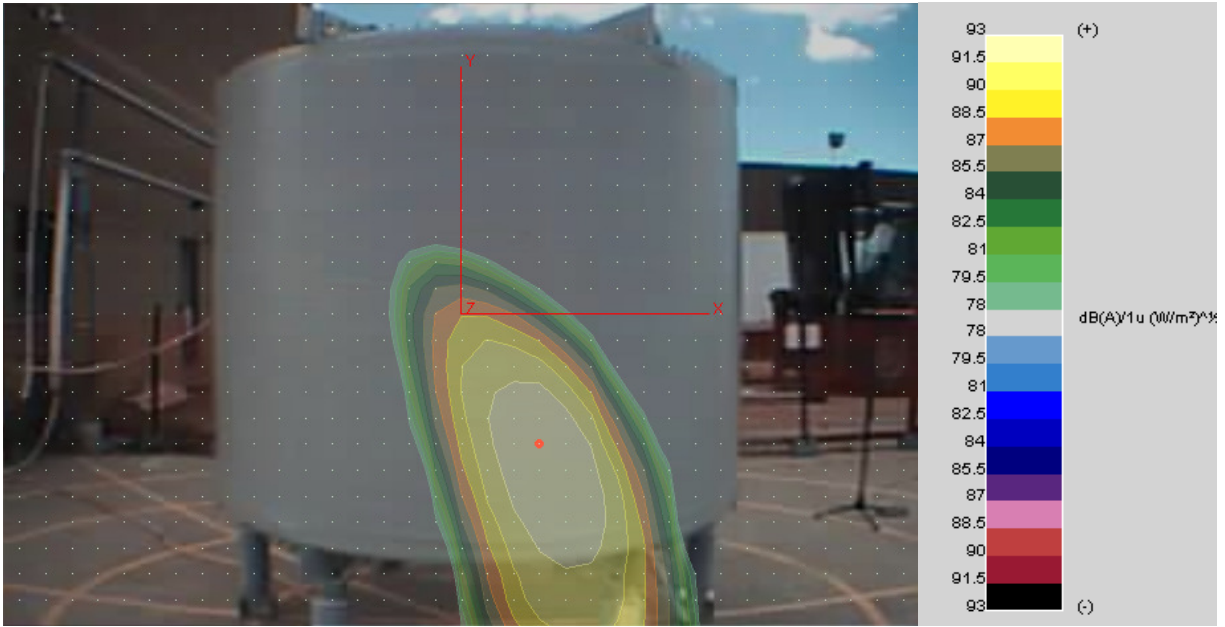


Figure 4-14 – Overall NSI contour plot of reactor sound intensity level energized at 360 Hz - Location 2.

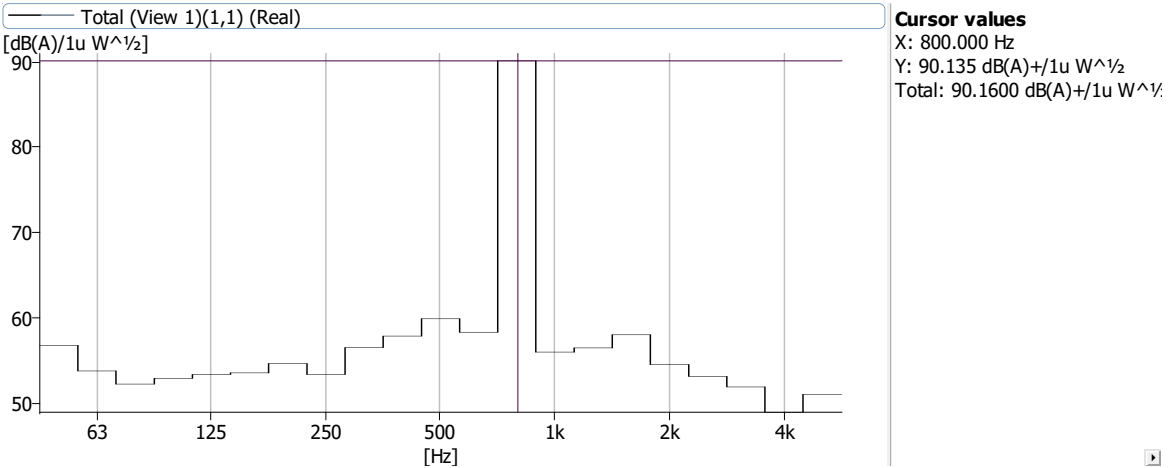


Figure 4-15 – NSI 1/3-octave sound power level plot of reactor energized at 360 Hz - Location 2.

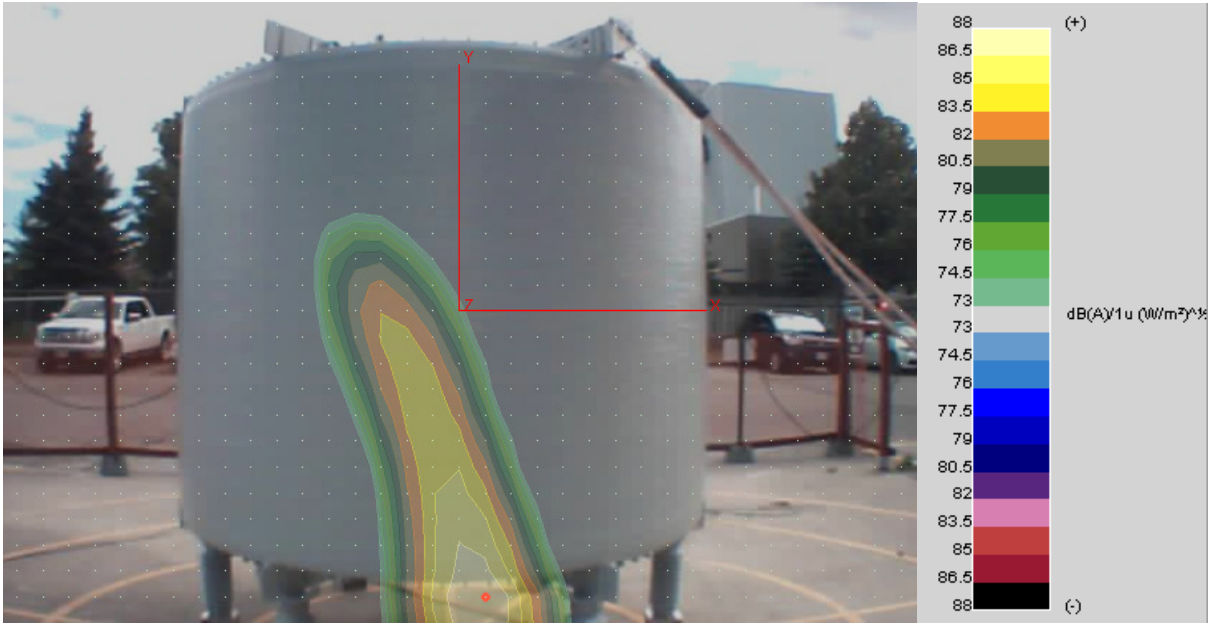


Figure 4-16 – Overall NSI contour plot of reactor sound intensity level energized at 360 Hz - Location 3.

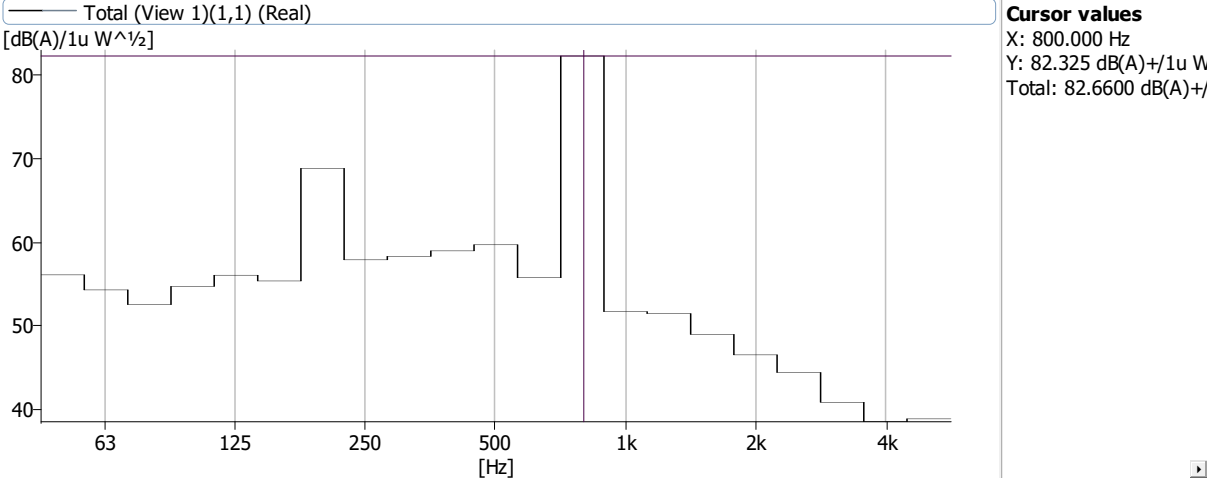


Figure 4-17 – NSI 1/3-octave sound power level plot of reactor energized at 360 Hz - Location 3.

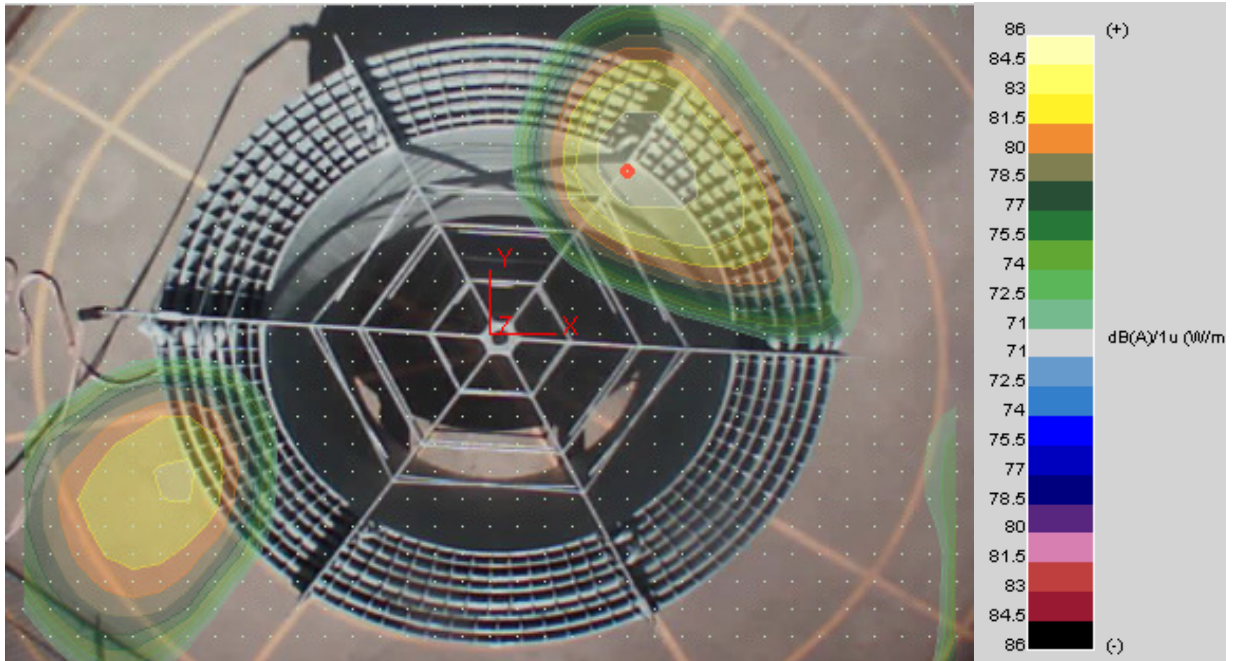


Figure 4-18 – Overall NSI contour plot of reactor sound intensity level energized at 360 Hz - aerial view.

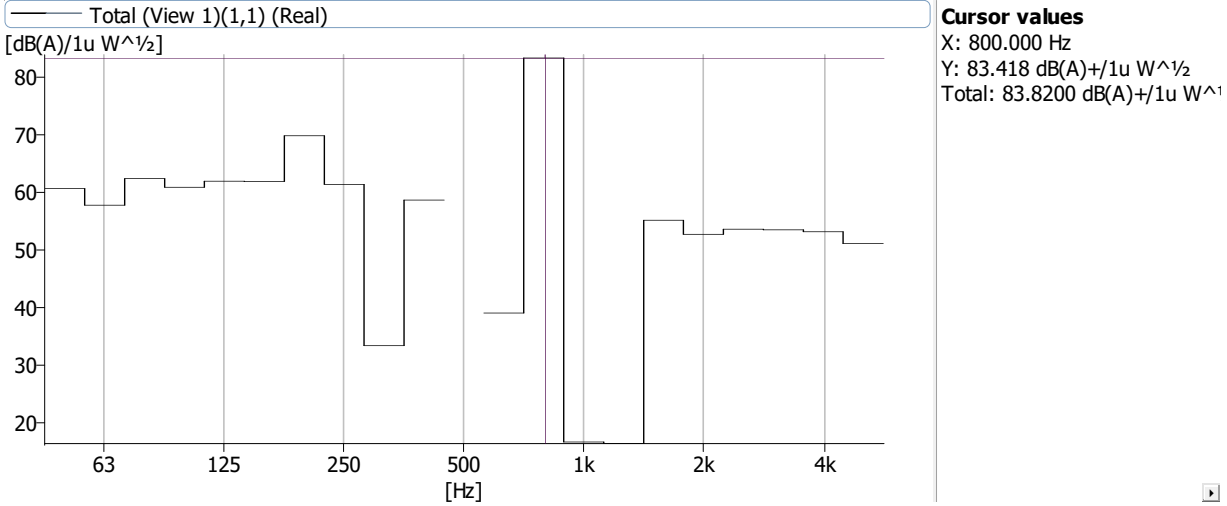


Figure 4-19 – NSI 1/3-octave sound power level plot of reactor energized at 360 Hz - aerial view.

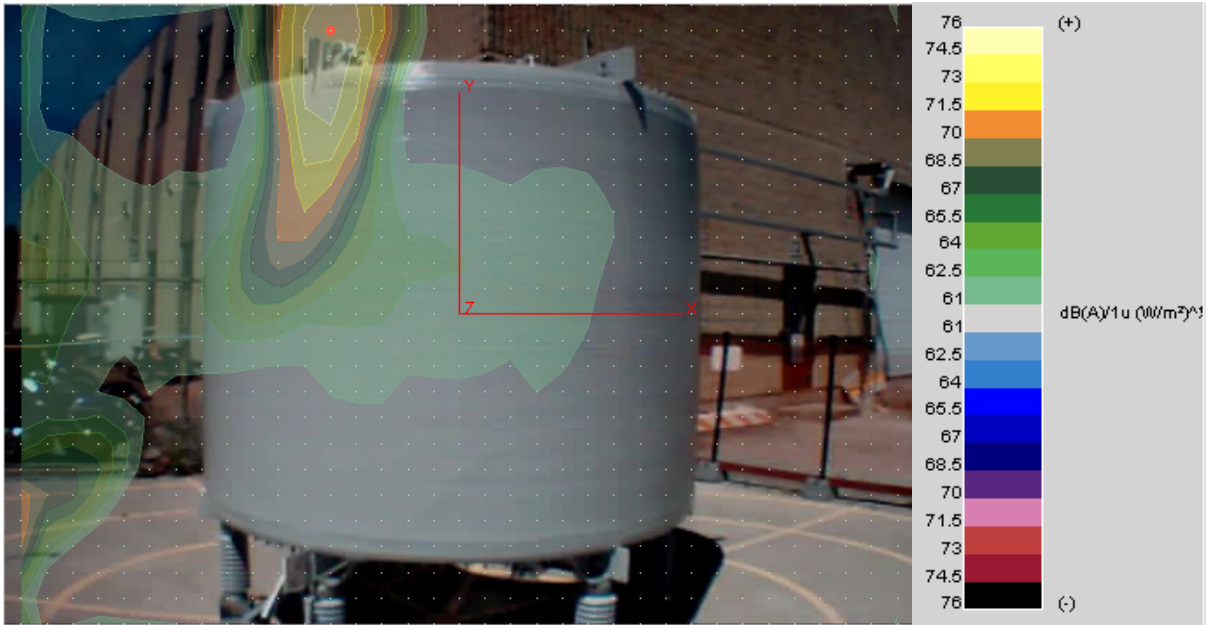


Figure 4-20 – Overall NSI contour plot of reactor sound intensity level energized at 420 Hz - Location 1.

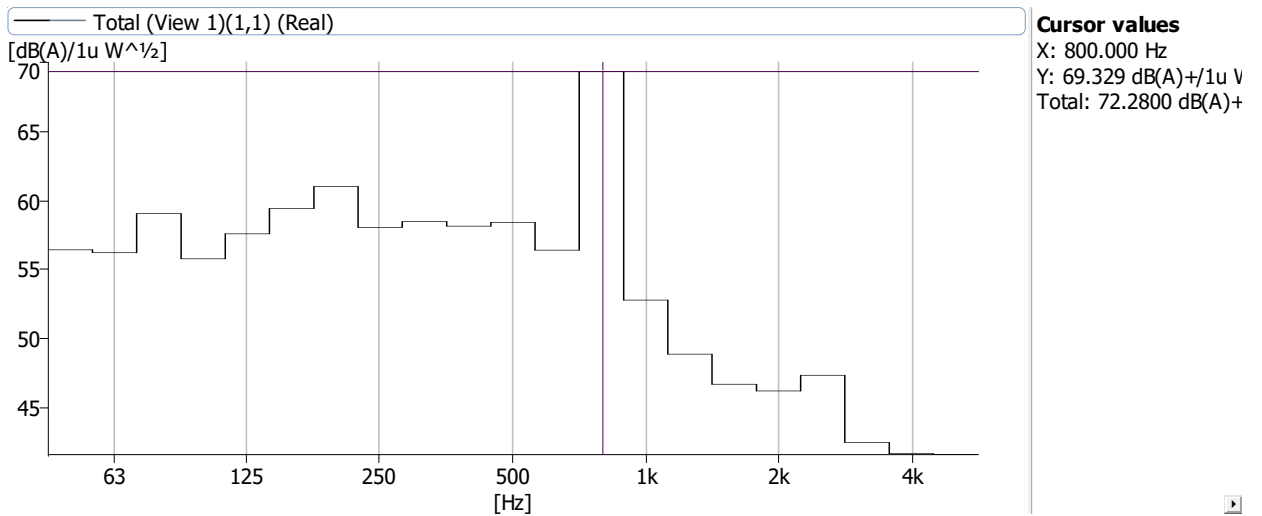


Figure 4-21 – NSI 1/3-octave sound power level plot of reactor energized at 420 Hz - Location 1.

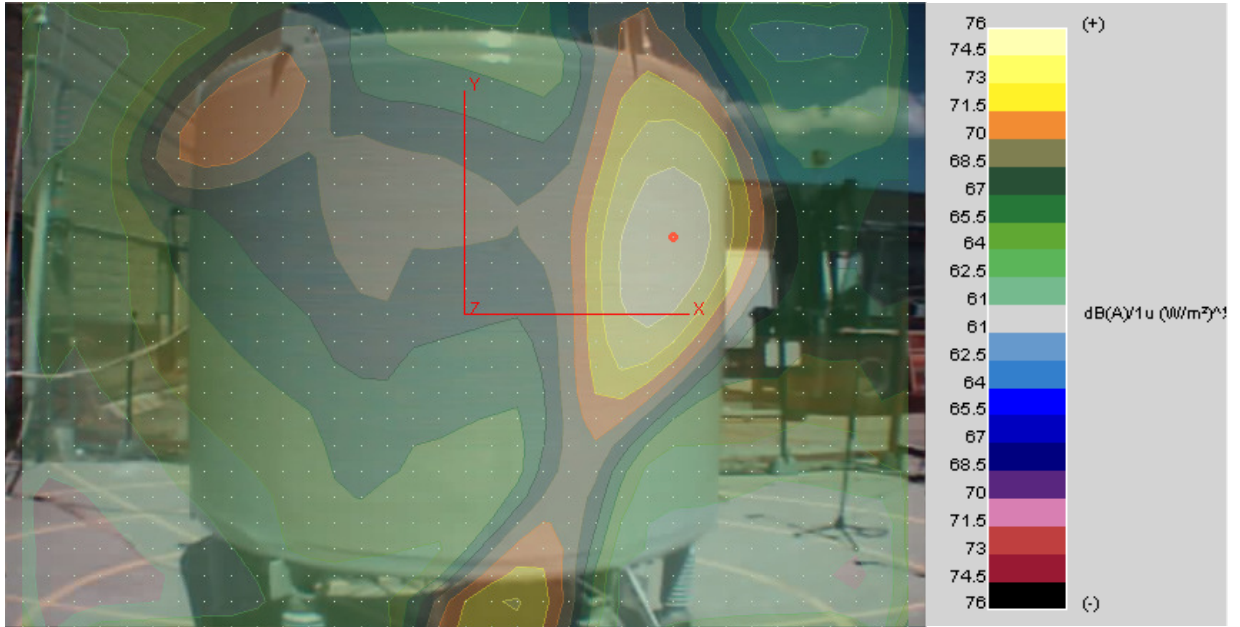


Figure 4-22 – Overall NSI contour plot of reactor sound intensity level energized at 420 Hz - Location 2.

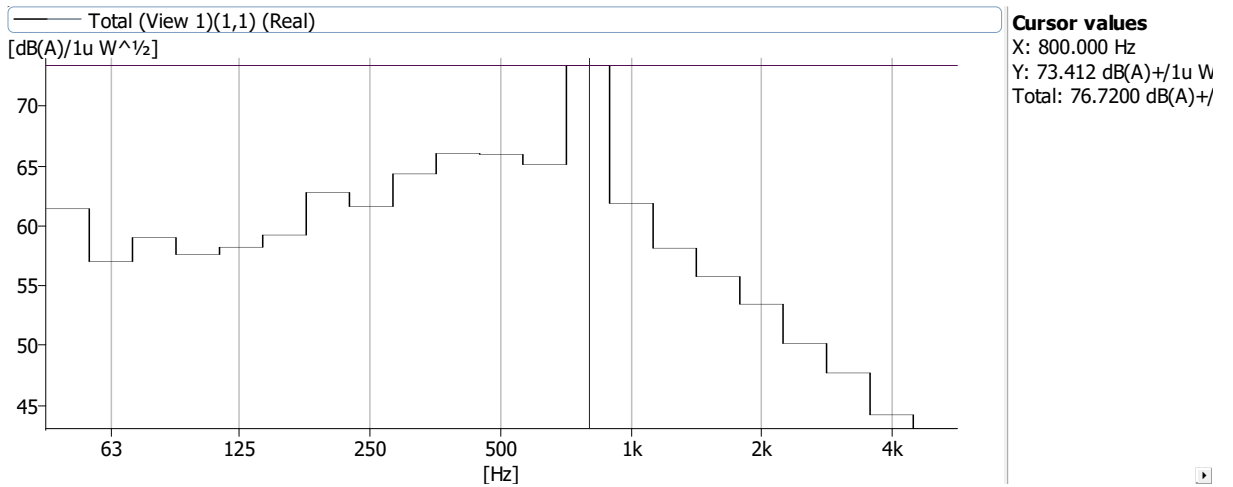


Figure 4-23 – NSI 1/3-octave sound power level plot of reactor energized at 420 Hz - Location 2.

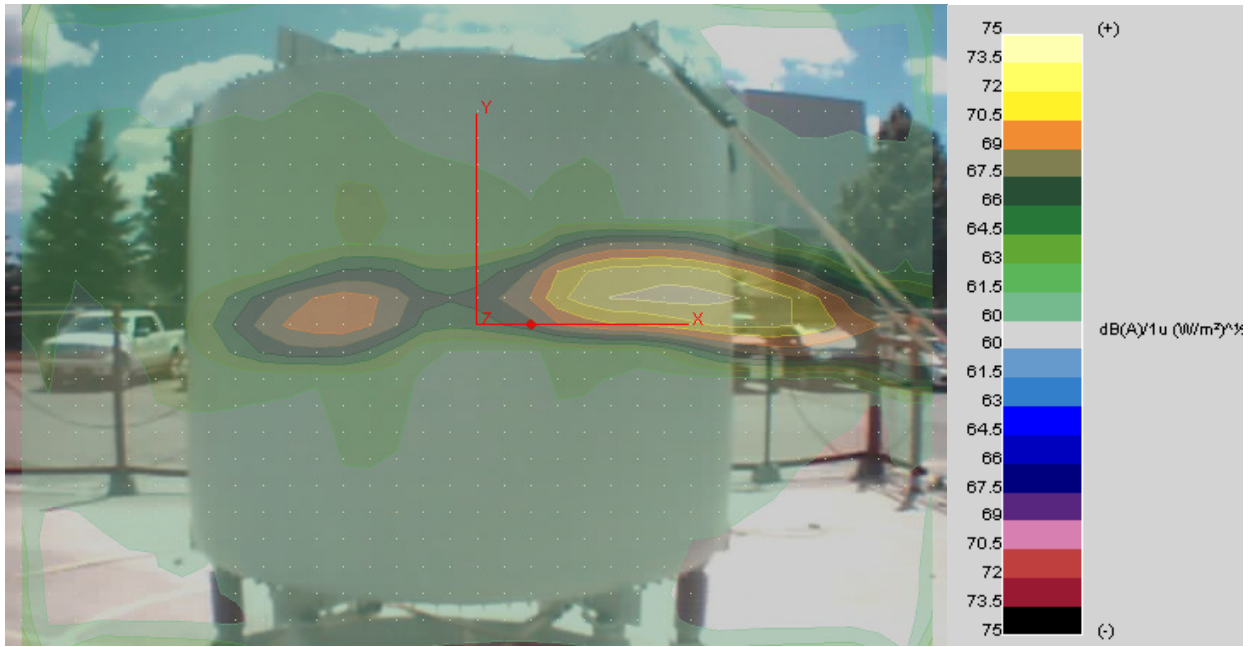


Figure 4-24 – Overall NSI contour plot of reactor sound intensity level energized at 420 Hz - Location 3.

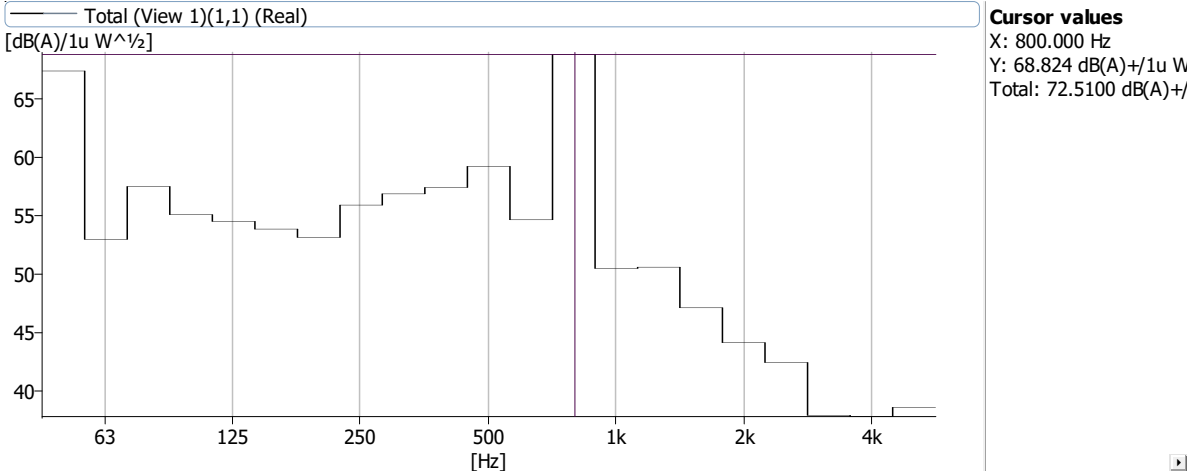


Figure 4-25 – NSI 1/3-octave sound power level plot of reactor energized 420 Hz - Location 3.

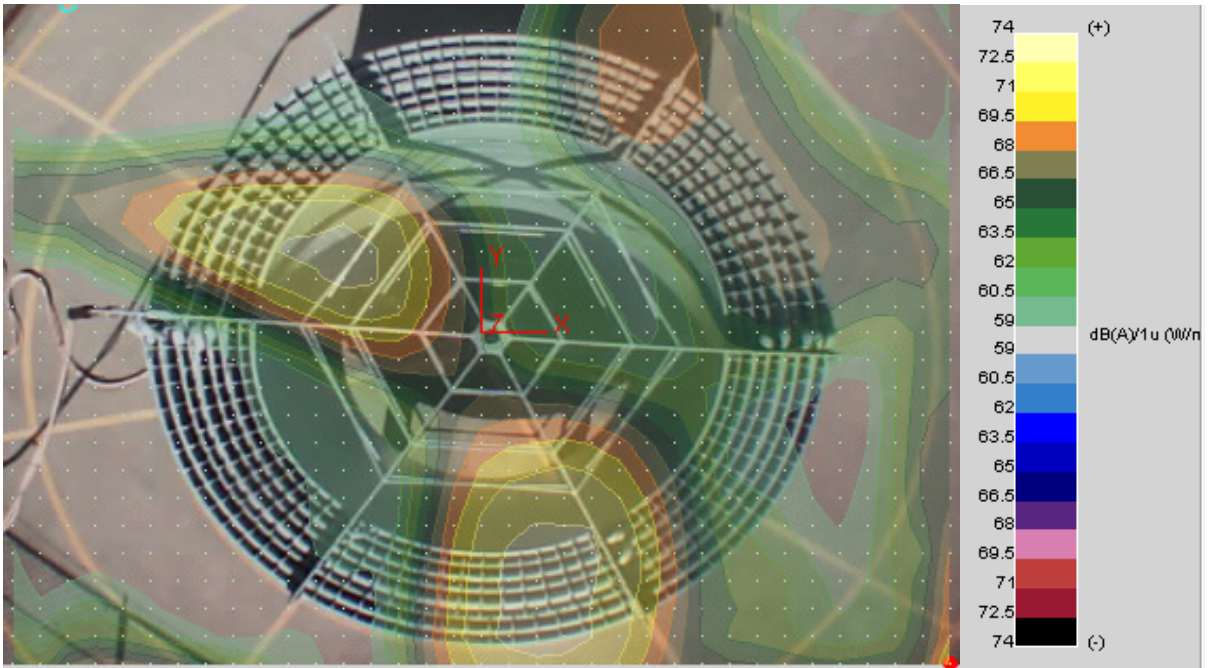


Figure 4-26 – Overall NSI contour plot of reactor sound intensity level energized at 420 Hz - aerial view.

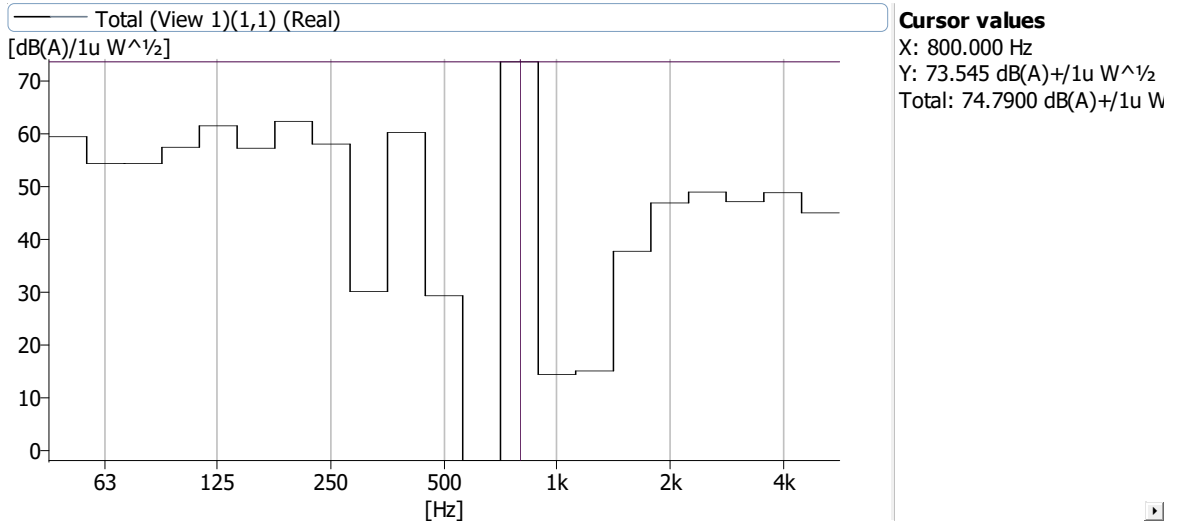


Figure 4-27 – NSI 1/3-octave sound power level plot of reactor energized at 420 Hz - aerial view.

An analysis by which the frequency bands were isolated was also conducted to identify the noise sub-sources for each frequency band. The contour plots identified that the only significant contributing sub-source emits sound in the 1/3-octave band which corresponds to that of the double of the electrical excitation frequency. These results are provided in Appendix C Noise Source Identification Results.

The areas with high source emission levels are depicted in white or bright yellow overlay, while the low sound emission areas are depicted as green or clear contours. The resulting contours illustrate that the areas of high and low noise emissions vary depending on the electrical excitation frequency. This is thought to be a result of the excitation of different structural modes of the reactor. It is also worthwhile to point out that the relationship of the electrical excitation to the mechanical excitation frequency is 1:2 and thus corresponds to a specific wavelength in the reactor's wire packages. Given that these wavelengths correspond to different wave numbers within the circumference and the length of the reactor in cylindrical vibration, the electrical excitation alone will result in varying modal shapes that depend on the frequency of excitation.

The areas of various noise emissions on the reactor identify discrepancies between measured noise and the noise prediction models currently in use. These prediction methods take the mid-plane of the reactor wire package to be the most significant noise emitter as this is the location of maximum deflection for the winding packages breathing mode. The NSI confirmed that this is not always the case. Depending on the electrical excitation frequency, the spider and termination regions were identified as significant sources of noise for the 420 Hz case. Even if the mid-plane was responsible for the noise emissions, it is not consistent around the entire reactor, nor are the noise emissions completely localized to the

mid-plane. In other words, the NSI contour plots show that the noise emissions are not constant around the reactor, which supports the findings from the directivity analysis, which identified strong directivity characteristics at the various electrical excitation frequencies.

The aerial view of the NSI contour plot identifies that the different noise contributors are not evenly distributed along the circumference of the inner or outer packages. For the case of the 360 Hz and 420 Hz electrical excitation frequencies, there are various circumferential nodal patterns in the noise emission distribution. This coincides with the modes described by Blevins cylindrical breathing modes [3]. It is now apparent that the circumferential nodal pattern changes depending on the reactor's electrical excitation frequency. This does not agree with the simple breathing vibrational displacement as laid out in the Blevins cylindrical breathing theory. With multiple excitation frequencies, identifying this nodal pattern becomes increasingly difficult.

The aerial NSI outputs also show noise emissions in the axial direction, as well as noise generation by the spiders. Examining the 300 Hz electrical excitation frequency contour plot given in the aerial view, the noise map differs greatly between the 360 Hz and 420 Hz aerial plots. The noise emission was identified as originating from the inner diameter of the inner wire package for only half of the reactor circumference. It appears that at this electrical excitation frequency (below the Blevins natural breathing mode frequency of the reactor), the noise radiation is generated at the inner diameter of the packages, and as such, the NSI for the outer package varies greatly from the other two electrical excitation frequencies. It is important to understand that the contour plots of the 300 Hz electrical excitation frequency identified the noise origin as the edges of the bottom

of the reactor. This corresponds to the aerial view as showing that significant noise emission was emitted from the inner package of the reactor. The NSI analysis shows that the inner package does not emit noise in the same manner as the outer wire package. Thus, an assumption of lumped mass across all wire packages and for all electrical frequencies is invalid. For example, the inner diameter of the reactor body at 300 Hz produced the greatest noise emission, while at 420 Hz, the middle and outer packages are identified as the significant noise contributors. The conclusion that can be taken from this analysis of the NSI data is that a more complex model, compared to the present state of science is needed to more accurately predict the reactor noise emission characteristics.

4.3 *Modal Analysis*

Modal analysis is a testing procedure that gives the physical dynamic properties of a structure while under induced vibrational excitation. This analysis quantifies the dynamic response of the structure at various measurement locations and relates them to the excitation input level. This results in a quantified response due to a forced structural excitation given as the frequency response functions (FRFs). Using the measured FRF data detailed in section 3.3, Modal Analysis Measurements, the FRF output graphs from the modal tests will identify the structural modes, or natural frequencies of the reactor structure.

The objective of the modal test and analysis was to determine whether the reactor noise emissions are related to a structural excitation of the reactor at any of the reactor's natural frequencies. The outcome was that natural frequencies were indeed identified near to some excitation frequencies. The consequence is that excitation of a natural frequency

can result in amplified vibration of the reactor structure, and as a result, an increase in the generation of noise.

In order to identify the structural modes and compute the natural frequencies, mode shapes, and damping ratio of the reactor structure, the FRFs were computed from the modal test data using the Brüel & Kjær Reflex post-processing software. A rational fraction polynomial (RFP) curve fitting method was used to solve the linear set of equations representing the FRF data for the unknown numerator and denominator polynomial coefficient. Poles and residues are found by numerical root solving and partial fraction expansion. Orthogonal rather than ordinary polynomials are used to improve the numerical stability of the RFP method, but they also uncouple the numerator and denominator coefficient solution equations. This allows the curve fitting problem to be divided into two steps and compatible with our data. Once the curve fitting is completed, difference mode indicator functions (MIF) are employed to determine the structural modes. Both MIF and complex MIF identifiers are used to determine the structural modes. These applications are integrated into the Brüel & Kjær Reflex software.

The modal analysis results can provide insight to the noise generation given that any induced excitation at a natural frequency of the structure can result in significant dynamic amplification of any structure-borne noise. Thus, the identification of the natural structural frequencies can be vital in explaining some of the reactor noise generation. Establishing a correlation between the strong natural modes and the excitation frequencies is significant for the development of the complex theories for the structural noise generation.

The strong modes were identified by locating the mode shapes with the amplified deflection. Using modal post-processing software with the described mode indicator functions, the strong structural modes were identified along with the resultant percent damping. These are given in Table 4-7 and Table 4-8 for the important modes which were selected to demonstrate the complexity of the reactors' structural modes.

Table 4-7 – Natural Structural Mode Frequencies and Damping Ratios for Reactor 1.

Mode	Damped Frequency (Hz)	Damping (%)
1	40.72658	0.64672
2	57.41719	1.01756
3	66.73911	1.16328
4	102.9903	1.05821
5	336.0363	0.58904
6	352.0696	0.7581
7	723.1832	0.56854
8	842.7357	0.31576
9	858.1283	0.47964
10	876.0401	0.34415
11	902.0988	0.48756
12	919.2144	0.50861
13	926.5649	0.43972
14	935.805	0.55342
15	952.1841	0.3568
16	969.3121	0.47145
17	970.7461	0.59599
18	986.2484	0.39193

Table 4-8 – Natural Structural Mode Frequencies and Damping Ratios for Reactor 2.

Mode	Damped Frequency (Hz)	Damping (%)
1	42.82423	0.4224
2	64.05716	0.6358
3	75.52245	1.24263
4	133.9121	1.60324
5	163.6101	1.2441
6	221.4747	0.4499
7	271.2677	0.83622
8	383.951	0.69014
9	439.2939	0.81935
10	527.2567	0.7156
11	743.3426	0.59997
12	831.853	0.73441
13	888.0308	0.70576
14	955.623	0.62177
15	1048.383	0.98272
16	1081.231	0.49345
17	1153.331	0.48614

Using the Brüel & Kjaer Reflex modal software, outputs of the structural modes were created which illustrate the resultant deflection shapes of the reactor under various structural excitation frequencies. It was found that the assumed simple breathing mode shape of the reactor occurred at approximately 40 Hz for both reactors and that higher frequency modes did not have the assumed mid-plane deflection at all frequencies. Depending on the electrical excitation frequency, the deflection of the reactor was found to vary. Given that the reactor construction is comprised of multiple wire packages and

complex geometries, it is not unexpected to encounter complex modes. The mode shapes are shown in Appendix D Modal Analysis Results.

Another important reason to do the modal test and analysis was to determine the damping coefficient of the structure to be used for the computation of the dynamic vibration displacement through dynamic amplification. No other method exists to determine the damping information other than from modal testing. The damping information is a crucial parameter used in the current state of the science noise models and is usually assumed. The damping percentage dictates the stiffness of the coil structure, and in the models, impacts the magnitude of the displacement and in turn the magnitude of the predicted generated noise. Table 4-7 and Table 4-8 show the damping data resulting from the modal testing; the damping percentages are in the range of 0.1-1.2% for reactor 1 and 0.4-1.6% for reactor 2. The mean damping percentage for all the representative structural modes are 0.60% and 0.78% for reactors 1 and 2 respectively. The damping values are very low which suggests a very stiff structure; one which can cause significant amplification at the structural natural frequencies.

Most research in the prediction of reactor noise emissions has been proven to be accurate at limited frequency ranges for single package reactors. For the prediction of noise emissions of multi-package reactors, up to six wire packages in the case of this research, the structure-borne excitation is significantly more difficult to predict. It is common to assume a lumped mass representing all the wire packages such that the entire reactor is represented by a single hollow cylinder of the same material property. In reality, there are interactions between the wire packages and the duct sticks which separate the packages. These can have a significant impact on the resulting structural excitation.

For the modal test of prototype reactor 1, accelerometers were placed on the inner most package of the reactor in addition to the outer package. The result is shown in Figure 4- which shows the deflection of the reactor at the 66.7 Hz structural mode.

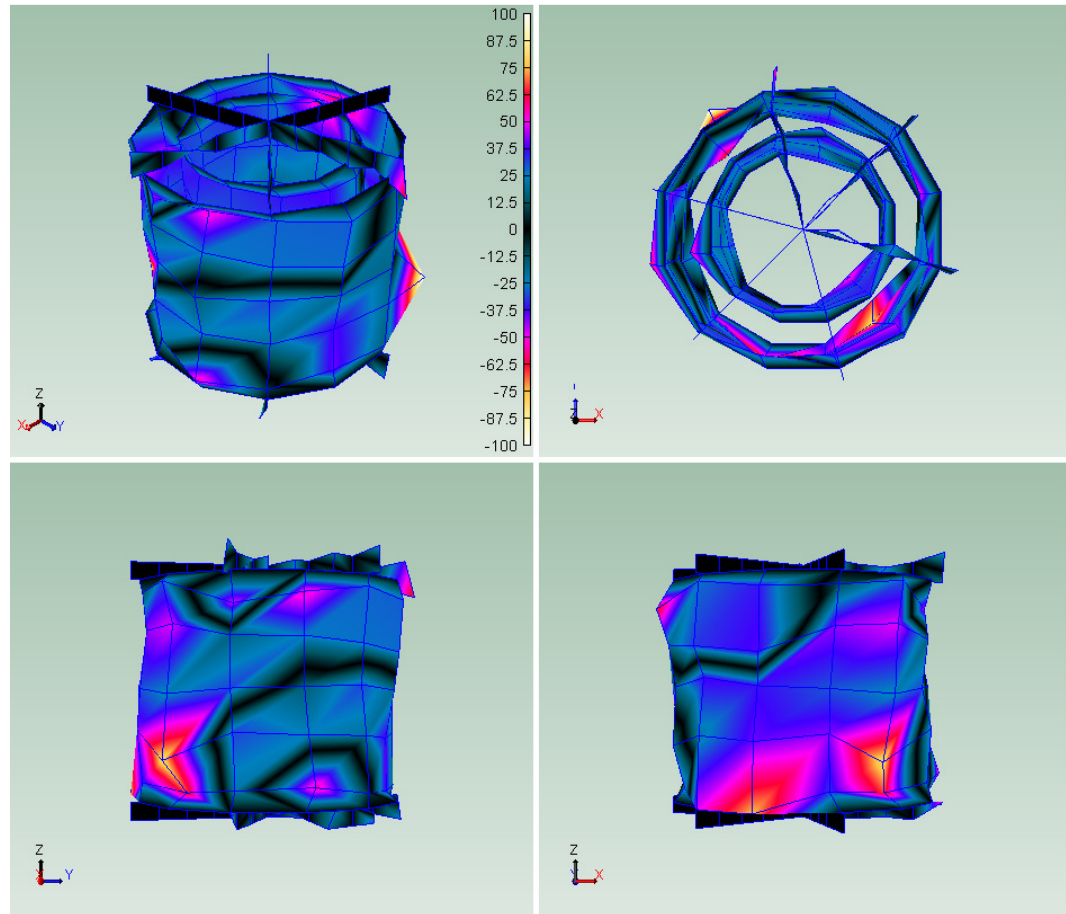


Figure 4-27 – Reactor 1 66.7 Hz Structural Mode.

Figure 4-Examining the top view, it is apparent that the inner and outer package move with different amplitudes, but with similar shapes. This is likely because the magnetic field varies across the wire packages, and as a result, the forces applied to each package are not equal. Although the packages are connected via duct sticks, the results show that the packages have different structural displacements under excitation. The wire packages may influence each other but are not in perfect synchronization, as the lump mass

methodology would assume. Also, for a lump mass assumption, the noise generated by the faces of other wire packages are eliminated and their vibrational contribution, or resistance to vibration, are not considered. Working toward a multi-wire package representation of the reactor is more realistic and will eliminate the oversimplification errors that occur using a lumped mass model.

Mode estimation using Blevins theory of cylindrical breathing modes can be used to determine the dynamically amplified displacement of the reactor. While it is possible to assume the reactor wire package to be a cylindrical shell, this assumption may not be appropriate as the reactor may not be sufficiently tall for the Blevins breathing formulae.

The visualization of the measured modes provided insight to the structural mode shapes of the excited reactor. Figure 4-28 and Figure 4-29 show the first identified mode in the frequency spectrum for both reactors. The structural excitation resembles the simple breathing of the wire package, but it occurs at 40.7 Hz and 42.8 Hz for reactor 1 and 2 respectively. Using the Blevins formulae, the radial breathing mode is calculated to be at 724 Hz for reactor 1. A structural mode of 723.2 Hz was identified for reactor 1, but the visualization of the structural mode in Figure 4-30 shows a complex mode shape which is combination of multiple twisting and bending components. As a reactor is assumed to (simply) breath in the radial direction with the mid-point having maximum; this is not the case when the reactor is excited at the structural resonance of 724 Hz.

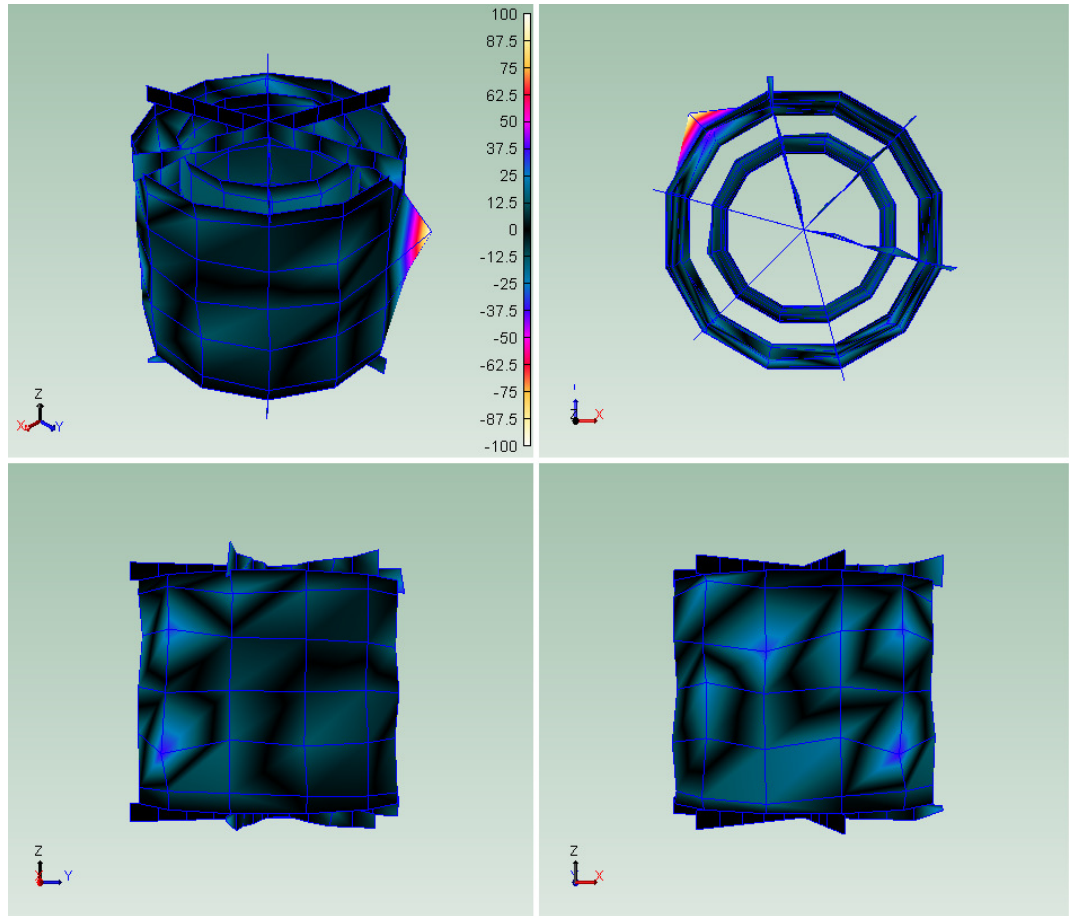


Figure 4-28 – Reactor 1 40.7 Hz Structural Mode.

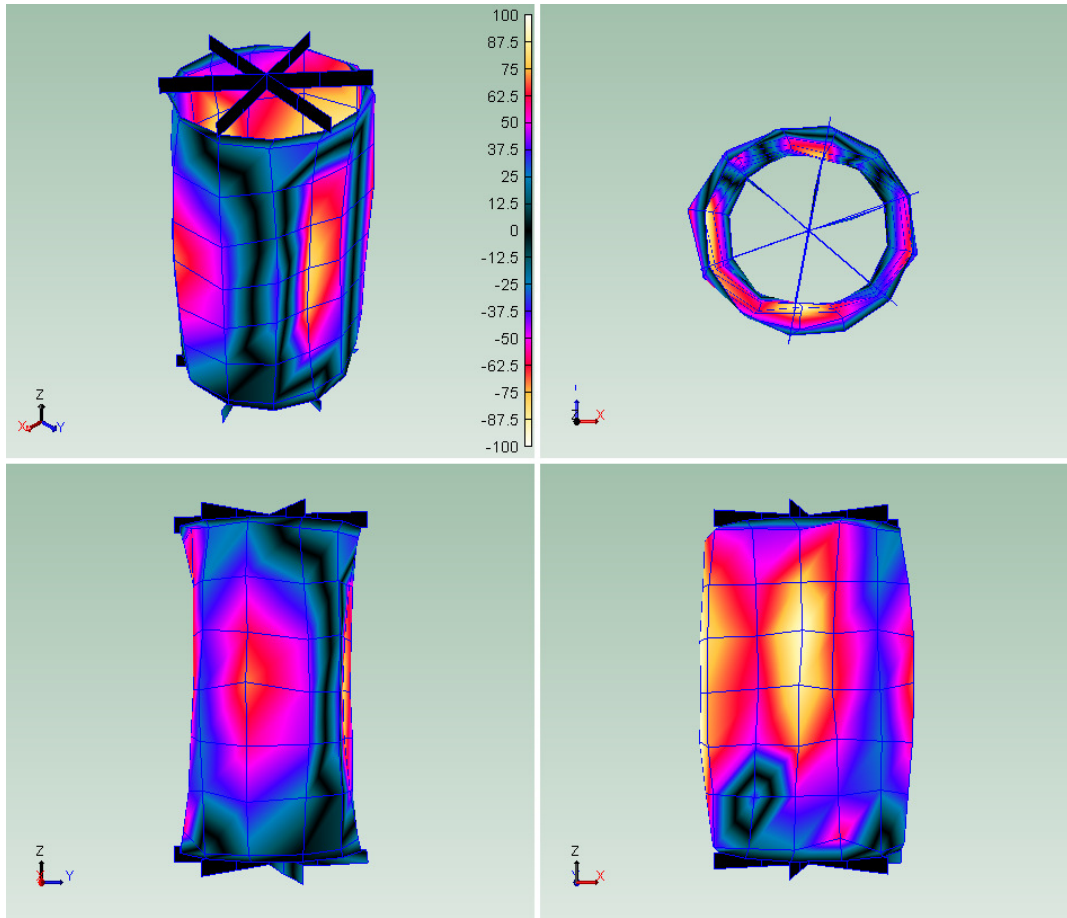


Figure 4-29 – Reactor 2 42.8 Hz Structural Mode.

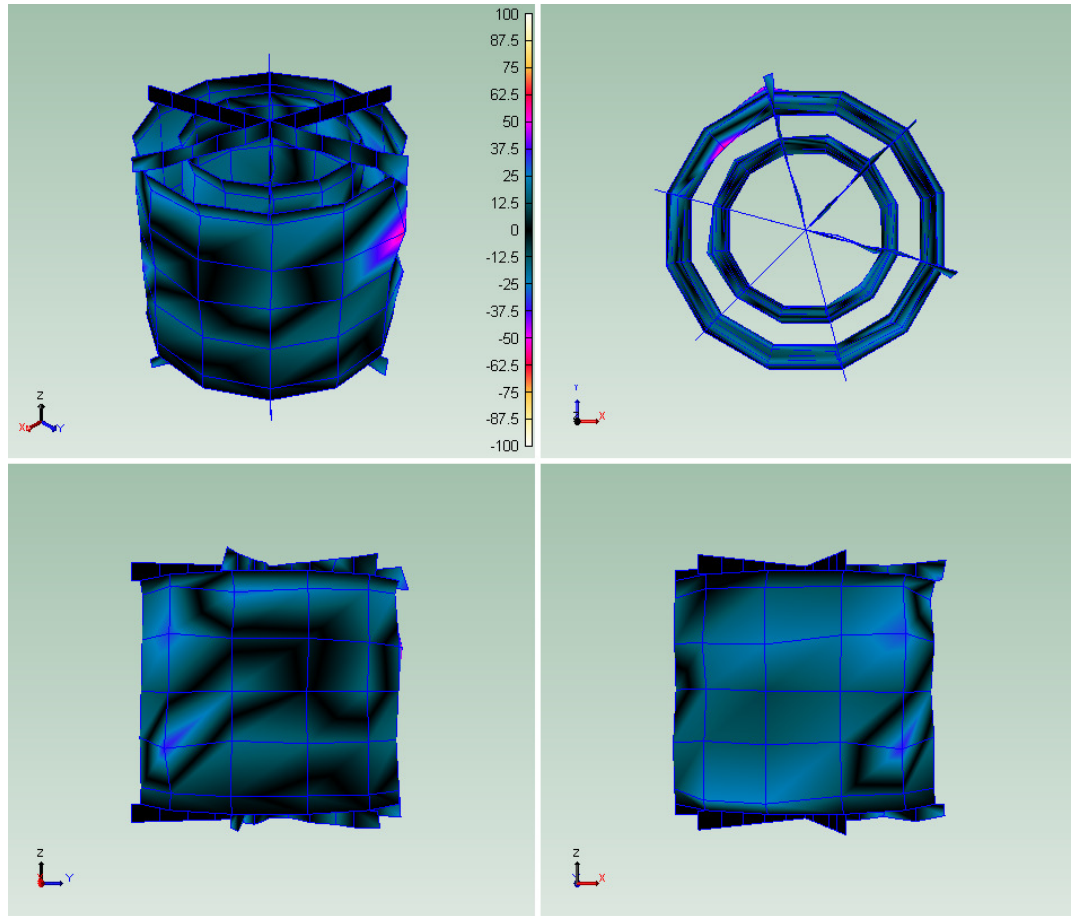


Figure 4-30 – Reactor 1 723.2 Hz Structural Mode.

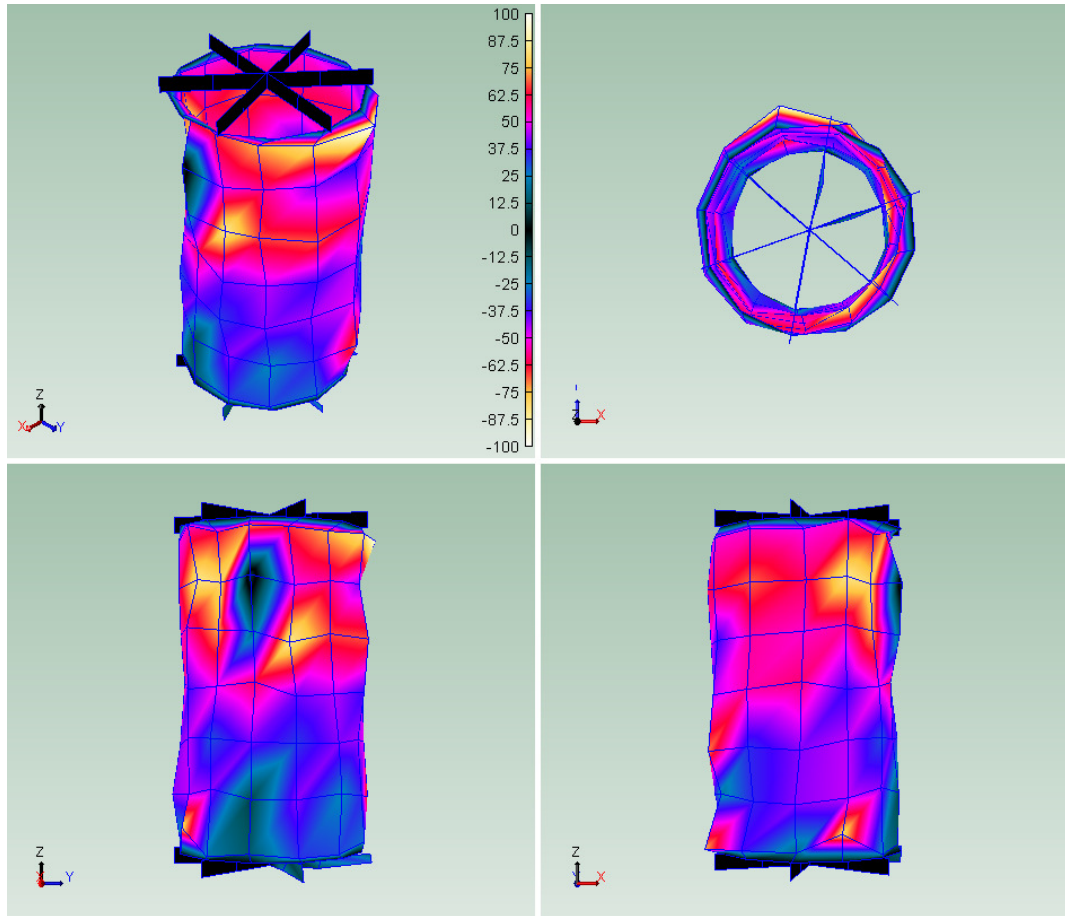


Figure 4-31 – Reactor 2 743.3 Hz Structural Mode.

The complex structural modes provide resistance to resonance due to the many bending and twisting components. Although they are unlikely to cause failure, these modes may provide amplified noise generation. It can be concluded that for the typical operating frequencies, the structural resonance will not generate the simple breathing that is assumed in Blevins theories. As the magnetic field varies across the wire packages and along the length, the impact of the forces on specific points on the reactor varies. This can change the shape of the displacement of the reactor, and in turn, deviate from the mode shape identified at the structural resonances.

The modal analysis offered the following conclusions:

1. Both reactors have a simple breathing mode at approximately 40 Hz. Modes at frequencies above this prove to be complex and are comprised of multiple fundamental bending and twisting motions. This shows that at higher frequencies, excitation from the simple breathing assumption is invalid. The displacement at these frequencies is likely due to the changing magnetic forces on the reactor, which varies across packages and along the length of the reactor. The complex modes have resistance to resonance as they are made up of multiple bending and twisting components which 'stiffen' the reactor.
2. The inner and outer wire packages have different magnitudes of displacement but have consistent mode shapes. This means that a lump mass assumption is not appropriate as the reactor packages do not move as a single mass. The packages move together and influence one another given that they are connected by duct sticks, but the magnetic field varies across each package and provides different magnitudes of the Lorentz forces on each wire package layer.
3. Damping percentages were determined to be in the range of 0.3-1.2 % for reactor 1 and 0.4-1.6 % for reactor 2. The average damping percentages for all the identified modes were 0.6 % and 0.78 % for reactor 1 and 2, respectively. This damping percentage represents a stiff structure which will generate noise.

CHAPTER 5

PROPOSED MODEL

The current state of science for prediction of vibroacoustic reactions for cylindrical reactors is based on the principals from literature presented in chapter 2. Compiling the electromagnetic methodologies as the driving force for vibration, the construction of the simplified vibroacoustic models are described and used in the various literature. Currently, most literature assumes a simplified geometry for reactors that include one or two wire packages for the prediction of the vibroacoustic outputs. For thick cylindrical reactors consisting of large number of winding packages, the simplified theories do not account for a multitude of complex natural structural frequencies. As such, the error in predicting the vibration, and in turn noise output, becomes greater with the application of the oversimplified methodologies for these complex reactor geometries.

The subsequent sections of this chapter describe the proposed novel methods for determining the vibroacoustic behaviour of the complex reactor geometries when induced by electromagnetic forces. Multiple methods were investigated in order to identify the relevant parameters and acknowledge the benefits and shortcomings of the different approaches. The proposed methods were applied to the prototype reactors which were acoustically and vibrationally tested and analysed; this facilitated the verification of the accuracy of the noise emissions predictions.

5.1 Distributed Velocity Model

Considering the current state of science for the prediction of reactor noise emissions, an expansion to this approach is proposed. It is accepted in this work, as in the

literature, that the Lorentz force is the driving factor in reactor noise emissions. For all the proposed models described in this chapter, the Lorentz force is be calculated as was detailed in chapter 2. This electromagnetic force is the basis for determining the amplitude of vibration for the reactor, and subsequently the structurally induced noise emissions.

Like the models found in the literature, the distributed velocity model consists of three major parts: the calculation of the Lorentz force, the determination of the velocity of vibration, and the calculation of the resulting sound level emissions.

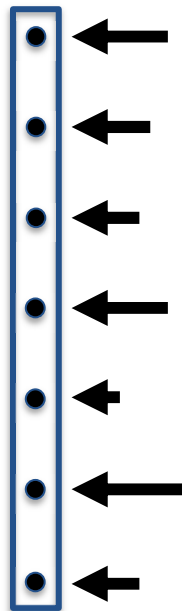


Figure 5-1 – Illustration of Lorentz force acting on segments along a wire package length.

Again, the calculation for the Lorentz force will remain the same as given by equation 2-1. The basis of the distributed velocity model is to break down the vibration velocity calculation by dividing the reactor into separate individual wire packages and dividing each package into multiple segments along the height of the reactor. This allows for the computation of the magnetic fields for each segment and each wire package instead

of representing the magnetic Lorentz force as a single value for the entire lumped mass. This is illustrated in Figure 5-1. Given this, the velocity of vibration can be calculated for each segment along each wire package. This allows for greater accuracy as the electromagnetic force, and in turn, the displacement amplitude of vibration differ along the height of the reactor.

From equation 2-1, the Lorentz force is computed for each of the segments in each wire package. The magnetic force is then used to compute the hoop stress within the cylindrical segment as follows.

Using the formula for mean radial vibration velocity of the reactor, the static amplitude of vibration can be determined. Given that there are natural frequencies at which the reactor will resonate, Blevins cylindrical breathing modes are used to estimate the natural frequencies of increases in vibrational excitation. Equation 2-5 is used in this approach to determine the natural frequency of the fundamental breathing mode. Given this, a dynamic amplification factor is applied. The formula for dynamic application factor is given in equation 2-12.

By multiplying the dynamic amplification factor for each of the frequencies to be modelled, the resultant dynamic amplitude of vibration is determined. From this value, along with the frequency of the current applied, the surface vibrational velocity is computed. From the surface velocity, area, density, and an assumed radiation efficiency, the magnitude of radiated sound power is estimated. This sound power is then converted into sound power level which in turn is converted to an estimated sound pressure level at two meters from the reactor.

This approach determines the natural frequencies separately in order to amplify the static displacement. It is assumed that the only amplifying factor is due to the first radial and axial breathing modes as estimated by Blevins. By breaking down the cylinder into its many individual wire packages, the various breathing modes for each individual package are considered. In addition, the breakdown of segments along the height of the reactor allows for an increased accuracy by facilitating different surface velocities at each segment on each package instead of assuming a singular surface velocity of vibration for the entire outer surface of the reactor. Although this will result in an increased accuracy from a lumped mass model approach, there are still shortcomings in terms of consideration of the natural frequencies and structural modes.

5.2 *Eigenfrequency MDOF Model*

The eigenfrequency multi-degree of freedom (MDOF) method was developed in this work to address the shortcomings of the previously proposed distributed velocity method. In the distributed velocity model, the only natural frequency considered was the natural breathing mode in the axial and radial directions for each of the wire packages of the reactor. In this method, the natural frequencies are determined by modelling the wire packages of the reactor as a multiple mass and spring system. This is possible by constructing and solving the eigenvalue problem.

Here, the reactor is represented as a multi-mass, multi-degree of freedom system. Expressing each wire package as its own mass connected by springs allows for the vibration of each mass to differ, and in theory, consider the effect of each package on one another. As the magnetic field differs along the length and package to package,

representing the problem as a multi-mass, multi-degree of freedom system is logical. The following diagram depicts the spring mass system representation of a reactor with multiple wire packages.

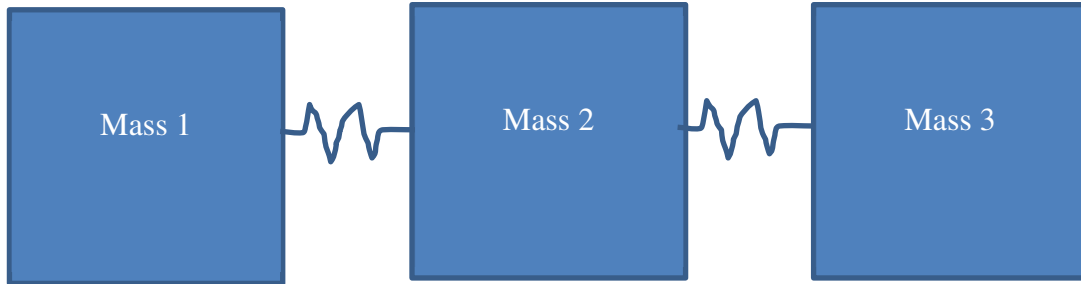


Figure 5-2 – Mass spring representation of a three-wire package reactor.

Given this representation, and writing the equations of motion for each of the wire packages, the matrix of the system of equations of motion is shown in equations 2-8 [20]. With this set of equations of motion in matrix form, the eigenfrequency problem can be outlined. At the natural frequencies, the damping $[D]$ and input force $[F]$ is set to zero. After rearranging, the eigenfrequency problem to solve for the natural frequencies of the system as shown in 2-10 [20] gives:

$$([S] - \omega^2[M])\{\phi\} = \{0\} \quad 5-1$$

Provided this, the following equation is determined to be the solution for the eigenvalues:

$$\omega^2 = \lambda = [M]^{-1}[S] \quad 5-2$$

Where the eigenvalue λ is proportional to the natural frequency. As such, the following is the resultant matrix of the eigenfrequencies:

$$\lambda = \begin{bmatrix} \omega_1^2 & 0 & \dots & 0 \\ 0 & \omega_2^2 & 0 & \vdots \\ \vdots & 0 & \ddots & 0 \\ 0 & \dots & 0 & \omega_n^2 \end{bmatrix} \quad 5-3$$

The eigenfrequencies here are then natural frequencies of the MDOF system. These frequencies, along with the dynamic amplification formula from equation 2-12 account for the natural frequencies of the interactions between the wire packages. This alternative method for determining the natural frequencies of the reactor considers the interaction between the wire packages with consideration of each wire package as its own mass. The vibration displacement amplitude is subsequently calculated using the same procedure as the distributed velocity model. This method more accurately represents the geometry of the multiple package reactor in terms of the natural frequencies.

In this, the wire packages are still considered as lumped mass and spring systems vibrating as flat plates. The cylindrical features are not considered when computing the vibration amplitude. This is considered in the next section.

5.3 Cylindrical Vibroacoustic Model (Single Layered)

The cylindrical vibration model was developed following the ideas described in section 2.4, Hollow Cylinder Vibration and adapting it for the specific application of electrically induced reactor noise emissions. Both this method and the multi-layered version are the final proposed solutions to model the reactor noise emissions developed for this research. The following sections of this chapter thoroughly describe the methodologies for the cylindrical vibration model.

Cylindrical vibration literature depicts the equation of motion in terms of stresses on an infinitesimal point located on the hollow cylinder as was shown in Figure 2-2. Given this geometry, and assuming a forced vibration problem, the equation of motion is derived to be equation 2-20. For the model in this work, the only direction considered is in the radial direction as customary in literature. The following is the equation of motion in the radial direction: [30]

$$\mu \nabla^2 u_r + (\lambda + \mu) \frac{\partial \epsilon}{\partial r} = \rho \frac{\partial^2 u_r}{\partial t^2} \quad 5-4$$

where, ϵ is defined as follows in the textbook *Vibration of Thick Cylindrical Structures* [30]:

$$\begin{aligned} \epsilon &= e_{rr} + e_{\theta\theta} + e_{zz} \\ \epsilon &= \frac{\partial u_r}{\partial r} + \frac{\partial u_\theta}{r \partial \theta} + \frac{u_r}{r} + \frac{\partial u_z}{\partial z} \end{aligned} \quad 5-5$$

Therefore, the equation of motion is expanded in terms of radial vibration displacement, u_r . Expanding by substituting equation 5-5 into 5-4 gives:

$$\begin{aligned} (2\mu + \lambda) \frac{\partial^2 u_r}{\partial r^2} + \frac{(2\mu + \lambda)}{r} \frac{\partial u_r}{\partial r} - \frac{\lambda + \mu}{r^2} u_r + \frac{\mu}{r^2} \frac{\partial^2 u_r}{\partial \theta^2} + \mu \frac{\partial^2 u_r}{\partial z^2} \\ = \rho \frac{\partial^2 u_r}{\partial t^2} \end{aligned} \quad 5-6$$

The goal of this equation is to determine the solution of radial vibration displacement, u_r , in order to estimate the emitted, structure-borne noise. Thus, the assumed general solution for this equation of motion is as follows:

$$u_r = U_r \cos(n\theta) \cos(\omega t + \zeta z) \quad 5-7$$

Where, n is the radial wave number, ζ is the axial wave number, and ω is the frequency of vibration. The following are the derivatives of u_r with respect to θ , z , and t :

$$\begin{aligned} \frac{\partial^2 u_r}{\partial \theta^2} &= -n^2 U_r \cos(n\theta) \cos(\omega t + \zeta z) \\ \frac{\partial^2 u_r}{\partial z^2} &= -\zeta^2 U_r \cos(n\theta) \cos(\omega t + \zeta z) \\ \frac{\partial^2 u_r}{\partial t^2} &= -\omega^2 U_r \cos(n\theta) \cos(\omega t + \zeta z) \end{aligned} \quad 5-8$$

Substituting equations 5-7 and 5-8 into equation 5-6, results in the following:

$$\frac{\partial^2 U_r}{\partial r^2} + \frac{1}{r} \frac{\partial U_r}{\partial r} + \left[-\frac{n^2 \mu}{r^2} + \omega^2 \rho - \mu \zeta^2 - \frac{\lambda + \mu}{r^2} \right] \frac{U_r}{\lambda + 2\mu} = 0 \quad 5-9$$

With the solution to u_r substituted into the equation of motion, variables α and n_2 are defined as follows:

$$\begin{aligned} \alpha^2 &= \left[\omega^2 \rho - \mu \zeta^2 - \frac{\lambda + \mu}{r^2} \right] \frac{1}{\lambda + 2\mu} \\ n_2^2 &= \frac{n^2 \mu}{\lambda + 2\mu} \end{aligned} \quad 5-10$$

Finally, equation 5-6 is written as:

$$\frac{\partial^2 U_r}{\partial r^2} + \frac{1}{r} \frac{\partial U_r}{\partial r} + \left[\alpha^2 - \frac{n_2^2}{r^2} \right] U_r = 0 \quad 5-11$$

Equation 5-11 is in the form of Bessel's equation, which in this case has the general solution in the form of:

$$U_r = A J_{n_2}(\alpha r) + B Y_{n_2}(\alpha r) \quad 5-12$$

With the general solution of the vibration displacement in the radial direction, the normal stress in the radial direction must be defined. From *Vibration of Thick Cylindrical Structures* [30], the normal stress is defined as:

$$\sigma_{rr} = \lambda \left(\frac{\partial u_r}{\partial r} + \frac{\partial u_\theta}{r \partial \theta} + \frac{u_r}{r} + \frac{\partial u_z}{\partial z} \right) + 2\mu \frac{\partial u_r}{\partial r} \quad 5-13$$

In the *Effect of magnetic field and non-homogeneity on the radial vibrations in hollow rotating elastic cylinder* [29], equation 5-13 is derived for the radial direction only. Thus, the normal stress in the radial direction when only considering vibration in the radial direction and is defined as follows:

$$\sigma_{rr} = \lambda \left(\frac{\partial u_r}{\partial r} + \frac{u_r}{r} \right) + 2\mu \frac{\partial u_r}{\partial r} \quad 5-14$$

Substituting equation 5-7 for radial vibration displacement into the normal stress equation 5-14, the following is derived:

$$\sigma_{rr} = \left[(\lambda + 2\mu) \frac{\partial U_r}{\partial r} + \lambda \frac{U_r}{r} \right] \cos(n\theta) \cos(\omega t + \zeta z) \quad 5-15$$

Let $h_1 = \cos(n\theta) \cos(\omega t + \zeta z)$ and divide both sides by h_1 . The following equation results:

$$\frac{\sigma_{rr}}{h_1} = (\lambda + 2\mu) \frac{\partial U_r}{\partial r} + \lambda \frac{U_r}{r} \quad 5-16$$

Using Bessel's equation general solution as shown in 5-12, 5-16 is then written as follows:

$$\begin{aligned} \frac{\sigma_{rr}}{h_1} = A & \left[\left(\lambda + \frac{n_2(\lambda + 2\mu)}{r} \right) J_{n_2}(\alpha r) - \alpha(\lambda + 2\mu) J_{n_2+1}(\alpha r) \right] \\ & + B \left[\left(\lambda + \frac{n_2(\lambda + 2\mu)}{r} \right) Y_{n_2}(\alpha r) - \alpha(\lambda + 2\mu) Y_{n_2+1}(\alpha r) \right] \end{aligned} \quad 5-17$$

With the stress and radial displacement equations defined, the problem can be defined solve for the constants A and B.

Given the computed stress for the inner and outer radius of the reactor hollow cylinder, the two equations for inner and outer normal stress can be solved to determine the values for constants A and B. Provided the determined constants A and B at each of the harmonic frequencies is considered, the vibrational radial displacement can then be calculated by substituting the result of A and B into equation 5-12.

With the radial vibration displacement magnitude for each electrically induced harmonic, the radiated sound power level and noise emissions at a given distance can be

calculated. Looking back at chapter 2, equation 2-2 was used to determine the sound power of the reactor's sound radiating surface (outer wire package surface). Following, the sound power level and sound pressure level are calculated.

The general idea behind this model is that the reactor is treated as a hollow cylindrical structure with the packages lumped together as one hollow cylinder. Thus, the structure, stresses, and vibration components are modeled as a cylindrical structure which is better representative of the measured findings. This method does not require an assumption for damping ratio or mode estimations as they are considered in the equation of motion. Therefore, this method eliminates the simplified reactor assumptions which precludes its use for a wide range of reactor models, making it more adaptable than previously examined methods; in both this chapter and the literature.

5.4 Cylindrical Vibroacoustic Model (Multi-Layered)

The multi-layered cylindrical vibration model takes the model proposed in the previous section and expands it to a cylindrical structure made up of multiple cylindrical shells. Using the theories put forth in *Vibration of Thick Cylindrical Structures* [30], the modelling methodologies are adapted for the intended application of this research.

The goal is to assess each cylindrical layer as explained in the previous section and relate the displacements at the layer borders in order to determine the outer package displacement. To accomplish this, formulae are taken from section 2.4 and expanded for this application.

Given equation 5-17, the normal stress equation is written for the inner and outer radius of a wire package. The two equations for normal stress can be then written in matrix

format as shown in 2-41. The following equation is equation 2-41 expanded for the radial direction for a single wire package:

$$\begin{Bmatrix} \frac{\sigma_{rr}(r=r_a)}{h_1} \\ \frac{\sigma_{rr}(r=r_b)}{h_1} \end{Bmatrix} = \begin{bmatrix} T_{1,1} & T_{1,2} \\ T_{2,1} & T_{2,2} \end{bmatrix} \begin{Bmatrix} A \\ B \end{Bmatrix} \quad 5-18$$

Where r_a and r_b are the inner and outer wire package radii, respectively. The matrix T is then defined as follows:

$$\begin{aligned} T_{1,1} &= \left(\lambda + \frac{n_2(\lambda + 2\mu)}{r_a} \right) J_{n_2}(\alpha r_a) - \alpha(\lambda + 2\mu) J_{n_2+1}(\alpha r_a) \\ T_{1,2} &= \left(\lambda + \frac{n_2(\lambda + 2\mu)}{r_a} \right) Y_{n_2}(\alpha r_a) - \alpha(\lambda + 2\mu) Y_{n_2+1}(\alpha r_a) \\ T_{2,1} &= \left(\lambda + \frac{n_2(\lambda + 2\mu)}{r_b} \right) J_{n_2}(\alpha r_b) - \alpha(\lambda + 2\mu) J_{n_2+1}(\alpha r_b) \\ T_{2,2} &= \left(\lambda + \frac{n_2(\lambda + 2\mu)}{r_b} \right) Y_{n_2}(\alpha r_b) - \alpha(\lambda + 2\mu) Y_{n_2+1}(\alpha r_b) \end{aligned} \quad 5-19$$

Given this relation for each of the wire packages, the matrix X of the constants A and B are determined. This is the first step in preparation of the multi-layered matrix solution.

As shown in equations 2-48 and 2-49, the vibrational displacement equations can be expanded for the radial direction as follows:

$$\{d\}_n = \begin{Bmatrix} \frac{u_r}{h_1} \\ \frac{\sigma_{rr}}{h_1} \end{Bmatrix}_n \quad 5-20$$

In order to determine the radial vibration displacement for each package as a system, a propagator matrix must first be characterized by defining individual $[D]$ matrices for each corresponding wire package. Thus, each wire package is represented by the following equation:

$$\{d\}_n = [D]_n X_n \quad 5-21$$

as shown in *Vibrations of Thick Cylindrical Structures* [30].

In terms of the reactor, each wire package layer is separated by a duct stick layer, which is assumed to be rigid. This assumption means that the vibration amplitude on the boundary from one wire package to the duct stick is equal to the vibration on the opposite boundary of the same duct stick layer and the other adjacent wire package. Thus, the two wire package surfaces connected by a duct stick layer vibrate with the same amplitude. The following can be taken for a two-wire package reactor.

$$\begin{aligned} \{d\}_1 &= [D]_1 X_1 \\ \{d\}_2 &= [D]_2 X_2 \\ \{d\}_3 &= [D]_3 X_3 \\ \{d\}_4 &= [D]_4 X_4 \end{aligned} \quad 5-22$$

The subtext number represents the surface of the wire packages. Thus, 1 represents the inner surface of a wire package, 2 represents the outer surface of a package, 3 represents the inner surface of the next wire package, and so forth.

For surfaces on the same layer, such as surface 1 and 2, the following is true:

$$X_1 = X_2 \quad 5-23$$

Also, layers separated by duct sticks, such as layers 2-3, are assumed to have the same radial vibration displacement, therefore:

$$\{d\}_2 = \{d\}_3 \quad 5-24$$

Further, the following relations are derived for this three-layer, two wire package reactor:

$$\{d\}_3 = [D]_2[D]_1^{-1}\{d\}_1$$

$$\{d\}_4 = [D]_4[D]_3^{-1}\{d\}_3$$

5-25

Therefore,

$$\{d\}_4 = [D]_4[D]_3^{-1}[D]_2[D]_1^{-1}\{d\}_1$$

In this case the propagator matrix $[P]$ is defined as follows:

$$[P] = [D]_4[D]_3^{-1}[D]_2[D]_1^{-1} \quad 5-26$$

As such, in general terms for a reactor with n wire packages, the following is given:

$$\{d\}_n = [P]\{d\}_1 \quad 5-27$$

Given equation 2-50, the following is provided for the radial direction only as shown in equations 5-20:

$$\begin{Bmatrix} \frac{u_r}{h_1} \\ \frac{\sigma_{rr}}{h_1} \end{Bmatrix}_n = \begin{bmatrix} P_{1,1} & P_{1,2} \\ P_{2,1} & P_{2,2} \end{bmatrix} \begin{Bmatrix} \frac{u_r}{h_1} \\ \frac{\sigma_{rr}}{h_1} \end{Bmatrix}_1 \quad 5-28$$

With this system of equations, it is possible to determine the inner and outer maximum vibration displacement by determining the normal stress due to the electromagnetic force acting on the reactor. With the vibration magnitude of displacement, magneto-electrical parameters and the noise radiation equation 2-2, the sound power emission of the reactor is estimated.

The benefit of this method is that the displacement of each wire package is considered along with the interactions between each package. The duct sticks are assumed to be ridged in this method. The approach given by the current state of science assumes the reactor to be a lumped mass, which does not consider the interactions between multiple wire packages and duct sticks. The vibration model using hollow cylinder vibration and the expansion of multi-layered cylinders provides a more accurate representation of the reactor vibroacoustic behaviour.

CHAPTER 6

MODEL VERIFICATION AND VALIDATION

6.1 *Model Correlation to Test Data*

The primary goal of the measured test data, using the various measurement techniques, was to benchmark the acoustic performance of electrical reactors and to guide the development of the proposed models. The benchmark data detailed in chapter 4 represents the target values for an ideal reactor noise prediction model. Figure 6-1 and Figure 6-2 provide the benchmarked A-weighted sound pressure level values for the corresponding 1/3-octave band for each electrical excitation frequency normalized to 100 amps at a distance of 2 m from the reactors outer surface (data tables were provided as Table 4-1 and Table 4-2).

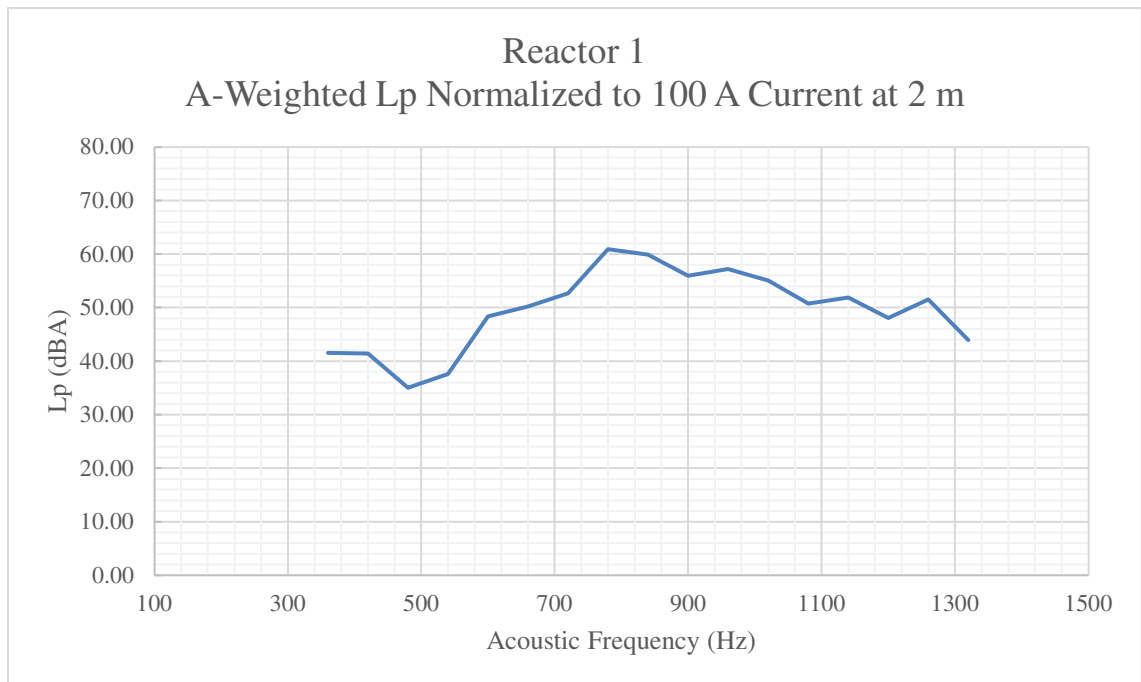


Figure 6-1 – Benchmarked A-weighted sound pressure levels normalized to 100 A at 2 m for reactor 1.

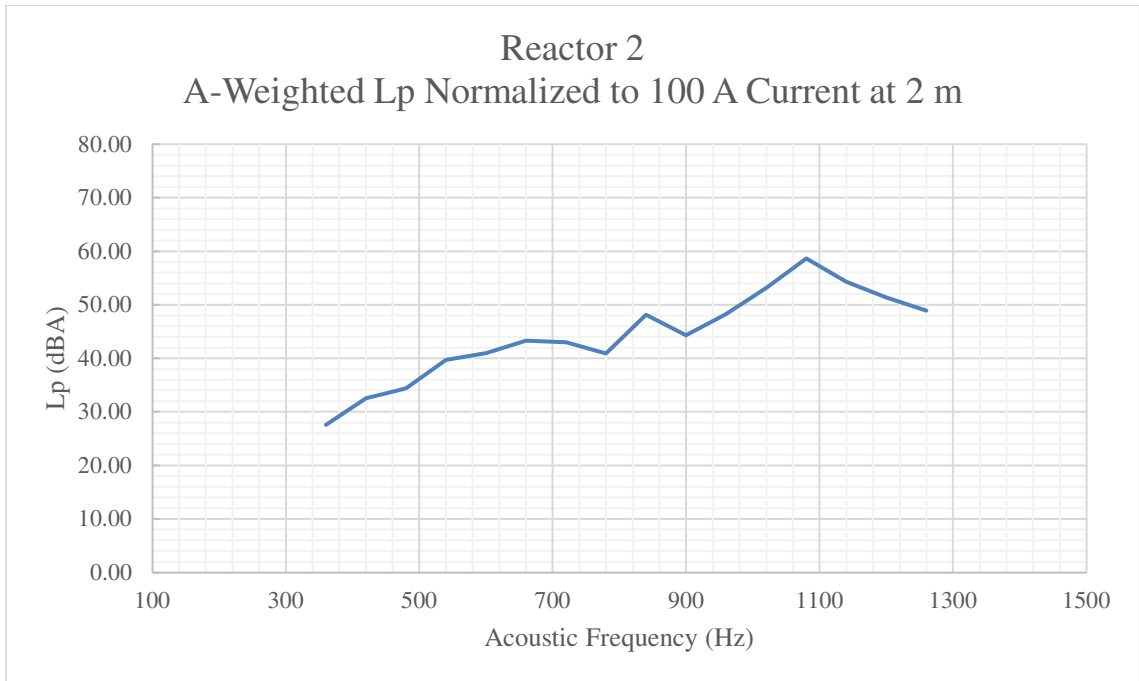


Figure 6-2 – Benchmarked A-weighted sound pressure levels normalized to 100 A at 2 m for reactor 2.

Using the models proposed in the previous chapter, noise prediction results are correlated to the acquired test data for the two prototype reactors. In this section, each model is correlated to the test data for both reactors and the methodologies are accessed for accuracy. The sound level comparison, as well as trend matching of the sound pressure level plots over the frequency range are considered when evaluating the accuracy of a model.

6.1.1 Reactor 1 Test Data Correlation

In order to understand the current state of reactor noise prediction methodology in the literature, a model was constructed using the methodologies outlined in section 2.1. This method used the most basic aspects of the electromagnetic forced vibration for structure-borne noise emission assuming only radial Blevin’s breathing modes. Figure 6-3

gives a plot of the reactor 1 collected test data overlaid with the data from the current state of science for noise prediction in literature.

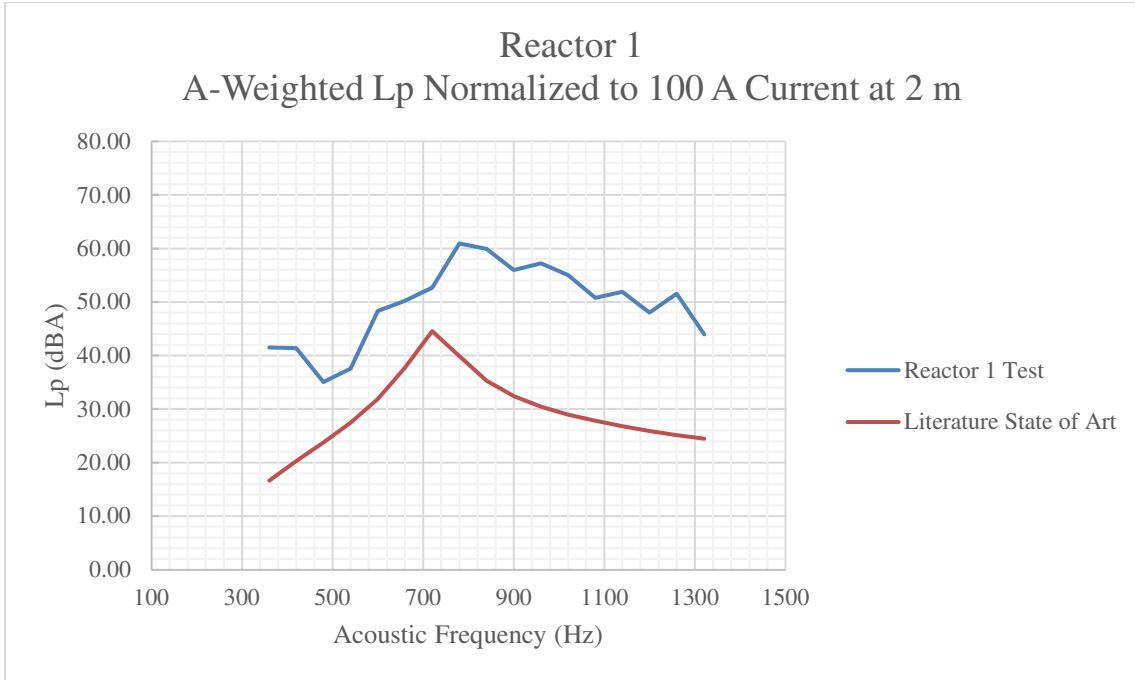


Figure 6-3 – Current reactor noise emission prediction state of science from literature correlation to reactor 1 test data.

Figure 6-3 shows that the current literature methodologies underestimate the real noise generated by the reactor. In addition to underestimating the noise emissions, the method does not account for all the complex vibration mechanisms as there is only one peak sound level apparent on the predicted result. The test data has shown to have a general trend for the noise level versus frequency. For the acoustic frequency range of 480 Hz to 720 Hz (240 Hz to 360 Hz electrical frequency), the methodology given in literature is close to estimating the sound pressure level; within 2-8 dB of the measured values. The trend of increasing sound pressure level with increasing electrical excitation frequency is consistent with the test data. A correlation coefficient of 0.66 was computed for the

literature methodology. The correlation coefficient does not take into consideration the magnitude, but rather the overall trend of the data. The correlation coefficient measures on a scale of -1 to 1, where -1 represents a perfect negative correlation and a value of 1 represents a perfect correlation.

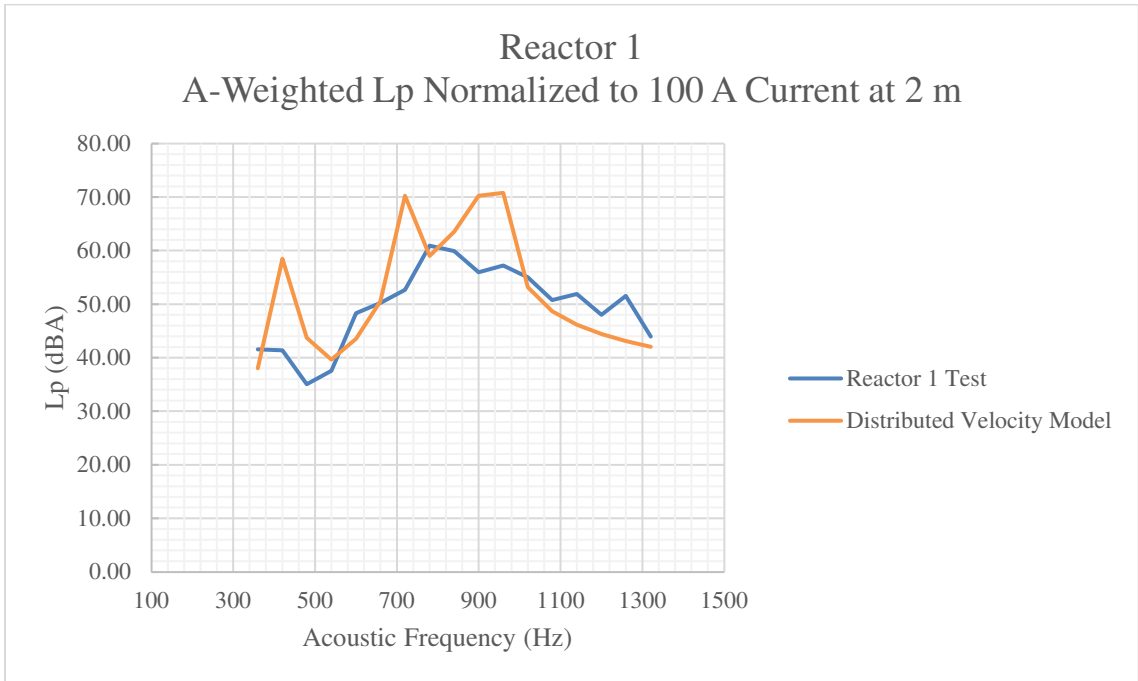


Figure 6-4 – Distributed velocity model correlation to reactor 1 test data.

The proposed distributed velocity model, as described in section 5.1, was correlated to the prototype reactor 1 test data as given in Figure 6-4. In this model, the acquired damping percentages from the modal testing were used to compute the dynamic amplification factors for the various excitation frequencies. Given such a stiff damping percentage, excitation frequencies that are close to the estimated Blevin’s breathing modes for the axial and radial directions are largely amplified. This is represented by the large peaks at 420 Hz, 720 Hz, 900 Hz, and 960 Hz acoustic frequencies. The acoustic frequency ranges of 480-660 Hz and 1020-1320 Hz accurately estimate the noise emissions. For these

frequency ranges, the prediction is within 9 dB of the tested sound pressure levels. The general trend matches the test data well for the entire tested frequency range. A correlation coefficient of 0.66 was calculated for the data representing this noise prediction model.

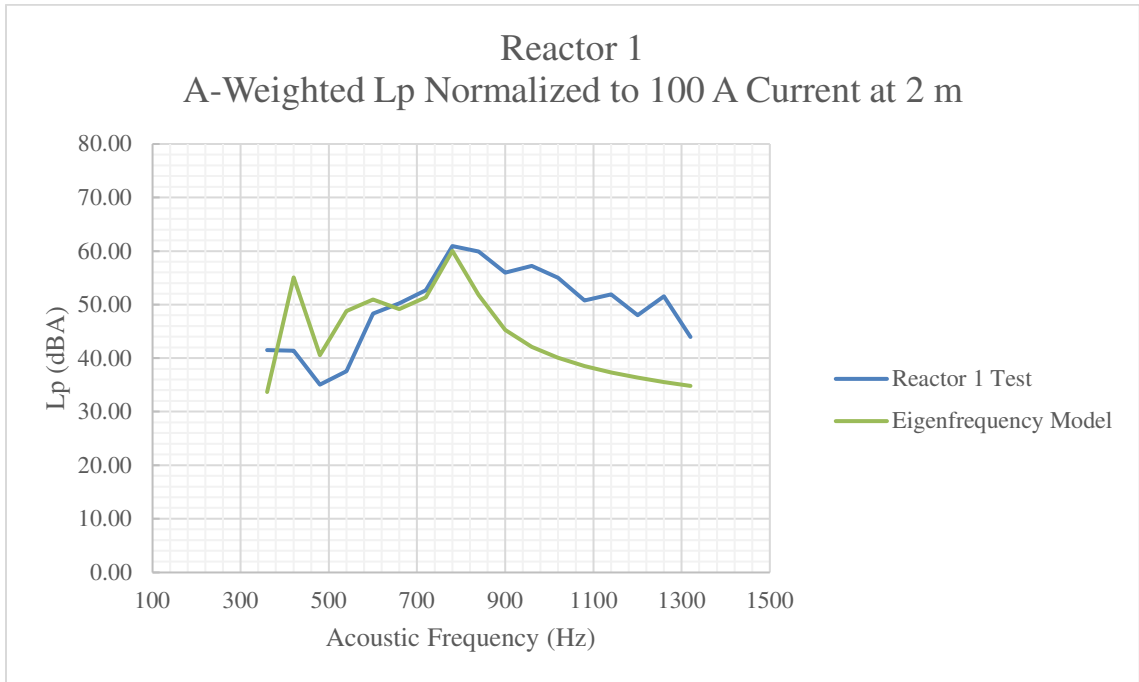


Figure 6-5 – Eigenfrequency model correlation to reactor 1 test data.

Figure 6-5 depicts the correlation of the eigenfrequency model, detailed in section 5.2, to the test data for reactor 1. At 780 Hz (390 Hz electrical frequency) and below the eigenfrequency model correlates well with the test data. Above 780 Hz, this model underestimated the noise emissions by as much as 16 dB. For this data set, the eigenfrequency model has a correlation coefficient of 0.27. It is important to note, the eigenfrequency model does not require Blevin’s breathing mode estimators as the modes are computed based on a MDOF system of equations. With this being the case, the eigenfrequency methods can identify peak frequencies of noise emission.

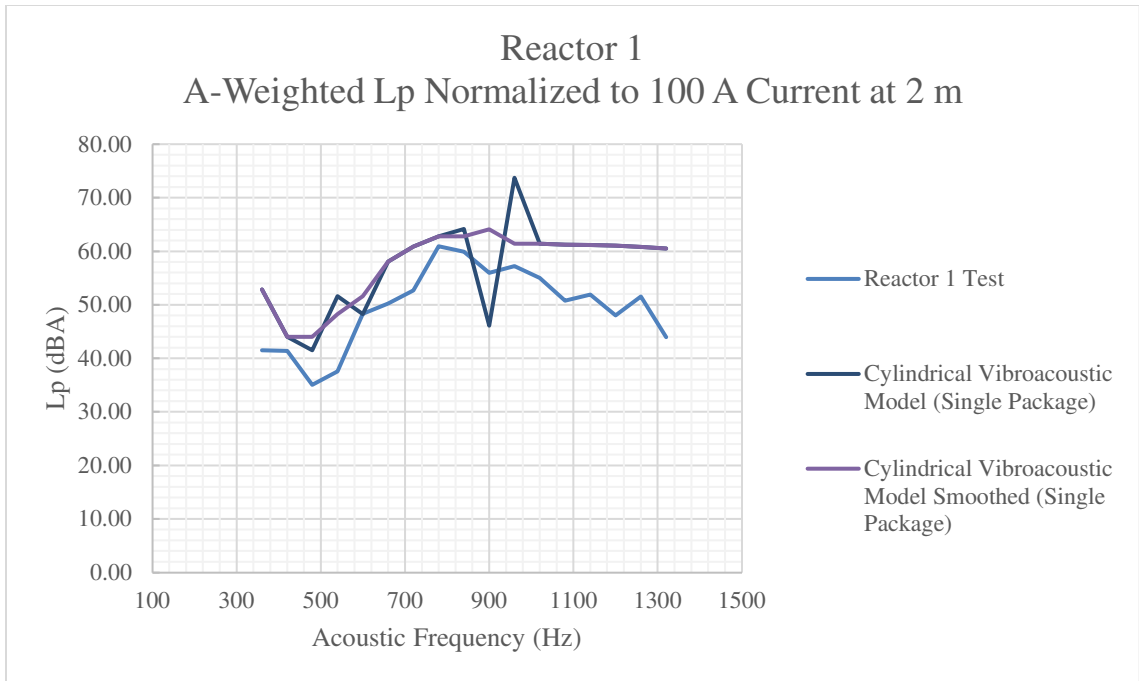


Figure 6-6 – Cylindrical vibroacoustic single package model correlation to reactor 1 test data.

The correlation of the cylindrical vibroacoustic single package model, shown in Figure 6-6, displays two data sets for this model. The first data set represents the raw noise prediction output, while the second data set is for the noise prediction results with the addition of an applied smoothing function. The smoothed results preserve the overall trend of the data set. In the computation of predicted results using the cylindrical vibroacoustic model, transitional points appear where the general solution varies depending on the driven excitation frequency. In transitioning from one general solution to another, extreme high and low values appear. These outliers do not represent the actual noise emissions from the reactor. As such, the smoothing function is applied to manage the outliers and preserve the general trend of the data set. The smoothed model shows an improvement in the fit to the test data. The same general trend is observed for both test and predicted data sets. This resulted in a correlation coefficient of 0.85 for the smoothed cylindrical vibroacoustic

single package model. The model estimates within 16 dB above the test data in the higher frequency range of 1080-1320 Hz. Below this range, the values are within 10 dB with most of the values being much closer in magnitude. The acoustic frequency range of 420-1020 Hz has been shown to be the region where the model performed the best.

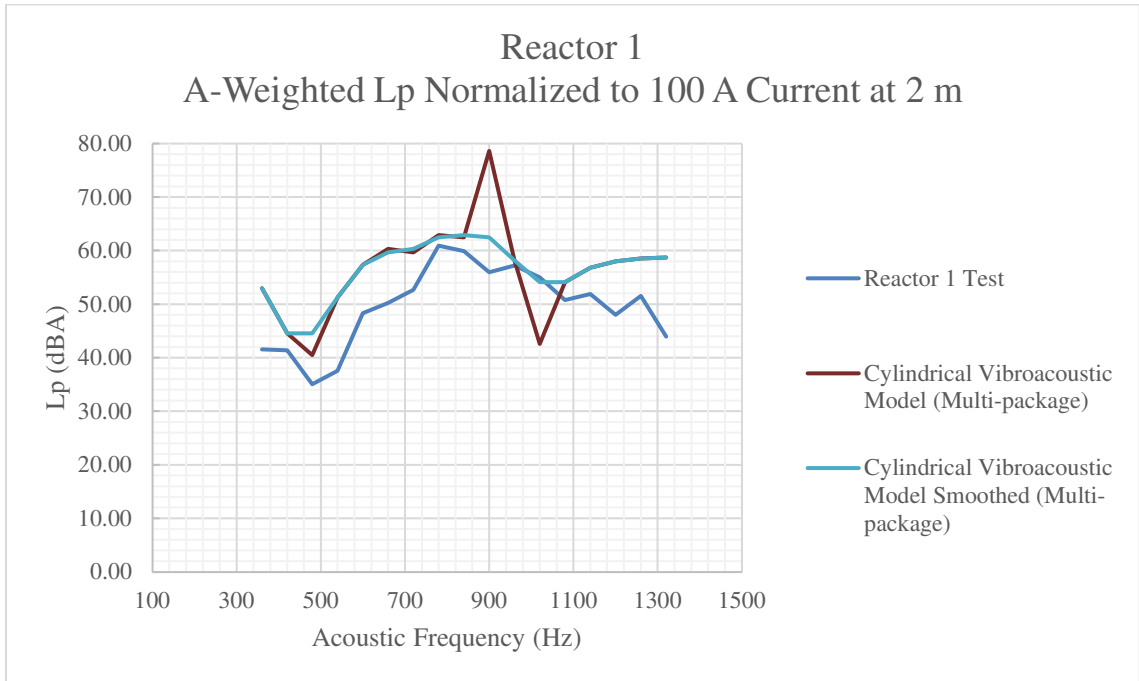


Figure 6-7 – Cylindrical Vibroacoustic multi-package model correlation to reactor 1 test data.

Figure 6-7 shows the noise prediction results for the expanded cylindrical vibroacoustic multi-package model correlated to the measured noise test data. In consideration of all the models, this approach, and the single package version of it, correlated best with the test data. The general trend was preserved in this prediction method which implies that the structural resonances and mode estimators are modeling the real-world geometry of the reactor most representatively. The frequency range at which this model performed the best is shown to be in the range of 420-1200 Hz. In terms of magnitude, the model consistently overestimated the sound pressure level, although most

of the results are close in value to the test data with a maximum overestimation of 15 dB. It is important to note that these two models do not require a mode estimator or assumed damping percentage. These factors are built in, creating a more robust prediction model without the need of dynamic amplification of vibration magnitude. With this, a correlation factor of 0.80 was calculated for the multi-package expansion of the cylindrical vibroacoustic model.

6.1.2 Reactor 2 Test Data Correlation

Reactor 2 test data was correlated to the various noise prediction models in the same manner as described in section 6.1.2. Given in Figure 6-8 is a comparison of the current state of science model given in the literature to the collected test data. Figure 6-8 shows the correlation of the literature noise emission prediction model results to the collected test data.

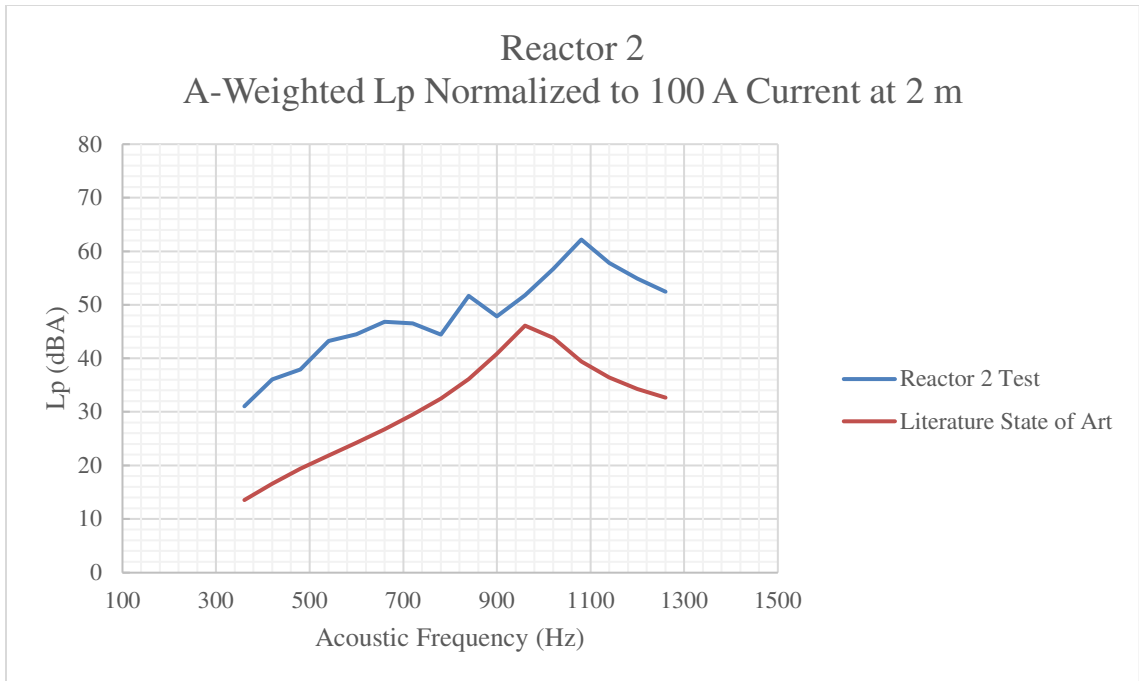


Figure 6-8 – Current reactor noise emission prediction state of science from literature correlation to reactor 2 test data.

In Figure 6-8, the state of science data is shown to underestimate the noise emissions of the reactor. It is apparent, when compared to reactor 1 test data, that the literature model does not account for the complex mechanisms responsible for the structure-borne noise emission of a multi-package reactor. Inspection of the correlation shown in the above figure, the state of science model prediction shows a similar trend when not considering the magnitude of the sound level. Also, the model does not accurately estimate the peak noise emission frequencies. A correlation coefficient of 0.75 was computed for this method.

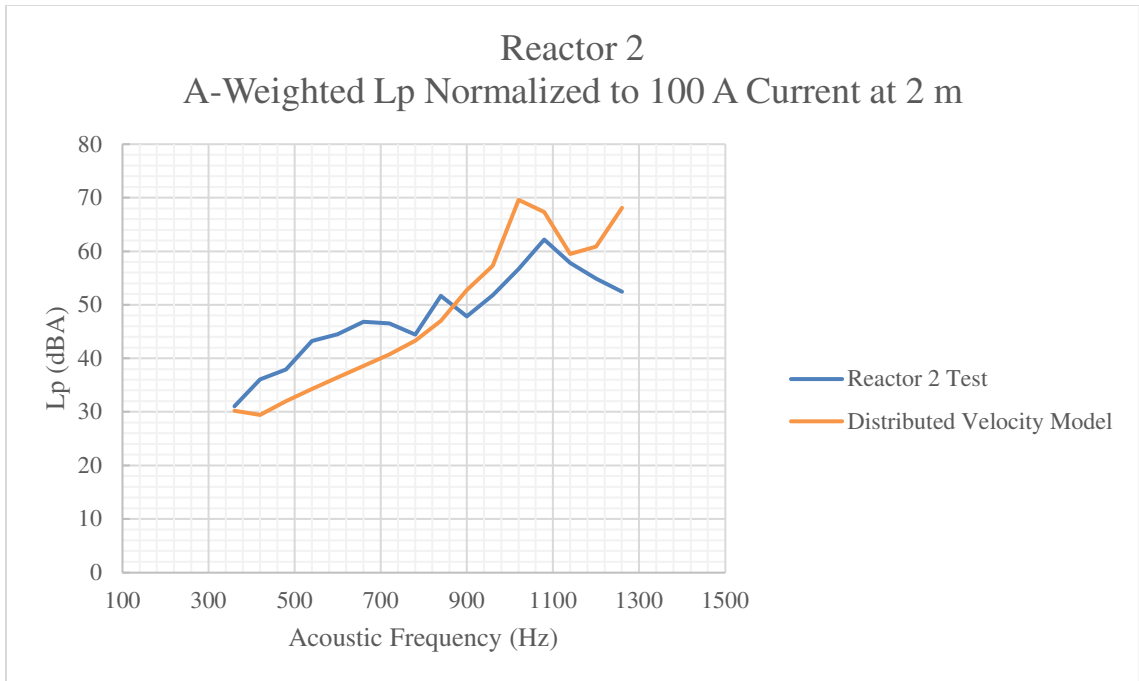


Figure 6-9 – Distributed velocity model correlation to reactor 2 test data.

The results for the distributed velocity model for reactor 2’s geometric and electrical operational parameters are shown in Figure 6-9. The correlation to the reactor test data in the above figure show that the results for the distributed velocity method closely resemble the measured data. Both the magnitude and overall trend of the two data sets are similar. The sound pressure level magnitude was underestimated by approximately 8 dB in the acoustic frequency range of 420 Hz to 720 Hz. At 780 Hz and above, the model either predicts the noise emissions accurately or with an overprediction. At 1260 Hz acoustic frequency, the model diverges from the trend of the collected data set. Comparing the general trend without magnitude, a correlation coefficient of 0.90 is computed for the distributed velocity model.

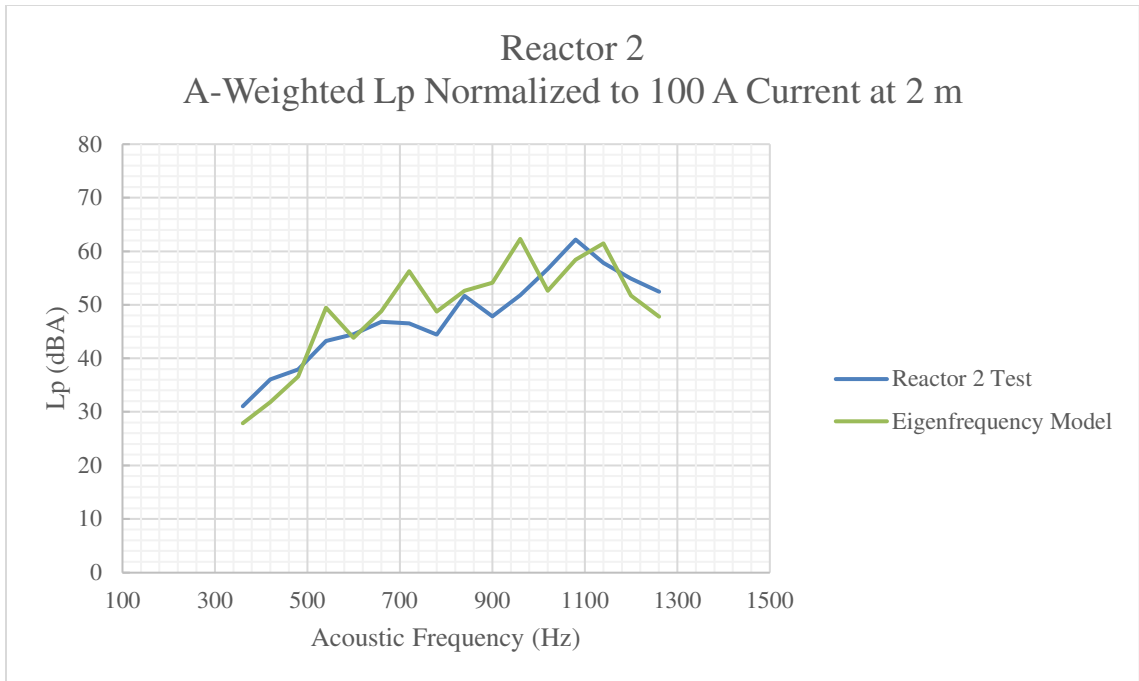


Figure 6-10 – Eigenfrequency model correlation to reactor 2 test data.

The correlation of the Eigenfrequency model to reactor 2 test data is shown in Figure 6-10. In terms of the sound pressure magnitude, the Eigenfrequency model is close to estimating the noise emissions except for the large peaks. Even at peak sound pressure levels in the eigenfrequency model, the values are still within 10 dB. The overestimation can be considered a safety factor, and as such, it is better than underestimating the emitted noise. The only underestimation is below 480 Hz acoustic frequency, with the largest difference being 4 dB. The overall trend again matches closely to the reactor 2 test data. The peak sound emission frequency is closely estimated using the Eigenfrequency model. A correlation coefficient of 0.86 is calculated for this model.

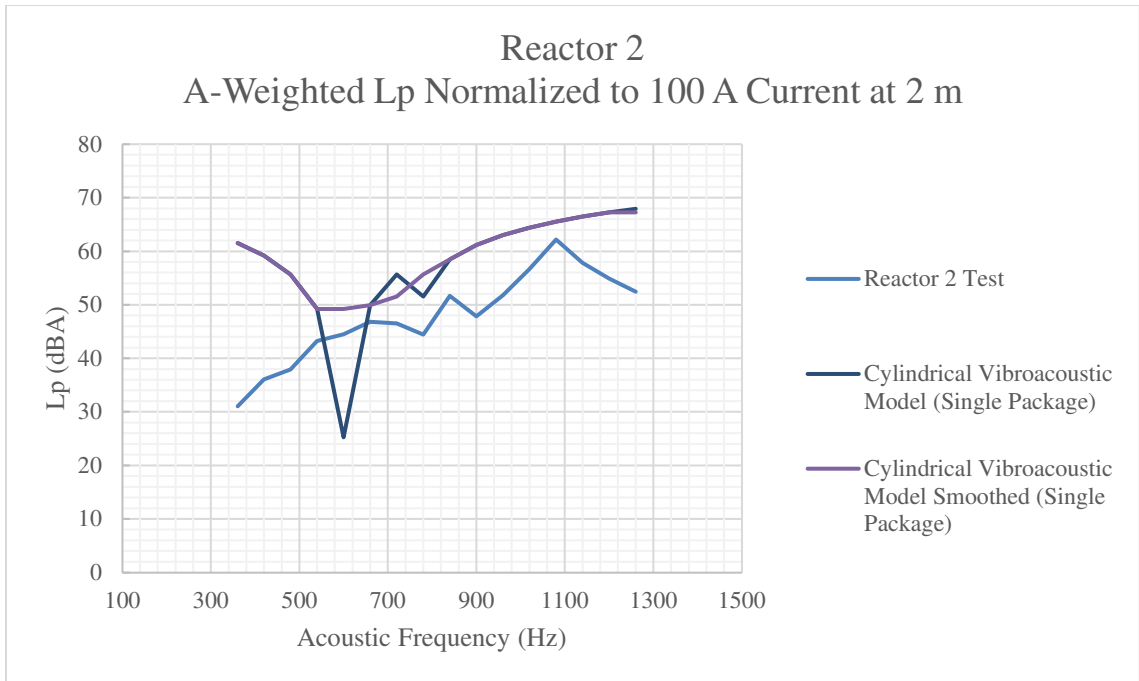


Figure 6-11 – Cylindrical vibroacoustic single package model correlation to reactor 2 test data.

Figure 6-11 shows the model results for the cylindrical vibroacoustic single package compared to the reactor 2 test data. As discussed in the previous section, key transition points were smoothed out due to the variability in the transition of the general solutions as the electrical frequency changed. Given this, the cylindrical vibroacoustic model has a similar trend above 500 Hz acoustic frequency. This model estimates very high levels in the lower frequency range. The Cylindrical Vibroacoustic model predicts values as much as 30 dB greater than the test data. Although it estimates a much larger magnitude of noise, it was conservative in the sense that it is an overestimation of noise when compared to the measured values. The magnitudes of noise emission results are much closer above 500 Hz. The trend is preserved in the range 540-1140 Hz acoustic frequency (270-570 Hz electrical frequency). A correlation coefficient of 0.51 is calculated for these

two data sets. When analyzing the frequencies from 540 Hz and above, the correlation coefficient is calculated to be 0.84.

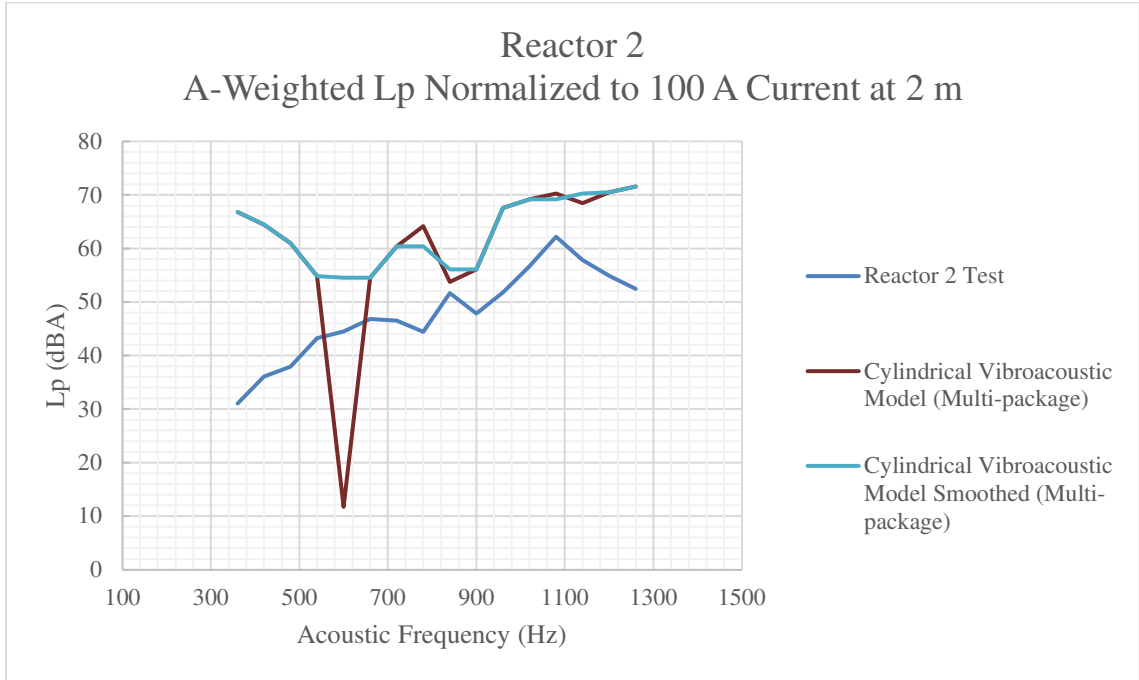


Figure 6-12 – Cylindrical vibroacoustic multi-package model correlation to reactor 2 test data.

The multi-package extension of the cylindrical vibroacoustic model was correlated to test data for reactor 2 as given in Figure 6-12. It is shown that the multi-package model, similar to the single package model, overestimates the noise by a large amount in the lower frequency range. The magnitude of sound pressure level is as much as 36 dB greater than the test values on the very low-end frequencies of the range. In the rest of the frequency range, the multi-package model still overestimates the noise emissions, but the results are much closer in magnitude to the test data. In the range of 540-1200 Hz (270-600 Hz electrical frequency), the maximum difference in magnitude is 16 dB. In terms of trend, it matches closely with the sound pressure level values of the test data for the range of 540-1200 Hz acoustic frequency (270-600 Hz electrical frequency). The correlation coefficient

for the entire frequency range is calculated to be 0.40. For the isolated range of 540 Hz and up, the correlation coefficient is calculated to be 0.80.

6.2 *Discussion of Model Validity*

In the previous section of this chapter, the proposed models were used to estimate the noise emissions of two prototype reactors and the results were correlated to the acquired test data. Limitations in access to the prototype reactors for acoustic and vibrational testing were due to the cost for the construction for each prototype reactor. Thus, the study was limited to the two supplied prototype reactors that were built specifically for this research. In the correlation comparisons, the distributed velocity, eigenfrequency, and the cylindrical vibroacoustic (single and multi-package) models were assessed.

The specific performance used to estimate the noise emissions was detailed for each model and for each of the two prototype reactors. The details of frequency range, trend and magnitude of estimation were discussed. The following section summarizes the performance of each of the models studied in this dissertation.

6.2.1 *Distributed Velocity Model*

The distributed velocity model provided noise prediction results that varied in over and under prediction of the tested results. It is apparent that when assessed for the first reactor, the acoustic frequency range of good correlation is 480-660 Hz and 1020-1320 Hz. For the second reactor, the frequency range of good correlation is 360-1140 Hz. This demonstrates that there are inconsistencies in the usable range of the prediction model for reactors of different geometry. This model overpredicts at the acoustic frequencies of identified radial and axial breathing modes for each of the wire packages of the reactor

build. These large peaks result in inconsistencies when correlating the trends of the reactors. The correlation coefficients for the distributed velocity model for both reactor 1 and reactor 2 test data sets were found to be 0.66 and 0.90, respectively. As such, it is apparent that the distributed model may be effective in identifying the mechanics in noise emissions for some reactors, but it not consistent. As such the confidence in this model is questionable.

In terms of the magnitude, this model is inconsistent in over and under predicting noise values. The magnitude of sound pressure level is underestimated by less than 8 dB for frequency ranges that are not near to the breathing modes. As for over estimations, they are found to be as much as 10 dB larger than the tested values.

All considered, the distributed velocity model adds dimensions of realism to the model by considering the distribution of the magnetic field along the length of the reactor and across all the packages separately. This is possible by super positioning the noise emission effects of each package for the calculation of the total reactor noise emission at each electrical frequency. Although the model shows some benefits in comparison to what is available in literature, there are still inconsistencies in the noise prediction capabilities of the model for various reactor constructions.

6.2.2 *Eigenfrequency MDOF Model*

The eigenfrequency model is an expansion of the distributed velocity model and has shown promise. Although the algorithms are similar in computing the structure-borne noise emission and break down of reactor segments and packages, the mode estimator is detailed using a different approach. The eigenfrequency model uses a mass-spring system

of multiple masses to represent the vibration problem as a MDOF system. Given this, the natural frequency modes are estimated based on the relation of the wire package interactions with each other. This model demonstrated good correlation with the test data for both reactors. The acoustic frequency range for good correlation is 360-780 Hz and 360-1260 Hz for reactor 1 and 2, respectively. This has more consistency than the distributed velocity model as the frequency ranges for good correlation are comparable for both tested reactors. Correlation coefficients of 0.27 and 0.86 were calculated for reactor 1 and reactor 2 test data sets, respectively. This shows an inconsistency in the modelling of reactors having various construction. Although the usable frequency ranges are similar, the overall trends throughout the entire frequency range tested are not consistent.

The eigenfrequency method is also not consistent in the estimation of sound pressure level in terms of magnitude. It is shown that for the reactor 2 test data, the model mostly overpredicts within approximately 10 dB and has little underprediction. In the case of reactor 1, large underprediction up to 16 dB is shown for acoustic frequencies above 780 Hz. It is shown that peak frequencies in the test data are identified by the eigenfrequency model; although, the magnitude was inconsistent. This implies that the MDOF mode estimator can better identify the natural frequencies due to the interaction of packages and can predict the peak frequencies. The method identifies more peak frequencies than measured, and in the case for reactor 1, underpredicts a large portion of the tested frequency range. This is inconsistent between the two reactors' test data sets.

6.2.3 *Cylindrical Vibroacoustic Model (Single Layered)*

The cylindrical vibroacoustic model took a different approach to structure-borne noise prediction as it considers the cylindrical vibration of the reactor driven by induced electromagnetic forces. This model removes the need for dynamic amplification and mode estimating as separate steps. The calculation of the vibration displacement considers the effect of the reactor's internal stresses due to body forces in the formulation of the problem. This model, in terms of the methodology, is more robust and easily implemented as no generic assumption of damping percentage is used in order to represent all reactors. Thus, the single layered version of the cylindrical vibroacoustic model has shown to have an acoustic frequency range that correlates well to the test data of 420-1020 Hz and 540-1140 Hz for reactor 1 and 2, respectively. This model is consistent in overestimating the noise emissions over the entire frequency range. Although this may not be accurate in the exact estimation of sound pressure level magnitude for the entire frequency range, there is confidence in its ability to not underestimate the noise. Underestimation can lead to potential worse outcomes when used to predict environmental noise emissions.

When correlating this model to the two prototype data sets, correlation coefficients of 0.85 and 0.51 were calculated for reactor 1 and 2, respectively. Since the frequency range of good correlation is consistent for this model, correlation coefficients were calculated for a representative frequency range of 540-1140 Hz for both reactor data sets. This resulted in correlation coefficient values of 0.88 and 0.87 for reactor 1 and 2, respectively. This proves that the cylindrical vibroacoustic model is more consistent in its usable frequency range and ability to predict the trend of sound pressure level for induced electrical excitation frequencies. This model is proven to be more robust and adaptable to

various reactor constructions. Although sound pressure levels are overestimated over the frequency range, the magnitudes are still closer in value and the trend is more accurately predicted than the other models reviewed so far.

6.2.4 Cylindrical Vibroacoustic Model (Multi-Layered)

The correlation results for the multi-layered expansion of the cylindrical vibroacoustic model has shown similar results to that of its single layered counterpart. The frequency range of good correlation is proven to be 420-1200 Hz and 540-1200 Hz for reactors 1 and 2, respectively. This correlation frequency range is consistent between multiple reactor constructions; and as such, demonstrates the robustness of this model and adaptability to accommodate varying parameters. This model can estimate the parameters that define the noise generation since it is able to estimate the noise emission for multiple reactors of varying characteristics. Below the usable frequency range, the model diverged from the test data and overestimated the noise emissions when compared to the test data for both reactors. As such the frequency range of usability is defined as 540-1200 Hz.

Over the entire frequency range, the correlation coefficients are calculated to be 0.80 and 0.40 for reactors 1 and 2, respectively. The correlation for the usable frequency range of 540-1200 Hz is 0.74 and 0.83 for reactors 1 and 2, respectively. This expansion demonstrates consistency for varying reactor construction; as shown by its single layered counterpart. In comparison to other noise emission models, the cylindrical vibroacoustic models are shown to be more consistent and accurate without underpredicting the noise emissions of the reactor in the usable frequency ranges. As such these models have the

largest usable frequency range with the best demonstrated correlation of the studied models.

6.2.5 Model Comparison

The previous sections of this chapter outlined the features and validity of the proposed models. The following tables summarize the comparison of the proposed models and their performance in noise prediction of reactor noise emissions.

Table 6-1 – Comparison of model performance in predicting reactor operating noise emissions to measure test data.

Models	Frequency Range	Correlation Coefficient	Over or Under Prediction
Distributed Velocity Method	R1 – 480-660 Hz & 1020-1320Hz R2 – 360-1140 Hz	R1 – 0.66 R2 – 0.90	Inconsistent 8-10 dB in over and under predictions
Eigenfrequency Model	R1 – 360-780 Hz R2 – 360-1260 Hz	R1 – 0.27 R2 – 0.86	R1 – Under as much as 16 dB R2 – Over <10 dB
Cylindrical Vibroacoustic Model Single-Layered	R1 – 420-1020 Hz R2 – 540-1140 Hz	R1 – 0.85 R2 – 0.51 For 540-1140 Hz R1 – 0.88 R2 – 0.87	Over majority of range within <10 dB
Cylindrical Vibroacoustic Model Multi-Layered	R1 – 420-1200 Hz R2 – 540-1200 Hz	R1 – 0.80 R2 -0.40 For 540-1200 Hz R1 – 0.74 R2 – 0.83	Over majority of range within <10 dB

Table 6-2 – Comparison of model fundamental methodologies.

Models	Mode Estimator	Uses Assumed Damping	Lumped Mass Assumption	Physics of vibration
Distributed Velocity Method	Blevin's breathing mode	Yes	No	Flat vibrating plate
Eigenfrequency Model	MDOF System Natural Frequencies	Yes	No	Flat vibrating plate
Cylindrical Vibroacoustic Model Single-Layered	Embedded in equation of motion using geometry and wavenumber of length and circumference	No, only material properties are required	Yes	Vibrating cylindrical shell
Cylindrical Vibroacoustic Model Multi-Layered	Embedded in equation of motion using geometry and wavenumber of length and circumference	No, only material properties are required	No	Vibrating cylindrical shell

From Table 6-1 it is apparent that the cylindrical vibroacoustic model provides the best performance in terms of fit to test data over a wide frequency range as well as consistency in estimation of the magnitude of sound pressure level. Although it provides an overestimation, it is consistent in its overestimation and provides a degree of safety to designing reactors for noise emission targets. Table 6-2 outlines the fundamental theories within the models. It is shown that the cylindrical vibroacoustic model provides more advance methodologies for hollow cylindrical shell vibration which eliminated assumed parameters, such as damping, and mode estimators that use dynamic amplification factors to compute dynamic vibration amplitude. Instead the cylindrical vibroacoustic model has the sensitivity of structural modes embedded into the equation of motion through the geometric parameters of the reactor. Thus, the cylindrical model removes source of error through by using advanced cylindrical vibration theories and eliminating assumed parameters.

CHAPTER 7

RECOMMENDATION AND CONCLUSIONS

7.1 Conclusions

The objective of the research was to critically analyse the present state of science in operational reactor noise emission prediction and to develop a model that can accurately predict the noise emissions for a reactor that has a complex construction; that one that has multiple packages and hollow cylinders. For this, a detailed literature review on the present state of science for reactor noise prediction as well as an in-depth review of structural dynamic modelling of cylindrical vibration of shells was conducted. Several forms of analysis, including acoustic signal analysis, NSI analysis, and modal analysis were conducted in order to obtain an in-depth understanding of the mechanisms of vibration for the reactors. From the literature review, the research developed and expanded on several methodologies referred to as the distributed velocity and eigenfrequency MDOF models. In the pursuit of a model that closely resembled the real-world complex construction and physical response of the reactor, cylindrical shell vibration research was conducted. This allowed for the construction of the cylindrical vibroacoustic single layered and multi-layered noise prediction models for electrical reactors. The details of the four developed models are given in chapter 5.

The proposed models were tested by examining the calculated correlation of the modelled outputs to the representative test data as presented in chapter 6. This validation identified the pros and cons of each model as well as the usable frequency ranges, trend correlation, and consistencies between the various reactor constructions studied. The

outcome of the validation concluded that the cylindrical vibroacoustic models performed best when correlated to measured test data. These models did not underpredict the reactor noise emissions and gave consistent results in the usable frequency range for both prototype reactors. It was also proven to be the most robust and adaptable while still maintaining the largest usable frequency range. The reason for this is that the methodologies used by the cylindrical vibroacoustic models more closely describe the vibration phenomena that the complex reactors builds exhibit. In conclusion, the cylindrical vibroacoustic model was validated as the most accurate proposed model and a significant improvement over what is currently used and given in the literature.

7.2 Recommendations

The outcome of this research is a robust noise prediction model with an improved ability to predict the structure-borne noise generating mechanics of a complex construction reactor. Having developed several models, the cylindrical vibroacoustic model, both single and multi-layered methods, were proven to be the best solution. As such, it is recommended that the cylindrical vibroacoustic model be adapted as a viable option for a consistent, robust, and advanced noise prediction model for complex reactor designs. Although its usable frequency range was determined to be 540-1140 Hz acoustical and 270-570 Hz electrical excitation frequency, the models give good estimations with a safety buffer that avoids the risk of underprediction. For the practical limitations of design, overprediction is desired over underprediction. Thus, the cylindrical vibroacoustic models are validated as the viable and recommended noise prediction model for the design of complex reactor construction.

7.3 *Future Work*

In the process of this research many possibilities emerged that can further advance this topic of research. The following are proposed areas for future work that could potentially advance the state of science for electromagnetically induced force, vibroacoustic, noise prediction models for the application of reactor design:

1. Further validation and verification of the cylindrical vibroacoustic model for a larger sample of differing complex reactor constructions would provide further assurance to the validity and accuracy of the recommended model and the useful frequency range. As this research was limited to two prototype reactors due to cost and access, continued verification is recommended.
2. The cylindrical vibroacoustic models were found to overestimate in the frequency range below 540 Hz acoustic frequency. Investigation into different mechanisms that explain why this is would be valuable. This is an important area for future work given that reactors can operate at these low frequencies. It was hypothesized in the research that the structure-borne noise radiation constant would not be constant over the entire frequency range; as it is more difficult to emit low frequency noise than higher frequency noise. More in-depth research into radiation efficiency of low frequency noise from structure-borne noise sources is recommended.
3. In creating the multi-layered cylindrical vibroacoustic model, assumptions were made to represent the duct sticks as layers. It was assumed that the

duct sticks were ridged and as such the vibration amplitude was equal on each surface of the adjacent wire packages connected by the duct stick. An investigation into the damping effect of the duct sticks and the overall impact that this may have on the calculated vibration magnitudes on the wire packages may provide another dimension of realism to this advanced methodology. It is recommended to assess this assumption in more detail and experiment with non-ridged representation of duct sticks in the model.

4. Further development of the cylindrical vibroacoustic model to be expanded from the radial direction to all three directions in the cylindrical coordinate system. Ignoring the effects of the other direction could be the cause of discrepancies in the low frequency region of the predicted results; as shown in previous chapters. In addition, this expansion would facilitate further development of the model to compute the modes shapes.
5. In the developed model, the Lorentz force is used as a boundary condition in order to solve the equation of motion. This boundary condition assumption may be the cause of the discrepancies in the low frequency performance of the model. Further research with the Lorentz force considered as a distributed force and as a source term embedded in the equations of motion would provide a more accurate representation of the body force and ultimately improve the accuracy of the cylindrical vibroacoustic model.

If pursued, the recommended future work can provide a guide for further advancement to the research presented in this dissertation. Further work toward more accurate methodologies for reactor noise prediction will also benefit the usable frequency range and better represent the mechanisms of the reactor vibroacoustic behaviour.

REFERENCES/BIBLIOGRAPHY

- [1] D. Caverly, K. Pointner, R. Presta, P. Griebler, H. Reisinger, and O. Haslehner, “Air core reactors: magnetic clearances, electrical connection, and grounding of their supports,” in *Proc. 53rd. Minnesota Power Systems Conference, MIPSYCON*, 2017.
- [2] P. Dopplmair, P. Griebler, H. Reisinger, and S. Salubro, “Acoustic aspects of dry-type air-core reactors—specification, design, testing, field measurements,” *e i Elektrotechnik und Informationstechnik*, vol. 134, no. 1, pp. 61–66, 2017.
- [3] R. D. Blevins, *Formulas for Natural Frequency and Mode Shape*. Krieger Publishing Company, 2001.
- [4] T. A. Fiorentin, L. F. Lopes, O. M. Da Silva, and A. Lenzi, “Vibroacoustic models of air-core reactors,” *Int. J. Acoust. Vib.*, vol. 21, no. 4, pp. 453–461, 2016.
- [5] J. L. Lilien, “Acoustic noise generated by air power reactor in open-air substation,” *Eur. Trans. Electr. Power*, vol. 16, no. 3, pp. 297–310, 2006.
- [6] J. Smede, G.-G. Johansson, O. Winroth, and H.-P. Schutt, “Design of HVDC converter stations with respect to audible noise requirements,” *IEEE Trans. Power Deliv.*, vol. 10, no. 2, pp. 747–758, 1995.
- [7] S. A. Counter, A. Olofsson, H. F. Grahn, and E. Borg, “MRI acoustic noise: Sound pressure and frequency analysis,” *J. Magn. Reson. Imaging*, vol. 7, no. 3, pp. 606–611, 1997.
- [8] S. A. Counter, Å. Olofsson, E. Borg, B. Bjelke, A. Häggström, and H. F. Grahn, “Analysis of magnetic resonance imaging acoustic noise generated by a 4.7 T experimental system,” *Acta Otolaryngol.*, vol. 120, no. 6, pp. 739–743, 2000.
- [9] M. E. Ravicz, J. R. Melcher, and N. Y.-S. Kiang, “Acoustic noise during functional magnetic resonance imaging,” *J. Acoust. Soc. Am.*, vol. 108, no. 4, pp. 1683–1696, 2000.

- [10] C. K. Mechefske, Y. Wu, and B. K. Rutt, "MRI Gradient Coil Cylinder Sound Field Simulation and Measurement," *J. Biomech. Eng.*, vol. 124, no. 4, p. 450, 2002.
- [11] R. A. Hedeem and W. A. Edelstein, "Characterization and prediction of gradient acoustic noise in MR imagers," *Magn. Reson. Med.*, vol. 37, no. 1, pp. 7–10, 1997.
- [12] W. Li, C. K. Mechefske, C. Gazdzinski, and B. K. Rutt, "Acoustic noise analysis and prediction in a 4-T MRI scanner," *Concepts Magn. Reson. Part B Magn. Reson. Eng.*, vol. 21, no. 1, pp. 19–25, 2004.
- [13] P. Mansfield, P. M. Glover, and J. Beaumont, "Sound generation in gradient coil structures for MRI," *Magn. Reson. Med.*, vol. 39, no. 4, pp. 539–550, 1998.
- [14] C. K. Mechefske, Y. Wu, and B. Rutt, "Characterization of acoustic noise and magnetic field fluctuations in a 4 T whole-body MRI scanner," *Mech. Syst. Signal Process.*, vol. 16, no. 2–3, pp. 459–473, 2002.
- [15] C. K. Mechefske, G. Yao, W. Li, C. Gazdzinski, and B. K. Rutt, "Modal analysis and acoustic noise characterization of a 4T MRI gradient coil insert," *Concepts Magn. Reson. Part B Magn. Reson. Eng.*, vol. 22, no. 1, pp. 37–49, 2004.
- [16] C. V. Rizzo Sierra, M. J. Versluis, J. M. Hoogduin, and H. Duifhuis, "Acoustic fMRI noise: Linear time-invariant system model," *IEEE Trans. Biomed. Eng.*, vol. 55, no. 9, pp. 2115–2123, 2008.
- [17] N. B. Roozen, A. H. Koevoets, and A. J. den Hamer, "Active vibration control of gradient coils to reduce acoustic noise of MRI systems," *IEEE/ASME Trans. Mechatronics*, vol. 13, no. 3, pp. 325–334, 2008.
- [18] G. Li and C. K. Mechefske, "Structural-acoustic modal analysis of cylindrical shells: Application to MRI scanner systems," *Magn. Reson. Mater. Physics, Biol. Med.*, vol. 22, no. 6, pp. 353–364, 2009.
- [19] M. Shakeri, M. Akhlaghi, and S. M. Hoseini, "Vibration and radial wave propagation velocity in functionally graded thick hollow cylinder," *Compos.*

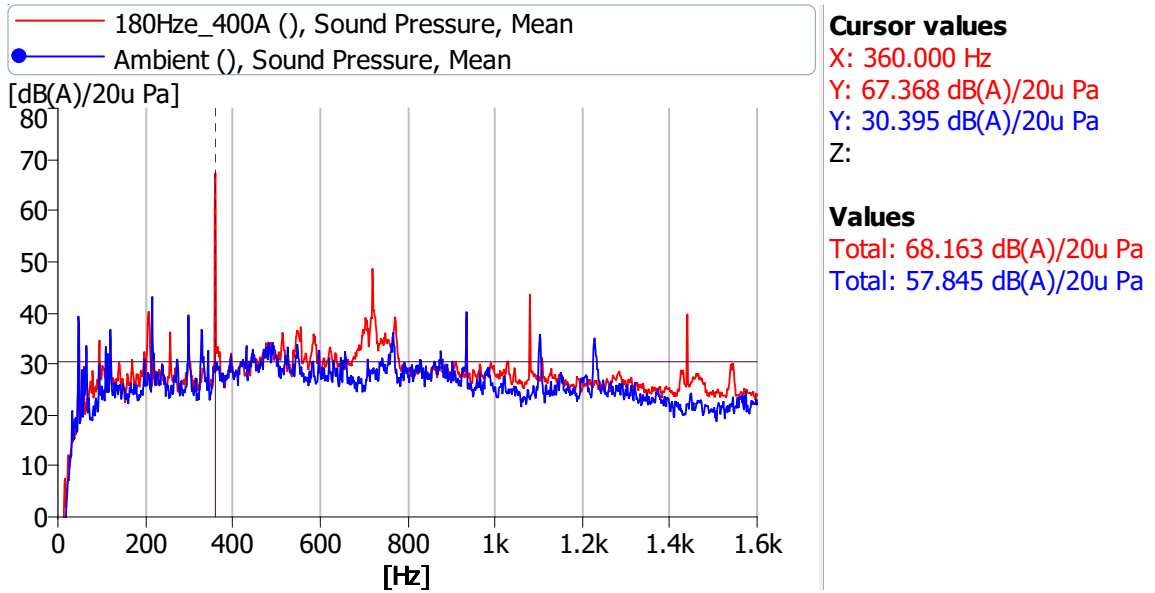
Struct., vol. 76, no. 1–2, pp. 174–181, Oct. 2006.

- [20] J. Li, S. Wang, J. Hong, Z. Yang, S. Jiang, and S. Xia, “Vibration and acoustic noise emitted by dry-type air-core reactors under PWM voltage excitation,” *AIP Adv.*, vol. 8, no. 5, 2018.
- [21] J. F. BIRD, R. W. Hart, and F. T. McClure, “Vibration of thick-walled hollow cylinders: Exact numerical solutions,” *J. Acoust. Soc. Am. - JACOUST SOC AMER*, vol. 32, no. 18, p. 35, 1960.
- [22] H. Levine, “On the natural frequencies of a hollow cylinder for acoustical and electrical excitations,” *J. d’Analyse Mathématique*, vol. 30, no. 1, pp. 355–371, Dec. 1976.
- [23] J. So and A. Leissa, “Free Vibrations of Thick Hollow Circular Cylinders From Three-Dimensional Analysis,” *J. Vib. Acoust.*, vol. 119, no. April 1995, pp. 89–95, 1997.
- [24] N. E. Smith, “Vibration of hollow cylindrical shells with partial constrained layer damping,” Rochester Institute of Technology, 2004.
- [25] W. L. Brogan, “Radial Vibrations of a Thin Cylindrical Shell,” *J. Acoust. Soc. Am.*, vol. 33, no. 12, pp. 1778–1781, 2005.
- [26] J. N. Sharma, H. Singh, and Y. D. Sharma, “Vibration analysis of a transversely isotropic hollow cylinder by using the matrix Frobenius method,” *J. Therm. Stress.*, vol. 34, no. 9, pp. 934–957, Sep. 2011.
- [27] Q. Tang, C. Li, and B. Wen, “Analysis on Forced Vibration of Thin-Wall Cylindrical Shell with Nonlinear Boundary Condition,” *Shock Vib.*, vol. 2016, pp. 1–22, 2016.
- [28] A. M. Abd-Alla, T. A. Nofal, and A. M. Farhan, “Effect of the non-homogeneity on the composite infinite cylinder of isotropic material,” *Phys. Lett. Sect. A Gen. At. Solid State Phys.*, vol. 372, no. 29, pp. 4861–4864, 2008.

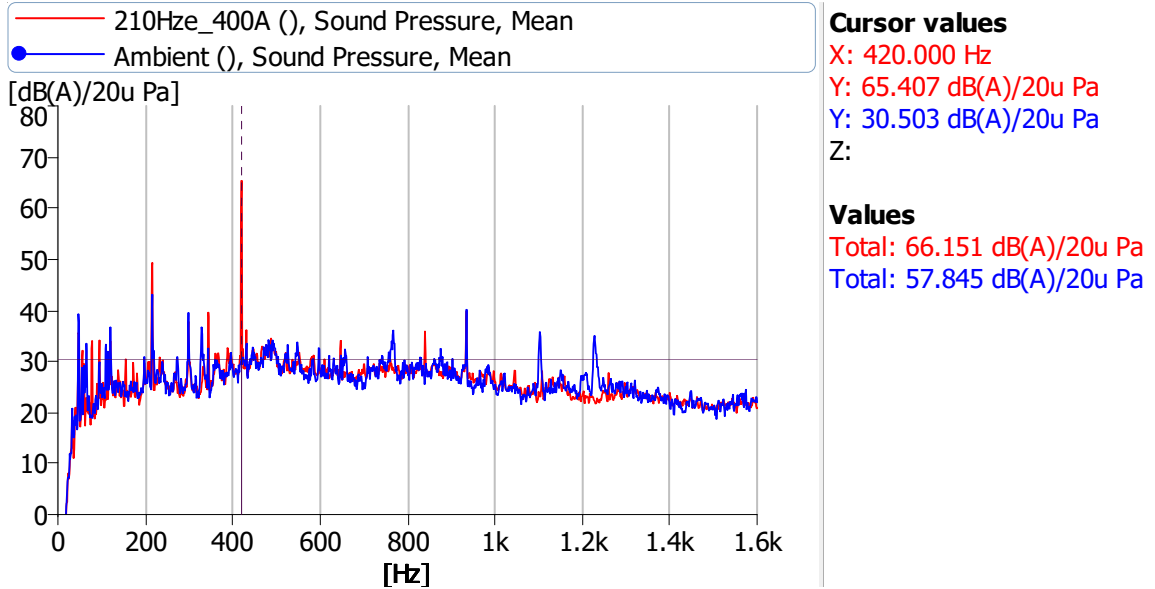
- [29] A. M. Abd-Alla, G. A. Yahya, and S. R. Mahmoud, "Effect of magnetic field and non-homogeneity on the radial vibrations in hollow rotating elastic cylinder," *Meccanica*, vol. 48, no. 3, pp. 555–566, 2013.
- [30] Hamidzadeh H.R. and Jazar R.N., *Vibrations of Thick Cylindrical Structures*. Springer, 2010.

APPENDICES

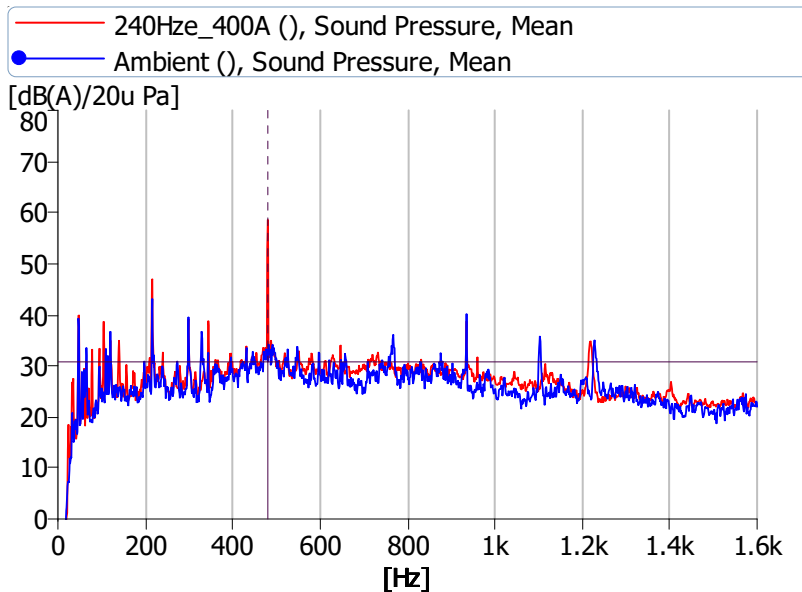
Appendix A FFT Analysis Results



A 1 – FFT analysis of 180 Hz electrical excitation frequency at 400 A for prototype reactor 1.



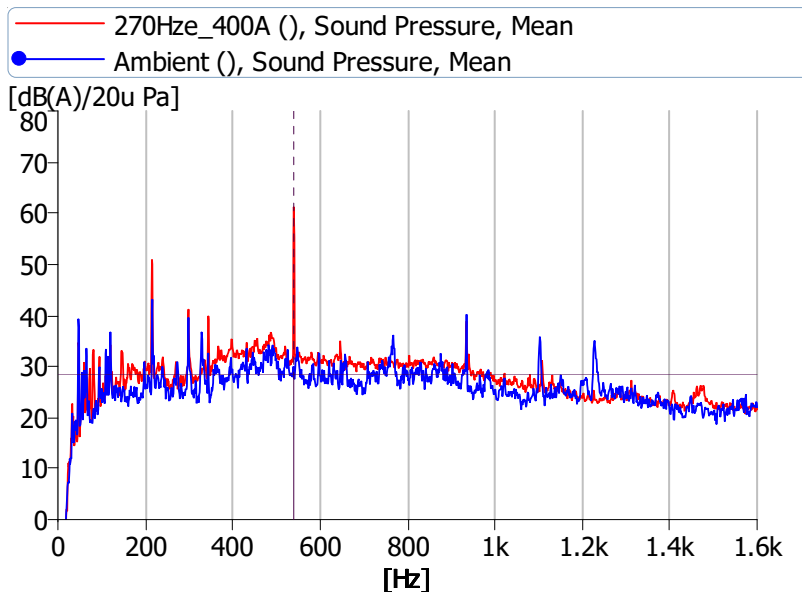
A 2 – FFT analysis of 210 Hz electrical excitation frequency at 400 A for prototype reactor 1.



Cursor values
 X: 480.000 Hz
 Y: 58.602 dB(A)/20u Pa
 Y: 30.784 dB(A)/20u Pa
 Z:

Values
 Total: 61.785 dB(A)/20u Pa
 Total: 57.845 dB(A)/20u Pa

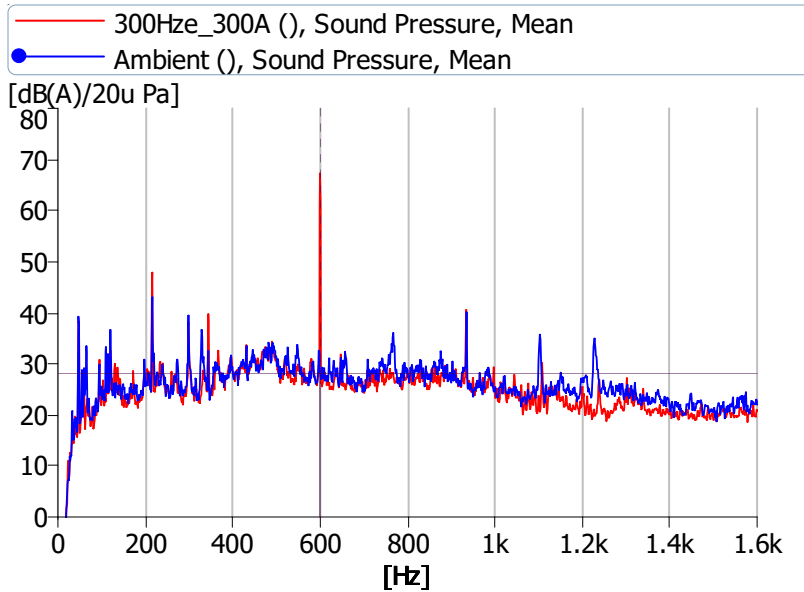
A 3 – FFT analysis of 240 Hz electrical excitation frequency at 400 A for prototype reactor 1.



Cursor values
 X: 540.000 Hz
 Y: 61.239 dB(A)/20u Pa
 Y: 28.525 dB(A)/20u Pa
 Z:

Values
 Total: 63.758 dB(A)/20u Pa
 Total: 57.845 dB(A)/20u Pa

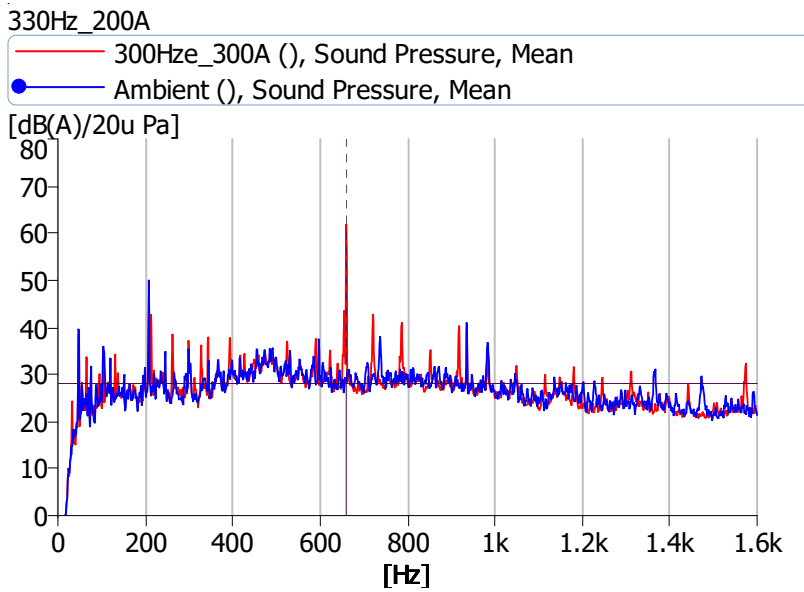
A 4 – FFT analysis of 270 Hz electrical excitation frequency at 400 A for prototype reactor 1.



Cursor values
 X: 600.000 Hz
 Y: 67.383 dB(A)/20u Pa
 Z: 28.197 dB(A)/20u Pa
 Z:

Values
 Total: 67.778 dB(A)/20u Pa
 Total: 57.845 dB(A)/20u Pa

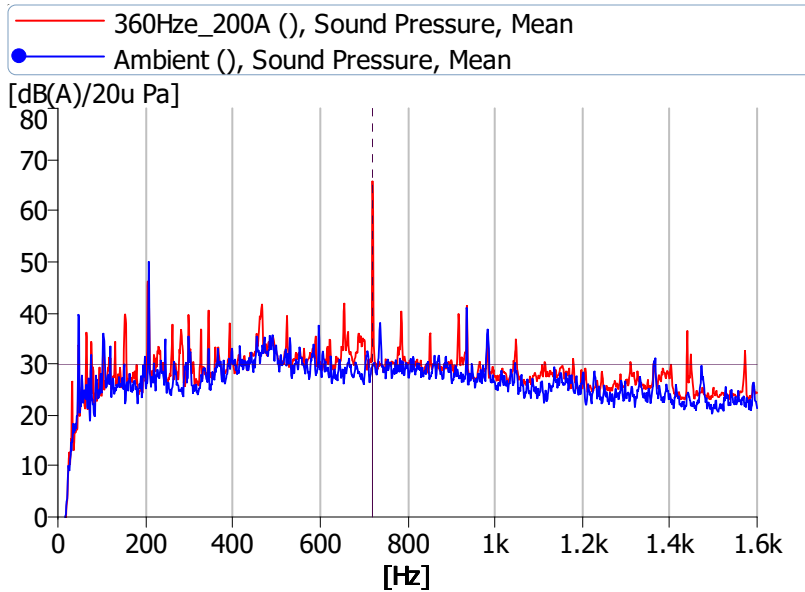
A 5 – FFT analysis of 300 Hz electrical excitation frequency at 300 A for prototype reactor 1.



Cursor values
 X: 660.000 Hz
 Y: 28.094 dB(A)/20u Pa
 Z:

Values
 Total: 59.028 dB(A)/20u Pa

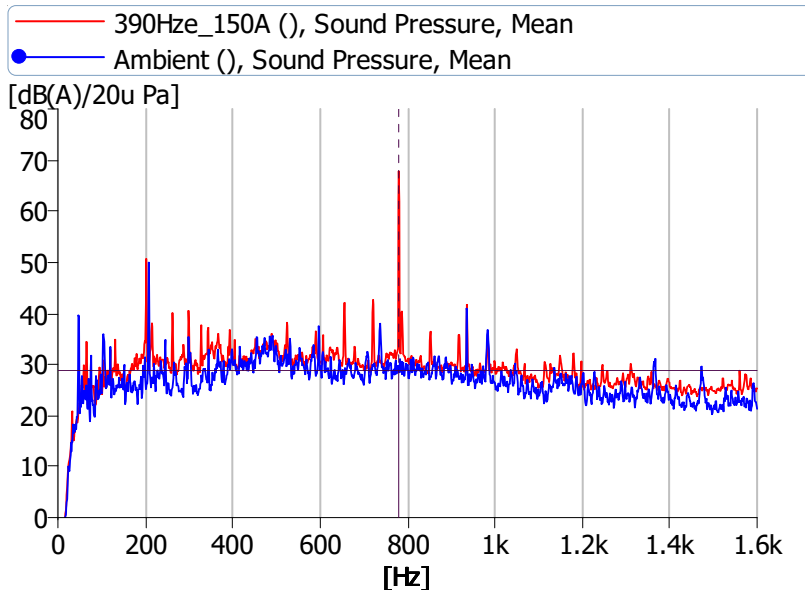
A 6 – FFT analysis of 330 Hz electrical excitation frequency at 200 A for prototype reactor 1.



Cursor values
 X: 720.000 Hz
 Y: 65.779 dB(A)/20u Pa
 Y: 29.961 dB(A)/20u Pa
 Z:

Values
 Total: 66.943 dB(A)/20u Pa
 Total: 59.028 dB(A)/20u Pa

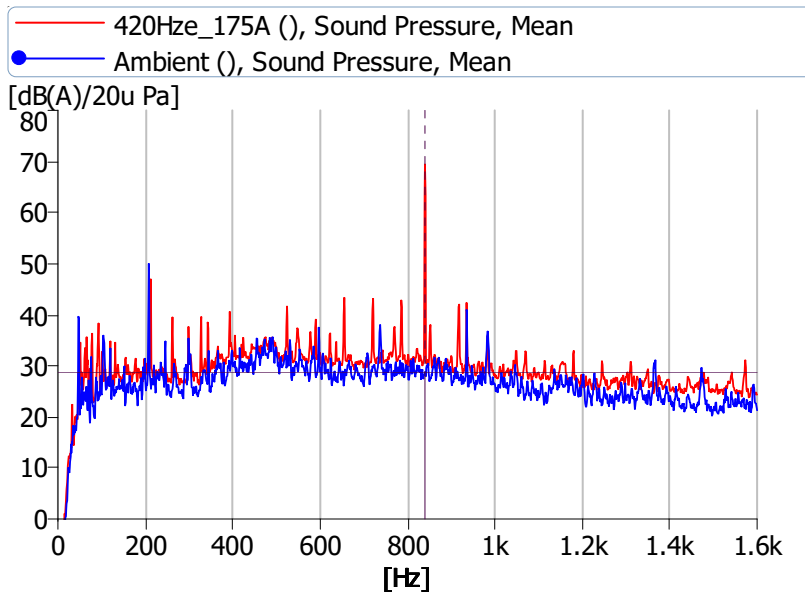
A 7 – FFT analysis of 360 Hz electrical excitation frequency at 200 A for prototype reactor 1.



Cursor values
 X: 780.000 Hz
 Y: 67.852 dB(A)/20u Pa
 Y: 28.862 dB(A)/20u Pa
 Z:

Values
 Total: 68.671 dB(A)/20u Pa
 Total: 59.028 dB(A)/20u Pa

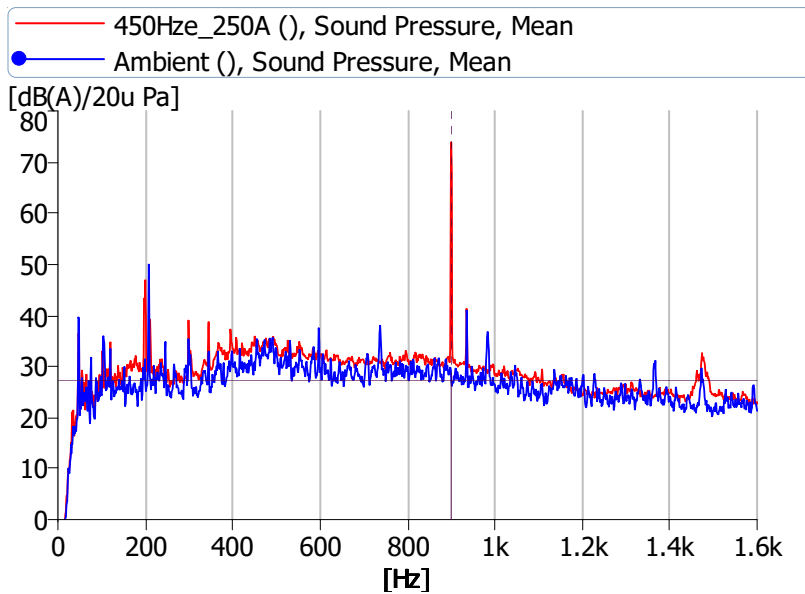
A 8 – FFT analysis of 390 Hz electrical excitation frequency at 150 A for prototype reactor 1.



Cursor values
 X: 840.000 Hz
 Y: 69.505 dB(A)/20u Pa
 Z: 28.812 dB(A)/20u Pa
 Z:

Values
 Total: 70.102 dB(A)/20u Pa
 Total: 59.028 dB(A)/20u Pa

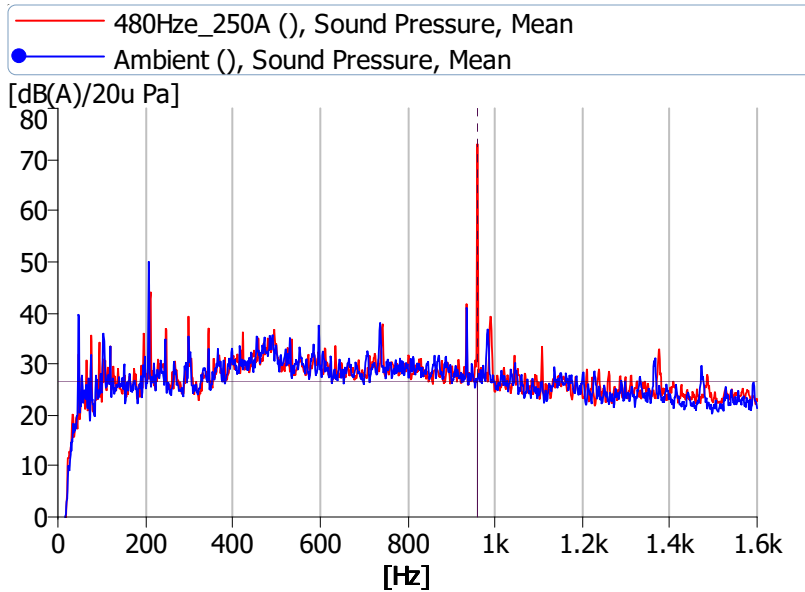
A 9 – FFT analysis of 420 Hz electrical excitation frequency at 175 A for prototype reactor 1.



Cursor values
 X: 900.000 Hz
 Y: 73.956 dB(A)/20u Pa
 Z: 27.353 dB(A)/20u Pa
 Z:

Values
 Total: 74.150 dB(A)/20u Pa
 Total: 59.028 dB(A)/20u Pa

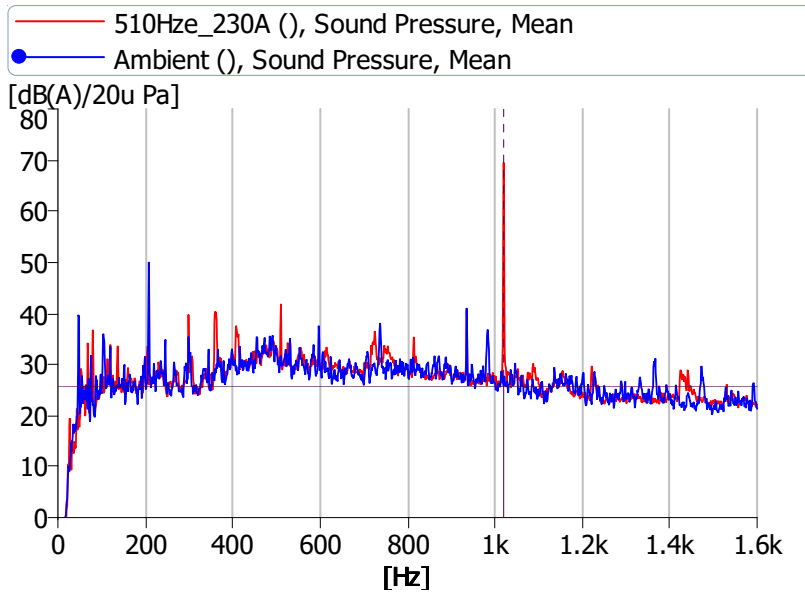
A 10 – FFT analysis of 450 Hz electrical excitation frequency at 250 A for prototype reactor 1.



Cursor values
 X: 960.000 Hz
 Y: 73.106 dB(A)/20u Pa
 Y: 26.664 dB(A)/20u Pa
 Z:

Values
 Total: 73.264 dB(A)/20u Pa
 Total: 59.028 dB(A)/20u Pa

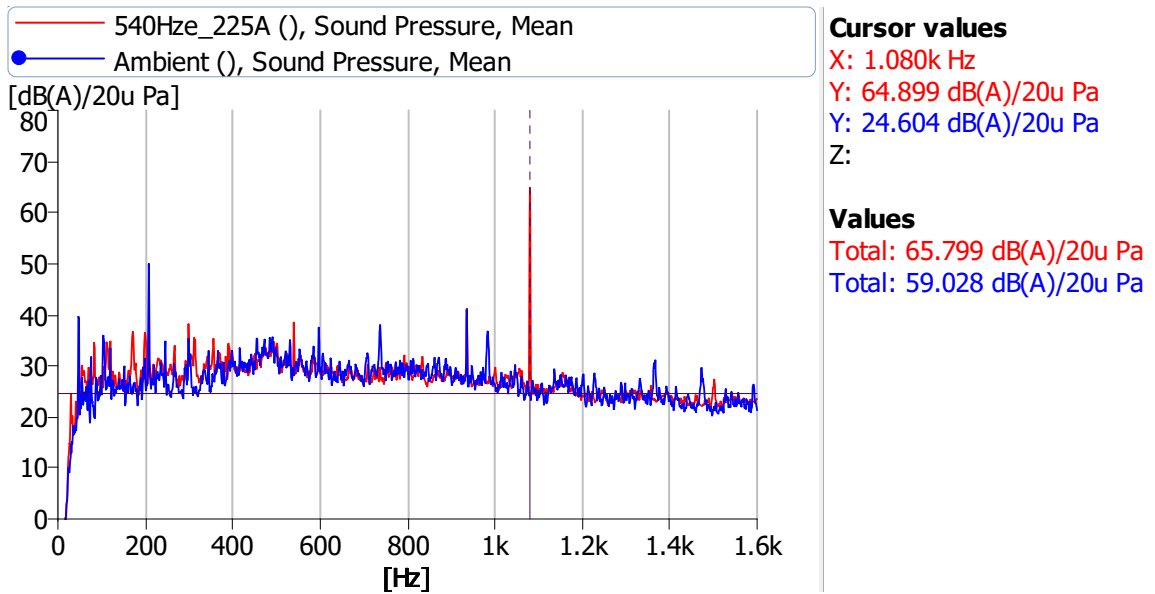
A 11 – FFT analysis of 480 Hz electrical excitation frequency at 250 A for prototype reactor 1.



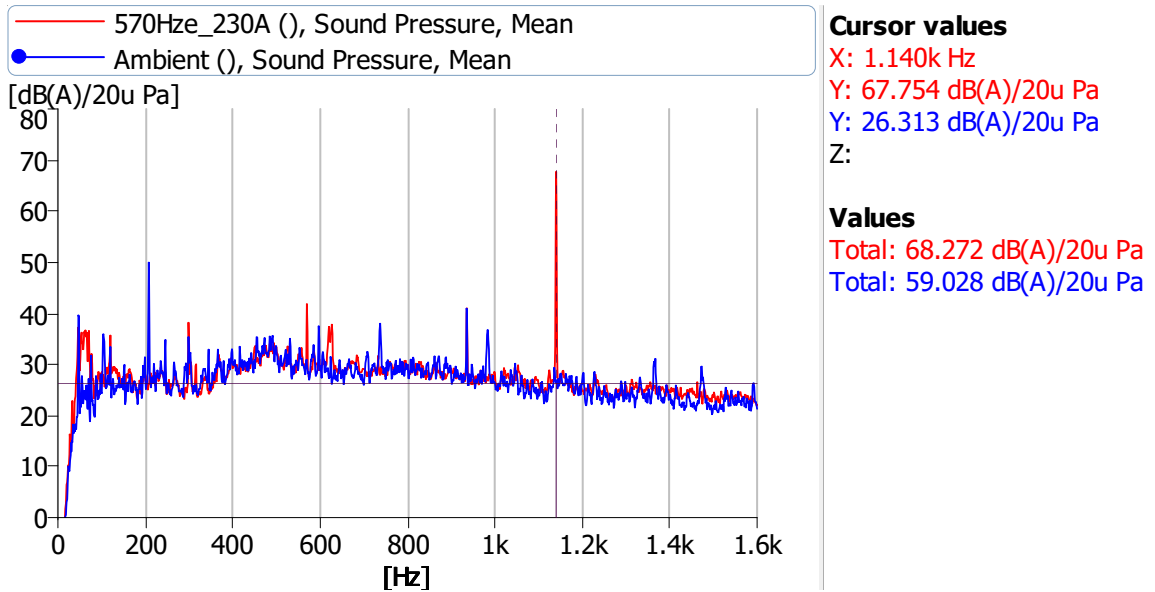
Cursor values
 X: 1.020k Hz
 Y: 69.479 dB(A)/20u Pa
 Y: 25.786 dB(A)/20u Pa
 Z:

Values
 Total: 69.841 dB(A)/20u Pa
 Total: 59.028 dB(A)/20u Pa

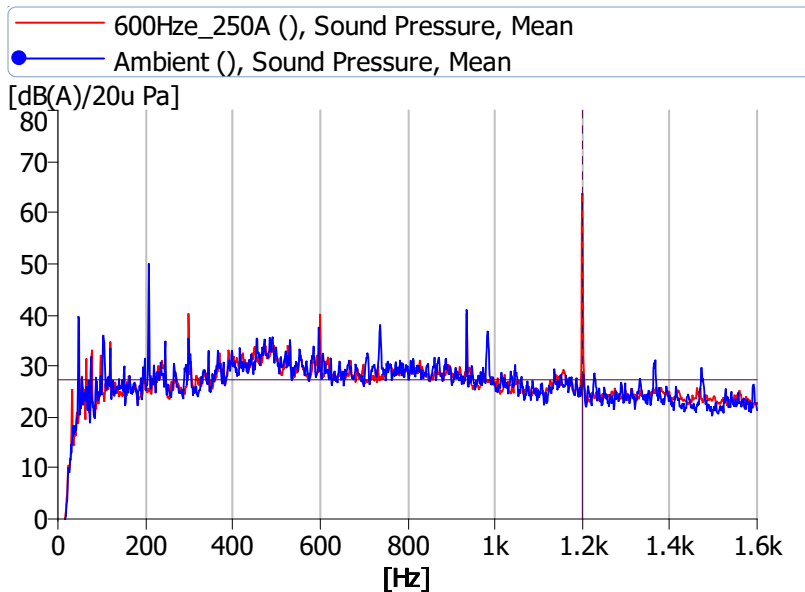
A 12 – FFT analysis of 510 Hz electrical excitation frequency at 230 A for prototype reactor 1.



A 13 – FFT analysis of 540 Hz electrical excitation frequency at 225 A for prototype reactor 1.



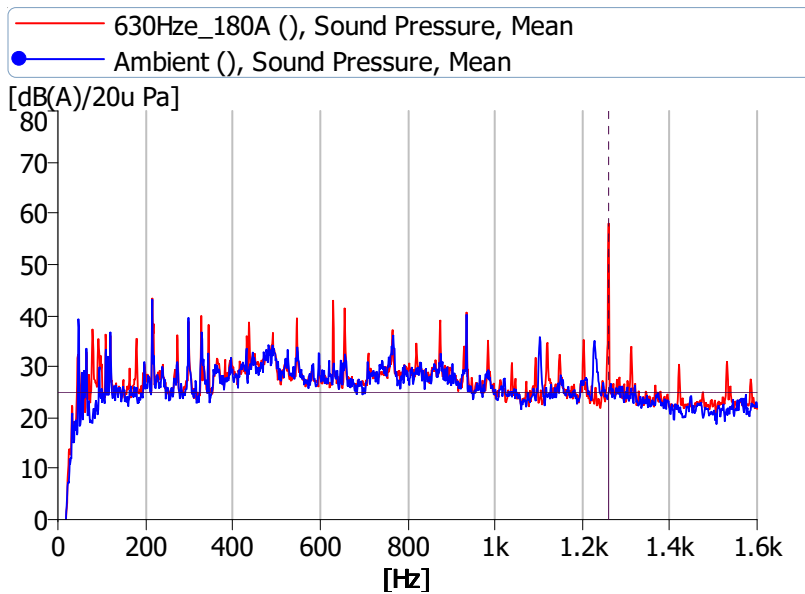
A 14 – FFT analysis of 570 Hz electrical excitation frequency at 230 A for prototype reactor 1.



Cursor values
 X: 1.200k Hz
 Y: 63.786 dB(A)/20u Pa
 Y: 27.249 dB(A)/20u Pa
 Z:

Values
 Total: 64.799 dB(A)/20u Pa
 Total: 59.028 dB(A)/20u Pa

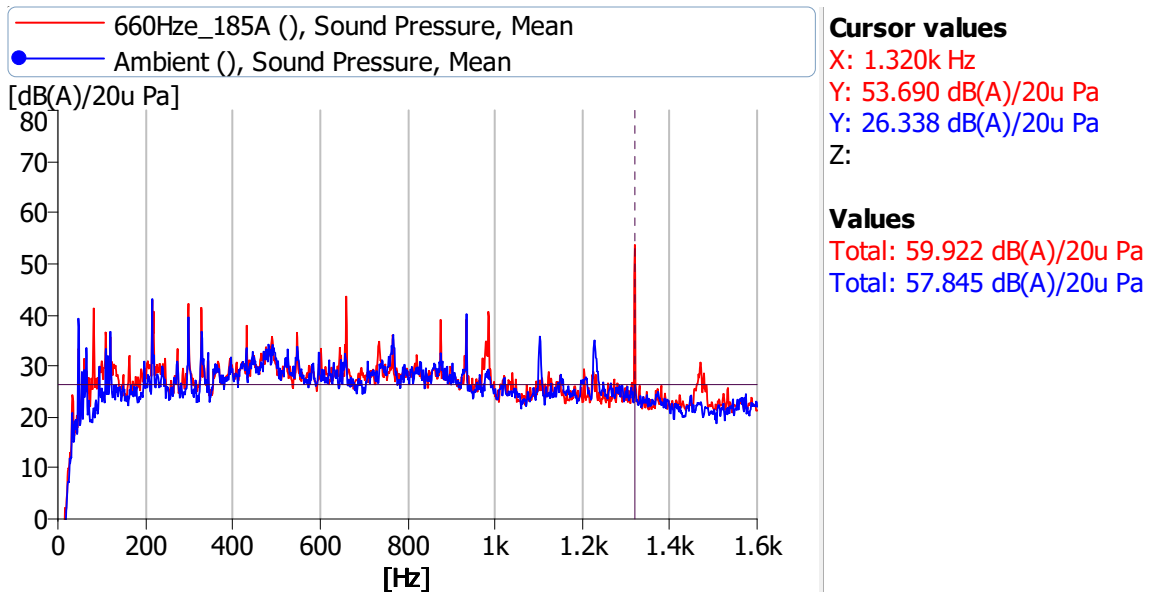
A 15 – FFT analysis of 600 Hz electrical excitation frequency at 250 A for prototype reactor 1.



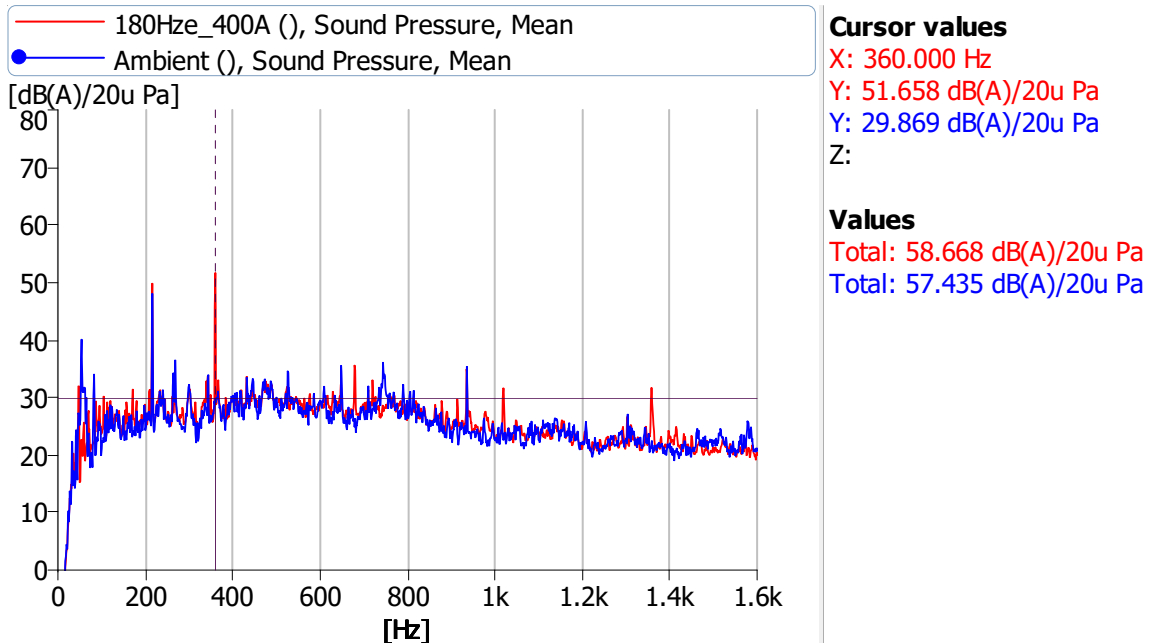
Cursor values
 X: 1.260k Hz
 Y: 58.022 dB(A)/20u Pa
 Y: 24.977 dB(A)/20u Pa
 Z:

Values
 Total: 61.427 dB(A)/20u Pa
 Total: 57.845 dB(A)/20u Pa

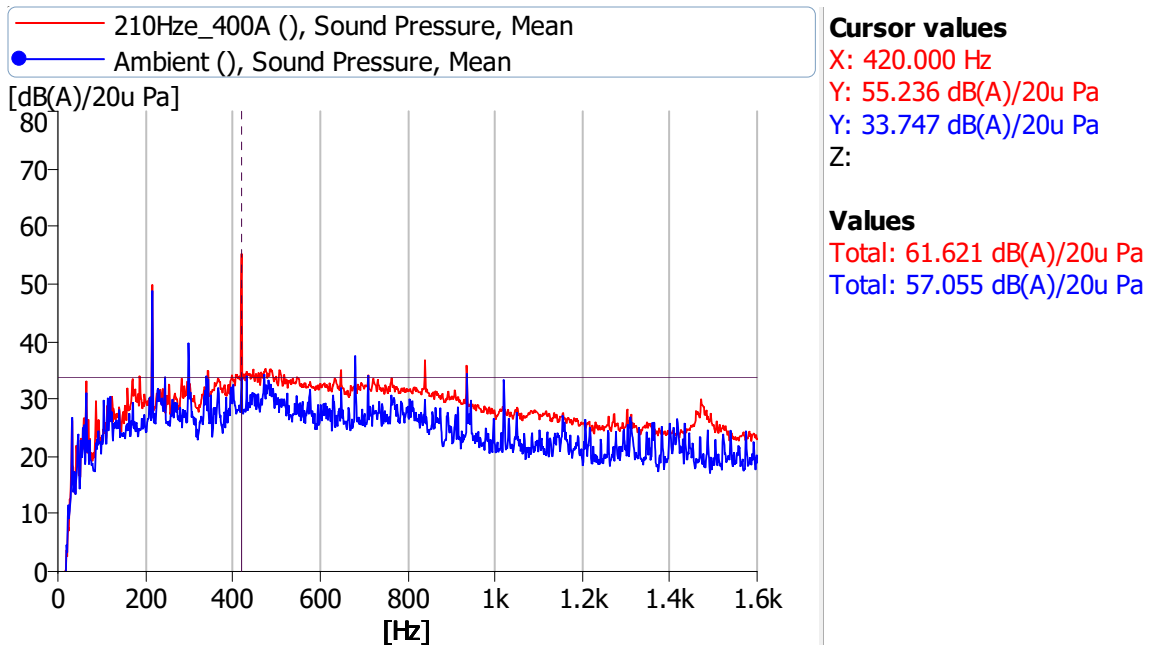
A 16 – FFT analysis of 630 Hz electrical excitation frequency at 180 A for prototype reactor 1.



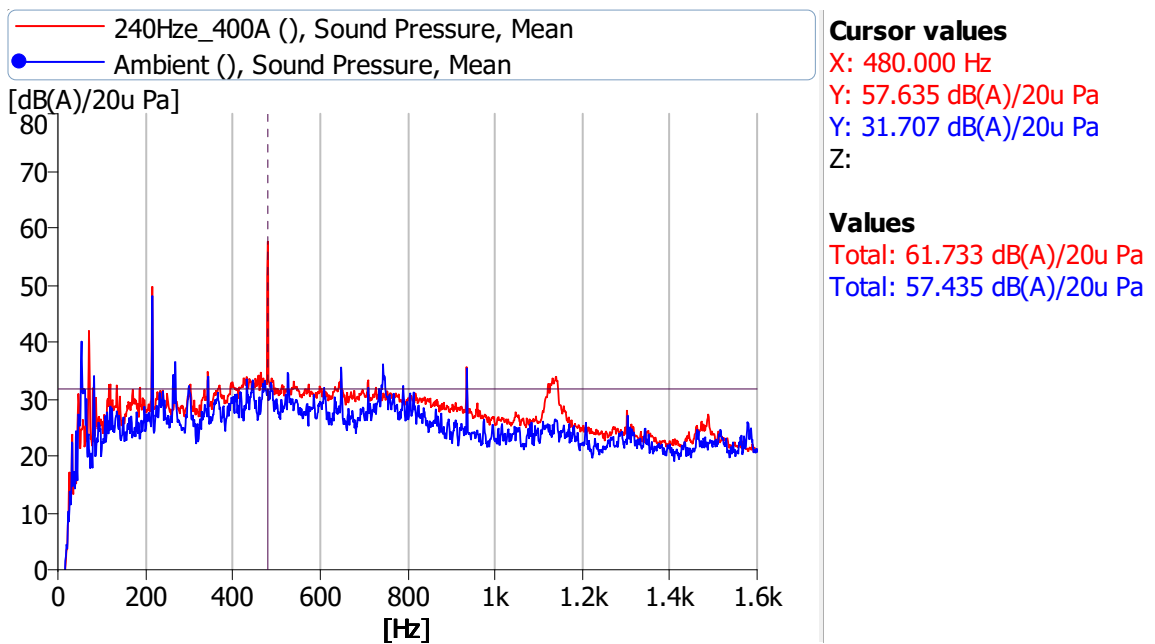
A 17 – FFT analysis of 660 Hz electrical excitation frequency at 185 A for prototype reactor 1.



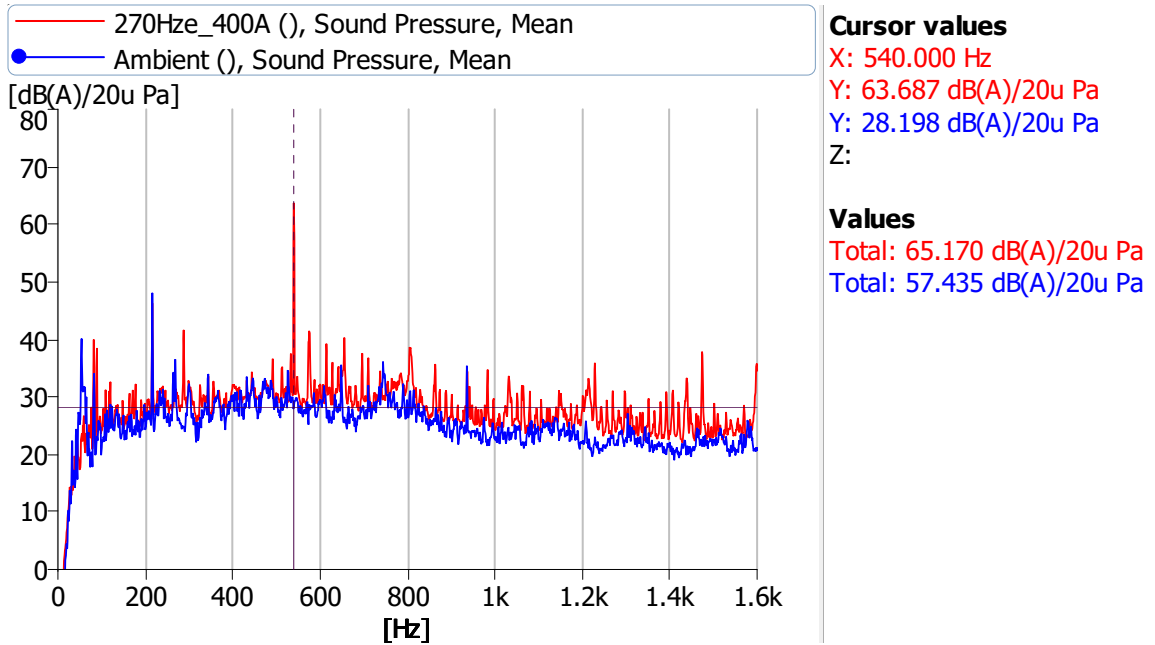
A 18 - FFT analysis of 180 Hz electrical excitation frequency at 400 A for prototype reactor 2.



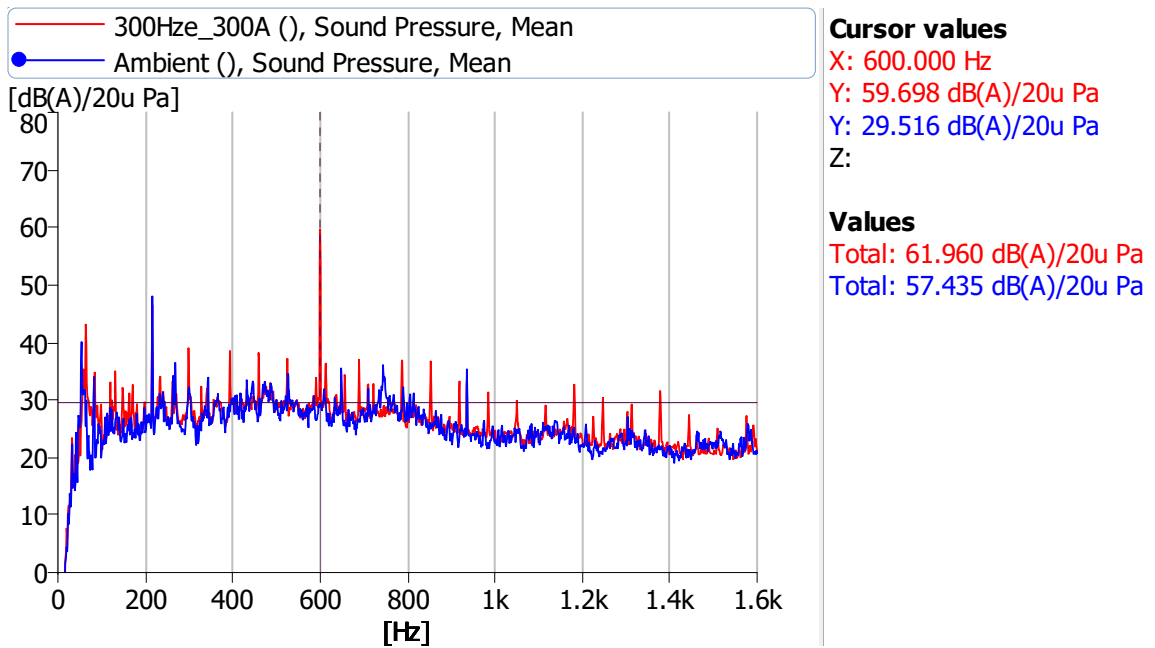
A 19 – FFT analysis of 210 Hz electrical excitation frequency at 400 A for prototype reactor 2.



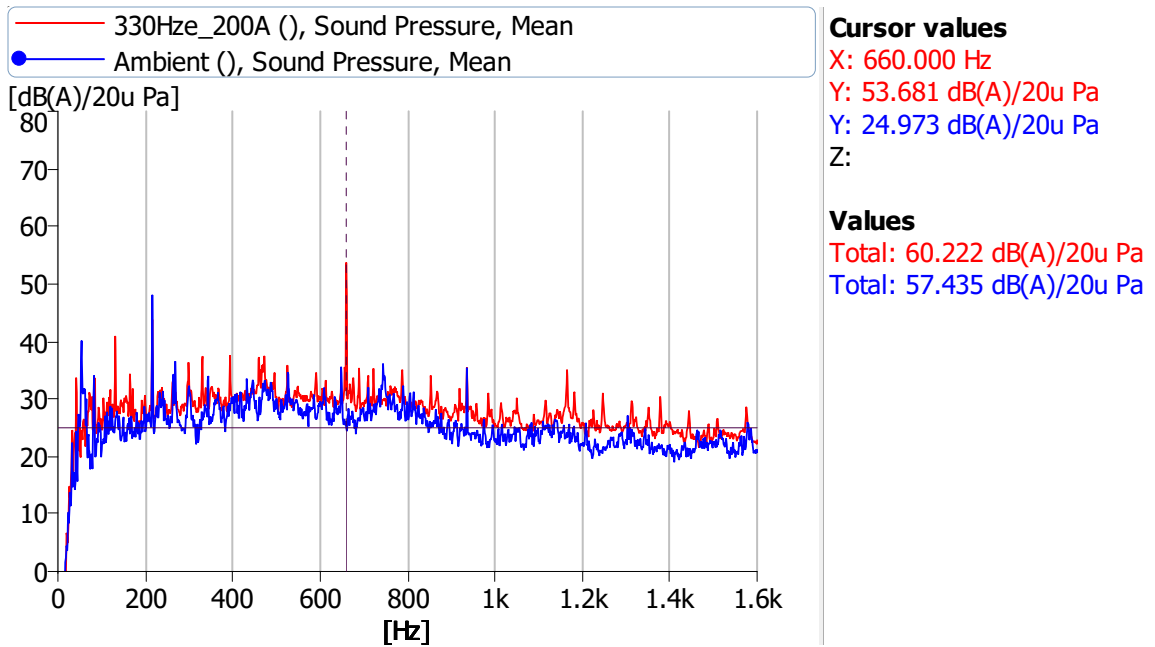
A 20 – FFT analysis of 240 Hz electrical excitation frequency at 400 A for prototype reactor 2.



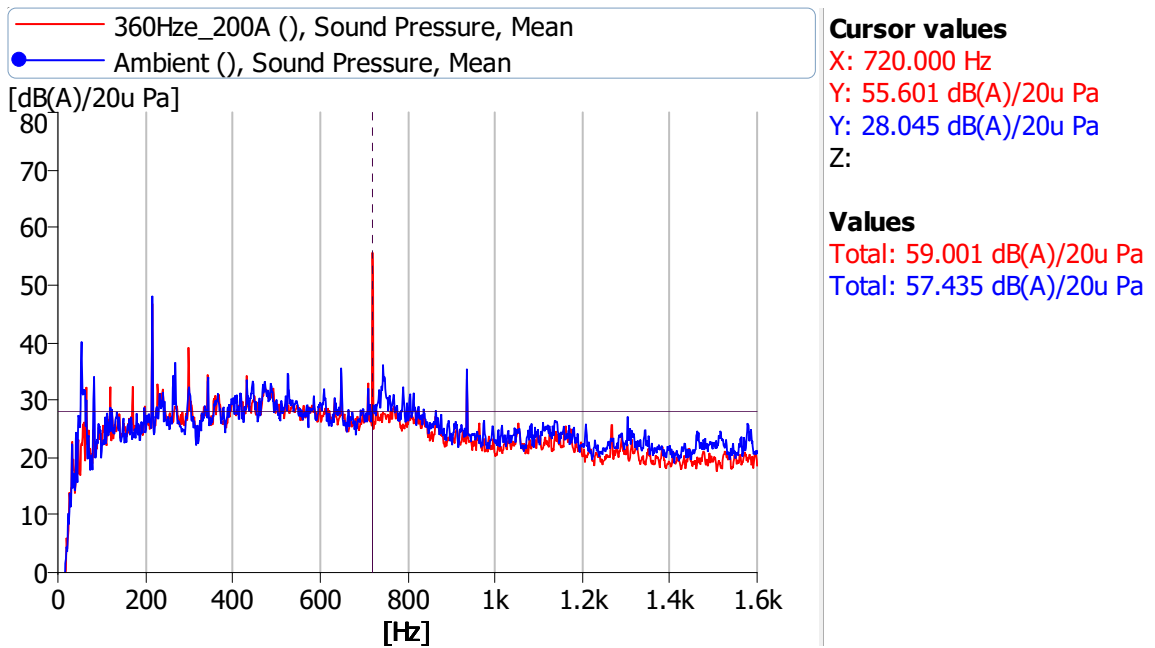
A 21 – FFT analysis of 270 Hz electrical excitation frequency at 400 A for prototype reactor 2.



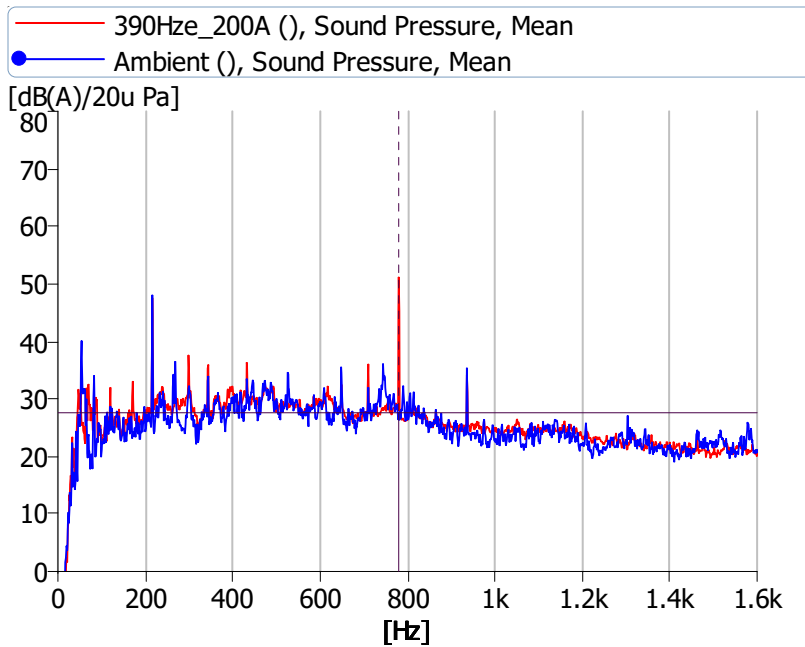
A 22 – FFT analysis of 300 Hz electrical excitation frequency at 300 A for prototype reactor 2.



A 23 – FFT analysis of 330 Hz electrical excitation frequency at 200 A for prototype reactor 2.



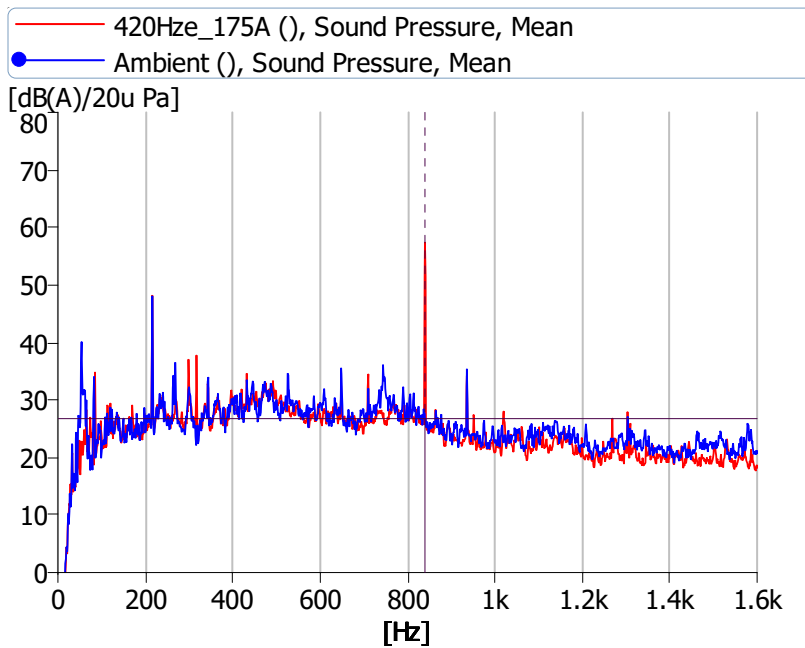
A 24 – FFT analysis of 360 Hz electrical excitation frequency at 200 A for prototype reactor 2.



Cursor values
 X: 780.000 Hz
 Y: 51.169 dB(A)/20u Pa
 Z: 27.549 dB(A)/20u Pa
 Z:

Values
 Total: 58.553 dB(A)/20u Pa
 Total: 57.435 dB(A)/20u Pa

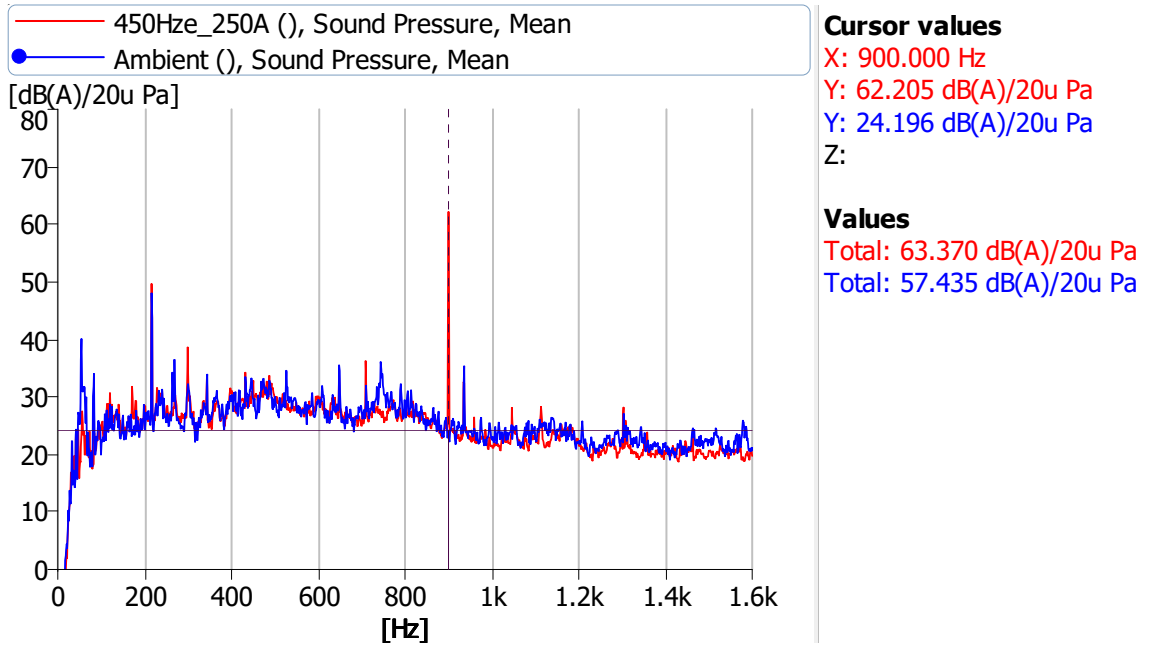
A 25 – FFT analysis of 390 Hz electrical excitation frequency at 200 A for prototype reactor 2.



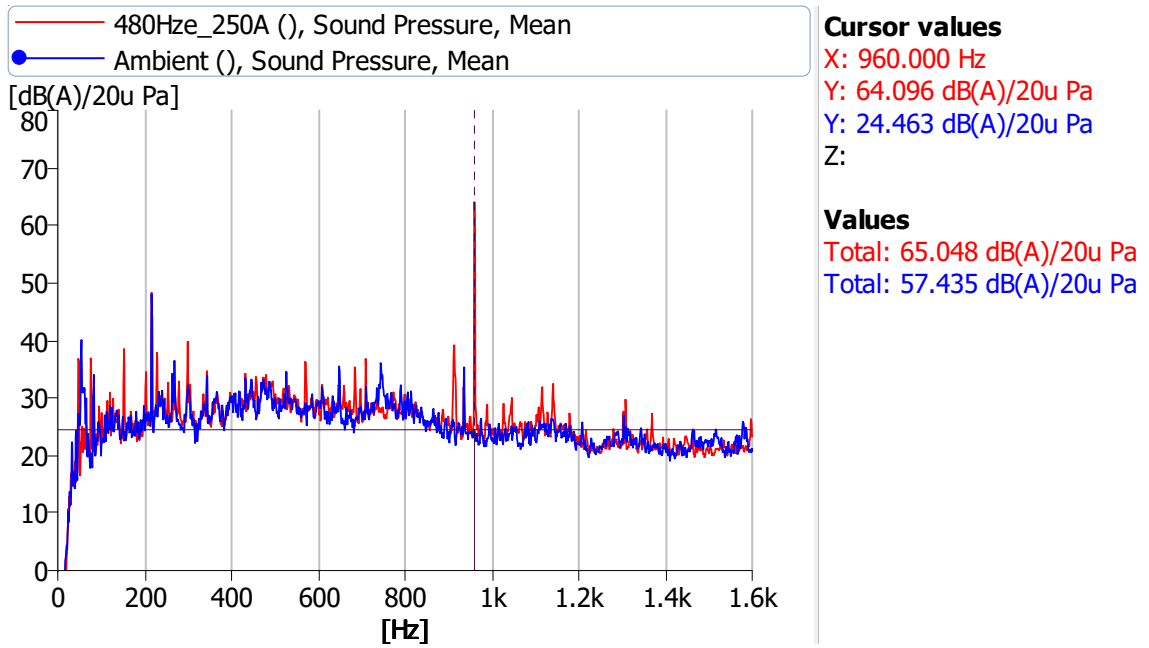
Cursor values
 X: 840.000 Hz
 Y: 57.408 dB(A)/20u Pa
 Y: 26.737 dB(A)/20u Pa
 Z:

Values
 Total: 60.062 dB(A)/20u Pa
 Total: 57.435 dB(A)/20u Pa

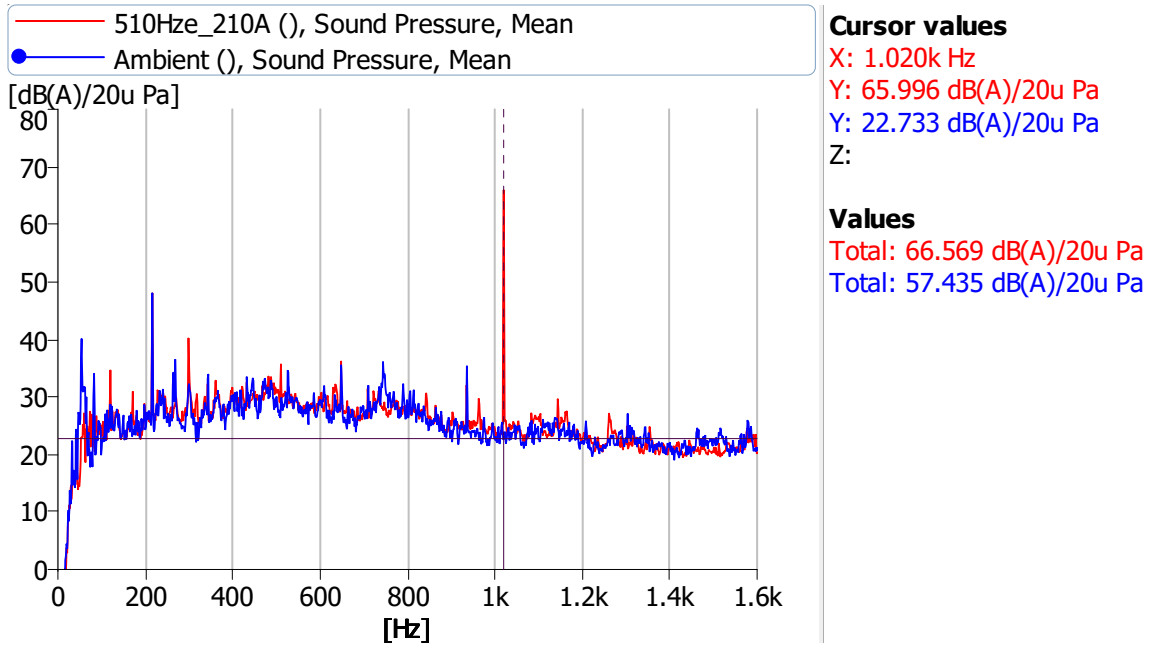
A 26 – FFT analysis of 420 Hz electrical excitation frequency at 175 A for prototype reactor 2.



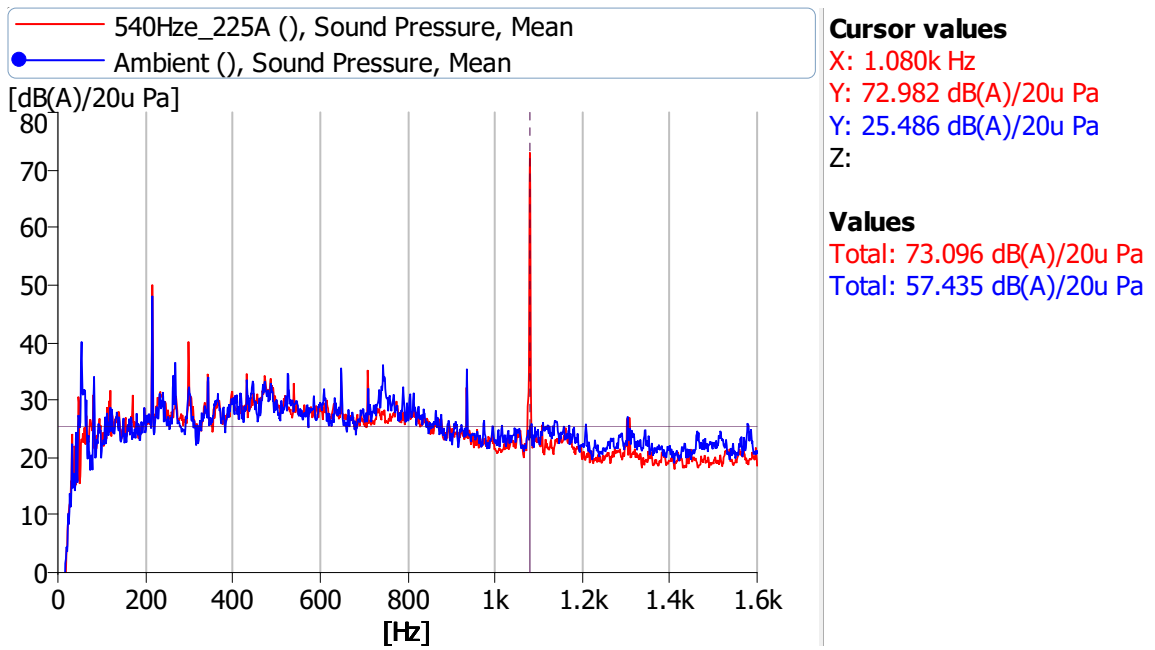
A 27 – FFT analysis of 450 Hz electrical excitation frequency at 250 A for prototype reactor 2.



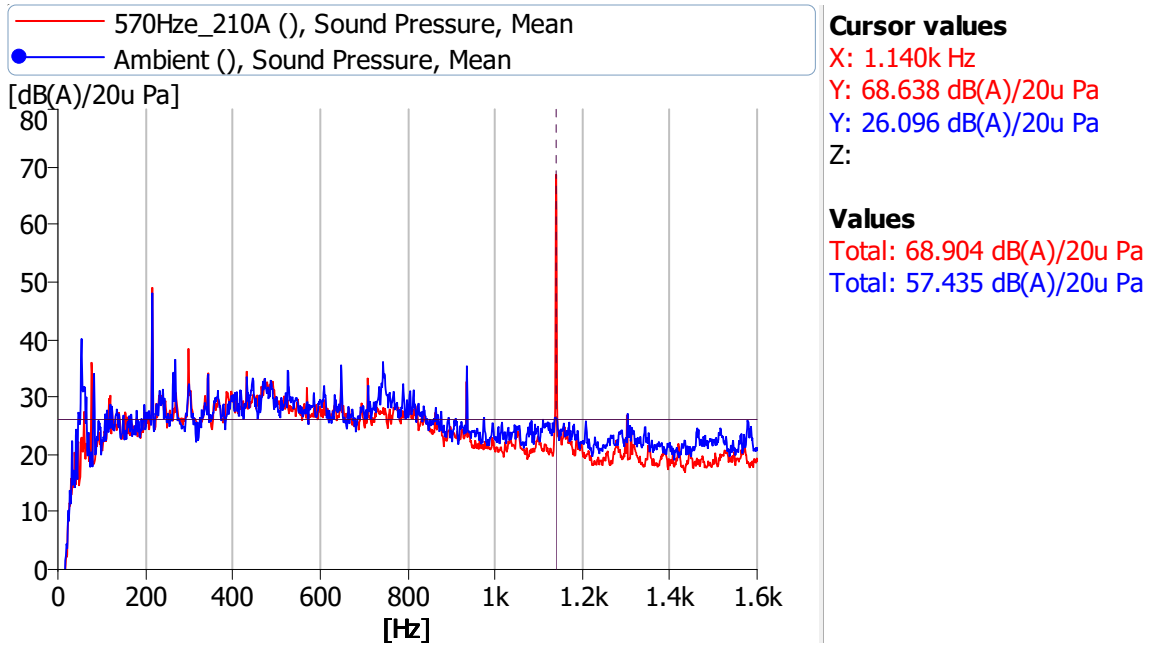
A 28 – FFT analysis of 480 Hz electrical excitation frequency at 250 A for prototype reactor 2.



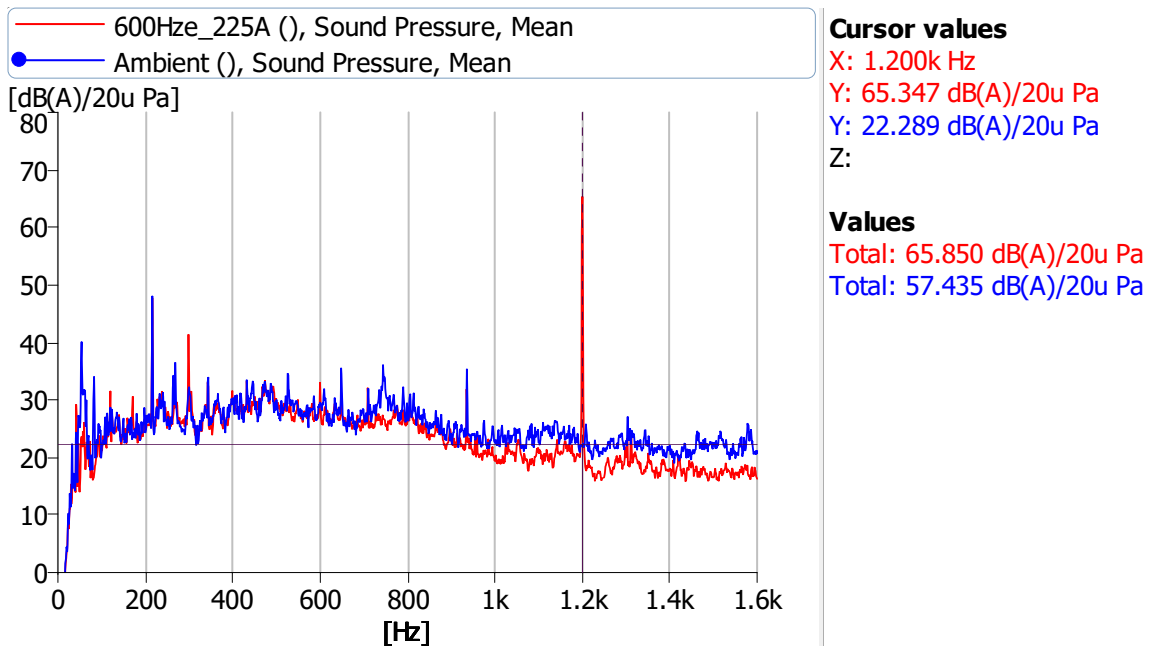
A 29 – FFT analysis of 510 Hz electrical excitation frequency at 210 Hz for prototype reactor 2.



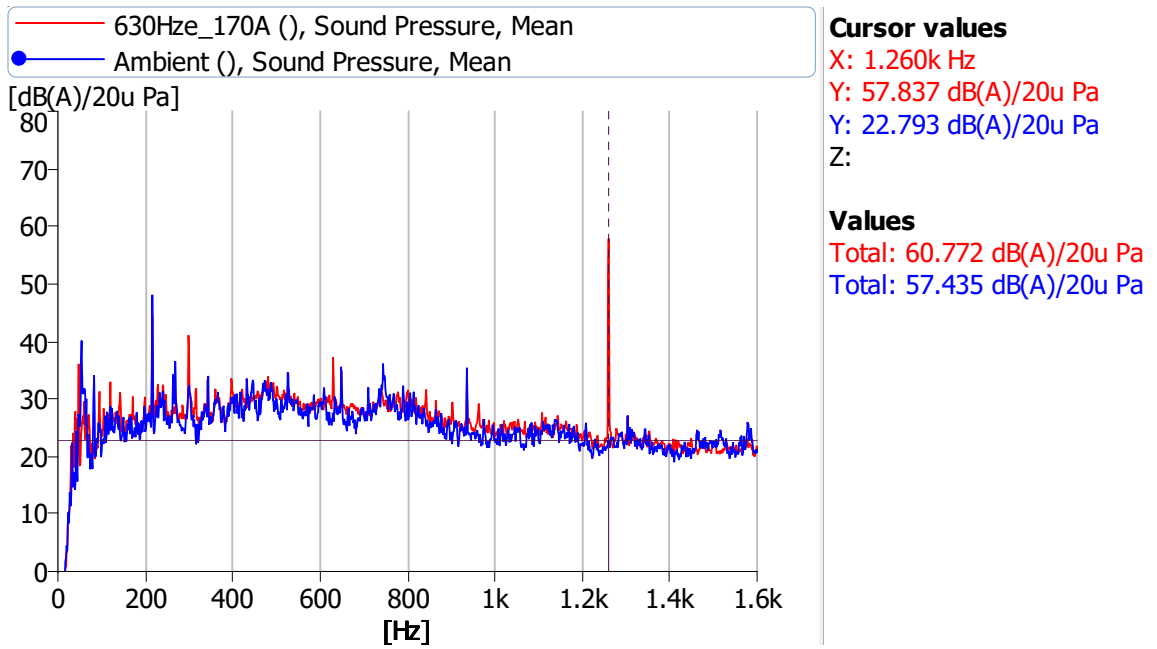
A 30 – FFT analysis of 540 Hz electrical excitation frequency at 225 A for prototype reactor 2.



A 31 – FFT analysis of 570 Hz electrical excitation frequency at 210 A for prototype reactor 2.

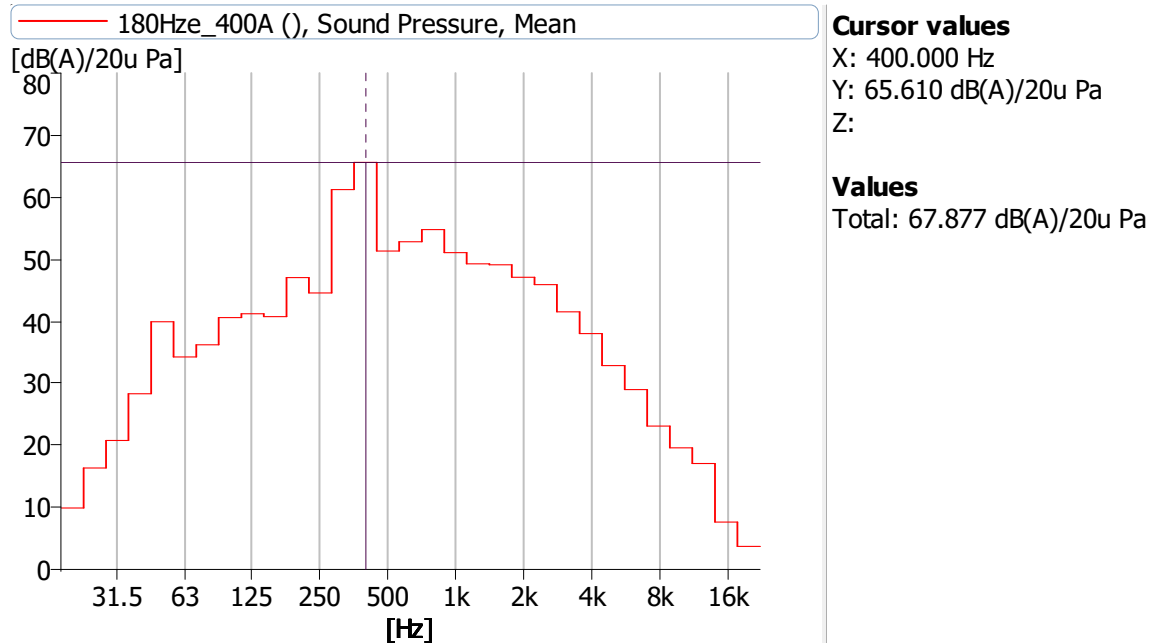


A 32 – FFT analysis of 600 Hz electrical excitation frequency at 225 A for prototype reactor 2.

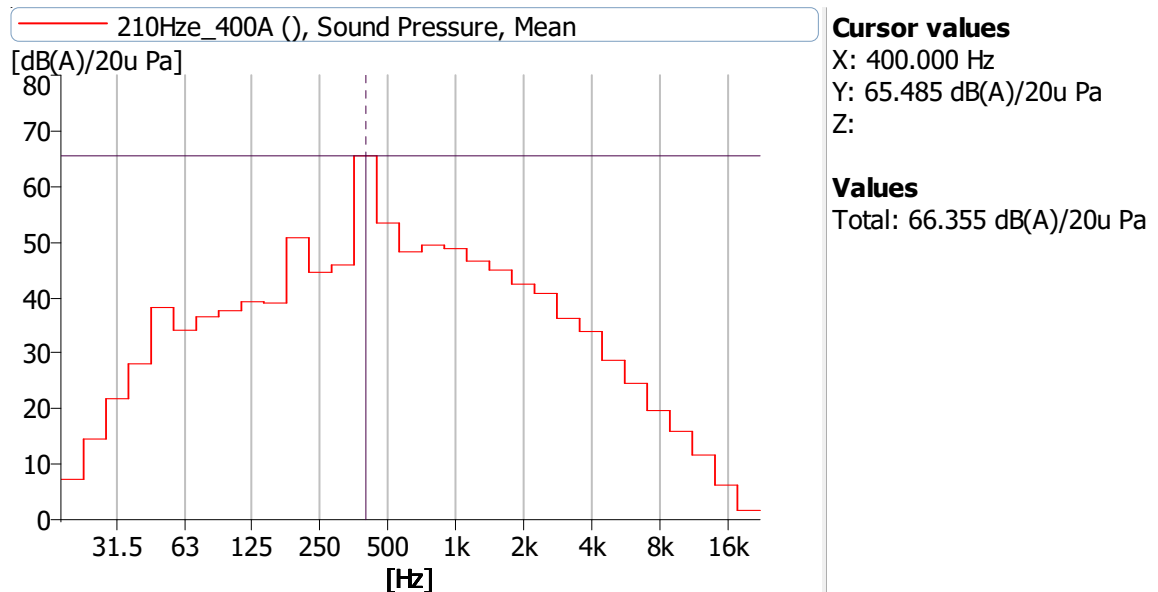


A 33 – FFT analysis of 630 Hz electrical excitation frequency at 170 A for prototype reactor 2.

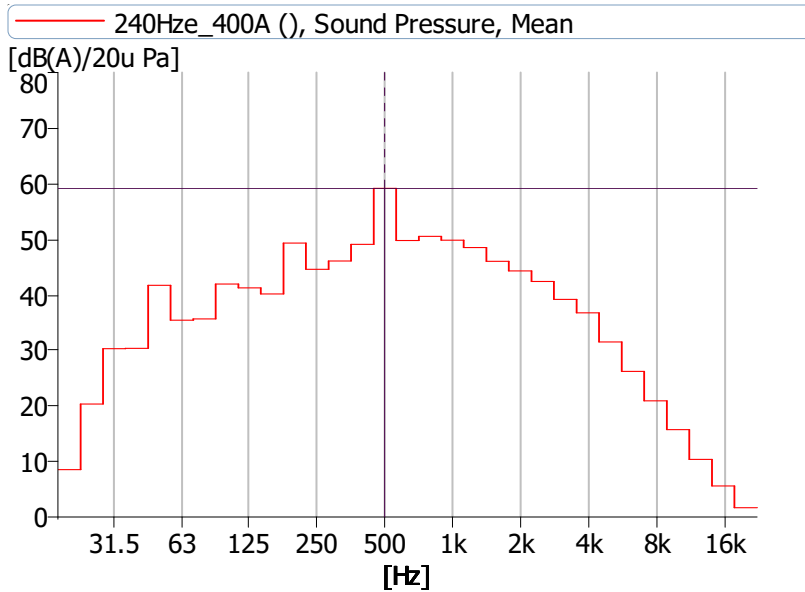
Appendix B CPB Analysis Results



B 1– CPB analysis for 180 Hz electrical excitation frequency at 400 A for prototype reactor 1.



B 2 – CPB analysis for 210 Hz electrical excitation frequency at 400 A for prototype reactor 1.



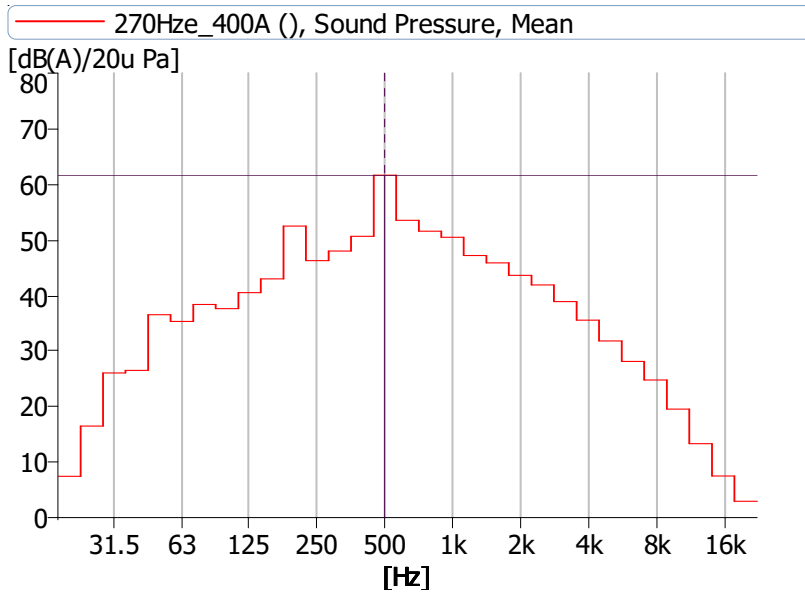
Cursor values

X: 500.000 Hz
 Y: 59.157 dB(A)/20u Pa
 Z:

Values

Total: 62.042 dB(A)/20u Pa

B 3 – CPB analysis for 240 Hz electrical excitation frequency at 400 A for prototype reactor 1.



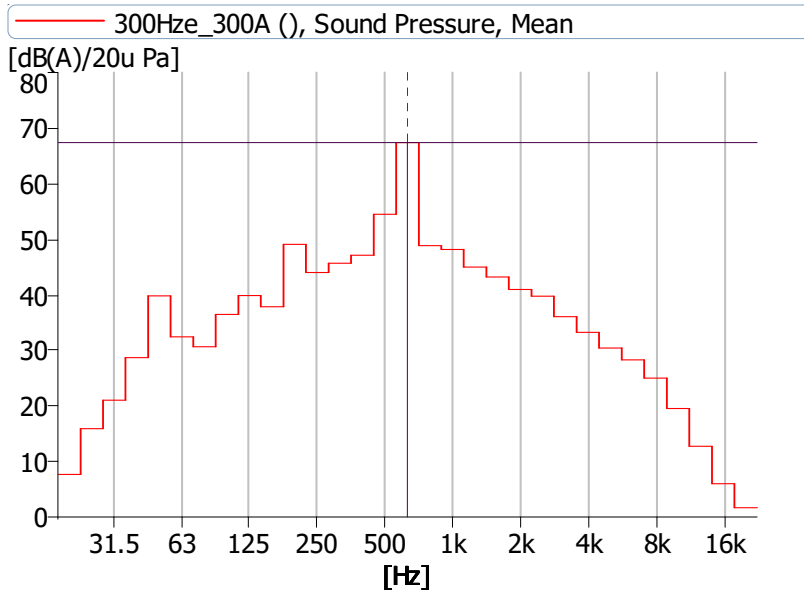
Cursor values

X: 500.000 Hz
 Y: 61.654 dB(A)/20u Pa
 Z:

Values

Total: 64.049 dB(A)/20u Pa

B 4 – CPB analysis for 270 Hz electrical excitation frequency at 400 A for prototype reactor 1.



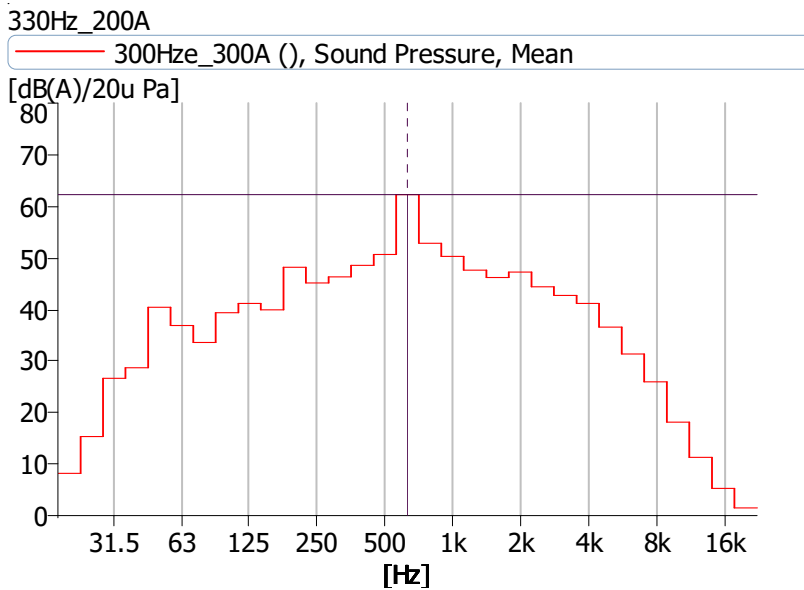
Cursor values

X: 630.000 Hz
 Y: 67.414 dB(A)/20u Pa
 Z:

Values

Total: 67.958 dB(A)/20u Pa

B 5 – CPB analysis for 300 Hz electrical excitation frequency at 300 A for prototype reactor 1.



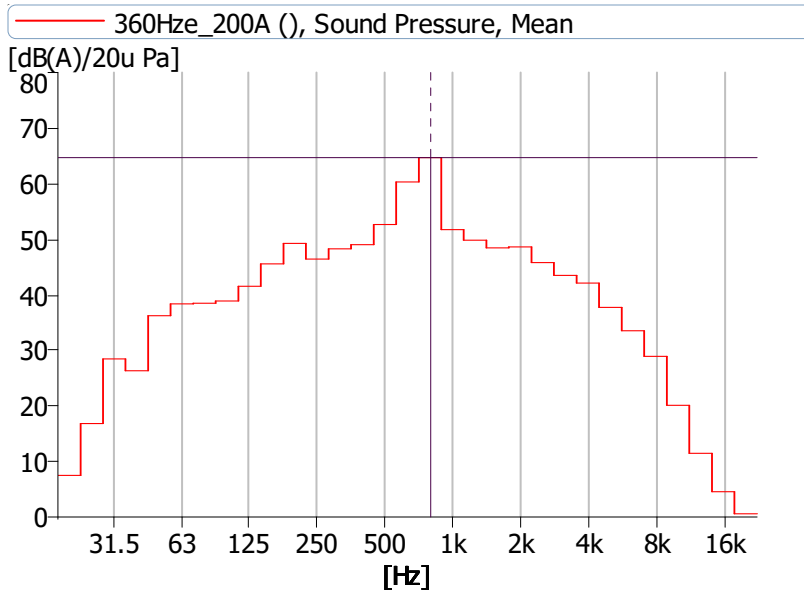
Cursor values

X: 630.000 Hz
 Y: 62.274 dB(A)/20u Pa
 Z:

Values

Total: 64.122 dB(A)/20u Pa

B 6 – CPB analysis for 330 Hz electrical excitation frequency at 200 A for prototype reactor 1.



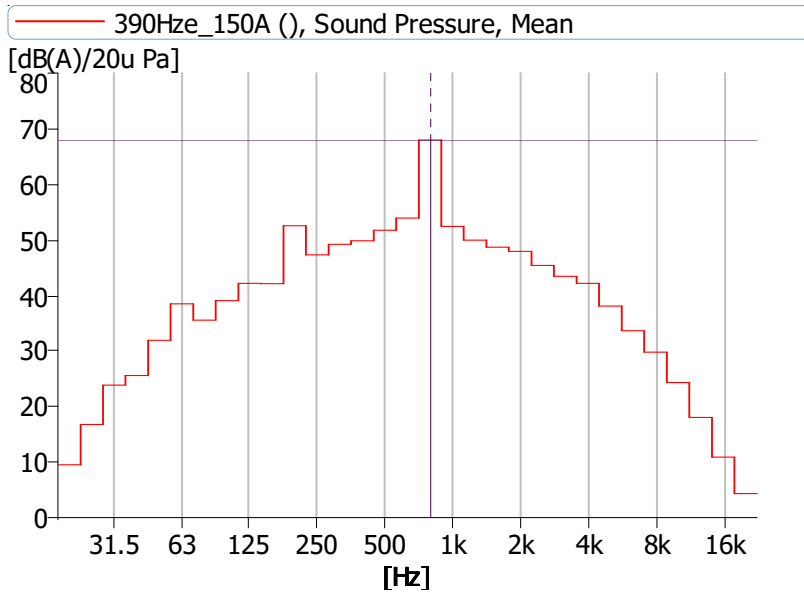
Cursor values

X: 800.000 Hz
 Y: 64.712 dB(A)/20u Pa
 Z:

Values

Total: 67.032 dB(A)/20u Pa

B 7 – CPB analysis for 360 Hz electrical excitation frequency at 200 A for prototype reactor 1.



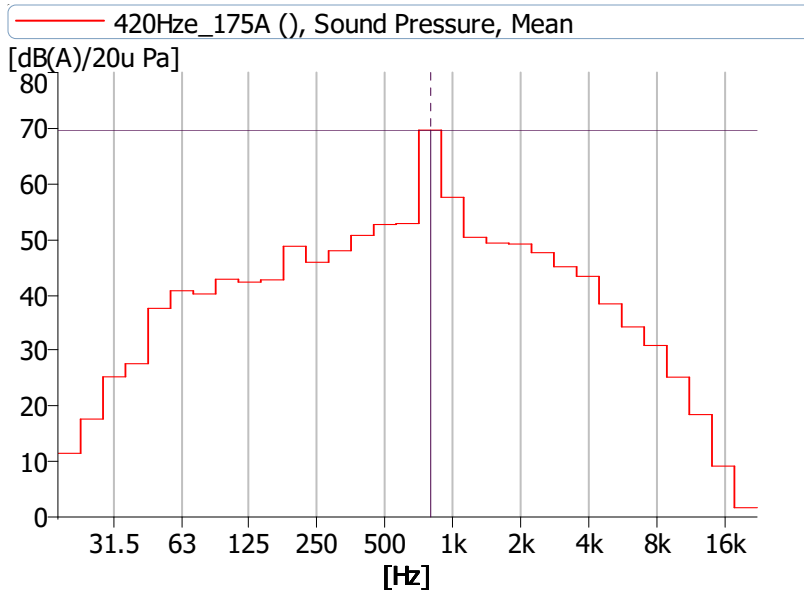
Cursor values

X: 800.000 Hz
 Y: 67.989 dB(A)/20u Pa
 Z:

Values

Total: 68.837 dB(A)/20u Pa

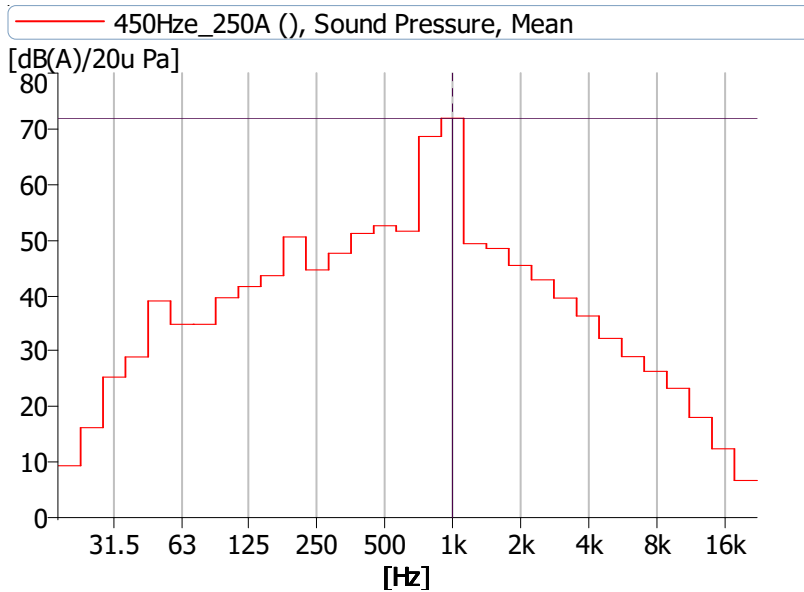
B 8 – CPB analysis for 390 Hz electrical excitation frequency at 150 A for prototype reactor 1.



Cursor values
 X: 800.000 Hz
 Y: 69.629 dB(A)/20u Pa
 Z:

Values
 Total: 70.377 dB(A)/20u Pa

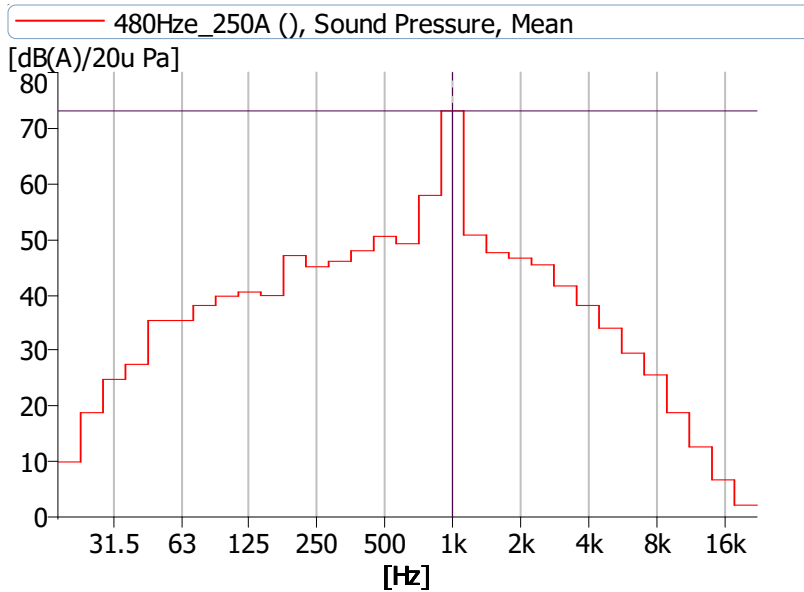
B 9 – CPB analysis for 420 Hz electrical excitation frequency at 175 A for prototype reactor 1.



Cursor values
 X: 1.000k Hz
 Y: 71.880 dB(A)/20u Pa
 Z:

Values
 Total: 73.738 dB(A)/20u Pa

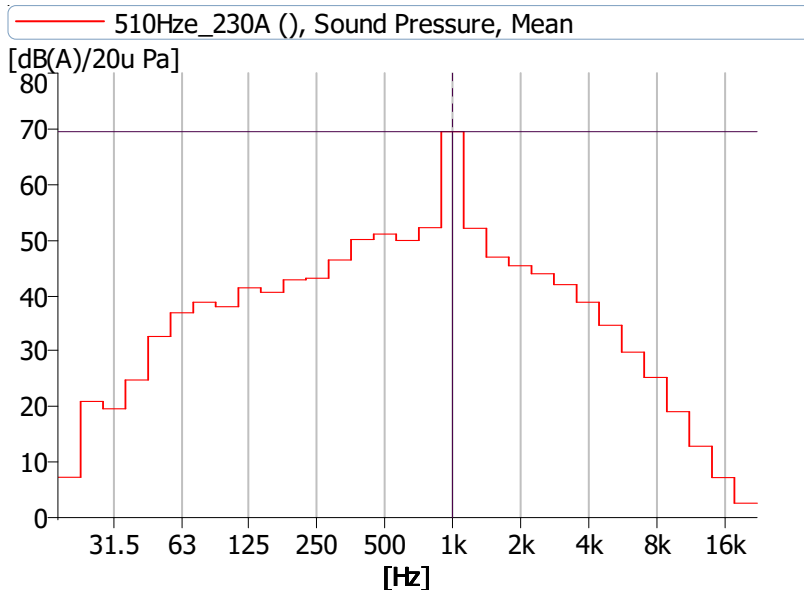
B 10 – CPB analysis for 450 Hz electrical excitation frequency at 250 A for prototype reactor 1.



Cursor values
 X: 1.000k Hz
 Y: 73.128 dB(A)/20u Pa
 Z:

Values
 Total: 73.400 dB(A)/20u Pa

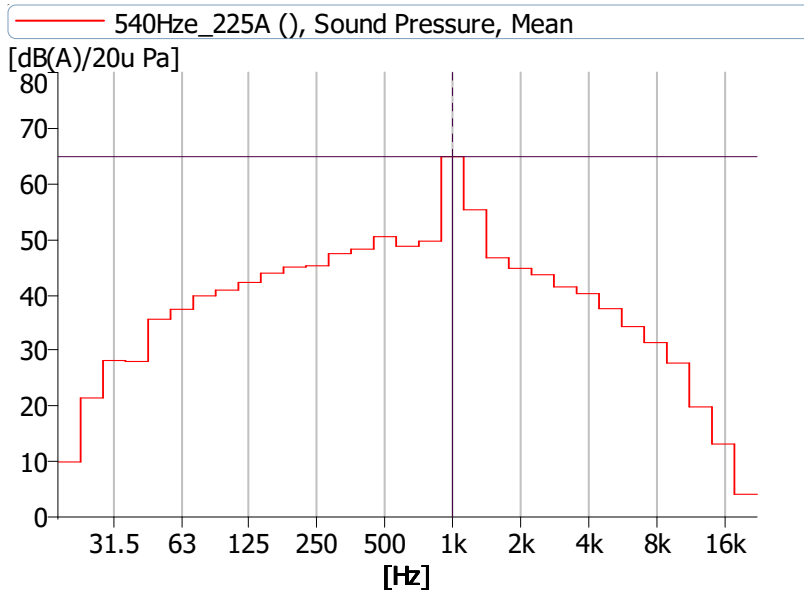
B 11 – CPB analysis for 480 Hz electrical excitation frequency at 250 A for prototype reactor 1.



Cursor values
 X: 1.000k Hz
 Y: 69.500 dB(A)/20u Pa
 Z:

Values
 Total: 69.927 dB(A)/20u Pa

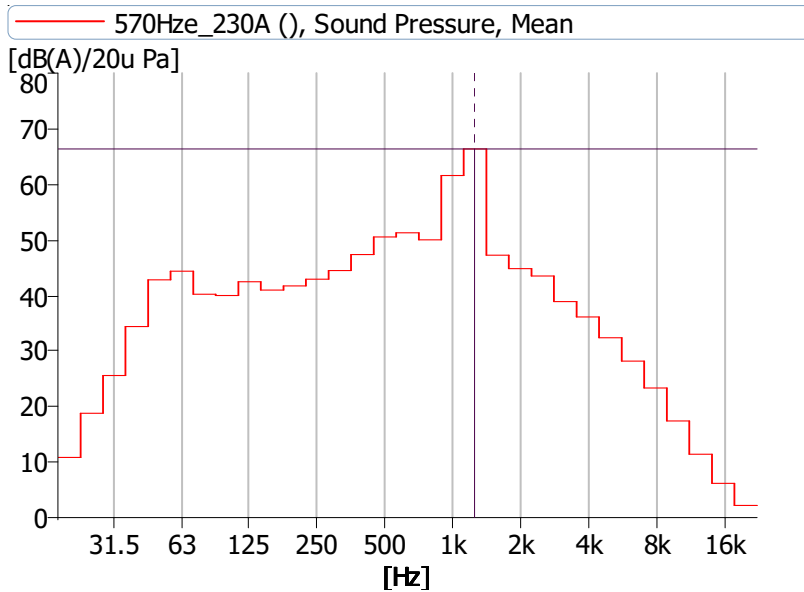
B 12 – CPB analysis for 510 Hz electrical excitation frequency at 230 A for prototype reactor 1.



Cursor values
 X: 1.000k Hz
 Y: 64.857 dB(A)/20u Pa
 Z:

Values
 Total: 66.101 dB(A)/20u Pa

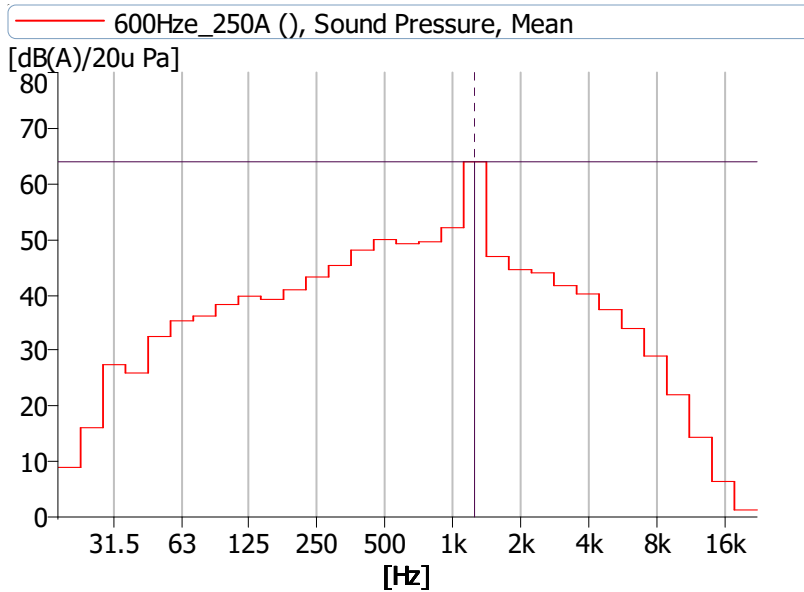
B 13 – CPB analysis for 540 Hz electrical excitation frequency at 225 A for prototype reactor 1.



Cursor values
 X: 1.250k Hz
 Y: 66.355 dB(A)/20u Pa
 Z:

Values
 Total: 68.094 dB(A)/20u Pa

B 14 – CPB analysis for 570 Hz electrical excitation frequency at 230 A for prototype reactor 1.



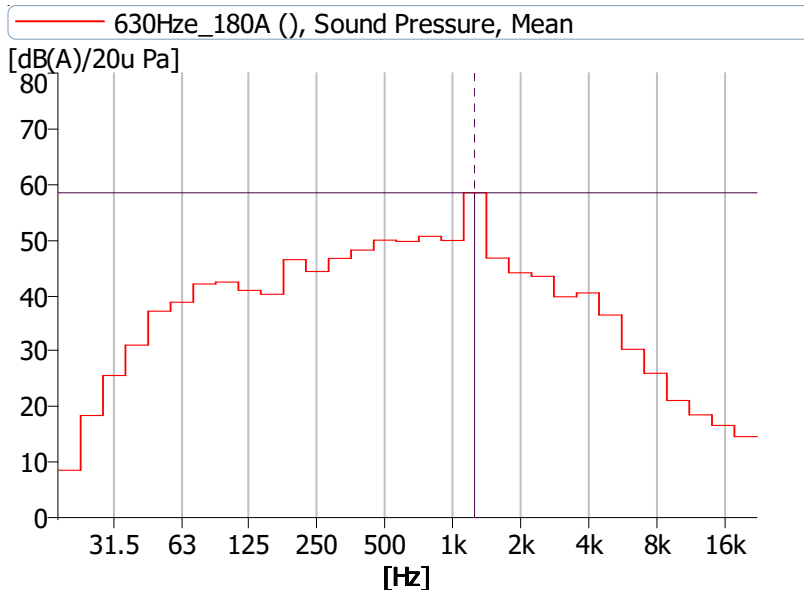
Cursor values

X: 1.250k Hz
 Y: 63.957 dB(A)/20u Pa
 Z:

Values

Total: 65.085 dB(A)/20u Pa

B 15 – CPB analysis for 600 Hz electrical excitation frequency at 250 A for prototype reactor 1.



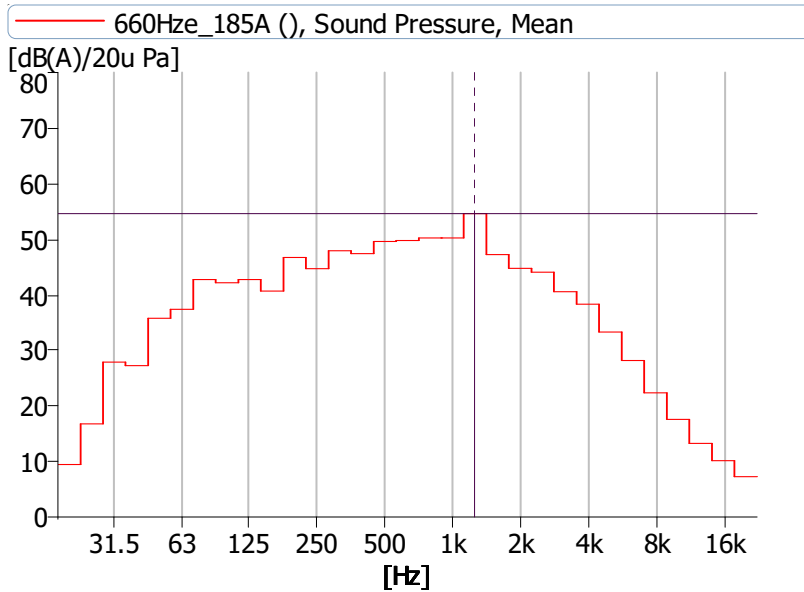
Cursor values

X: 1.250k Hz
 Y: 58.509 dB(A)/20u Pa
 Z:

Values

Total: 61.740 dB(A)/20u Pa

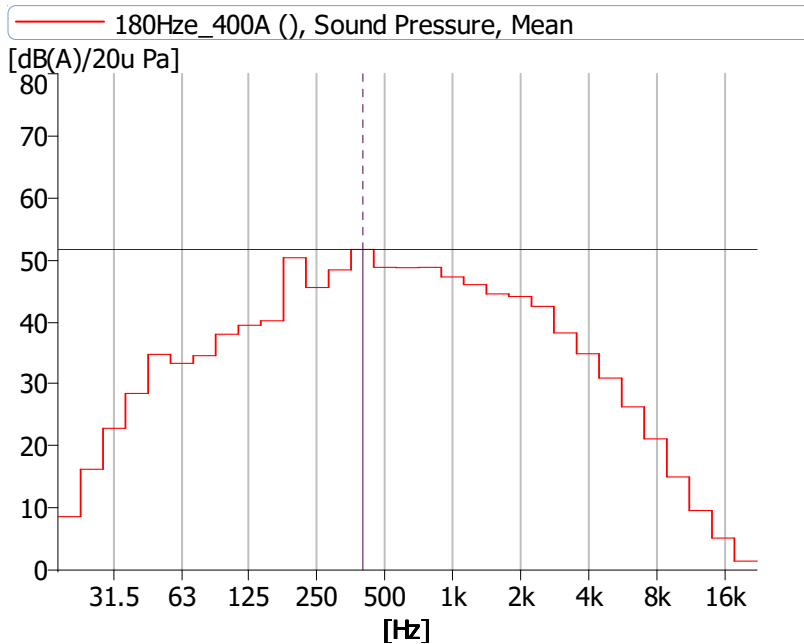
B 16 – CPB analysis for 360 Hz electrical excitation frequency at 180 A for prototype reactor 1.



Cursor values
 X: 1.250k Hz
 Y: 54.640 dB(A)/20u Pa
 Z:

Values
 Total: 60.372 dB(A)/20u Pa

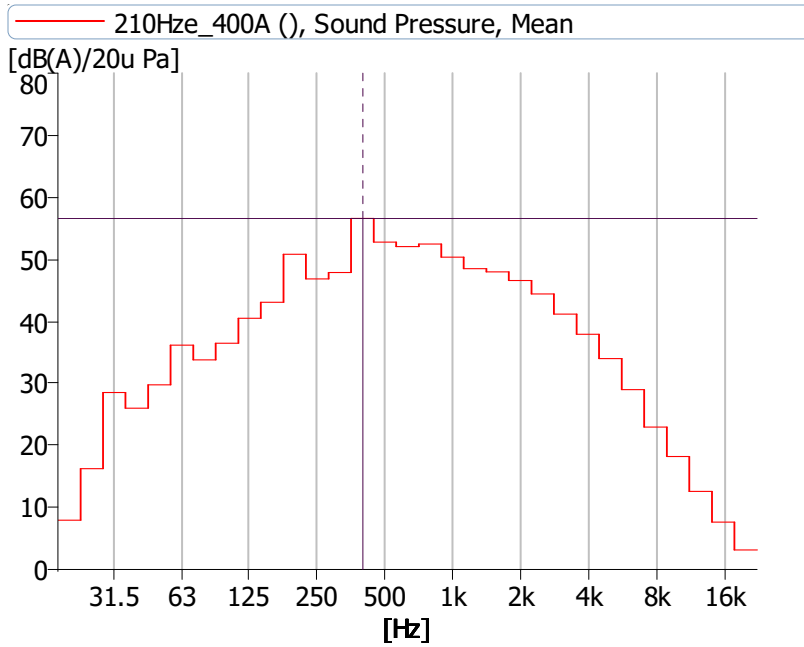
B 17 – CPB analysis for 660 Hz electrical excitation frequency at 185 A for prototype reactor 1.



Cursor values
 X: 400.000 Hz
 Y: 51.656 dB(A)/20u Pa
 Z:

Values
 Total: 59.002 dB(A)/20u Pa

B 18 – CPB analysis for 180 Hz electrical excitation frequency at 400 A for prototype reactor 2.



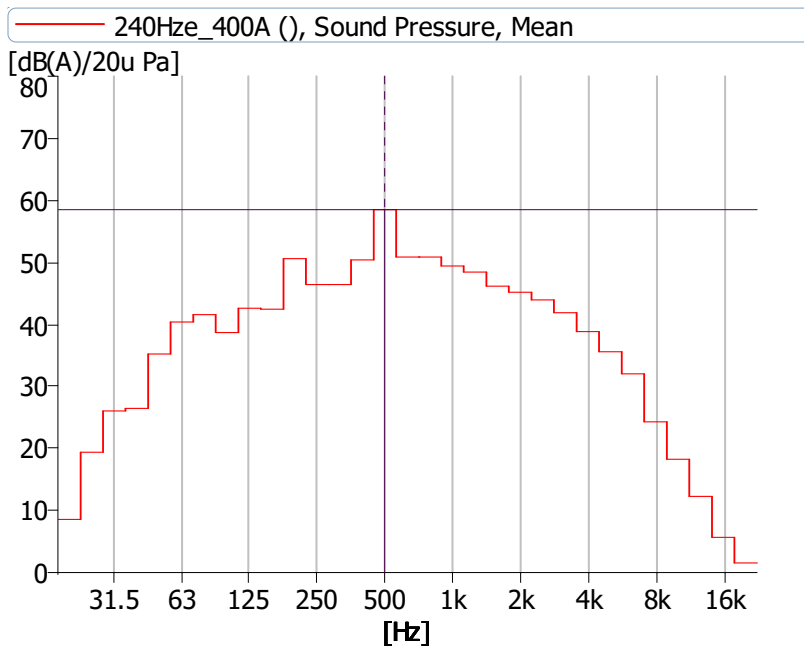
Cursor values

X: 400.000 Hz
 Y: 56.593 dB(A)/20u Pa
 Z:

Values

Total: 62.018 dB(A)/20u Pa

B 19 – CPB analysis for 210 Hz electrical excitation frequency at 400 A for prototype reactor 2.



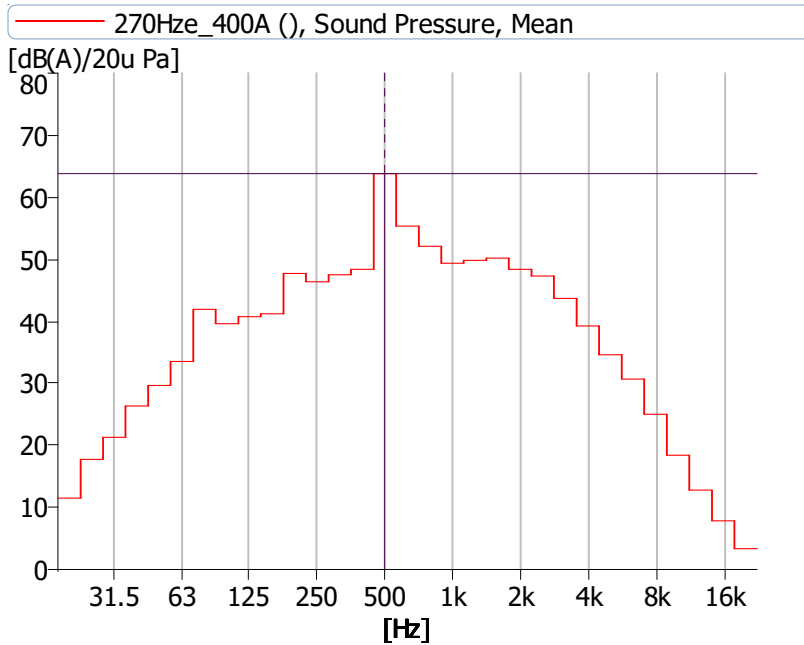
Cursor values

X: 500.000 Hz
 Y: 58.462 dB(A)/20u Pa
 Z:

Values

Total: 62.073 dB(A)/20u Pa

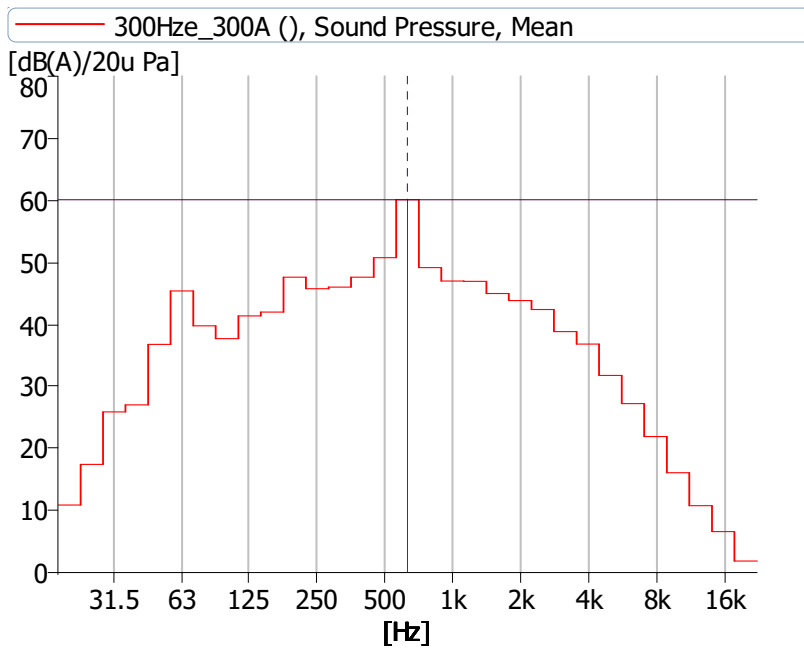
B 20 – CPB analysis for 240 Hz electrical excitation frequency at 400 A for prototype reactor 2.



Cursor values
 X: 500.000 Hz
 Y: 63.793 dB(A)/20u Pa
 Z:

Values
 Total: 65.591 dB(A)/20u Pa

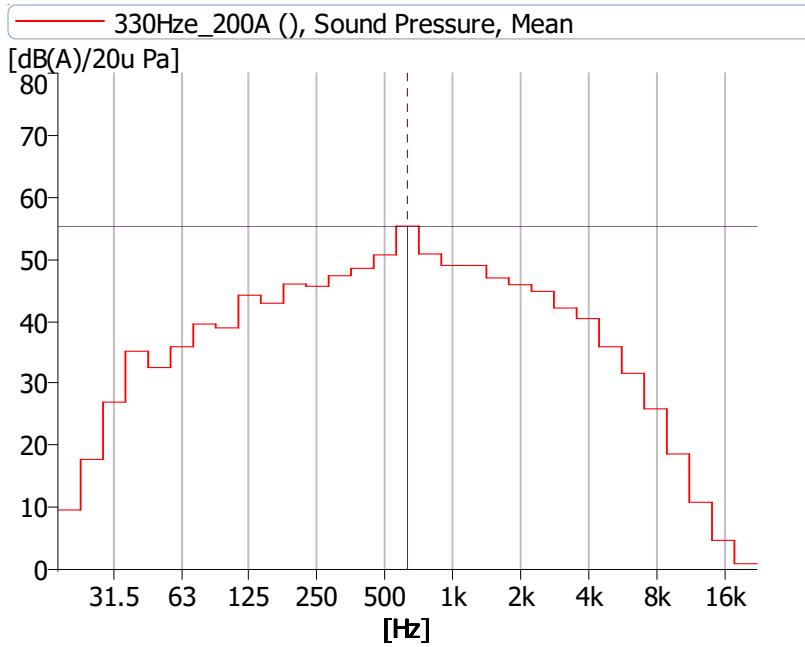
B 21 – CPB analysis for 270 Hz electrical excitation frequency at 400 A for prototype reactor 2.



Cursor values
 X: 630.000 Hz
 Y: 60.073 dB(A)/20u Pa
 Z:

Values
 Total: 62.260 dB(A)/20u Pa

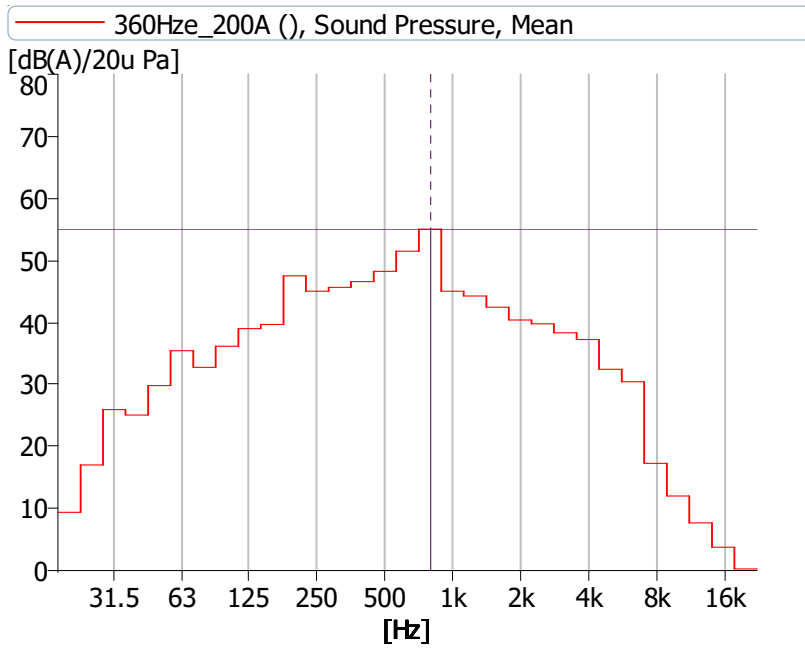
B 22 – CPB analysis for 300 Hz electrical excitation frequency at 300 A for prototype reactor 2.



Cursor values
 X: 630.000 Hz
 Y: 55.322 dB(A)/20u Pa
 Z:

Values
 Total: 60.661 dB(A)/20u Pa

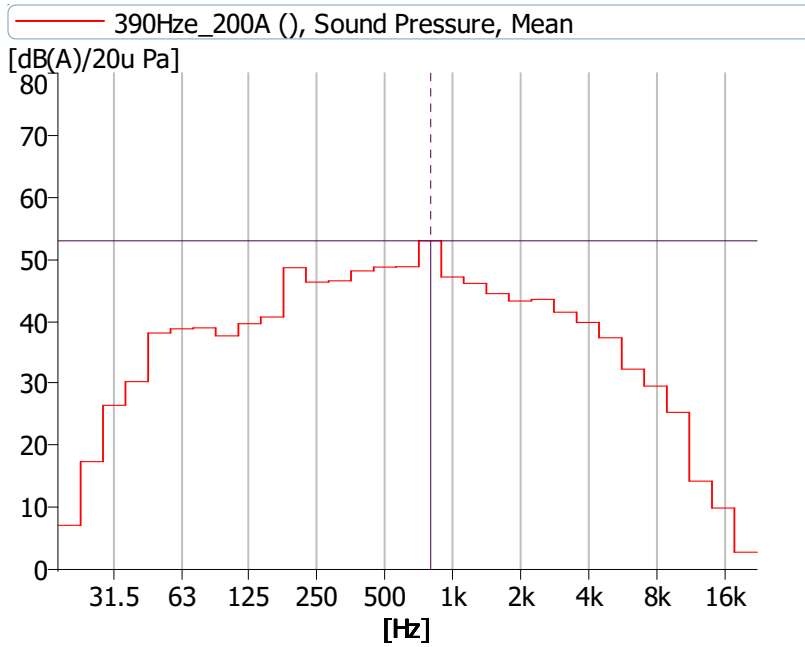
B 23 – CPB analysis for 330 Hz electrical excitation frequency at 200 A for prototype reactor 2.



Cursor values
 X: 800.000 Hz
 Y: 55.041 dB(A)/20u Pa
 Z:

Values
 Total: 59.214 dB(A)/20u Pa

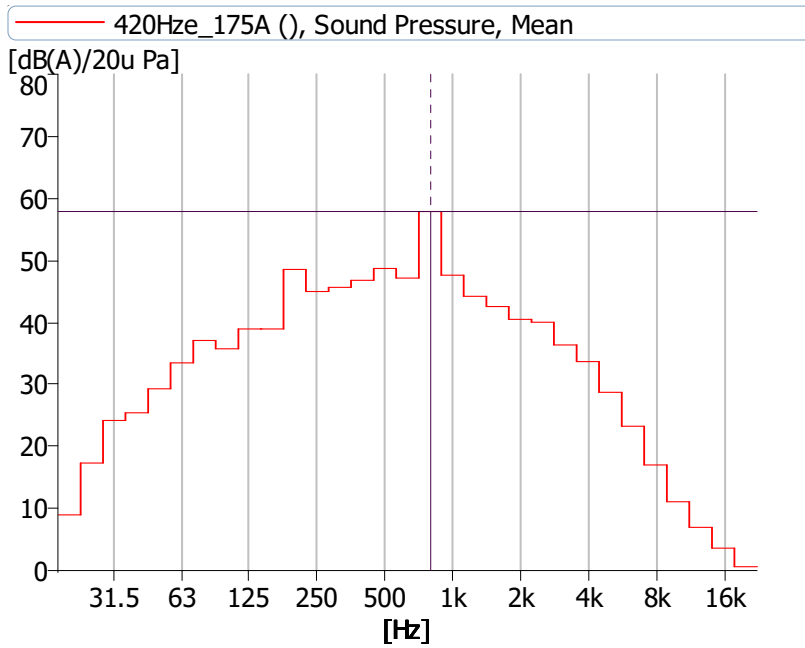
B 24 – CPB analysis for 360 Hz electrical excitation frequency at 200 A for prototype reactor 2.



Cursor values
 X: 800.000 Hz
 Y: 52.956 dB(A)/20u Pa
 Z:

Values
 Total: 59.134 dB(A)/20u Pa

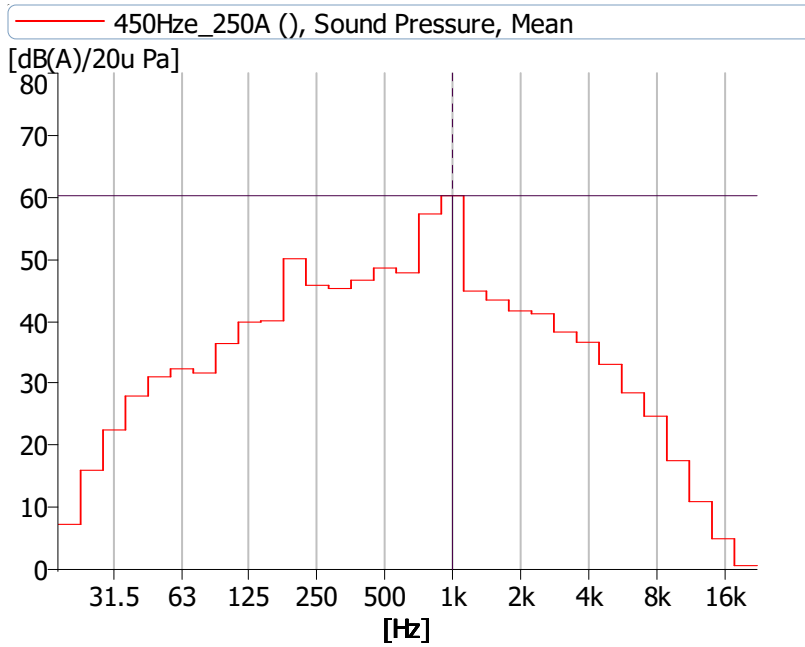
B 25 – CPB analysis for 390 Hz electrical excitation frequency at 200 A for prototype reactor 2.



Cursor values
 X: 800.000 Hz
 Y: 57.852 dB(A)/20u Pa
 Z:

Values
 Total: 60.339 dB(A)/20u Pa

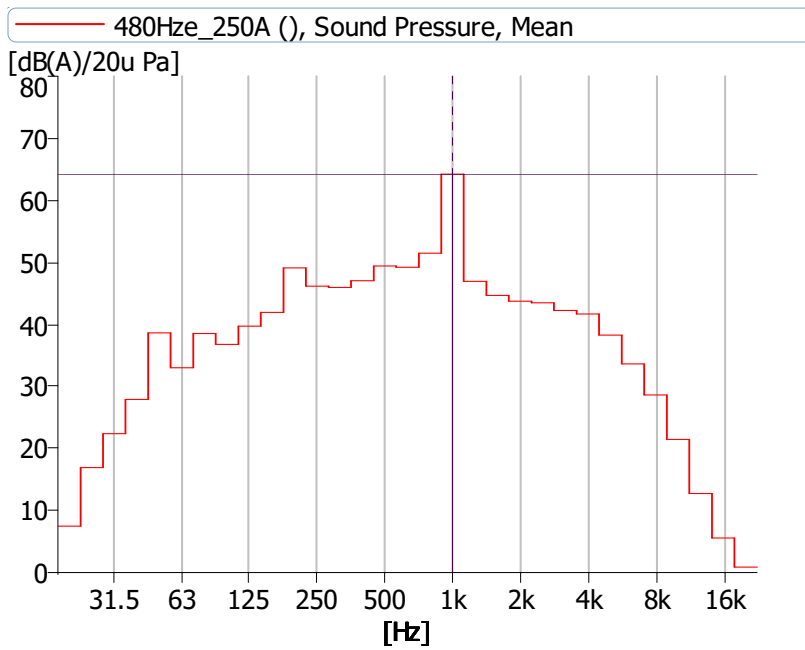
B 26 – CPB analysis for 420 Hz electrical excitation frequency at 175 A for prototype reactor 2.



Cursor values
 X: 1.000k Hz
 Y: 60.229 dB(A)/20u Pa
 Z:

Values
 Total: 63.153 dB(A)/20u Pa

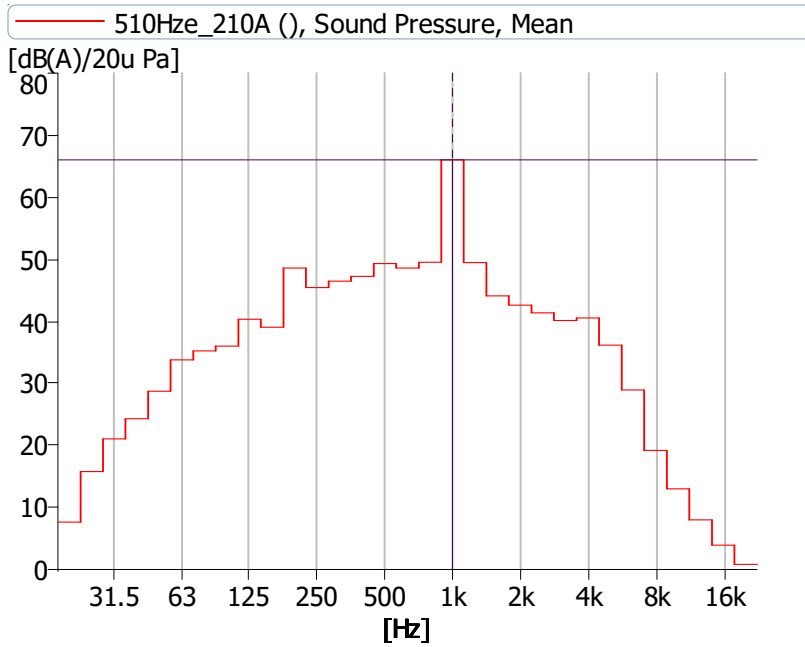
B 27 – CPB analysis for 450 Hz electrical excitation frequency at 250 A for prototype reactor 2.



Cursor values
 X: 1.000k Hz
 Y: 64.190 dB(A)/20u Pa
 Z:

Values
 Total: 65.261 dB(A)/20u Pa

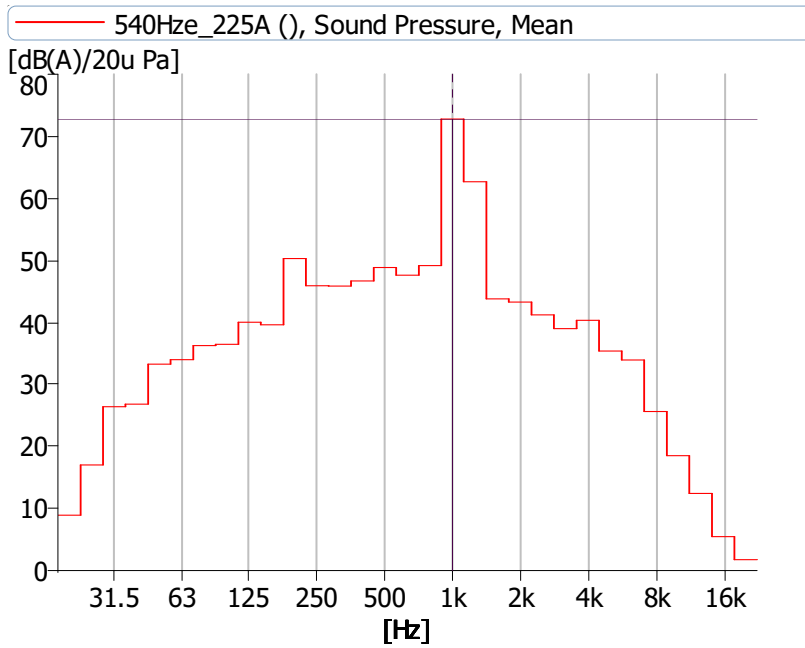
B 28 – CPB analysis for 480 Hz electrical excitation frequency at 250 A for prototype reactor 2.



Cursor values
 X: 1.000k Hz
 Y: 66.037 dB(A)/20u Pa
 Z:

Values
 Total: 66.690 dB(A)/20u Pa

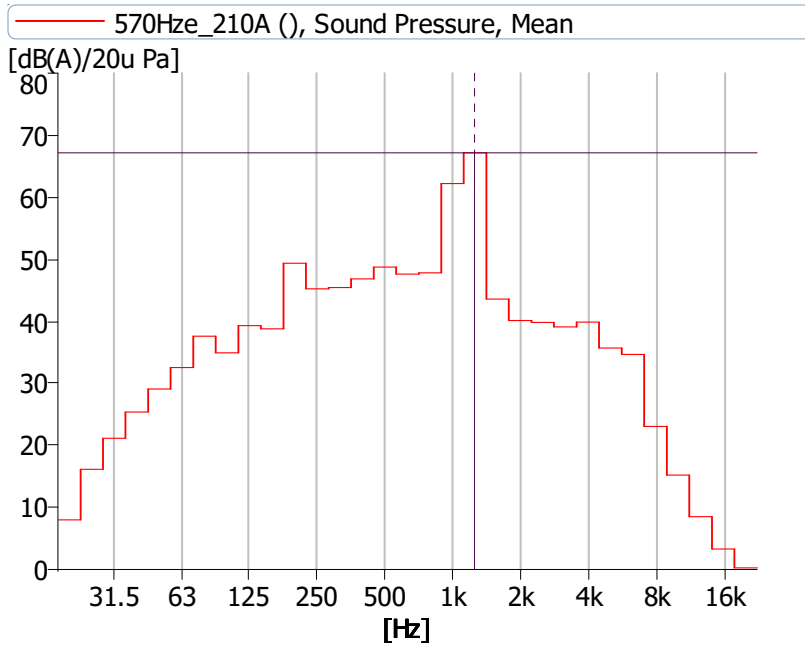
B 29 – CPB analysis for 510 Hz electrical excitation frequency at 210 A for prototype reactor 2.



Cursor values
 X: 1.000k Hz
 Y: 72.786 dB(A)/20u Pa
 Z:

Values
 Total: 73.305 dB(A)/20u Pa

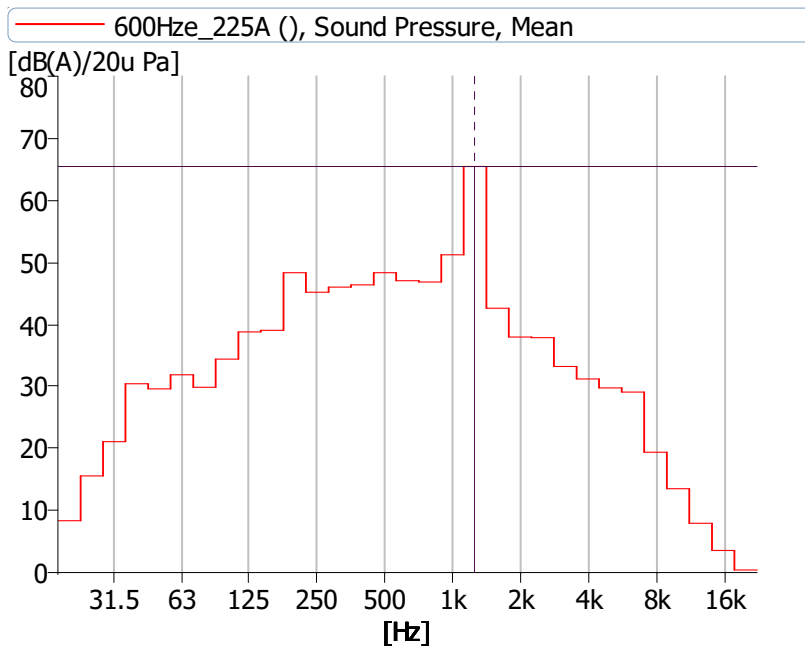
B 30 – CPB analysis for 540 Hz electrical excitation frequency at 225 A for prototype reactor 2.



Cursor values
 X: 1.250k Hz
 Y: 67.164 dB(A)/20u Pa
 Z:

Values
 Total: 68.670 dB(A)/20u Pa

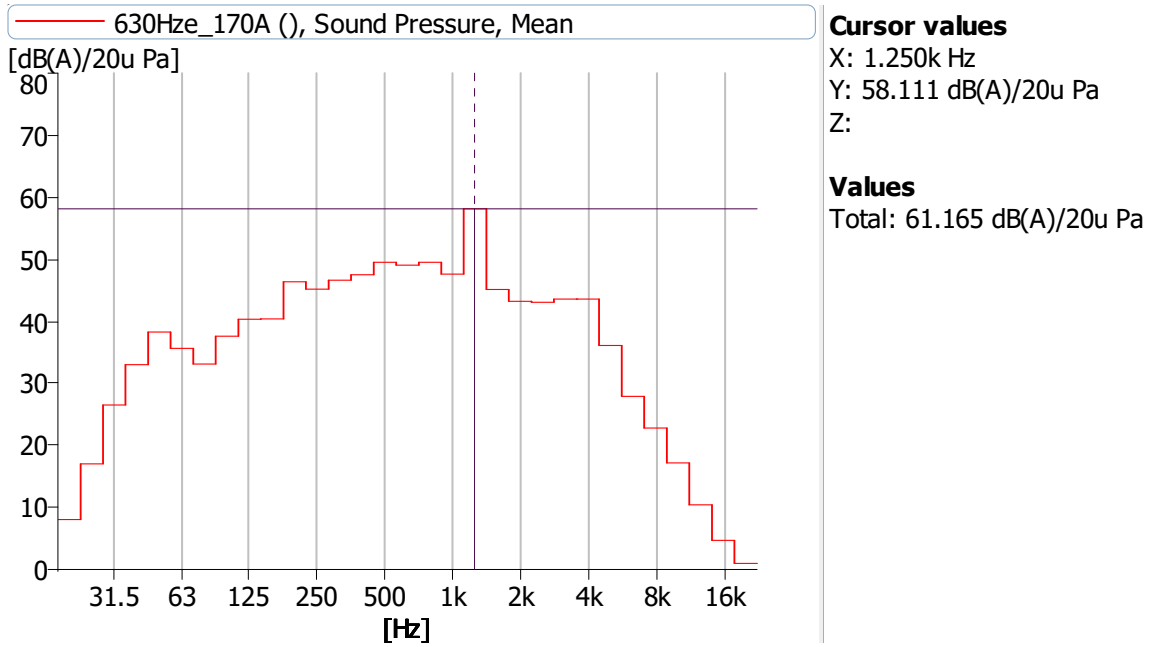
B 31 – CPB analysis for 570 Hz electrical excitation frequency at 210 A for prototype reactor 2.



Cursor values
 X: 1.250k Hz
 Y: 65.438 dB(A)/20u Pa
 Z:

Values
 Total: 66.062 dB(A)/20u Pa

B 32 – CPB analysis for 600 Hz electrical excitation frequency at 225 A for prototype reactor 2.

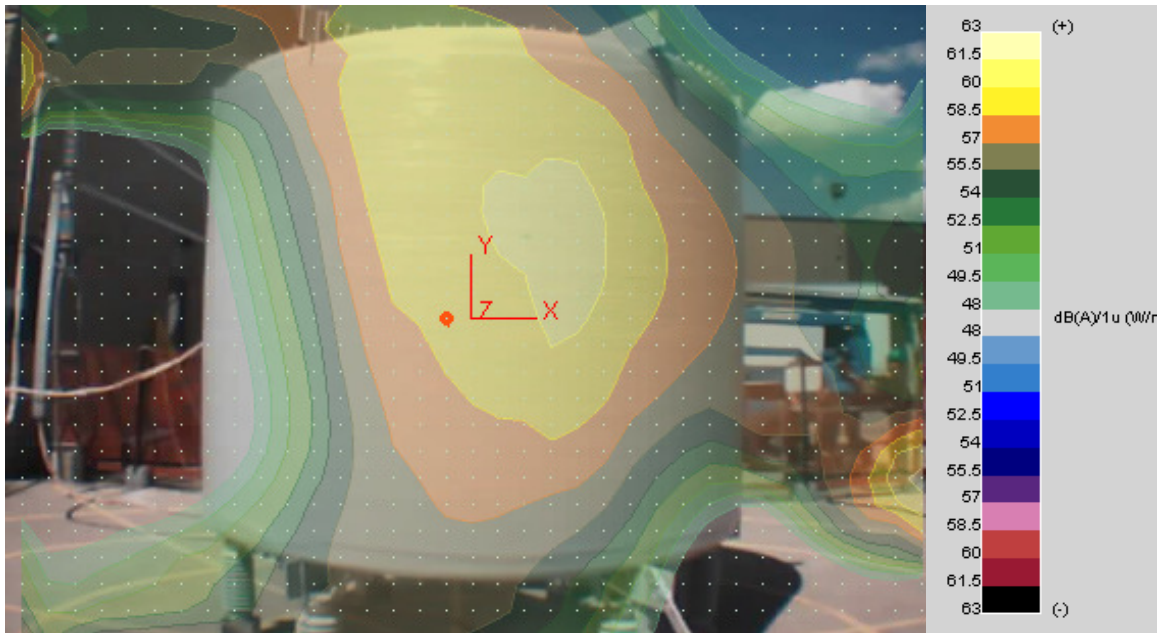


B 33 – CPB analysis for 630 Hz electrical excitation frequency at 170 A for prototype reactor 2.

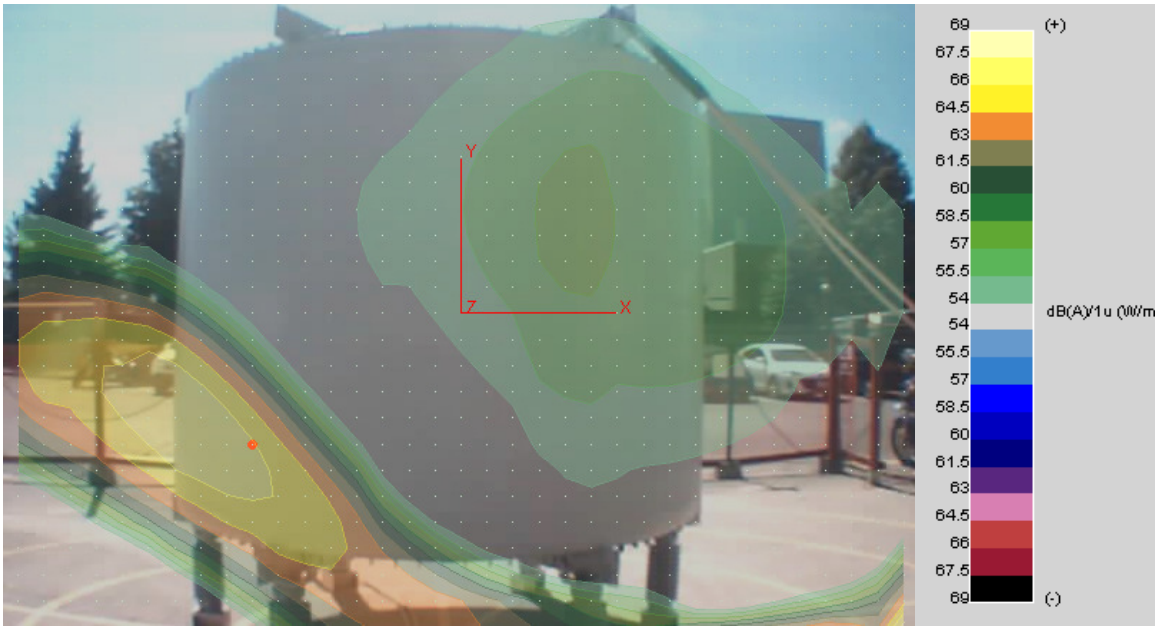
Appendix C Noise Source Identification Results



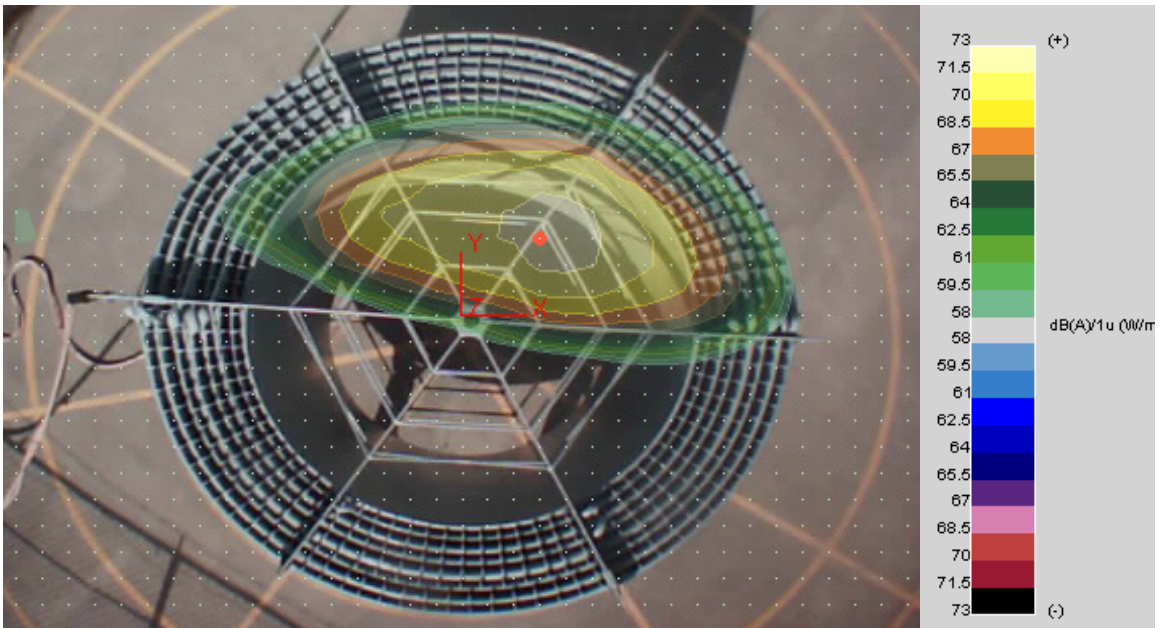
C 1 – 630 Hz NSI contour plot of reactor sound intensity level of reactor 1 energized at 300Hz location 1.



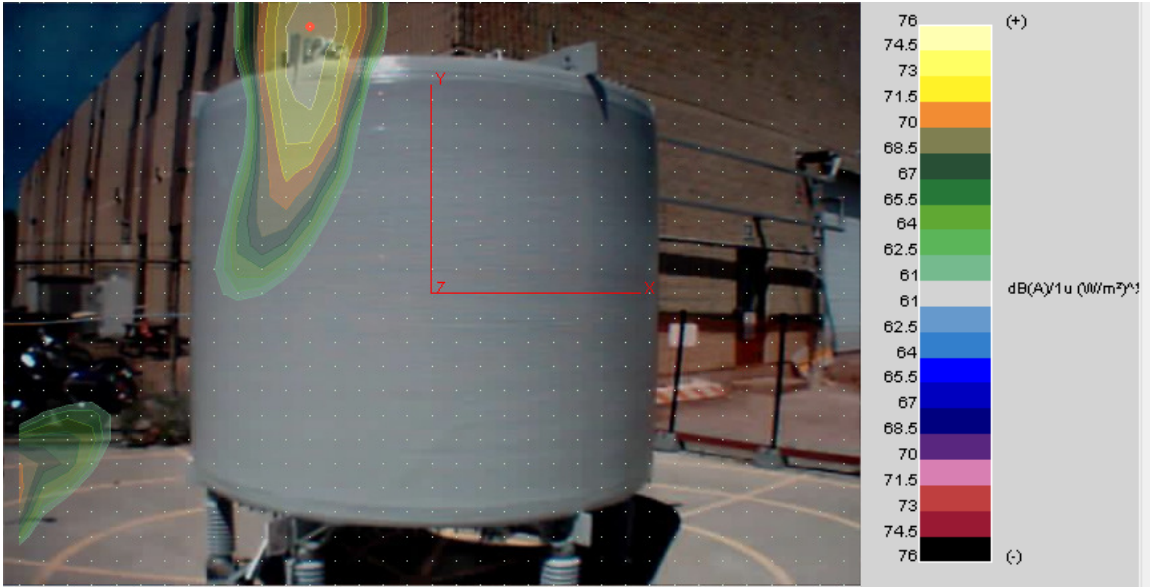
C 2 – 630 Hz NSI contour plot of reactor sound intensity level of reactor 1 energized at 300Hz location 2.



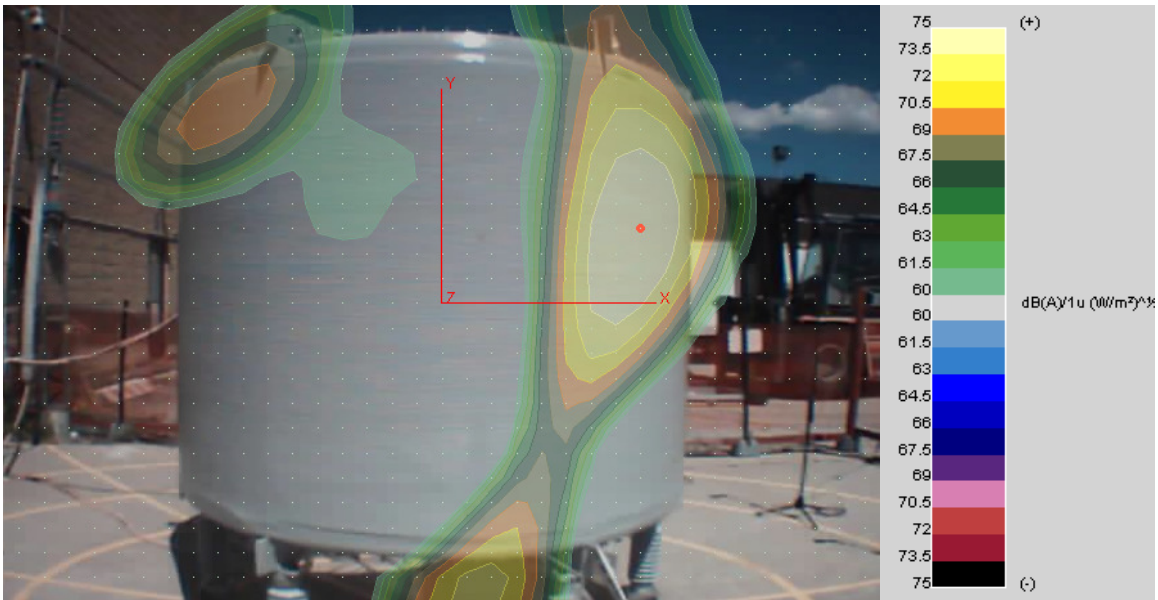
C 3 – 630 Hz NSI contour plot of reactor sound intensity level of reactor 1 energized at 300 Hz location 3.



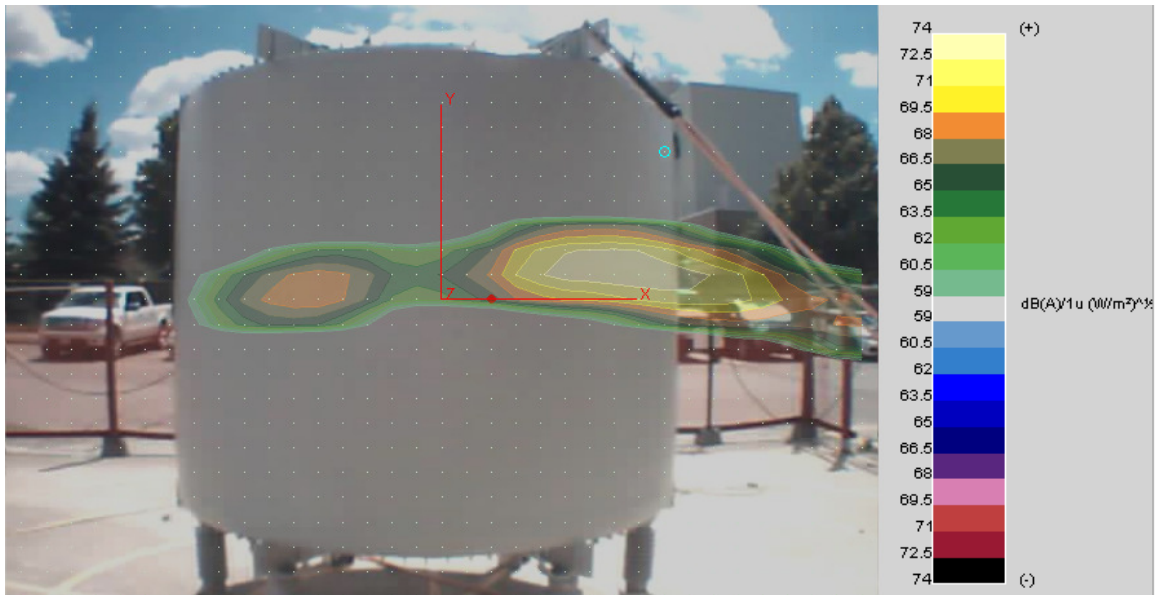
C 4 – 630 Hz NSI contour plot of reactor sound intensity level of reactor 1 energized at 300Hz - aerial view.



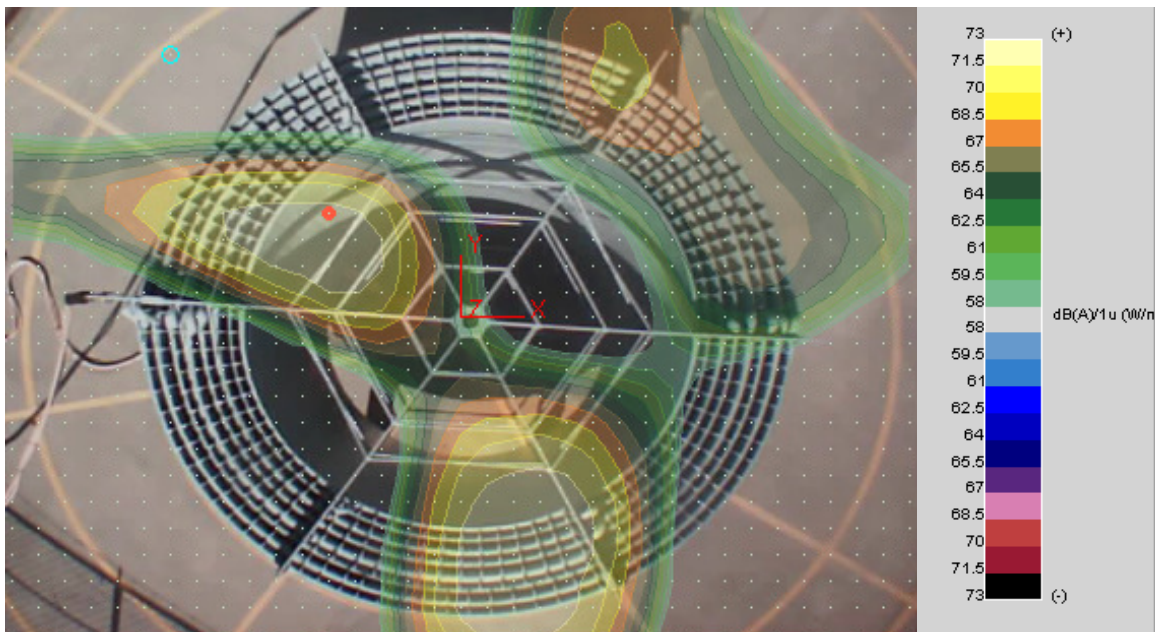
C 5 – 800 Hz NSI contour plot of reactor sound intensity level of reactor 1 energized at 420Hz location 1.



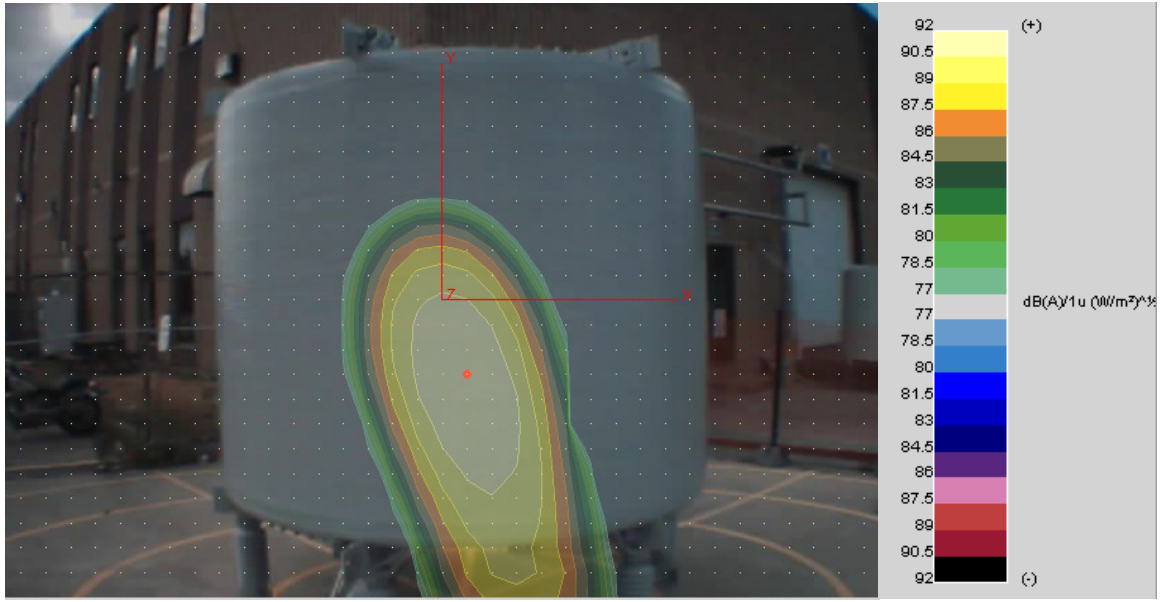
C 6 – 800 Hz NSI contour plot of reactor sound intensity level of reactor energized 1 at 420Hz location 2.



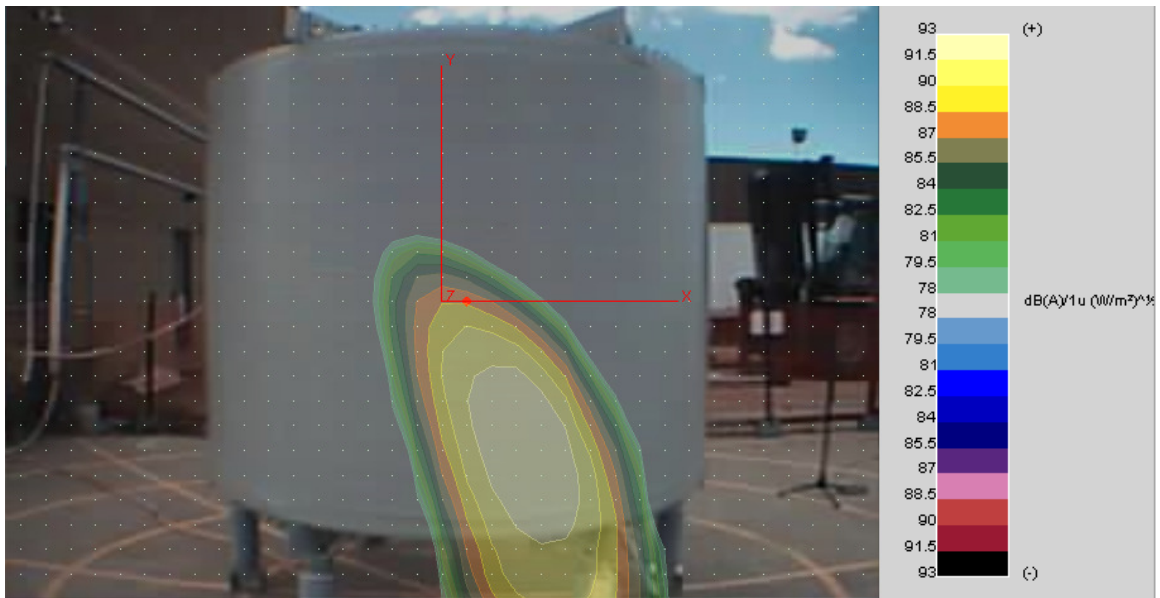
C 7 – 800 Hz NSI contour plot of reactor sound intensity level of reactor energized 1 at 420Hz location 3.



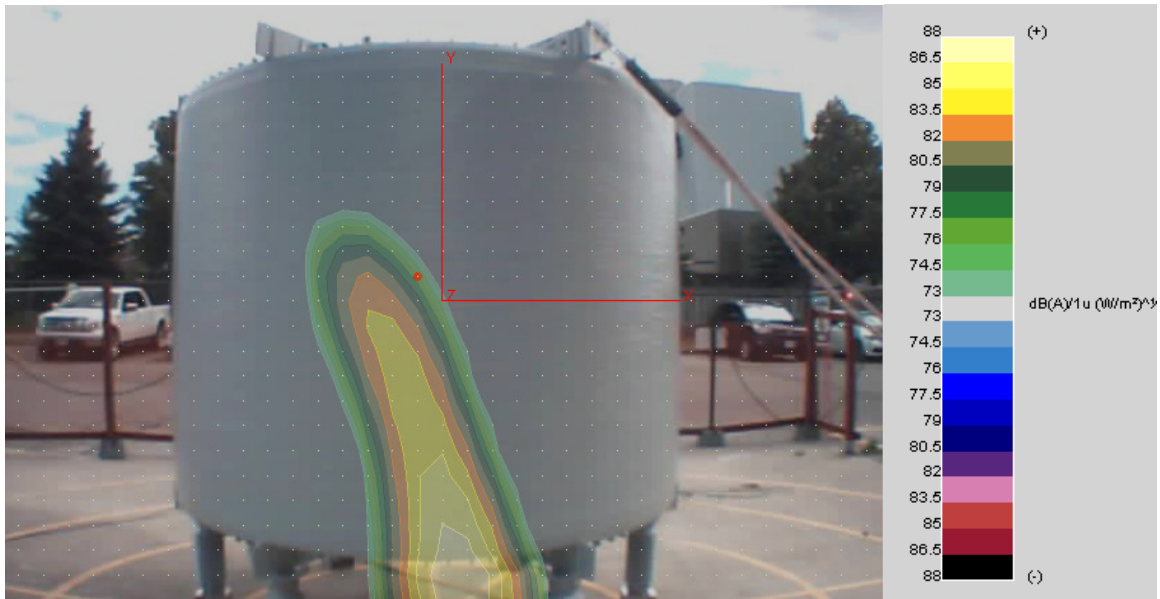
C 8 – 800 Hz NSI contour plot of reactor sound intensity level of reactor energized 1 at 420Hz aerial view.



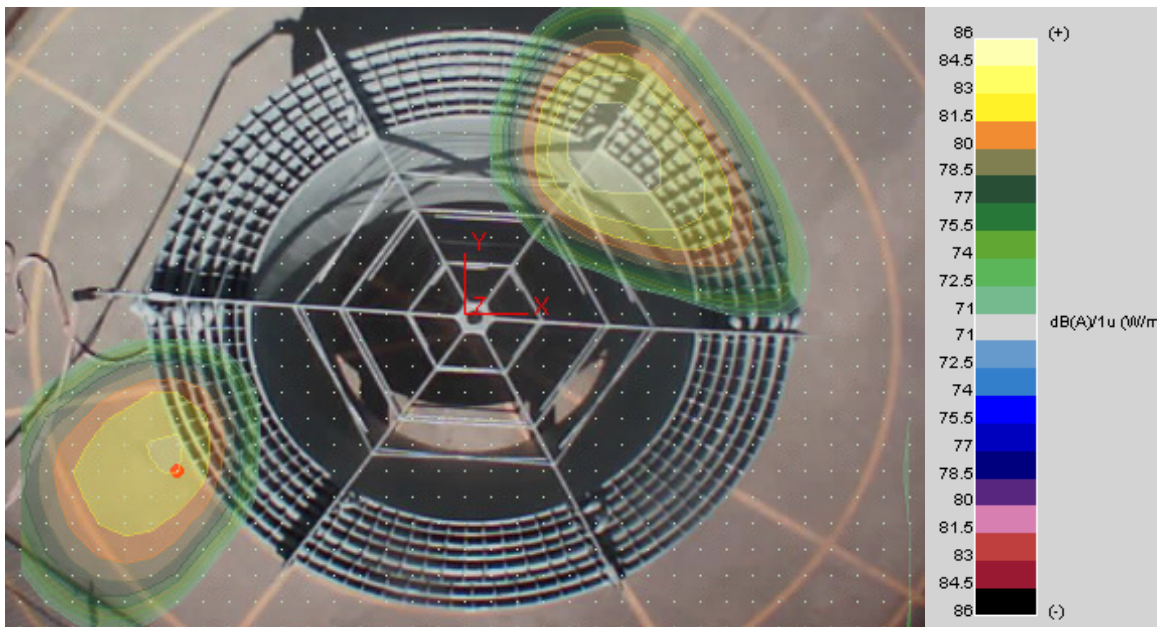
C 9 – 800 Hz NSI contour plot of reactor sound intensity level of reactor 1 energized at 360Hz location 1.



C 10 – 800 Hz NSI contour plot of reactor sound intensity level of reactor 1 energized at 360Hz location 2.

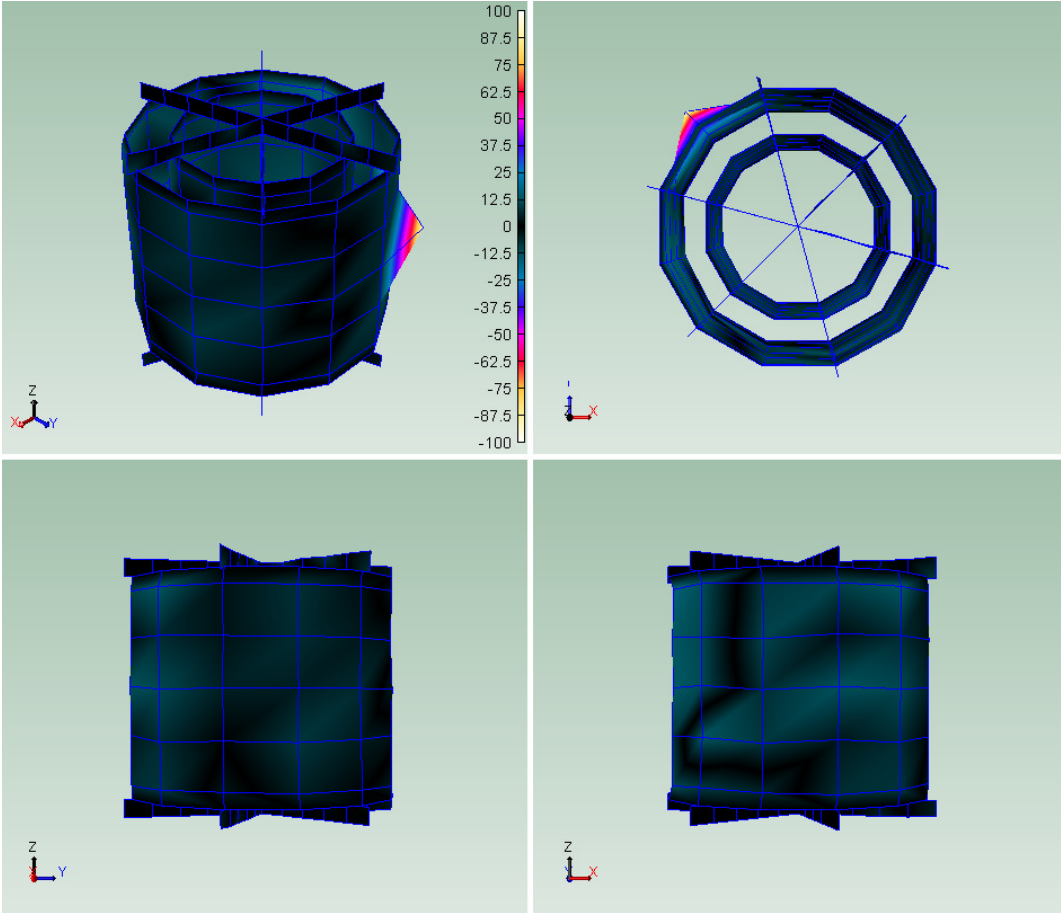


C 11 – 800 Hz contour plot of reactor sound intensity level of reactor 1 energized at 360Hz location 3.

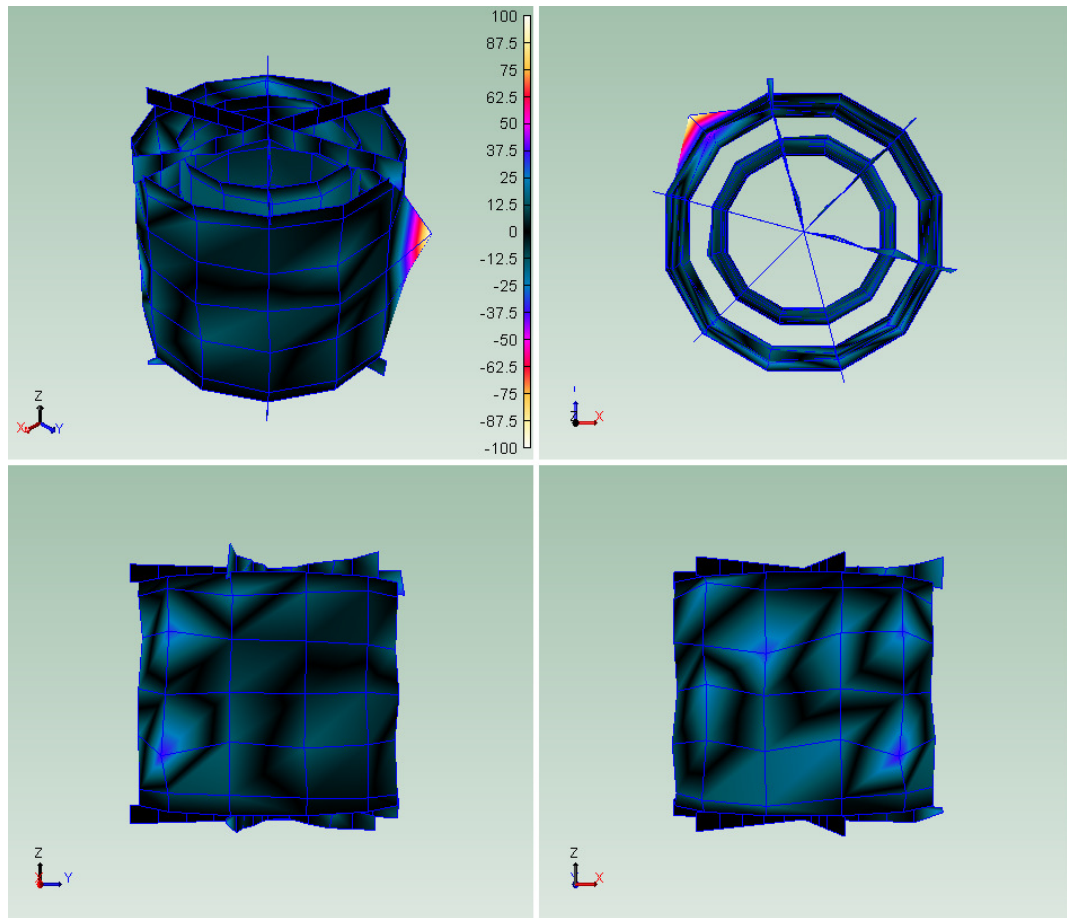


C 12 – 800 Hz NSI contour plot of reactor sound intensity level energized at 360Hz aerial view.

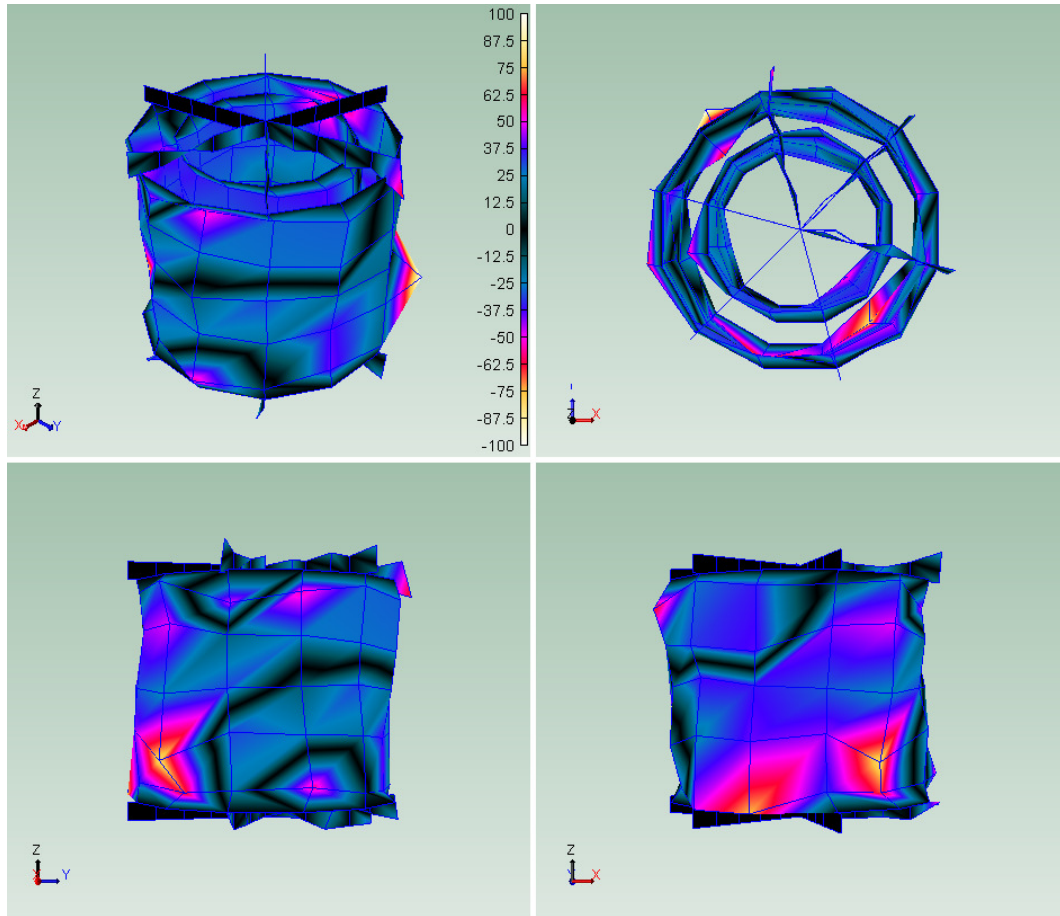
Appendix D Modal Analysis Results



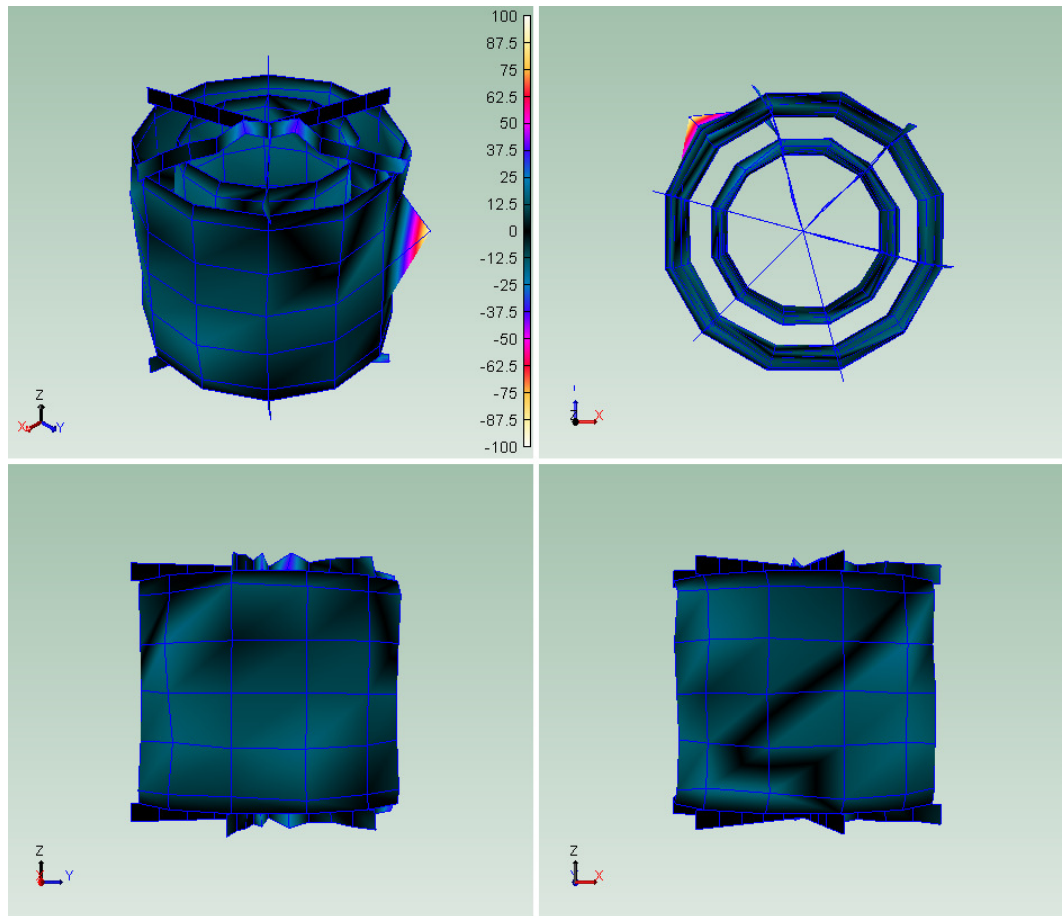
D 1 – Reactor 1 40.7 Hz Structural Mode.



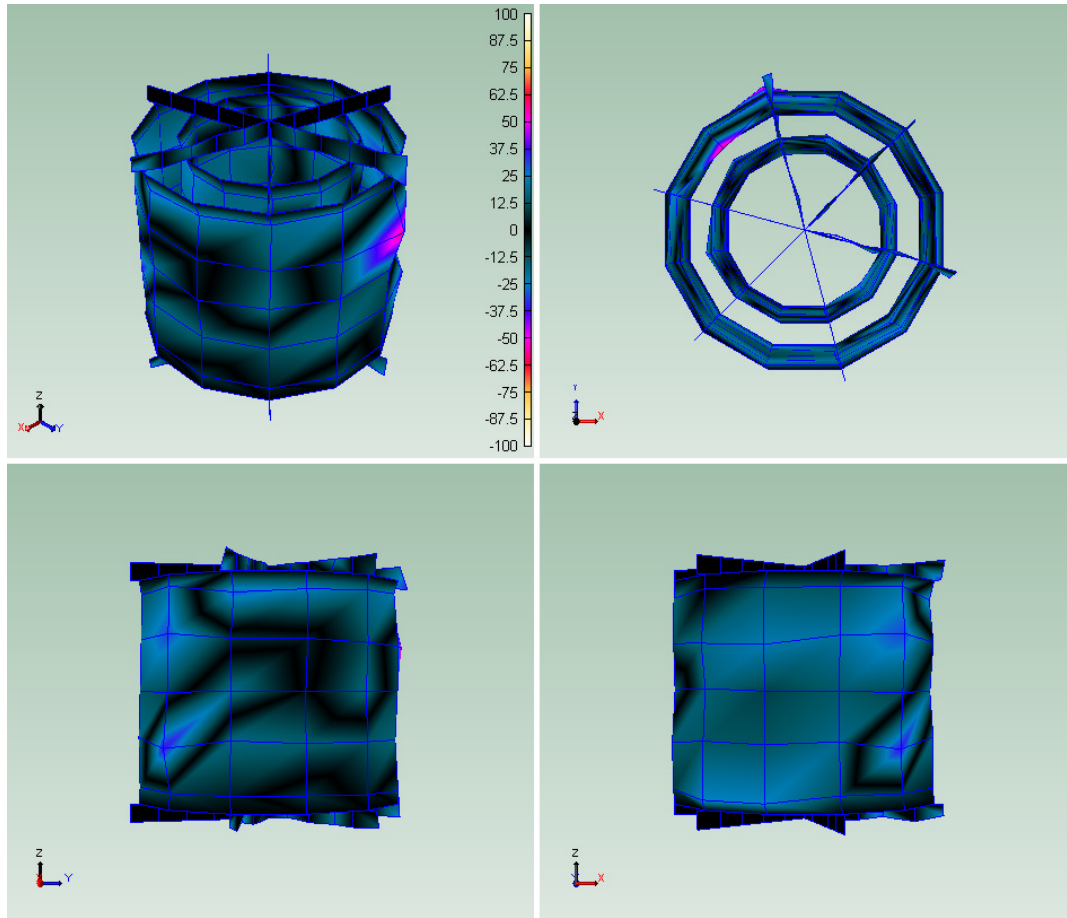
D 2 – Reactor 1 57.4 Hz Structural Mode.



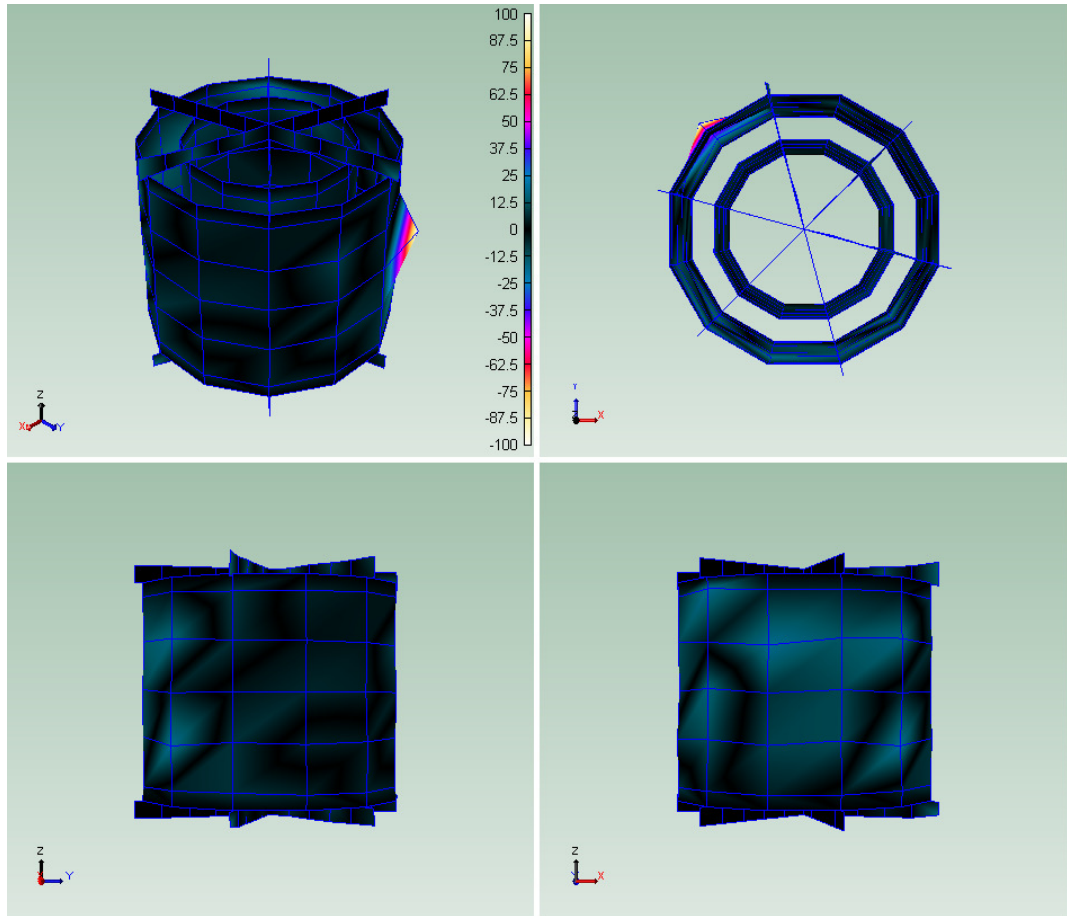
D 3 – Reactor 1 66.7 Hz Structural Mode.



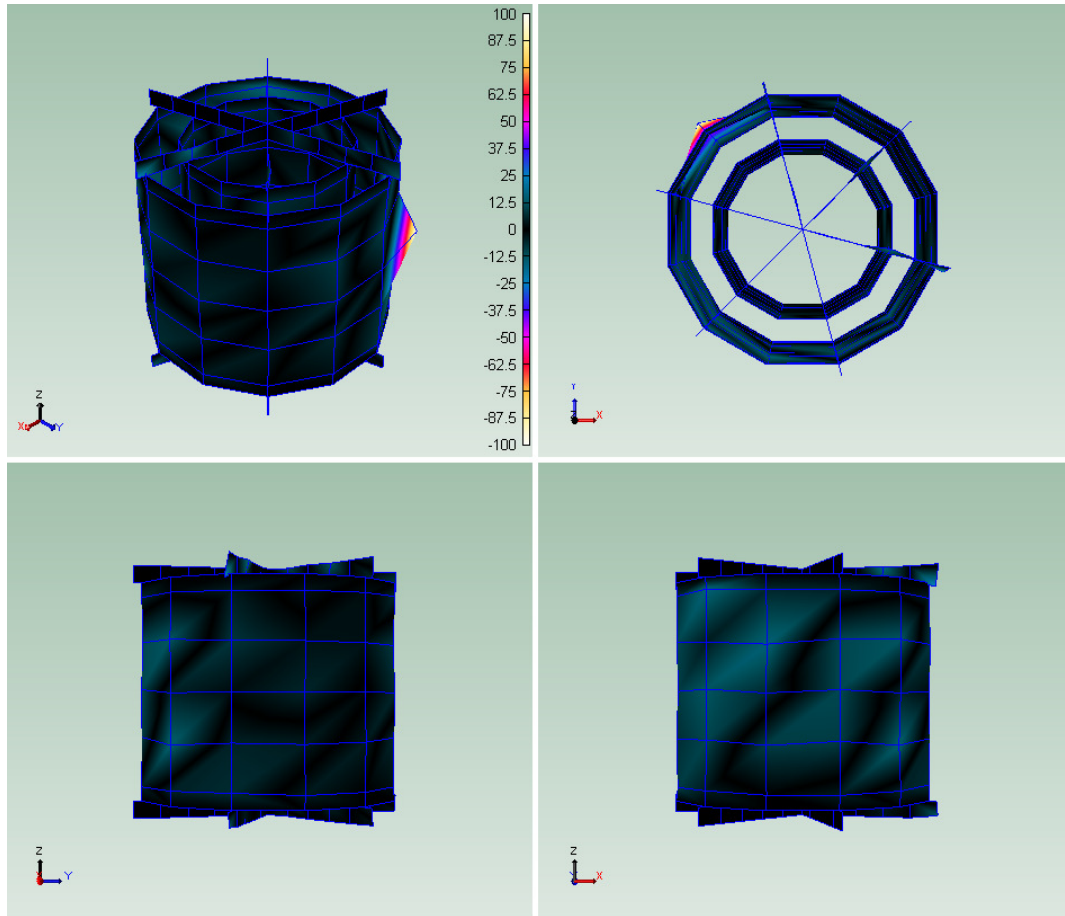
D 4 – Reactor 1 188.0 Hz Structural Mode.



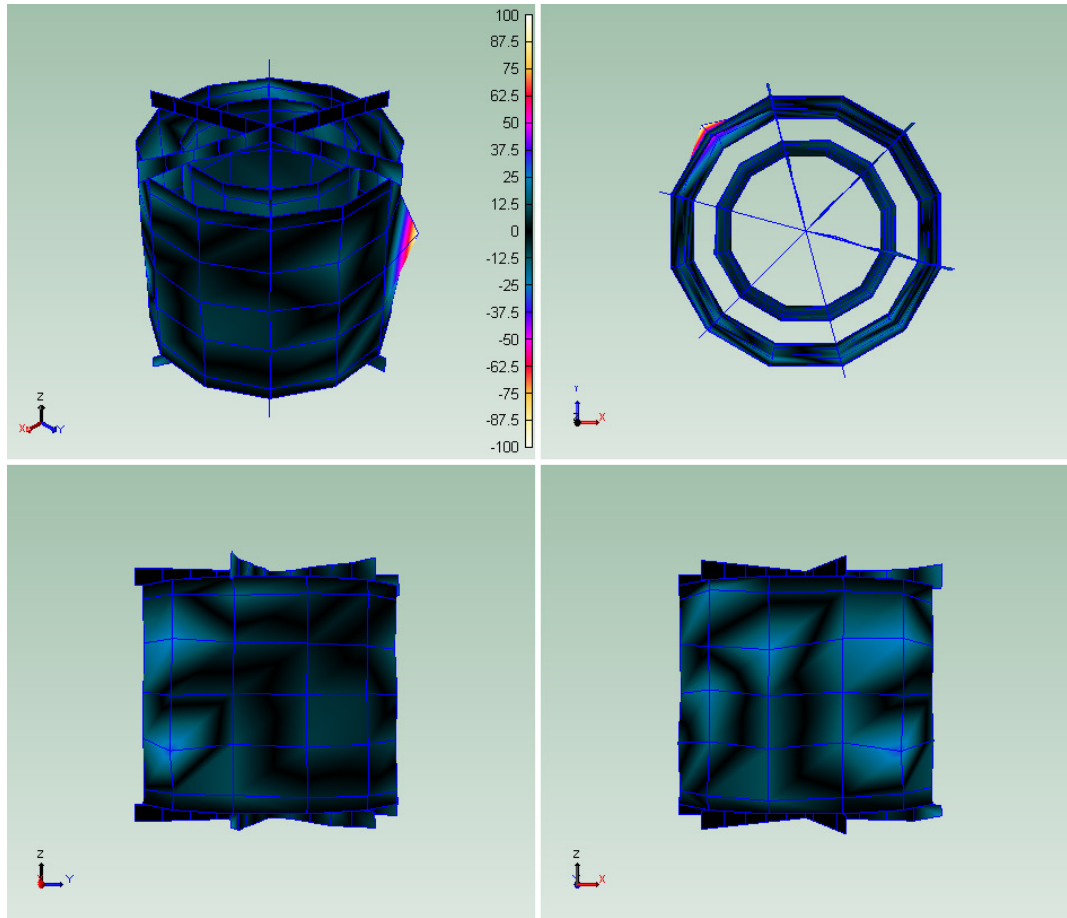
D 5 – Reactor 1 723.2 Hz Structural Mode.



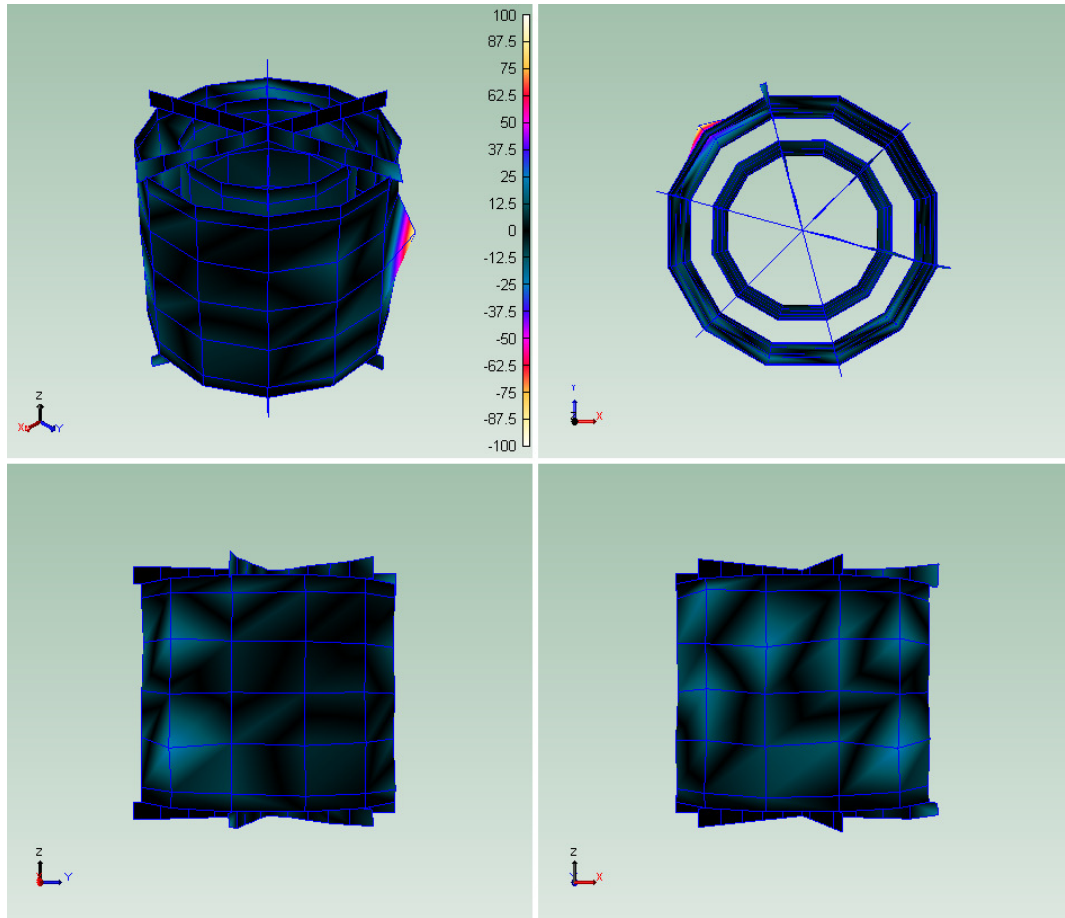
D 6 – Reactor 1 858.1 Hz Structural Mode.



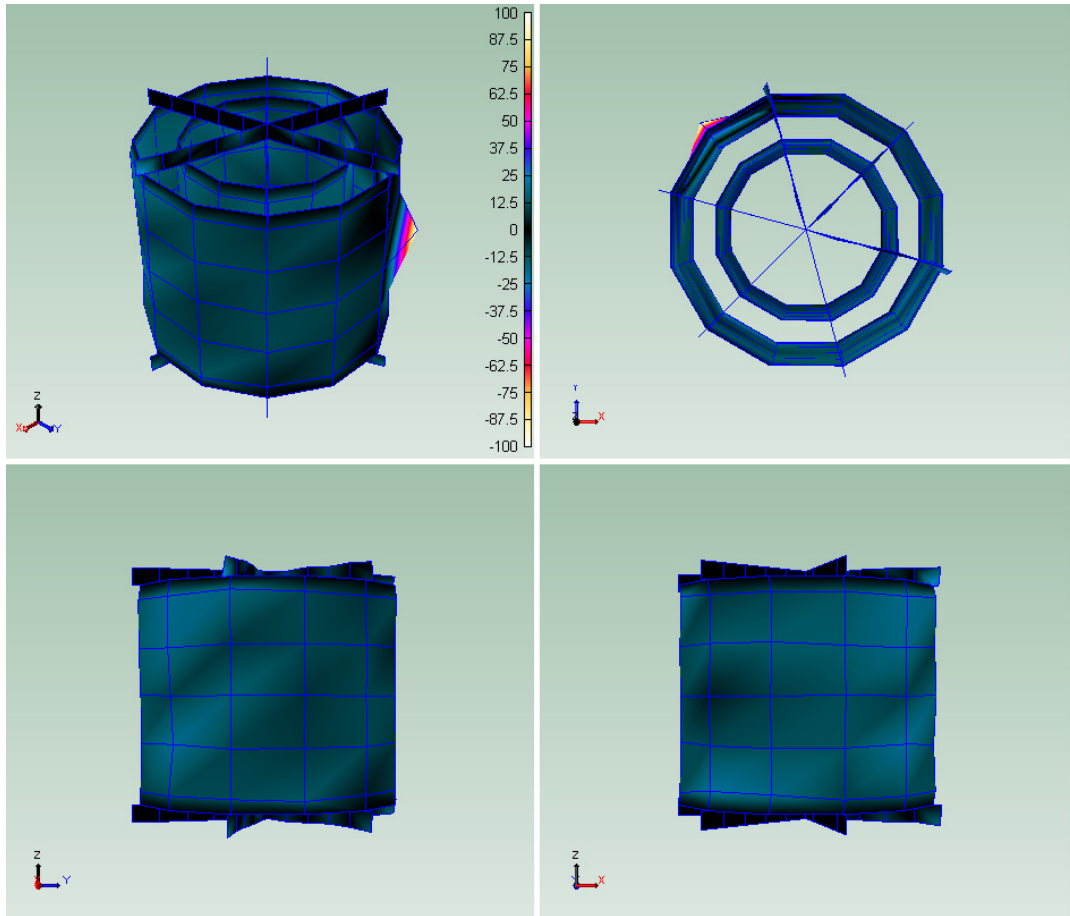
D 7 – Reactor 1 902.1 Hz Structural Mode.



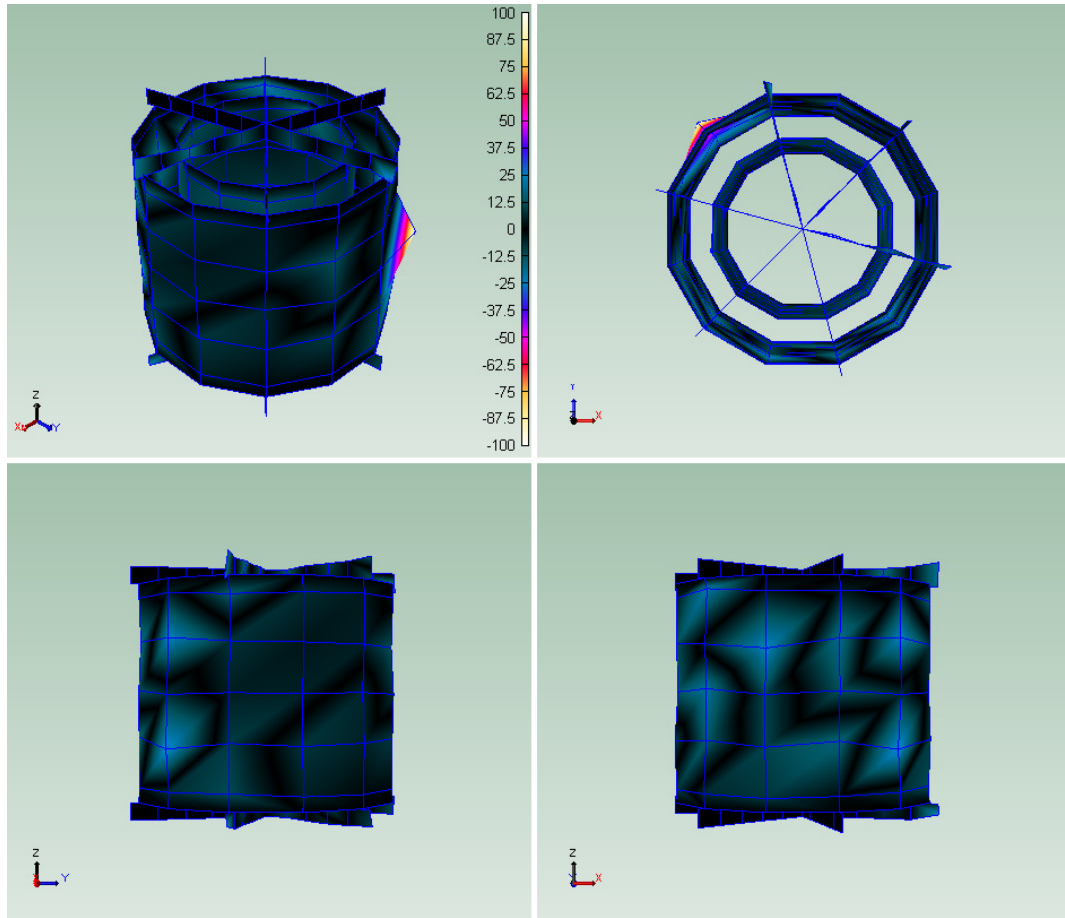
D 8 – reactor 1 919.2 Hz Structural Mode.



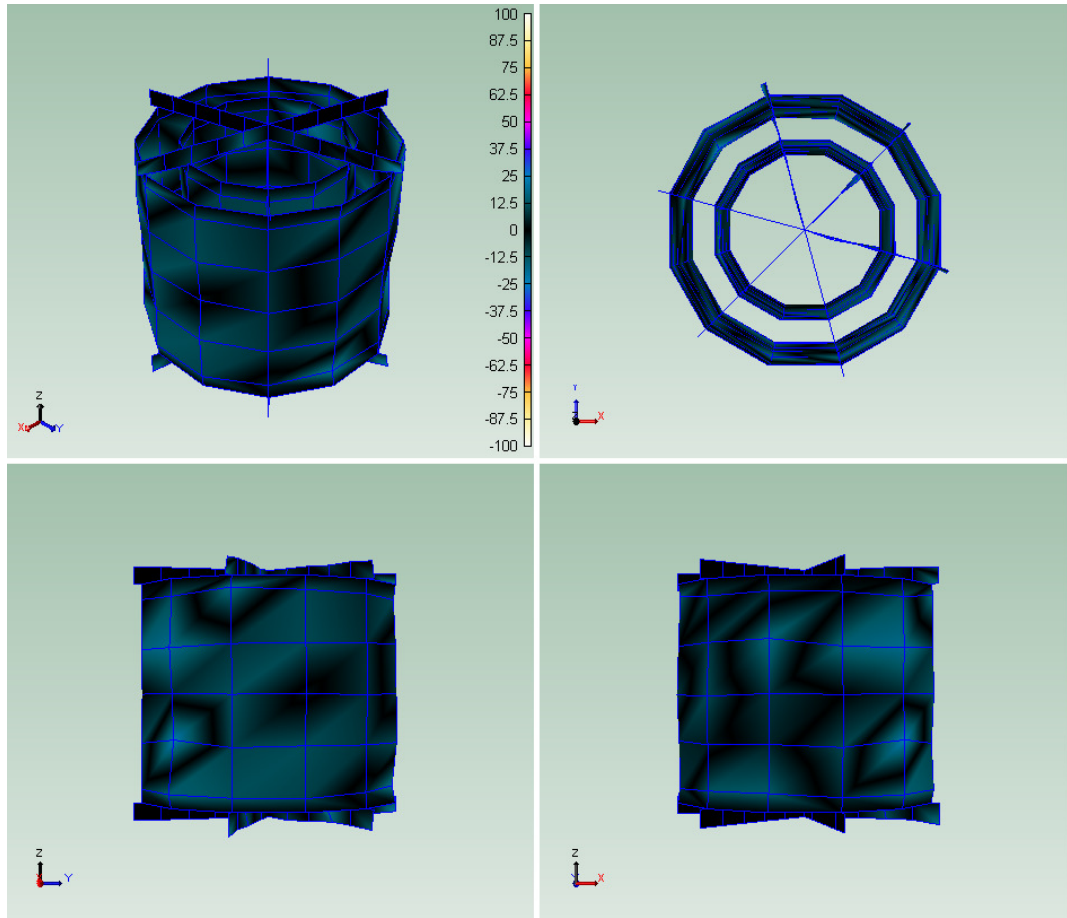
D 9– Reactor 1 935.8 Hz Structural Mode.



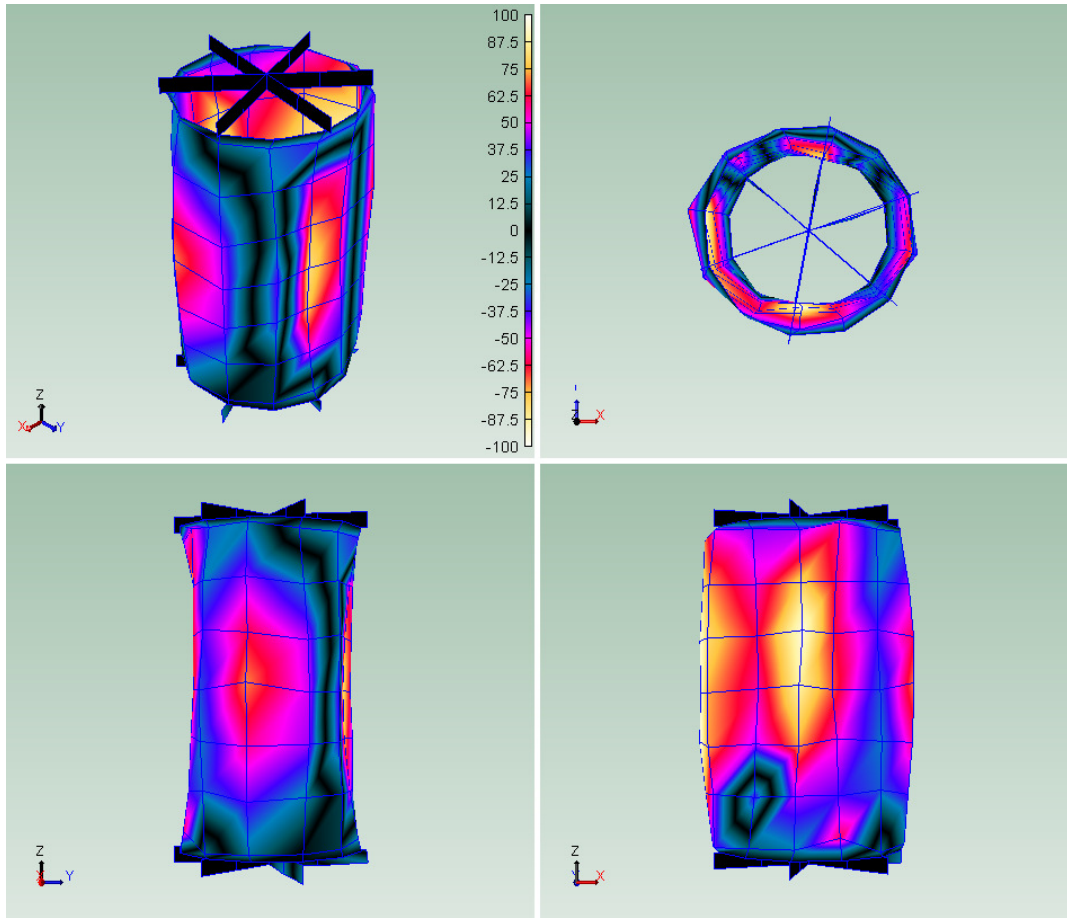
D 10 – Reactor 1 952.2 Hz Structural Mode.



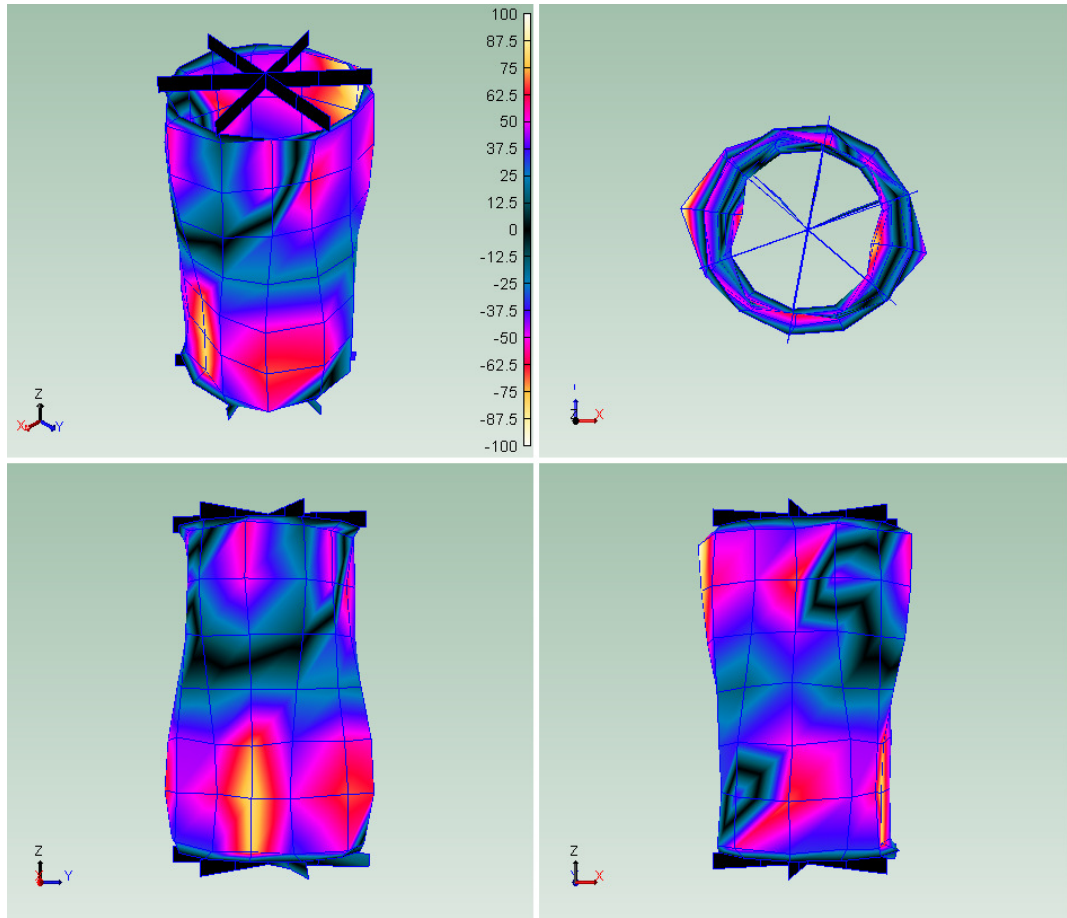
D 11 – Reactor 1 970.7 Hz Structural Mode.



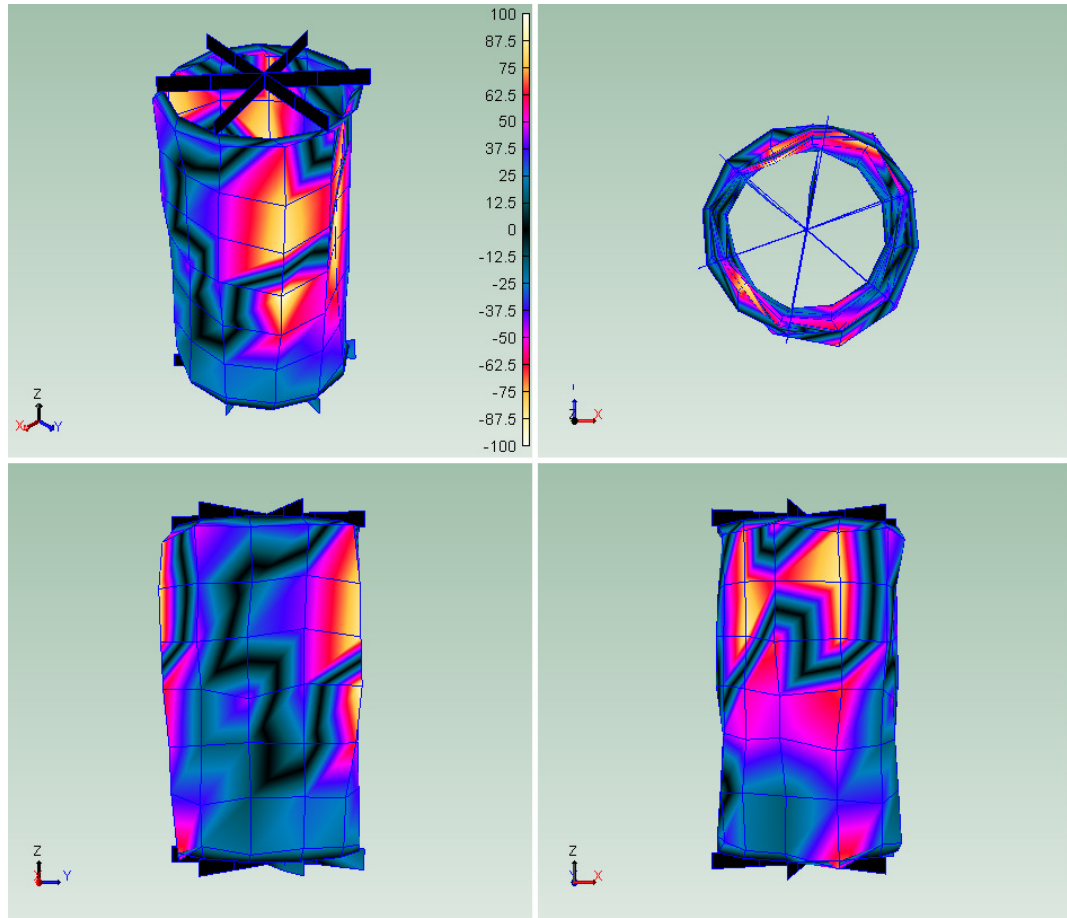
D 12 -Reactor 1 986.2 Hz Structural Mode.



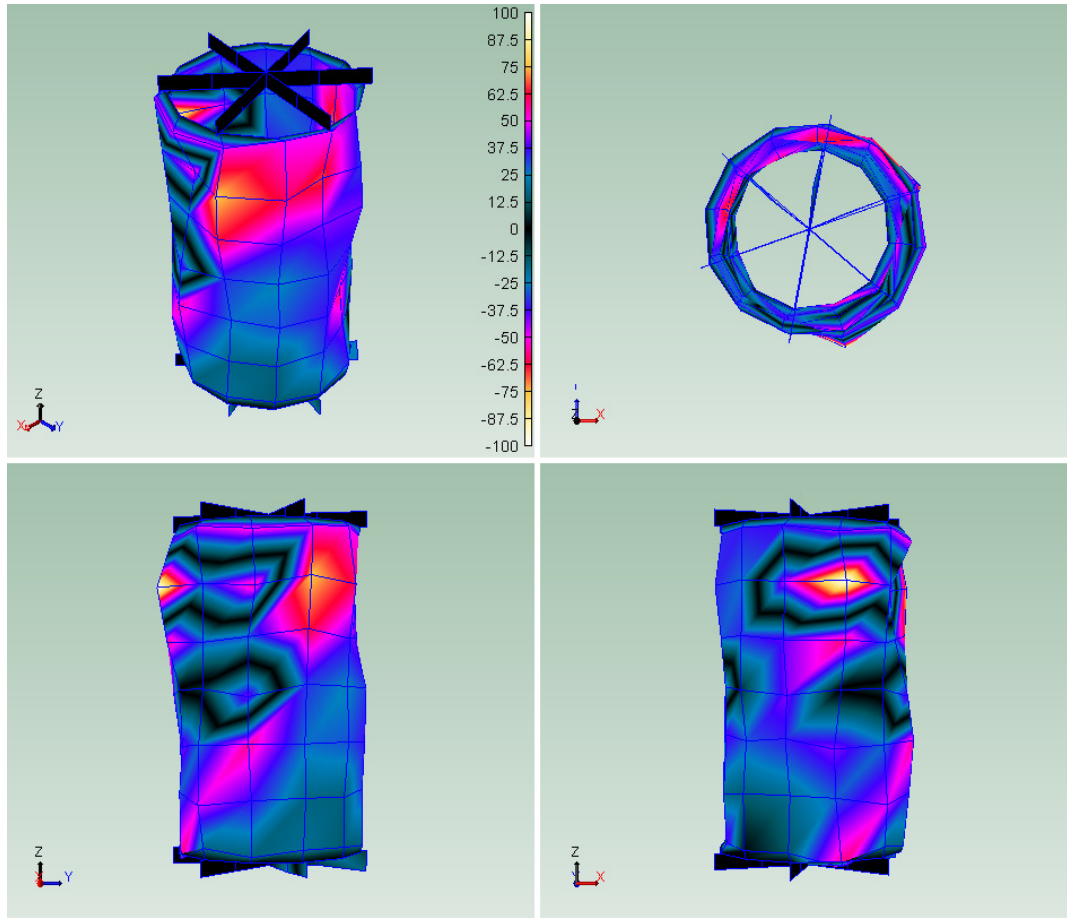
D 13 – Reactor 2 42.8 Hz Structural Mode.



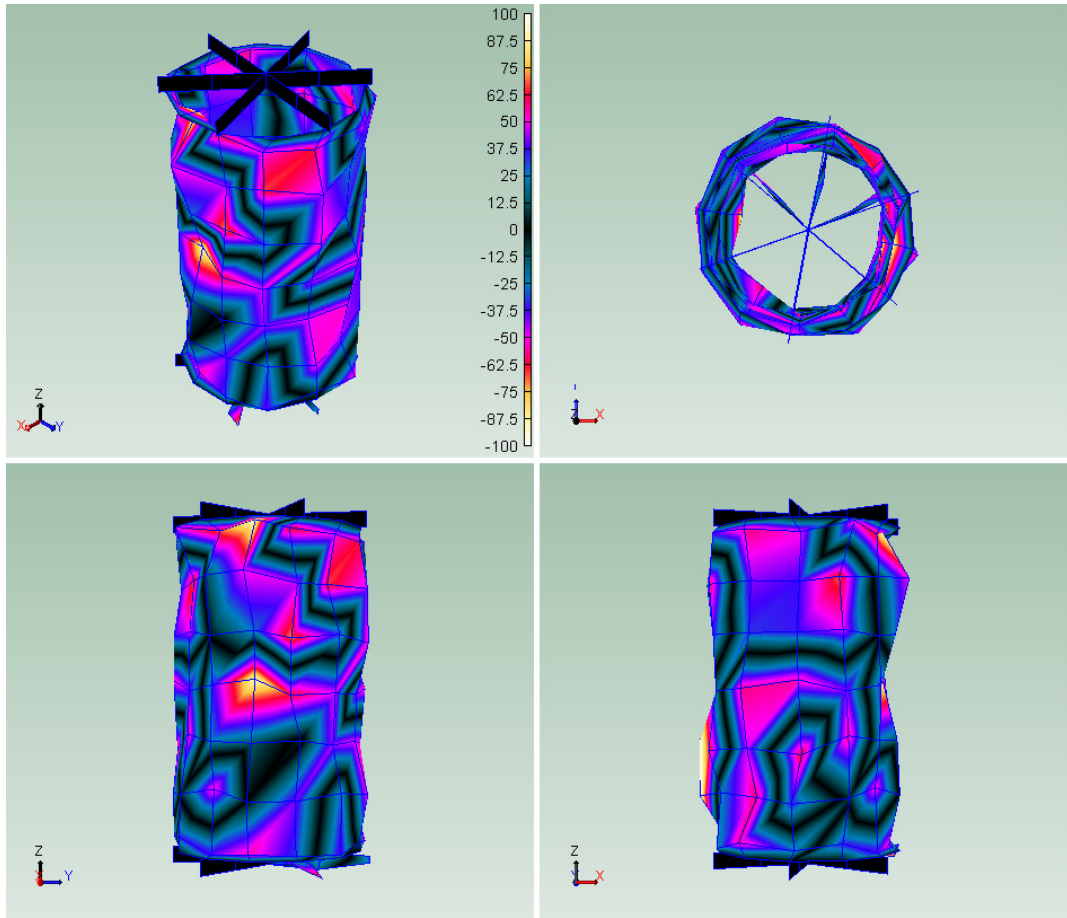
D 14 – Reactor 2 64.1 Hz Structural Mode.



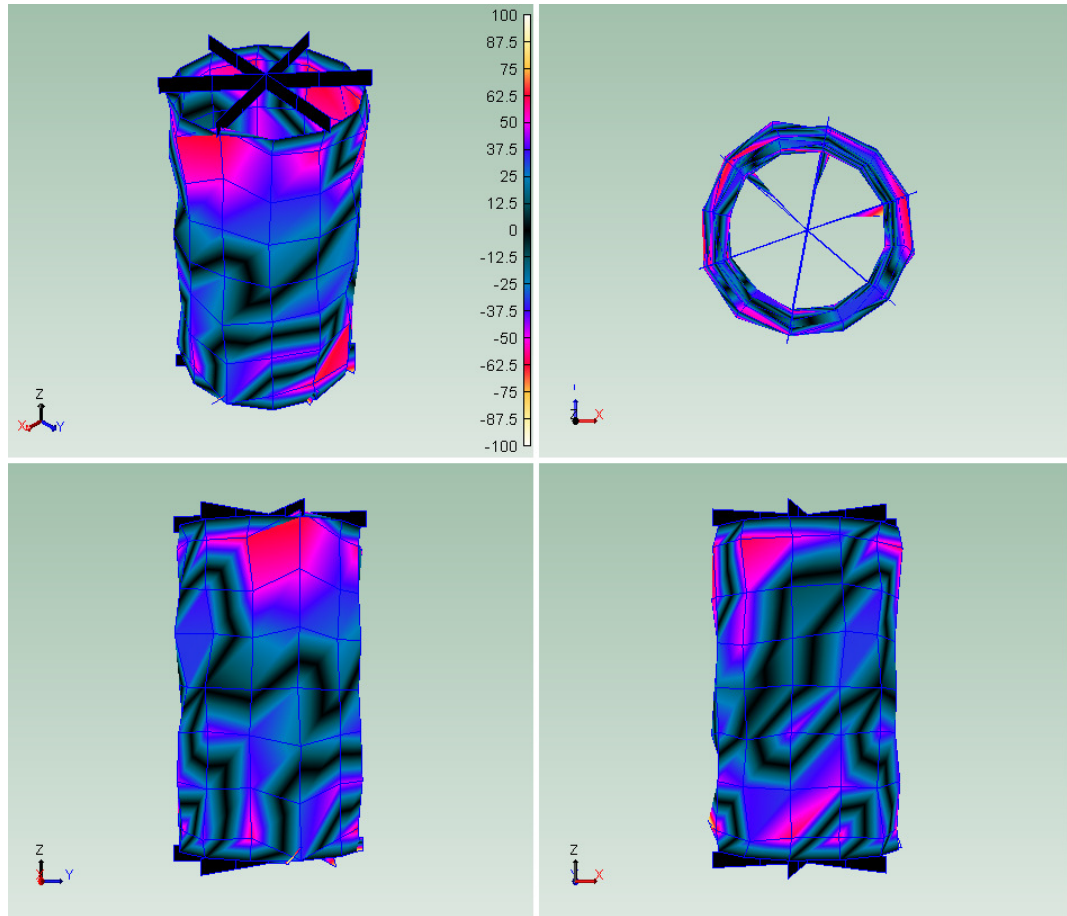
D 15 – Reactor 2 75.5 Hz Structural Mode.



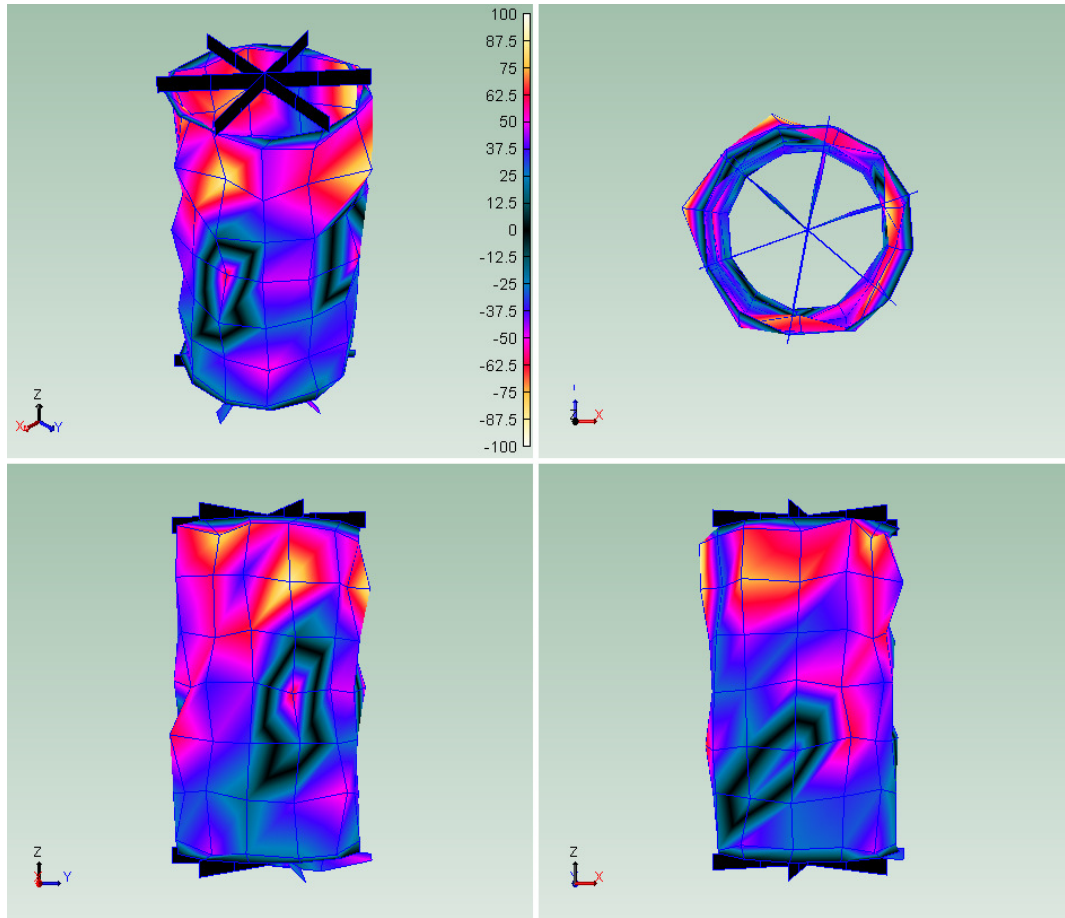
D 16 – Reactor 2 133.9 Hz Structural Mode.



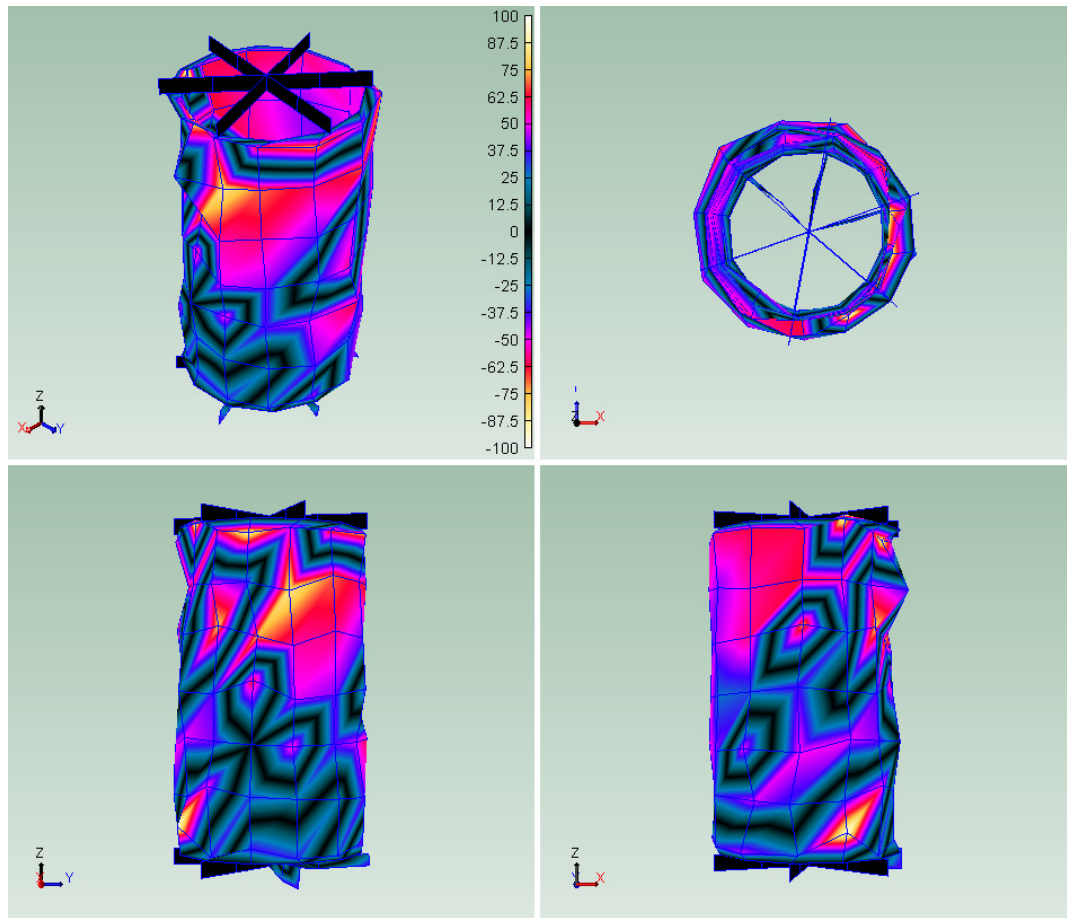
D 17 – Reactor 2 163.6 Hz Structural Mode.



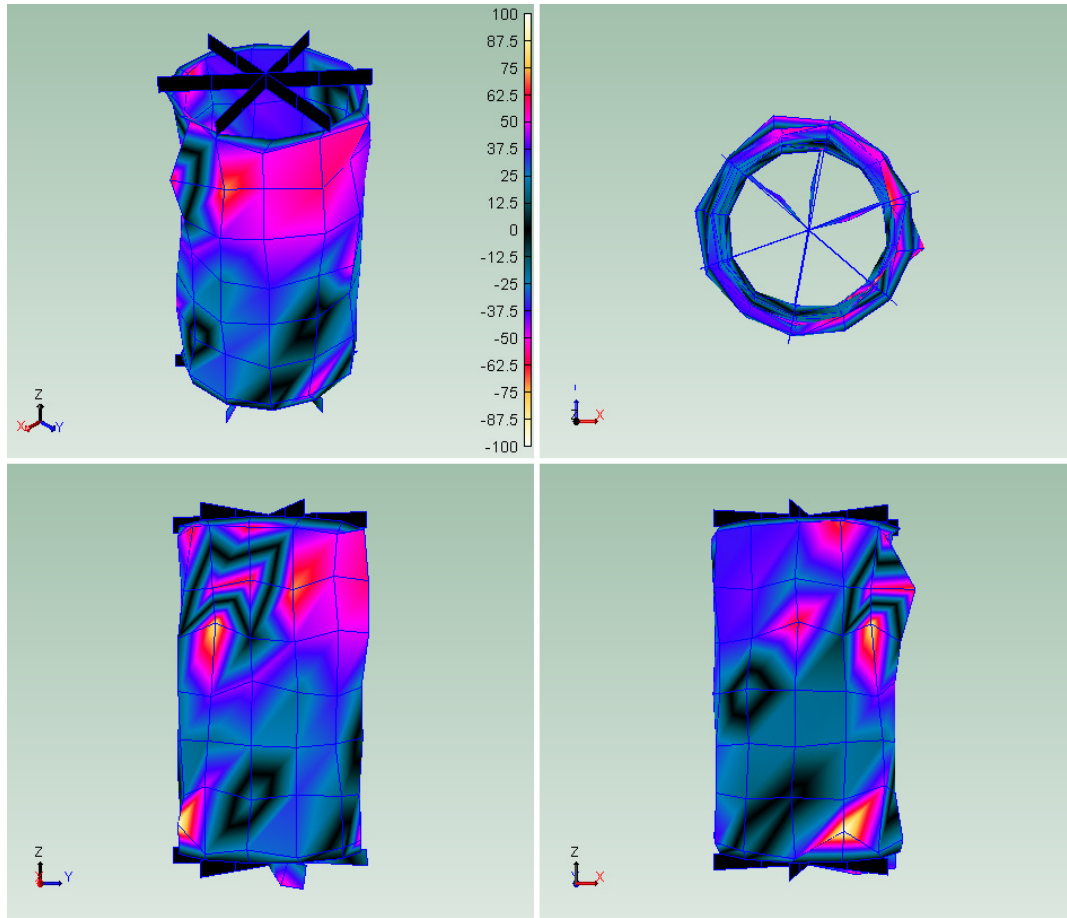
D 18 – Reactor 2 221.5 Hz Structural Mode.



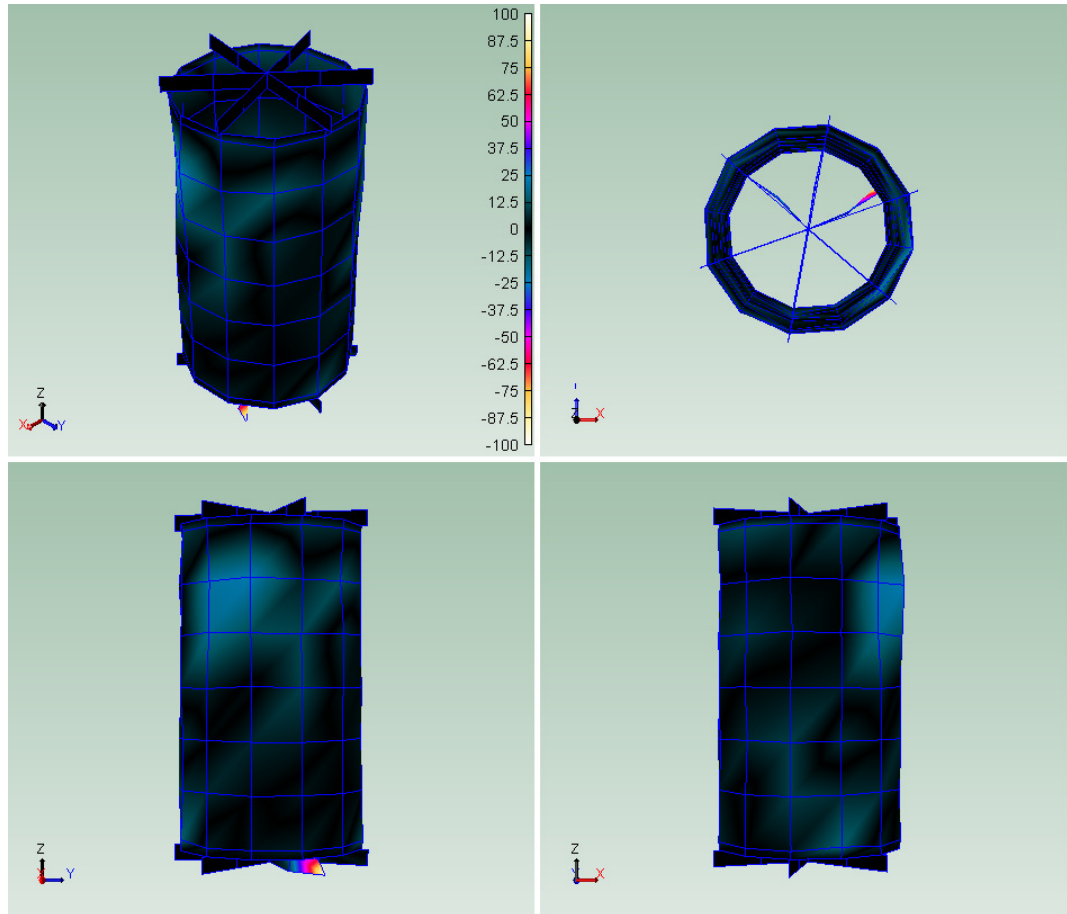
D 19 – Reactor 2 271.3 Hz Structural Mode.



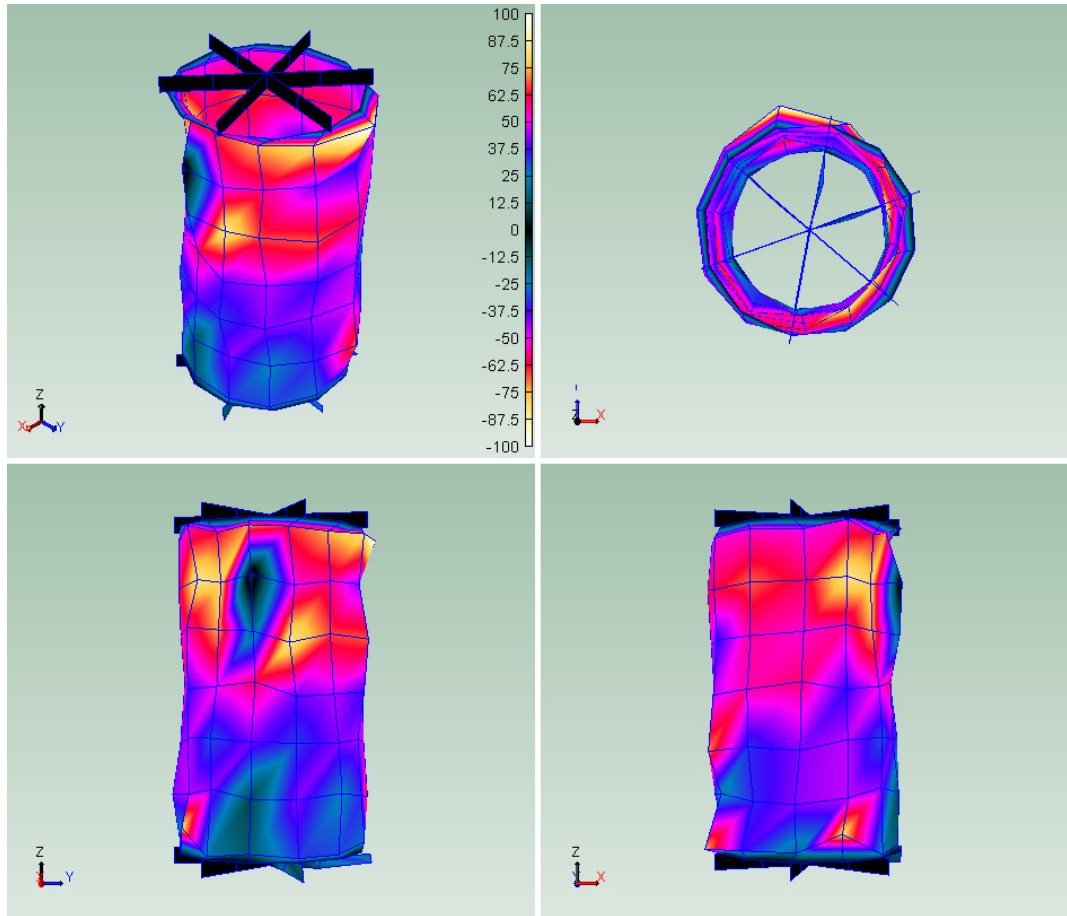
D 20 – Reactor 2 384.0 Hz Structural Mode.



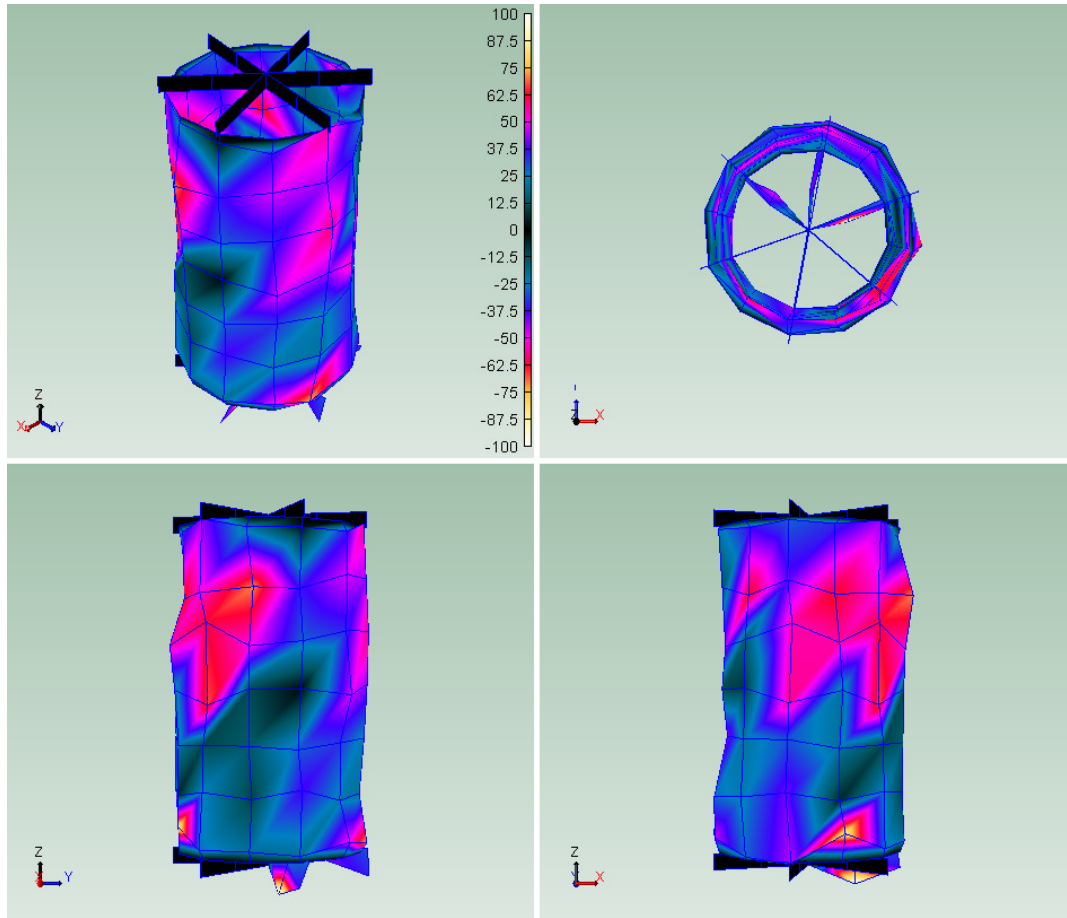
D 21 – Reactor 2 439.3 Hz Structural Mode.



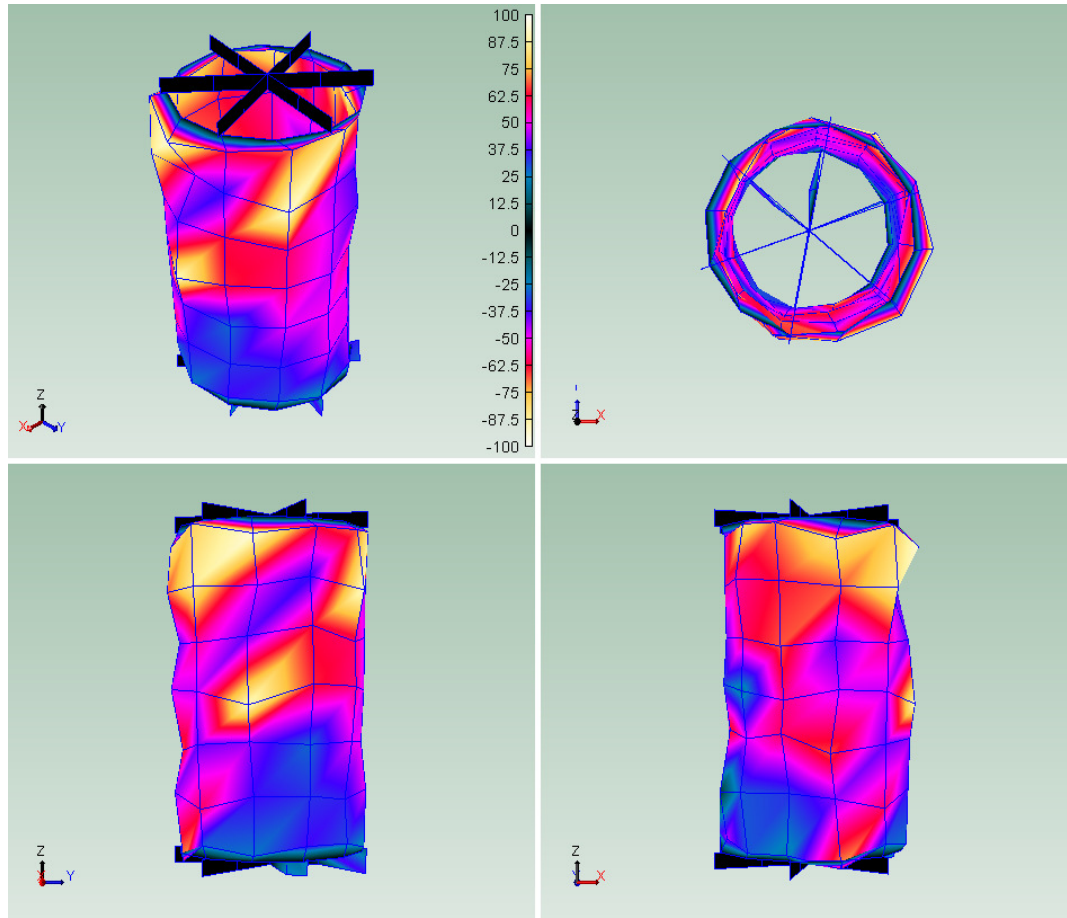
D 22 – Reactor 2 527.3 Hz Structural Mode.



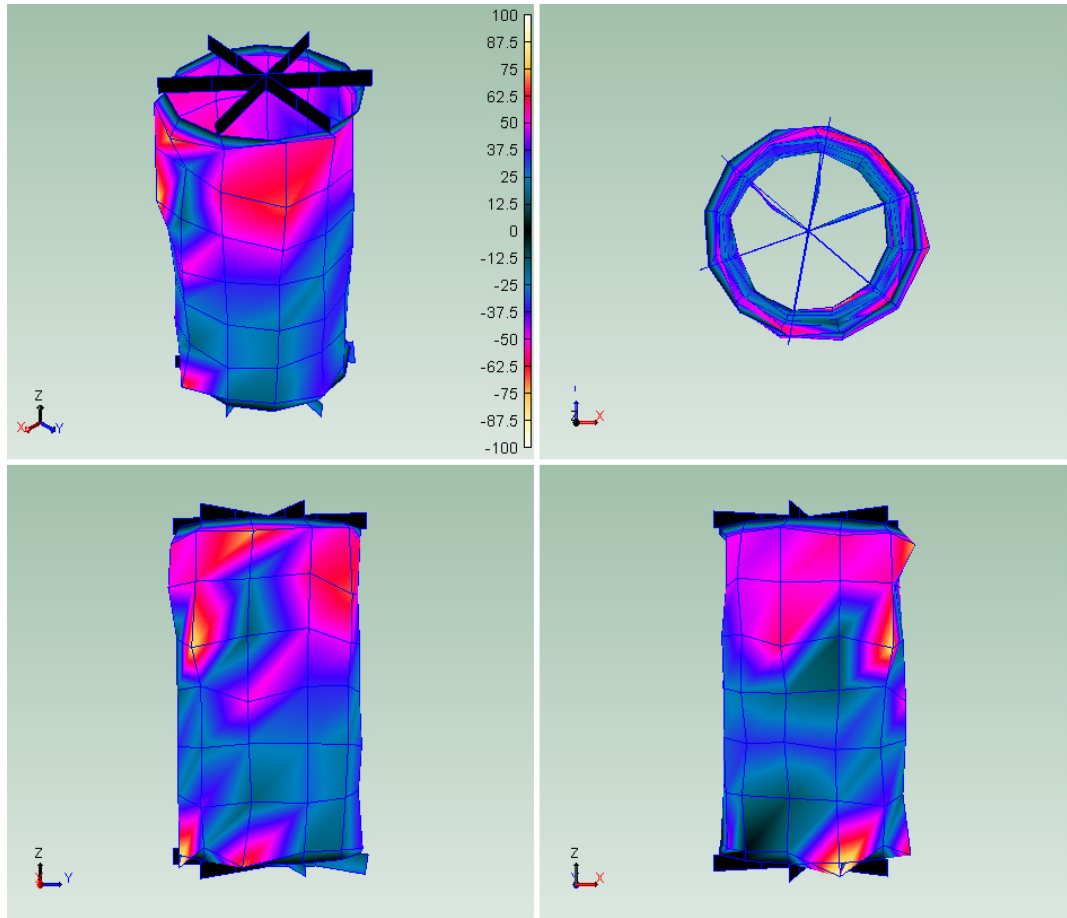
D 23 – Reactor 2 743.3 Hz Structural Mode.



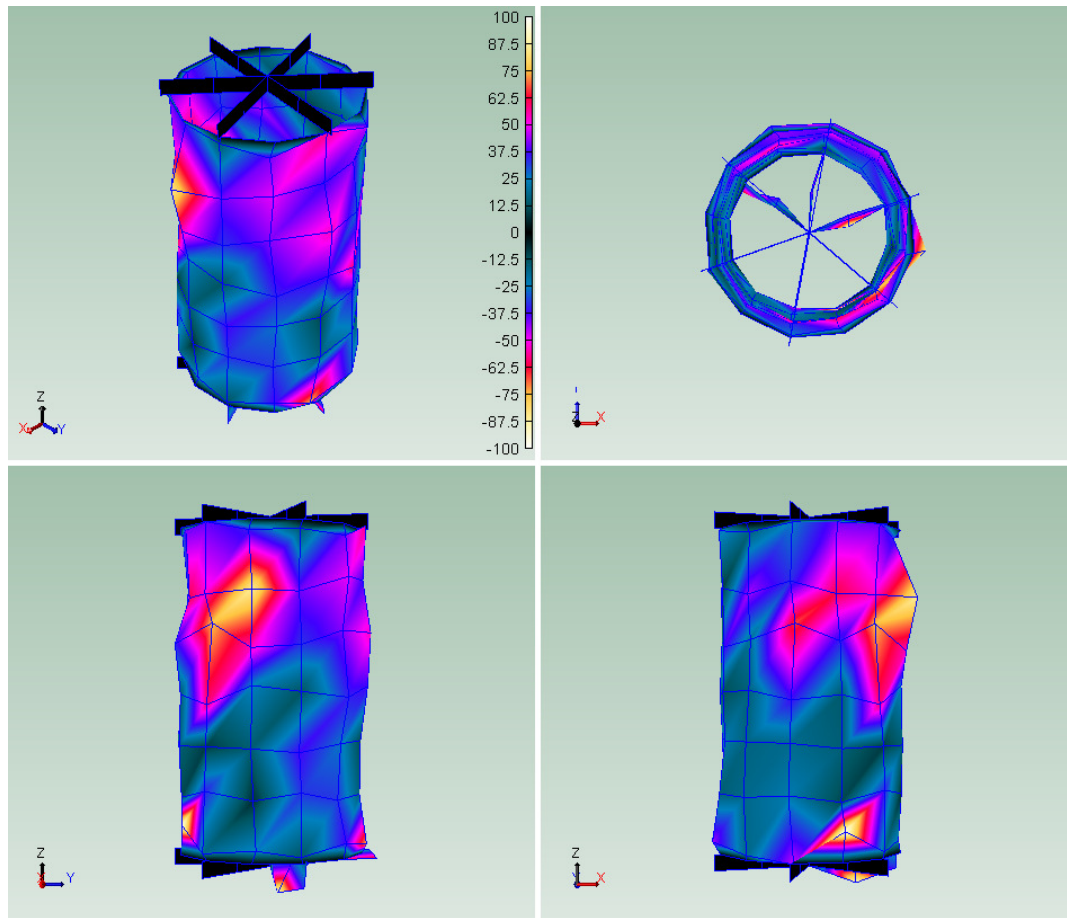
D 24 – Reactor 2 831.9 Hz Structural Mode.



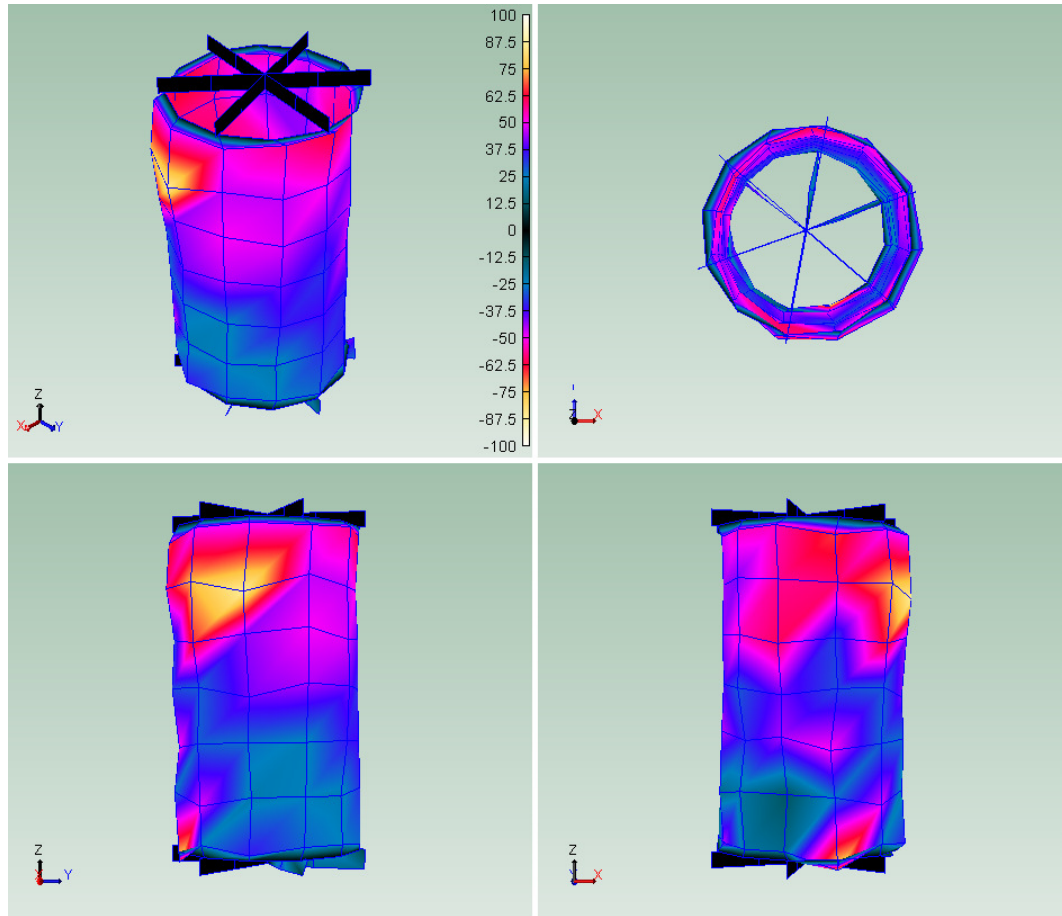
D 25 – Reactor 2 888.0 Hz Structural Mode.



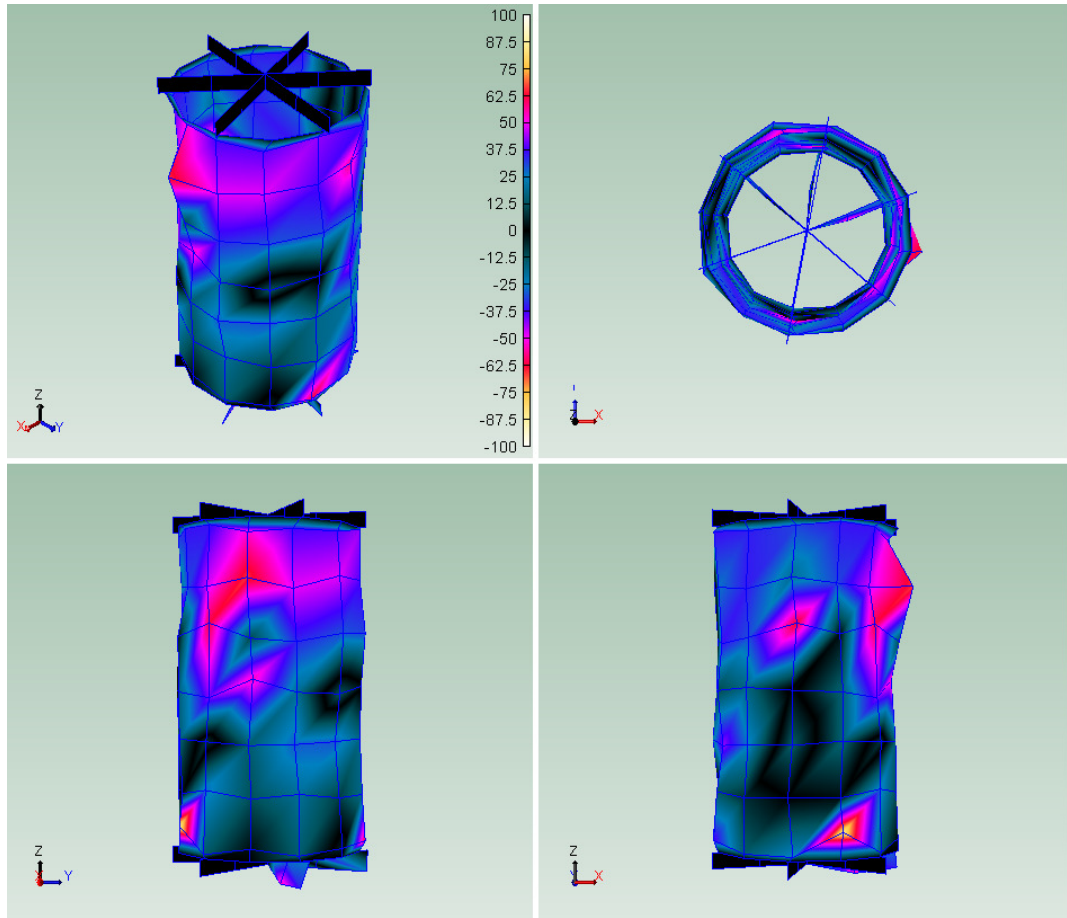
D 26 – Reactor 955.6 Hz Structural Mode.



D 27 – Reactor 2 1048.4 Hz Structural Mode.



D 28- Reactor 2 1081.2 Hz Structural Mode.



D 29 – Reactor 2 1153.3 Hz Structural Mode.

VITA AUCTORIS

NAME: Frank Angione

PLACE OF BIRTH: Windsor, ON

YEAR OF BIRTH: 1991

EDUCATION: Holy Names High School, Windsor, ON, 2009

University of Windsor, B.A.Sc., Windsor, ON,
2013

University of Windsor, M.A.Sc., Windsor, ON,
2015